UCLA
UCLA Electronic Theses and Dissertations

Title
Experimental Investigations of Convective Turbulence in Planetary Cores

Permalink
https://escholarship.org/uc/item/0c04t40v

Author
Hawkins, Emily Kate

Publication Date
2020

Peer reviewed|Thesis/dissertation

eScholarship.org Powered by the California Digital Library
University of California

UNIVERSITY OF CALIFORNIA
Los Angeles

Experimental Investigations of Convective Turbulence in Planetary Cores

A dissertation submitted in partial satisfaction
of the requirements for the degree
Doctor of Philosophy in Geophysics and Space Physics

by

Emily Kate Hawkins

2020

© Copyright by
Emily Kate Hawkins
2020

ABSTRACT OF THE DISSERTATION

Experimental Investigations of Convective Turbulence in Planetary Cores

by

Emily Kate Hawkins
Doctor of Philosophy in Geophysics and Space Physics
University of California, Los Angeles, 2020
Professor Jonathan M. Aurnou, Chair

The magnetic fields of planets and other bodies are created and sustained due to the turbulent motions of an internal fluid layer, a process known as dynamo action. Forward models are required to characterize the dynamics of rotating convective turbulence driving dynamo action due to the inability to obtain direct measurements of the internal fluid layers of planetary bodies. The characteristic flow velocities and length scales of dynamo systems remain poorly constrained due to the difficulty of modeling realistic planetary core conditions. Thus, the goal of this dissertation is to explore these key properties of core-style convection. To do so, I have conducted novel experiments aimed to better quantify the features of quasi-geostrophic turbulence using the UCLA large-scale rotating convection device, 'NoMag'.

I have completed a systematic study to simultaneously measure the heat transfer and bulk velocities of different rotating convective regimes at some of the most extreme laboratory conditions possible to date. The study of heat transfer is employed in most forward models of core-style convection. In laboratory experiments in particular, due to the relative difficulty of collecting velocity measurements, those of heat transfer alone are assessed, the dynamics of which are assumed to describe the the bulk velocity dynamics of the system. On the contrary, I utilize laser doppler velocimetry to obtain measurements of bulk velocities concurrently with the collection of temperature measurements for the characterization of system heat transfer. I find that heat transfer behavior is consistent with the results of past studies and is largely controlled by boundary layer dynamics. I further find that velocity behaviors do not directly

coincide with heat transfer behaviors in the parameter space studied. Instead, I show that a dynamical flow regime of quasi-geostrophic turbulence relevant to core flows is robustly reached, suggesting that it is possible to access realistic bulk dynamics in models that remain far from planetary core conditions.

Using the results of this study, I estimate the characteristic length scales of the flows of each experiment. These estimates from my data are compared with length scale estimates of numerous numerical models of planetary core convection. I conclude from this meta-analysis of forwards models that all evidence to date suggests that the theorized characteristic length scales of planetary dynamo systems co-scale with one another and are thus non-separable.

In two other studies that comprise the remainder of this dissertation, I further examine the applicability of laboratory models towards planetary settings. An experimental study on the influence of centrifugal buoyancy on rotating convection in water and in liquid metal was completed, where results agree with the recent numerical work of Horn and Aurnou (2018). It is found that the transition from Coriolis to centrifugally dominated convection depends on the strength of the centrifugal buoyancy relative to the gravitational buoyancy and the geometry of the cylinder in which experiments are conducted. These results are useful to ensure that the regime of rotating convection explored in a given experiment is relevant to planetary core flows, i.e. not centrifugally dominated. Separately, I conducted a series of spin up experiments with well-established theory to calibrate the NoMag apparatus and its measuring components. Further, the results from spin up experiments conducted with rough boundaries might have geophysical implications for the possible viscous coupling at Earth's core mantle boundary, as well as turbulent mixing in the global ocean.

The results of the studies presented in this dissertation clarify the relevance of long theorized and poorly tested dynamic length and velocity scalings of planetary core flows. Flows that are quasi-geostrophically turbulent are robustly observed in the laboratory data collected in this dissertation. The need for next generation models of planetary core flows is motivated by the results of the work herein. In particular, studies in which the characteristic length scales of core-style flows are directly quantified will undoubtedly enhance our understanding of the multi-scale turbulent physics driving planetary dynamo systems.

The dissertation of Emily Kate Hawkins is approved.

Carolina Lithgow-Bertelloni

James C. McWilliams

Lars Stixrude

Jonathan M. Aurnou, Committee Chair

University of California, Los Angeles

2020

Dedicated to my papa, Steve Burg

TABLE OF CONTENTS

LIST OF FIGURES

LIST OF TABLES

ACKNOWLEDGMENTS

First and foremost, I hold the deepest gratitude for my thesis advisor, Jonathan Aurnou, whose constant support, frequent feedback and guidance, and enthusiasm for the science we conducted together have shaped me into the scientist I am today. I remain thankful that he not only encouraged me to develop scientific ideas of my own, but he also allowed me to independently develop the skills needed to become the first scientist to manage and run the newest large-scale rotating convection device at the UCLA Spinlab, 'NoMag'. Thank you to my thesis committee members (past and present), Carolina Lithgow-Bertelloni, James McWilliams, Jonathan Mitchell, Gerald Schubert, and Lars Stixrude, each of whom devoted their time to provide helpful feedback that greatly improved the studies presented in this dissertation. I also thank Keith Julien and Stephan Stellmach for insightful discussions that generated crucial revelations in regards to the results presented in Chapters 4 and 5.

Thank you to my lab mates Jewel Abbate, Ashna Aggarwal, Jonathan Cheng, Alexander Grannan, and Yufan Xu, and to our lab visitors Vincent Bertin, Susanne Horn, Daphné Lemasquerier, Robert Long, Jonathan Mound, and Sietze Oostveen for many engaging discussions and welcome distractions. I also acknowledge undergraduate students Rebecca Deshetler, Norris Khoo, Taylor Lonner, and Timothy Pilegard for providing me with a mentoring role by working closely with me in the lab. I thank the 2014 NoMag Fabrication Team for helping me to complete the construction of this new laboratory device: Jonathan Bridgeman, Christina Daniel, Ryan Marakas, Samuel May, Tong Mu, David Ortega, Steffan Tai, Steven Tomlinson, and Anthony Vong. I also thank my most recent office mates Lydia Bingley, Richard Hart, Mark Hubbert, Yi Qi, Yanan Yu, and Cong Zhao for sharing a productive work space to write and reflect with one another.

I sincerely thank Alexandra Doyle, Michelle Gaston, Rachel Kennison, Erin Sanders O'Leary, and Shanna Shaked for allowing me to join them in improving instructional development at UCLA through my work as a Teaching Assistant Consultant. I would like to thank a few professors in particular who additionally supported me in my numerous academic endeavors: Mackenzie Day, David Jewitt, Abby Kavner, Christopher Russell, William Schopf,

and Tina Treude. Without the continual support of academic staff including Richard Fort, Henry Gonzalez, William Greer, Emmanuel Masongsong, David Riley, Shylo Stiteler, and Eric Wessenauer, I also would not have been successful in completing my graduate studies.

I cannot thank fellow grad students Amanda Garcia, Ky Hughson, Erin Leonard, Raquel Nuno, Rob Ulrich, and Mickey Villarreal enough for their constant support, in particular for always making me laugh on a tough day and for calming me down whenever I had a panicked moment about being able to complete my graduate studies. I also thank my close friends Georgia Moriyama and Elle Noon for their endless support and encouraging words. I thank Evoke Dance Company and all of its members for providing me with a much needed and unique outlet to release stress during my graduate studies. I also thank Alexandrea Arnold, Jordyn Moscoso, Zoe Pierrat, and Katie Tutie for co-founding the UCLA Society of Women Geoscientists with me in order to create a healthy outlet to share our stories as women in academia. Thank you to the UCLA Bruin Spacecraft Group and its members for supporting me to lead a team to send a small experiment into microgravity, an indescribably fun and unforgettable experience.

It most certainly would not have been possible for me to finish this dissertation without the support of my family. I thank my mother Shari Hawkins for always taking my phone calls–no matter what the hour–and listening to my daily trials and tribulations with an open mind. Thank you to my father Vince Hawkins for always providing positive words of encouragement, and to my brother Ben Hawkins for his love and support. I thank my grandparents Sue and Steve Burg for their special support on a weekly basis, and my aunt Cynthia Burg, uncle Scott Burg, and cousins Julie Burg, Jill, Ken, Madison, Sasha, and Ari Cooper for being a frequent and local support in the Los Angeles area. Thank you to my godmother Denise Miney and her son Kenny Shima for their continued support as well. I must thank the loving pets in my life that have sat by my side, bringing me immense comfort as I completed my dissertation work: dogs Biscuit, Rhaego, Sammy, and cat Violet. Lastly, a note about the dedication of this dissertation: my loving grandfather, 'papa' Steve Burg, particularly supported my academic endeavors and edited nearly all of my manuscripts until he passed in January of 2019. It is my honor to dedicate my graduate work in his name.

This work is supported by the Earth Sciences Division Geophysics Program of the United States National Science Foundation (Grants 1547269 and 1853196). The contents of Chapters 2, 3, and 4 are modified from a manuscript in review for publication in which I am the lead author. The material in Chapters 5, 6, and 7 are separate studies, each of which are in preparation for submission to scientific journals in which I am also lead author.

VITA

2014	B.A., Physics, Occidental College.
2014	Minor, Mathematics, Occidental College.
2014–2020	Graduate Student Researcher, University of California, Los Angeles.
2014–2020	Teaching Assistant, University of California, Los Angeles.
2016	NASA Space Grant.
2017	M.S., Geophysics and Space Physics, University of California, Los Angeles.
2017	ASGSR Ken Souza Student Spaceflight Competition Grant.
2017–2020	Lead Teaching Assistant for the EPSS Department, University of California, Los Angeles.
2019	Charles E. and Sue K. Young Fellowship, University of California, Los Angeles.
2020	Tenure-track Assistant Professor of Physics, Loyola Marymount University.

PUBLICATIONS

E. K. Hawkins, J. S. Cheng, T. Pilegard, S. Stellmach, K. Julien, and J. M. Aurnou (2020), "Geostrophic turbulence in laboratory models of planetary core convection" *Geophys. J. Int.*, In review.

E. K. Hawkins, K. Julien, and J. M. Aurnou (2020), "Assessing length scales in models of planetary core flow", *Nature Geoscience*, In prep.

E. K. Hawkins and J. M. Aurnou (2020), "The effects of centrifugal buoyancy on rotating convection in water and in liquid metal", *Phys. Rev. Fluids*, In prep.

E. K. Hawkins, T. Pilegard, A. M. Grannan, J. S. Cheng, and J. M. Aurnou (2020),"The spin up of a fluid in a cylindrical container using smooth and rough boundaries", *Phys. of Fluids*, In prep.

CHAPTER 1

Introduction

1.1 Geophysical and Astrophysical Context

The global magnetic fields of planets and other bodies are generated and sustained due to the turbulent motions of an internal conducting fluid layer via a mechanism termed "dynamo action" [Elsassar (1939), Jackson (2003), Finlay et al. (2012), Roberts and King (2013), Nataf and Schaeffer (2015)]. Planetary dynamo action converts the the mechanical, or kinetic, energy of turbulent fluid motions into magnetic energy. Convective instability in planetary cores is driven by the release of heat that is generated due to: 1) planetary formation, 2) radioactive decay, and 3) the growth of an inner core [e.g., Stacey (1992), Davidson (2001), Jones (2011), Christensen (2019)]. This release of heat drives thermocompositional convective motions. Other possible sources of fluid instabilities that can give rise to turbulent motions include various mechanical forcings due to the precession, nutation, libration, and tides of a body [Comstock and Bills (2003), Tilgner (2005), Cébron and Hollerbach (2014), Grannan et al. (2014), Le Bars et al. (2015), Grannan et al. (2017), Cébron et al. (2019)].

In Earth's case, its structure is the best constrained of all of the planets in our solar system due to the combination of seismological and spacecraft measurements [e.g., Elsasser (1950), Merrill et al. (1998), Poirier (2000), Mandea and Korte (2011), Olsen and Stolle (2012)]. Earth is comprised of an innermost layer (labeled the inner core) primarily consisting of solid iron, a liquid outer core also primarily comprised of iron but in the liquid state, a rocky mantle region, and several thin outermost layers containing the crust, the liquid ocean, and the gaseous atmosphere. Paleomagnetic data of the geomagnetic field show that the field has existed on a long geologic timescale, upwards of 4 billion years [McElhinny

and Senanayake (1980), Tarduno et al. (2007), Hulot et al. (2010), Tarduno et al. (2015)]. In addition, observations that the geomagnetic field varies on differing timescales suggest that geomagnetic field generation must be due to a dynamic process involving motion. For example, secular variations in Earth's field are observed on timescales that are short, i.e. on the order of tens to hundreds of years, in comparison to its overall long term existence [Bloxham et al. (1989), Gubbins and Bloxham (1987), Finlay and Jackson (2003), Gillet et al. (2010), Cao et al. (2018)]. The only possible place that motion can produce planetary scale magnetic fields is in the large internal liquid metal layers of the planets, such as Earth's liquid iron outer core. Furthermore, it is not possible that permanent magnetization exists in Earth's interior since local temperatures are much hotter than the Curie temperatures of its interior materials [Ahrens (1995), Stacey and Davis (2008)]. In addition, any ancient magnetic field originating from Earth's formation decayed on a timescale that is much shorter than the observed length of existence of the geomagnetic field. Thus, the generation and sustainment of the geomagnetic field must be due to fluid motions in the outer core.

The observations of the global scale magnetic fields of other planets in our solar system, primarily from spacecraft magnetometer measurements, also suggest the existence of temporal variations [cf. Stanley and Glatzmaier (2010), Schubert and Soderlund (2011), Christensen (2019)]. The global field of Jupiter, for example, was recently mapped by the Juno spacecraft, revealing a unique structure in which most of the planet's magnetic flux emerges from a narrow band in the northern hemisphere and returns through an intense, isolated magnetic flux patch near Jupiter's equator [Connerney et al. (2018)]. These strong concentrations of magnetic flux imply the existence of horizontal magnetic field gradients at the borders of these patches, suggesting that strong secular (temporal) variation of the magnetic field is likely [Moore et al. (2018)].

Perplexingly, only two planets in our solar system do not presently possess global scale fields: Mars and Venus. The Mars Global Surveyor detected magnetic anomalies associated with the permanent, remnant magnetization of crustal rocks due to an ancient, extinct dynamo [e.g. Connerney et al. (2001), Lillis et al. (2004)]. While evidence exists that Mars possesses a metallic core that is at least partially molten, it is surmised that either this

metallic core cooled to the point that thermal convection and thus dynamo action were no longer sustainable, or the core cooled to the point of growing a large enough solid inner core such that dynamo action could no longer occur in the small surviving liquid outer core [Folkner et al. (1997), Yoder et al. (2003), Langlais et al. (2010)]. In the case of Venus, there is no direct evidence from any spacecraft measurements that an ancient dynamo existed since the high surface temperatures of this body make it unlikely for crustal magnetization to have preserved the signature of a past dynamo. It is possible that Venus has cooled such that purely thermally driven convection cannot drive dynamo action, while not being cooled enough for an inner core to form and drive compositionally buoyant convection to drive a dynamo [O'Rourke et al. (2018)]. Alternatively, it is also plausible that a small heat flow out of Venus' core exists with a lack of plate tectonic activity such that the core is not convective [Nimmo (2002), Driscoll and Bercovici (2013), Driscoll and Bercovici (2014)].

Our knowledge of global planetary magnetic fields indicates that the fields are driven by convective turbulence. It is thought that mechanical forcing mechanisms to drive dynamo action may be relevant for smaller bodies such as Earth's moon [e.g. Cébron et al. (2019)], Ganymede (moon of Jupiter) [e.g. Cébron et al. (2012)], and Vesta (asteroid) [e.g. Fu et al. (2012)], and therefore will not be a focus of this dissertation aimed to study planetary magnetic field generation. The magnetohydrodynamic flow involved in the conversion of mechanical to electrical energy in planetary dynamos is quantified by a set of governing equations. Specifically, these equations are: 1) the continuity equation governing the conservation of fluid mass in the system, 2) the Navier-Stokes equation governing the evolution of momentum in the rotating reference frame of the fluid, 3) the heat equation governing the evolution of temperature, and 4) the induction equation governing the evolution of the magnetic field, and can be given respectively as:

$$\nabla \cdot \vec{u} = 0, \tag{1.1}$$

$$\frac{D\vec{u}}{Dt} + 2\vec{\Omega} \times \vec{u} = -\frac{1}{\rho_0}\nabla P + \alpha\vec{g}(T - T_0) + \alpha\Omega^2\vec{r}(T - T_0) + \nu\nabla^2\vec{u} + \frac{1}{\rho_0}\vec{J} \times \vec{B}, \tag{1.2}$$

$$\frac{DT}{Dt} = \kappa \nabla^2 T, \tag{1.3}$$

$$\frac{D\vec{B}}{Dt} = \vec{B} \cdot \nabla \vec{u} + \eta \nabla^2 \vec{B} \tag{1.4}$$

[cf. Davidson (2001)]. Equations (1.1)–(1.4) are valid under the Boussinesq approximation in which variations in density are accounted for only in the gravitational buoyancy term and are neglected in all other terms in (1.2). The Boussinesq approximation simplifies the system in a manner that is well-founded, widely used, and argued to be relevant to the fluid processes involved in planetary dynamo action. We comment below on the exclusion of the consideration of compositionally driven convection in (1.1)–(1.4).

In (1.1)–(1.4), dimensional quantities are as follows: $\vec{u}$ [m/s] is the fluid velocity, Ω [rad/s] is the rotation rate of the fluid, ρ_0 [kg/m^3] is the mean density of the fluid, P [kg/(m s^2)] is the pressure, α [1/K] is the thermal expansivity of the fluid, $\vec{g}$ [m/s^2] is the gravitational acceleration, $(T - T_0)$ [K] is the local temperature difference in the fluid with respect to the mean fluid temperature, T_0, $\vec{r}$ [m] is the radial position vector, ν [m^2/s] is the kinematic viscosity of the fluid, $\vec{J}$ [A/m^2] is the electric current density of the fluid, B [T] is the magnetic field, T [K] is the local fluid temperature, κ [m^2/s] is the thermal diffusivity of the fluid, and η [m^2/s] is the magnetic diffusivity of the fluid. The terms in (1.2), from left to right, are: the material rate of change of momentum, the Coriolis acceleration, the pressure gradient, thermal buoyancy, centrifugal buoyancy, viscous diffusion, and the Lorentz term. In the thermal energy equation, (1.3), the lefthand side term is the material rate of change of the temperature field, which is balanced on the righthand side by thermal diffusion. For the magnetic induction equation, the material rate of change of the magnetic field on the lefthand side of (1.4) is balanced by the induction and the diffusion of the magnetic field on the righthand side of (1.4).

The Boussinesq approximation is employed in the majority of dynamo studies [Jones (2011), Roberts and King (2013)]. Focusing on thermally driven convection, we neglect compositional convection when using this approximation in the system of governing equations

(1.1)–(1.4), where the equation of state (e.o.s.) for the fluid density is given as:

$$\rho = \rho_0 + \rho' = \rho_0(1 - \alpha(T - T_0)), \tag{1.5}$$

where ρ_0 is the mean (background) fluid density and ρ' is any perturbation to ρ_0 [Kundu et al. (2012)]. While the physical origins of thermal and compositional convection are different, it remains unclear whether or not the dynamics of these two phenomena are very different [cf. Jones (2015), Bouffard et al. (2019)]. In this dissertation, I focus on the system described by (1.1)–(1.4) in which thermally driven convection occurs as a crucial first step towards characterizing the thermocompositional convection underlying planetary dynamos.

Under the Boussinesq approximation with the density e.o.s. given by (1.5), the buoyancy term in (1.2), generally $\rho\vec{g}$ where $\rho(P, T)$ is the fluid density, becomes a purely thermally driven convective term, and heating caused by viscous and ohmic dissipation drops out of the thermal energy equation, (1.3) [cf. Davidson (2001)]. In order for this approximation to be applicable to planetary cores, density perturbations that are caused by variations in temperature or pressure must be small (i.e. much smaller than the mean fluid density). It is argued that the Boussinesq assumption can be used in the study of dynamo systems since an isentropic adiabatic temperature gradient can be used decently well to describe the actual (superadiabatic) temperature gradient in Earth's core [e.g. Smylie and Rochester (1981), Schubert and Soderlund (2011)]. This assumption therefore neglects compressibility effects, which play a role in convective processes of planetary bodies, including in Earth's core [cf. Glatzmaier and Roberts (1996), Jones (2009), Sreenivasan (2010), Davies and Gubbins (2011), Glatzmaier (2013)].

Furthermore, the thickness of the convecting region must be small compared to the density scale height in order for the Boussinesq approximation to be valid to describe core flows. The number of density scale heights in a layer is given by $N_\rho = ln(\rho_\mathrm{b}/\rho_\mathrm{t})$, where ρ_b (ρ_t) is the density at the bottom (top) of the outer core region, respectively [Schubert (2001)]. In Earth's core, for example, density increases by roughly 23% across the fluid layer and thus the layer thickness corresponds to only $N_\rho \simeq 0.2$ density scale heights, further

indicating the applicability of the Boussinesq approximation to Earth's core [Schubert and Soderlund (2011)]. In contrast, the ratio of dynamo region thickness to density scale height is of order unity or larger in the gas and ice planets, indicating that compressibility effects may not be ignored [Guillot (2005), Evonuk (2008), Gastine et al. (2012)].

Equations (1.1)–(1.4) are coupled, namely the flow velocity, $\vec{u}$, characterized by the momentum equation of (1.2) is directly coupled to the magnetic induction equation of (1.4) describing the evolution of the magnetic field, $\vec{B}$. The first term on the righthand side of (1.4) generates the magnetic field via shearing motion. Commonly referred to as the 'Ω-effect', zonal flows can shear magnetic field components that are perpendicular to the flow direction, creating now parallelly directed field components. The schematic of Figure 1.1a) illustrates the Ω-effect in which an initially vertical magnetic field line is sheared by a perpendicular velocity field, resulting in a bent field line that gains a horizontally directed component [cf. Roberts (2015)].

In addition, according to mean field dynamo theory, helical motions, characterized by the fluid's helicity, $H = \vec{u} \cdot \vec{\omega}$, where $\vec{\omega}$ is the vorticity ($\vec{\omega} = \nabla \times \vec{u}$), are an essential ingredient in dynamo systems [cf. Parker (1955), Radler (2007), Krause and Radler (2016), Moffatt and Dormy (2019)]. As illustrated in Figure 1.1b), these inherently three-dimensional fluid motions can deform an initially toroidal (i.e. (θ, ϕ) spherically directed) field component that is simultaneously twisted into a loop of magnetic flux by motion due to rotation with vorticity $\vec{\omega}$. This process is often referred to as the 'α-effect'. Such twisted magnetic flux loops may detach, thus creating a field component that is perpendicular to the original field orientation when magnetic diffusion is large enough for magnetic reconnection to occur [cf. Roberts (2015)]. Dynamo action is possible even without mean helicity existing in the flow, so long as random helicity variance exists [Yousef et al. (2008), McWilliams (2012)]. Lastly, the rightmost term in (1.4) is the diffusion of the magnetic field and must not be larger in magnitude than induction processes in order for a large-scale (i.e. global) magnetic field to be sustained over time [e.g. Starchenko and Jones (2002)].

Figure 1.2 displays a schematic of the dynamo process occurring in Earth's core. In the yellow-orange fluid outer core, (blue) magnetic field lines are altered via (red) helical

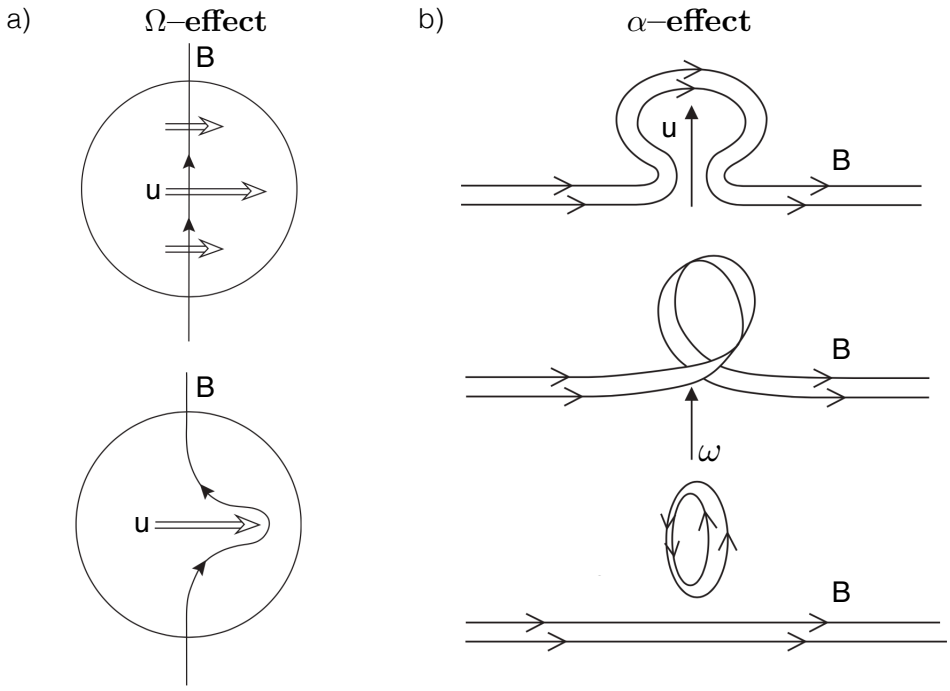

Figure 1.1: a) Illustration of the Ω-effect: an initially vertical magnetic field line (labeled B) is sheared by a perpendicular velocity field (labeled u), resulting in a bent field line that gains a horizontally directed component. b) Illustration of the α-effect: a poloidal (i.e. spherical coordinate r directed) magnetic field component is created from an initially toroidal (i.e. (θ,ϕ) directed) magnetic field line via helical fluid motions. Specifically, the initial field line is simultaneously deformed and twisted into a loop of magnetic flux by motion due to rotation with vorticity ω. These magnetic flux loops can detach, creating a field component that is perpendicular to the original field orientation when magnetic diffusion is large enough for magnetic reconnection to occur. Figure modified from Roberts (2015).

fluid motions that are primarily driven by convective fluid instabilities (indicated by orange arrows). This alteration of field lines into different directional components allows for continual generation of the global magnetic field. The vertical dashed lines in Fig. 1.2 that are separated in width by the entire diameter of the (red) solid inner core indicate the imaginary tangent cylinder region of core fluid. In this region, fluid structures in the outer core above and below the central solid inner core, i.e. in high latitude regions, are considered to be strongly aligned with the rotation axis [cf. Aurnou et al. (2003)]. Specifically, the Taylor-Proudman theorem implies that the vorticity, $\vec{\omega}$, in a rotating fluid will tend to align with the axis of rotation such that fluid motions become nearly two-dimensional [Proudman (1916), Taylor (1917)]. The resulting fluid structures that form will resist any stretching or bending [Panton (2013)]. Thus, quasi-2D vortices in Earth's outer core will be inhibited

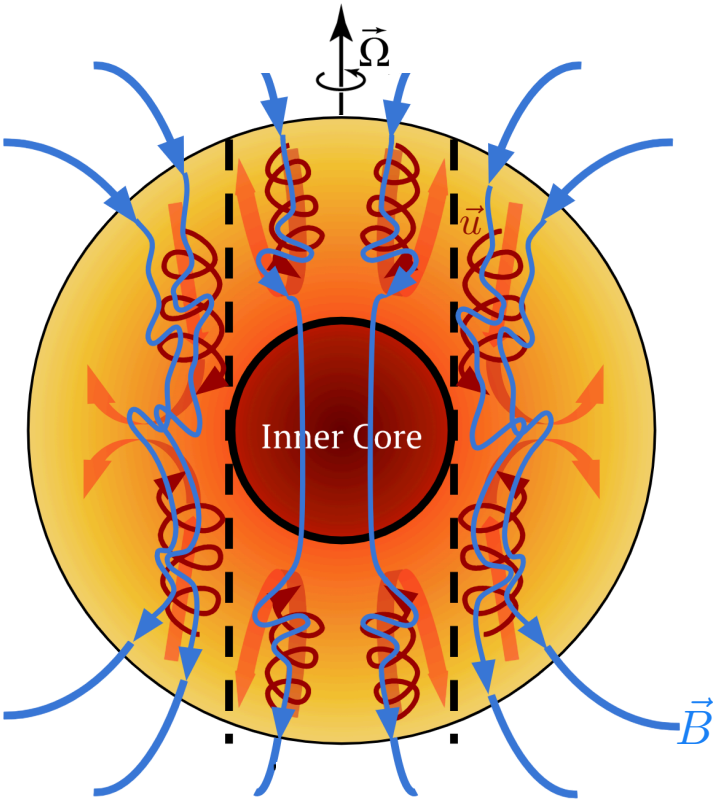

Figure 1.2: A schematic of the dynamo process occurring in Earth's core. In the yellow-orange fluid outer core, (blue) magnetic field lines are altered via (red) helical fluid motions that are primarily driven by convective fluid instabilities (indicated by orange arrows). This alteration of field lines into different directional components allows for continual generation of the global magnetic field. The vertical dashed lines that are separated in width by the entire diameter of the (red) solid inner core indicate the imaginary tangent cylinder region of core fluid. Image credit: Yufan Xu.

from crossing the imaginary tangent cylinder lines of Fig. 1.2. Two distinct regions of flow in the outer core therefore exist due to the presence of Earth's inner core: flow within this tangent cylinder region (often referred to as high latitude flow), and flow outside of the tangent cylinder region.

Some geophysical evidence can be found suggesting that the tangent cylinder region exists in Earth's core. This includes the observation of concentrated magnetic field strength at the core-mantle boundary at high latitude regions, as well as seismic detection of a possible (small) super-rotation of the inner core [Bloxham and Jackson (1992), Song and Richards (1996), Vidale et al. (2000), Pais and Hulot (2000), Constable et al. (2000), Korte and Mandea (2008), Gillet et al. (2010), Tkalcic et al. (2013)]. Additionally, numerous models

of core flows find inherent distinctions of flows inside versus outside of the tangent cylinder region [e.g. Hulot et al. (2002), Livermore et al. (2017)]. In subsection 1.2 below, I describe the laboratory model of core-style flows used in the studies presented in this dissertation that focus on high latitude flows inside of the tangent cylinder regions of planetary cores.

1.2 Simulating Planetary Core Flows

While the remote nature of the fluid motions involved in the dynamo process does not allow for direct measurements, a variety of forward models are used to examine the underlying dynamics in dynamo generating regions in a simplified setting. Numerical simulations have historically been the primary tool used to investigate planetary core flows. These models simulate the large scale processes involved in dynamo generation by solving the governing equations of magnetohydrodynamic flow prescribed by (1.1)–(1.4) [Glatzmeier and Roberts (1996), Christensen and Aubert (2006), Schubert and Soderlund (2011), Yadav et al. (2016), Schaeffer et al. (2017), Wicht and Sanchez (2019)]. However, due to computational limitations, these models possess overly strong viscous effects that are many orders of magnitude larger than estimates for the Earth's core. Thus, these models remain 'quasi-laminar', only capturing dynamics at the largest scales of the system [Glatzmaier and Clune (2000), Glatzmaier (2002), Soderlund et al. (2012), Aurnou et al. (2015)].

Quasi-geostrophic turbulence (QGT), rather than viscous laminar flow, is thought to dominate planetary core flows [cf. Calkins et al. (2015), Yadav et al. (2016), Schaeffer et al. (2017), Aurnou and King (2017), Aubert (2019)]. In QGT flows, geostrophic balance between the Coriolis and pressure gradient forces exists at leading order:

$$2\vec{\Omega} \times \vec{u} \sim -\frac{1}{\rho_0}\nabla P. \tag{1.6}$$

The dynamics that result from small departures in geostrophy are generally referred to as quasi-geostrophic motions, which evolve on timescales that are typically much longer than the dimensional background rotation timescale, $t_\Omega \sim 1/(2\Omega)$ [Calkins (2018)]. Thus, in QGT

flows, geostrophy exists at leading order in the presence of inertially turbulent convective motions. We further quantify these flows in Chapters 2 and 4.

We turn to a simplified system in which core-style turbulence can be studied. Laboratory experiments are capable of characterizing core-style rapidly rotating convective turbulence due to the ability to approach extreme, geophysically relevant conditions [Niemela et al. (2000), Weiss and Ahlers (2011), Ecke and Niemela (2014), Kunnen et al. (2016), Cheng et al. (2018), Cheng et al. (2020)]. The laboratory experiments in this dissertation implement a commonly used reduced geometry of a right cylinder, removing any effects of spherical curvature. Thus, our experiments simulate a local, polar parcel of planetary core convecting fluid under the influence of axial rotation and buoyancy forcing. In connection to the schematic shown in Fig. 1.2, our model cylinder exists inside of the tangent cylinder region of Earth's core. Figure 1.3 shows, on the right, a numerical simulation of rapidly rotating spherical convection by Gastine et al. (2016) as representative of Earth's core region, and on the left, a schematic of the NoMag laboratory device that models a small, local parcel in the polar region of the outer core. The comparison between numerical models and laboratory experiments is advantageous for gaining a detailed understanding of the convective dynamics involved in dynamo generation.

It has long been argued that a state of 'magnetostrophic balance' exists in which Lorentz (i.e. magnetic), Coriolis (i.e. rotational), and pressure forces control the system [e.g. Roberts and King (2013), King and Aurnou (2015)]. However, there is little evidence that such a leading order balance exists in present-day dynamo models [Soderlund et al. (2012), Soderlund et al. (2015), Yadav et al. (2016), Sheyko et al. (2018), Schwaiger et al. (2019), Aubert (2019)]. Instead, dynamo simulations typically exhibit a leading order quasi-geostrophic (QG) force balance in which Coriolis and pressure forces dominate the system [Calkins et al. (2015)]. Aurnou and King (2017) compare linear rotating magnetoconvection stability theory and present day dynamo models in order to argue that magnetostrophic balance is likely to exist only on small scales in planetary cores. Similarly, they argue that large-scale flows in planetary dynamo systems are likely to be governed by quasi-geostrophy, the dynamics of which seem to be captured by present-day dynamo models. These recent works provide

motivation to further study a purely hydrodynamic rapidly rotating turbulent system, neglecting magnetic effects, in order to better characterize leading order QGT core convective flows.

This dissertation encompasses a purely hydrodynamic framework in order to examine the properties of rapidly rotating convective turbulence. In Chapter 2, the governing equations (1.1)–(1.4) are non-dimensionalized in this hydrodynamic framework. In this framework, the fluid is considered to be non-conducting electrically (ex: water), and thus purely hydrodynamic as opposed to magnetohydrodynamic. Therefore, the magnetic Lorentz force, the rightmost term in (1.2) and equation (1.4), the magnetic induction equation, do not exist in our system of study.

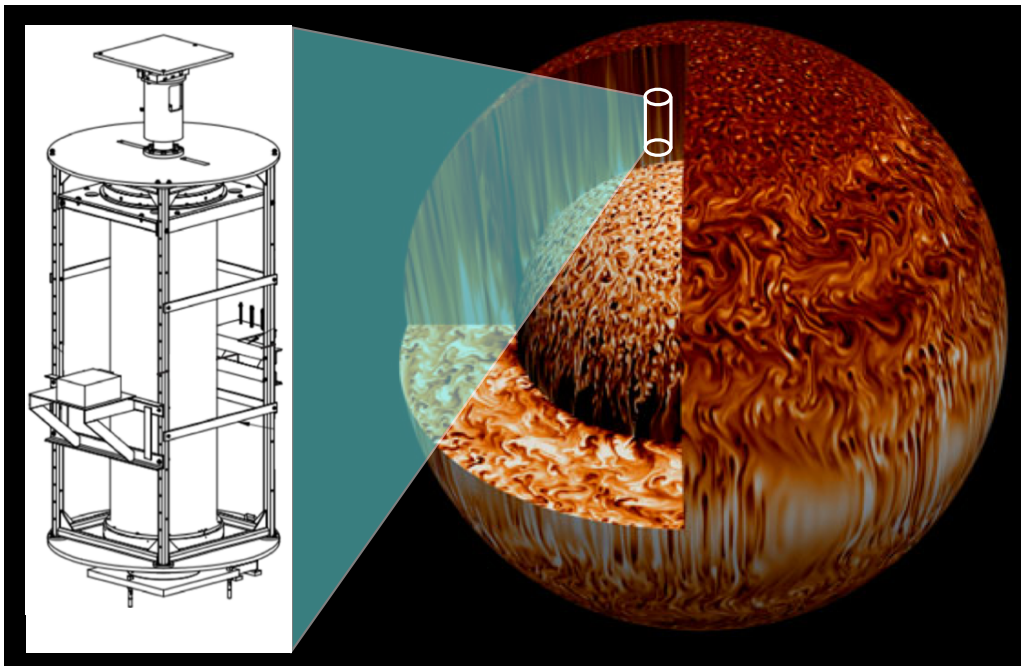

Figure 1.3: Analogue models of planetary dynamos: on the right, a numerical simulation of rapidly rotating convection by Gastine et al. (2016) representing a model of Earth's spherical shell outer core region and on the left, a schematic of the experimental device, NoMag, used herein to represent a polar parcel of core fluid within Earth's imaginary tangent cylinder region.

1.3 Open Questions

The ability to predict magnetic field behavior has important implications for forecasting future changes in the field, for example, during occurrences of magnetic reversals in which the surface of Earth becomes exposed to high levels of solar radiation [e.g. McFadden et al. (1991), Tarduno (2009), Wei et al. (2014), Doglioni et al. (2016)]. There exist a number of theoretical scalings for the magnetic field strength, B_0, at the surface of a given planet. These theories are expressed in terms of fundamental properties of the planet, as well as its dynamo region. For example, under magnetostrophic balance, one finds that $B_0 \propto \mu_0 \rho 2\Omega l U$, where μ_0 is the permittivity of free space, ρ is the mean density of the dynamo region, Ω is the rotation rate of the planet, l is the characteristic length scale of the dynamo region, and U the characteristic velocity, all of which inherently depend on the convected energy flux across the dynamo region [Christensen (2010)]. While several different forms of such a theoretical scaling for B_0 exist, all depend on a dynamical characteristic length, l and velocity, U, scale of the dynamo generating region, neither of which are well-characterized for planets. Thus, in order to begin to accurately constrain magnetic field intensity predictions for Earth and other bodies, this dissertation focuses on answering the following open questions:

- **How do velocity scaling behaviors couple to heat transfer behaviors in quasi-geostrophically turbulent (QGT) systems?**
- **What are the relevant length scales of the flow governing planetary dynamo action, and what can be learned from these scales in terms of the leading order forces driving core flows?**
- **How can the findings from the laboratory experiments and numerical simulations presented in this dissertation be extended to planetary settings?**

In this dissertation, I provide insight into answering these outstanding questions using a series of laboratory studies that I have performed in conjunction with published studies of relevant numerical simulations.

1.4 Summary of Chapters

This dissertation contains seven additional chapters. Chapter 2 contains the system parameters and theoretical scaling behaviors of non-rotating and rotating convection in a cylindrical framework relevant to subsequent chapters. Chapter 3 describes the large-scale rotating convection device, NoMag, in the UCLA Spinlab. The main components, electrical connections, and fundamental operation of the NoMag device are detailed for completeness and for the edification of future operators.

Chapter 4 contains the results of a systematic laboratory study to simultaneously characterize heat and momentum transfer in rapidly rotating convective turbulence. The characteristic flow velocities and length scales of dynamo systems are poorly constrained due to the difficulty of modeling realistic planetary core conditions, as discussed in subsection 1.1. To address this deficit, I conducted novel laboratory experiments using water on the NoMag device in which heat and momentum transfer were simultaneously measured in both non-rotating and rotating convection (RC) cases. Resultant heat transfer data agree with previous studies and show that RC heat transfer behavioral transitions are largely controlled by boundary layer dynamics. Laser doppler velocimetry (LDV) was utilized to obtain experimental point measurements of bulk axial velocities. I find that behavioral transitions in the RC velocity data do not occur where transitions in heat transfer behaviors exist, indicating that RC bulk dynamics are not controlled by the boundary layers of the system. Instead, I show that the velocity data agree well with the theorized Coriolis-Inertia-Archimedian (CIA) scaling over the range of parameters explored. I further demonstrate the CIA scaling approximately co-scales with the Viscous-Archimedian-Coriolis (VAC) scaling over the range of parameters studied. This observation is explained by demonstrating that when the local Reynolds number in the fluid bulk is of order unity, the VAC and CIA relations will co-scale. Scaling theory shows that a leading order VAC balance cannot exist, even at convective onset. Thus, I conclude that a bulk dynamical regime of quasi-geostrophic turbulence (QGT) relevant to core flows is robustly reached in which the diffusion-free CIA scaling accurately predicts flow behavior.

The findings of a meta-analysis of the hypothesized length scales in models of planetary core convection are provided in Chapter 5. The characterization of the length scales of rotating convective turbulence have important implications for the underlying dynamics of core-style flows and are not well characterized to date. The results of the dynamo models of Soderlund et al. (2012), the QG models of Guervilly et al. (2019), and the RC laboratory experiments and DNS of Hawkins et al. (2020) are co-analyzed in order to evaluate the relevance of theorized length scales in planetary dynamo systems. Specifically, I examine the ratio of estimated convective onset to turbulent length scales. Hawkins et al. (2020) first demonstrate that these two length scale estimates scale equivalently when the local Reynolds in the geostrophic fluid bulk is of order unity. Indeed, my meta-analyses of these varying core convection models show that for all of models analyzed, the ratio of onset to turbulent length scales is of order unity, indicating that the two hypothesized length scales are non-separable. I further examine the behavior of these equivalent length scales relative to the supercriticality (Ra/Ra_C) of each model, or the strength by which each of these RC models is convecting thermally. Two behavioral trends are observed, one for models that have low supercriticalities [i.e. $Ra/Ra_C \lesssim 10$] and another for models with high supercriticalities [above $Ra/Ra_C > 10$]. I compare these two behavioral trends to linear convective onset theory and find that onset theory acts as a lower bound to the observed behaviors. The finding that dynamo models do not have theoretically scale-separable length scales is of crucial importance towards extrapolating model results to planetary conditions. My ongoing work to explain the observed behaviors of these length scales with respect to supercriticality will shed light on the connection between dynamic length scales and the leading order forces involved in planetary dynamo action.

During instances of rapid rotation, the large diameter NoMag experimental device can contain an effect on RC that is not considered to significantly affect planetary core dynamics: centrifugal acceleration. While centrifugal effects can be ignored in most planetary dynamo settings, their characterization is crucial in the use of rapidly rotating laboratory devices that allow for an understanding of relevant planetary dynamics. Chapter 6 contains the results of an experimental study I conducted in both water and liquid metal to character-

ize the transition from Coriolis to centrifugally dominated rotating convection. I designed experiments specifically to better characterize the properties and occurrence of centrifugally dominated convection in RC under the presence of turbulence with varied fluid properties and container geometries. My collected data is the first to test the recent numerical results of Horn and Aurnou (2018) and Horn and Aurnou (2019), which, if verified in a laboratory setting, have important implications for the use of extreme RC laboratory devices in the study of core-style rotating turbulence. Analyses of experimental data in both water and liquid metal appear to agree with and validate both the theory and the results of Horn and Aurnou (2018). Specifically, a horizontal dependence on temperature in which an anomalous strong central upwelling and a simultaneous outer downwelling develops in a regime described as Coriolis-centrifugal (CC) convection. My experimental results extend the findings of Horn and Aurnou (2018) far past the onset of convection for the first time.

Chapter 7 provides the results of a set of experiments in which I measured azimuthal point velocities during the spin up of a homogeneous fluid confined by both smooth and rough boundaries using the NoMag device. The fluid dynamical theory surrounding the impulsively generated linear spin up of a homogeneous fluid in an axisymmetric container confined by smooth boundaries has been well-verified both numerically and experimentally. However, the fluid mechanical theory involving the spin up of a fluid confined by rough boundaries is not well-characterized to date [e.g. Warn-Varnas et al. (1978), Noir et al. (2010), Burmann and Noir (2018)]. Spin up is defined as the flow resulting when a state of steady fluid rotation, known as solid body rotation, is disturbed by slightly increasing the rotation rate of the container [Greenspan and Howard (1963), Benton and Clark (1974), Weidman (1976)]. The spin up process over small-scale roughness, alongside thermal convection, is not only suggested to be responsible for possible viscous coupling at Earth's core mantle boundary, but is also suggested to play a central role in the turbulent mixing of the global ocean [e.g. Bell and Soward (1996), Brito et al. (2004), Kunze and Smith (2004), Mouel et al. (2006), Buffett and Christensen (2007) Roberts and Aurnou (2012b), Calkins et al. (2012b)]. I find strong agreement between well-established theory and experimental measurements of the spin up of a homogeneous fluid in an axisymmetric container confined by smooth boundaries. My

laboratory results show that rough boundaries quicken the spin up process. My ongoing analysis of these results will help provide an explanation for the difference in the physical processes that occur with the introduction of small-scale roughness.

Lastly, in Chapter 8, I summarize my work presented in each chapter of this dissertation. Specifically, I describe the manner in which each study connects to one another as well as to planetary dynamos systems. I will also briefly discuss possible future research topics resulting from the work that I have performed in this dissertation. In terms of my direct contributions to each chapter, I created all of the figures in Chapter 2 on hydrodynamic RC theory. In a team effort (https://spinlab.epss.ucla.edu/?page_id=727), the construction of the NoMag large-scale laboratory device was completed in the 2013-2014 academic year. As I am the first scientist to conduct experimental studies using the new NoMag apparatus, the device and associated methodology descriptions in Chapter 3 are my own. Chapter 4 is modified from a paper that is currently being revised for publication in Geophysical Journal International, in which I am the first author. I contributed all experimental data, figures, and analysis. Co-author Stephan Stellmach provided the DNS data of this study. Chapter 5 is modified from a manuscript in preparation for submission to a scientific journal in which I am also the first author. I compiled all of the results of past studies used in this work and contributed all figures and analysis. I also contributed all experimental data, figures, and analysis in Chapters 6 and 7, which are in preparation for submission to scientific journals. The experimental data in Chapter 7 was collected and analyzed by me and co-authors Jonathan Cheng, Alexander Grannan, and Timothy Pilegard.

CHAPTER 2

Hydrodynamic System Parameters and Theoretical Scaling Behaviors of Non-Rotating and Rotating Convection

2.1 Rayleigh-Bénard Convection (RBC)

In order to explore rotating convection, it is important to first consider the analogous system without the effect of rotation. Non-rotating Rayleigh-Bénard convection (RBC) occurs when a horizontally confined fluid layer is heated from below and cooled from above, causing fluid motions due to local gravitational instabilities arising from temperature driven changes in density. RBC is relevant in planetary core dynamics as it is thought to represent the behavior of a rotating system when convection greatly overcomes rotation [e.g. Cheng et al. (2015), Gastine et al. (2015)]. Specifically, in rotating convection, system diagnostics of the analogous RBC system, such as those characterizing the heat transfer of the system, often act as upper bounding values. The scope of this work, in a simplified approach towards understanding core flows, considers high latitude core convection. As such, a cylindrical framework is considered. The dimensionless set of hydrodynamic equations governing the incompressible flow of non-rotating, non-electrically conducting Rayleigh-Bénard convection in a cylindrical geometry under the the Boussinesq approximation[1] is given as:

$$\nabla \cdot \vec{u} = 0, \tag{2.1}$$

[1]Under the Boussinesq approximation, variations in density are accounted for only in the gravitational buoyancy term and are neglected in all other terms in 2.2 [Kundu et al. (2012)].

$$\frac{D\vec{u}}{Dt} = -\nabla P + \frac{Ra}{Pr} T\hat{z} + \nabla^2 \vec{u}, \tag{2.2}$$

$$\frac{DT}{Dt} = \frac{1}{Pr}\nabla^2 T, \tag{2.3}$$

where $\vec{u}, P$, and T are the dimensionless velocity, pressure, and temperature of the system, respectively. The following dimensionless scales are used in the derivation of (2.1)–(2.3): $\vec{r} \sim \vec{r^*}/H$ ($\nabla \sim H\nabla^*$), $t \sim (\nu/H^2)t^*$ (i.e. a viscous timescale), $\vec{u} \sim (H/\nu)\vec{u^*}$, $P \sim (1/\rho_0)(H^2/\nu^2)P^*$, and $T \sim T^*/\Delta T$, where asterisks denote dimensional values and where H [m] is the height of the cylindrical container, ν [m^2/s] is the kinematic viscosity of the fluid, ρ_0 [kg/m^3] is the mean density of the fluid, and ΔT [K] is the temperature difference across the fluid layer [Glatzmaier (2013)].

In (2.2), the dimensionless Rayleigh number, Ra, describes the ratio of thermal buoyancy to viscous and thermal diffusion and is given as:

$$Ra = \frac{\text{thermal buoyancy}}{\text{thermal \& viscous diffusion}} = \frac{\alpha g \Delta T H^3}{\nu\kappa}, \tag{2.4}$$

where α [1/K] is the thermal expansivity of the fluid, g [m/s^2] is gravitational acceleration, and κ [m^2/s] is the thermal diffusivity of the fluid. In (2.2) and (2.3), the Prandtl number, Pr, is the ratio between viscous and thermal diffusion and is given as:

$$Pr = \frac{\text{viscous diffusion}}{\text{thermal diffusion}} = \frac{\nu}{\kappa}. \tag{2.5}$$

2.1.1 Heat Transfer Characterization (RBC)

In any RBC system, the non-dimensional heat transfer is described by the Nusselt number, the ratio of the total heat flux through the system relative to the conductive heat flux in the absence of convection:

$$Nu = \frac{\text{total heat flux}}{\text{conductive heat flux}} = \frac{qH}{k\Delta T}, \tag{2.6}$$

where q [W/m^2] is the total heat flux through the system and k [W/mK] is the thermal conductivity of the fluid. The Nusselt number is a useful output parameter that describes

the efficiency of global heat transport and the vigor of convection in a system. Trends in the Nusselt number can reveal fundamental convective behaviors [Spiegel (1971), Plumley and Julien (2019)]. In an RBC water system ($Pr \simeq 7$), there exist two well studied scaling relationships between Nu and the input parameter Ra of the form:

$$Nu = cRa^{\alpha}, \tag{2.7}$$

where c is the pre-factor and α is the scaling exponent.

For low to moderate buoyancy forcing ($Ra \lesssim 10^{10}$), Shraiman and Siggia (1990) argue that an $\alpha = 2/7$ heat transfer scaling develops of the form:

$$Nu \sim Ra^{2/7} \tag{2.8}$$

by including the effects of a shear flow across the thermal boundary layers. In experiments containing such low to moderate buoyancy forcing, a container size overturning circulation occurs in the fluid bulk, providing a shear flow across the boundaries of the fluid layer. The presence of this circulation indicates that communication exists between the boundary layers. The scaling relation in (2.8) has been observed in a number of experiments where $10^5 \lesssim Ra \lesssim 10^{10}$ [Rossby (1969), Chilla et al. (1993), Glazier et al. (1999), Ahlers and Xu (2001), Funfschilling et al. (2005), King et al. (2012), Cheng et al. (2015), Gastine et al. (2015)].

For water experiments containing stronger thermal forcing ($Ra > 10^{10}$), a scaling containing an $\alpha = 1/3$ exponent exists of the form:

$$Nu \sim Ra^{1/3} \tag{2.9}$$

[Caistaing et al. (1989), Niemela et al. (2000) Funfschilling et al. (2005), Ahlers et al. (2009), Chilla and Schumacher (2012), Doering et al. (2019), Cheng et al. (2020)]. The relation in (2.9) arises under conditions in which boundary layers do not interact due to vigorous bulk convective mixing in the system in which the fluid bulk becomes isothermal [Priestly (1953),

Malkus (1954)]. Thus, time-averaged temperature gradients are localized to thin thermal boundary layers adjacent to the top and bottom of the fluid layer in which conductive heat transfer dominates.

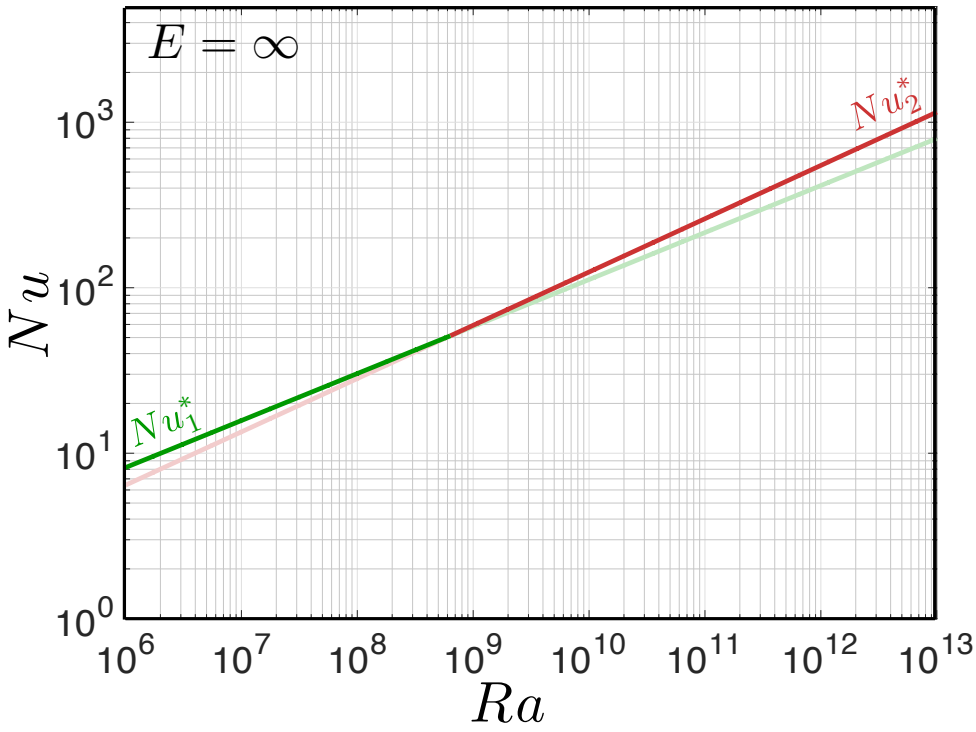

Figure 2.1: Global heat transfer efficiency, Nu, versus input thermal forcing, Ra, for an RBC water system. The solid green line, $Nu_1^* = 0.162Ra^{0.284}$ [Cheng et al. (2015)], is valid for low to moderate values of Ra. The solid fuchsia line, $Nu_2^* = 0.075Ra^{0.322}$ [Cheng et al. (2015)], is valid near and above $Ra \simeq 10^{10}$. The onset of convection ($Ra_C = 1708$, $Nu = 1$) is not shown.

Figure 2.1 shows the RBC heat transport behavior of Nu for a given Ra, where the pre-factors, $c = 0.170$, $c = 0.075$, and exponents $\alpha = 0.287 \sim 2/7$, $\alpha = 0.322 \sim 1/3$ correspond to empirical best-fits of the experiments of Cheng et al. (2015). Due to the similarity of the exponent values 2/7 and 1/3, a broad overlap region (nearly two orders of magnitude) exists over which the transition from a 2/7 scaling behavior to a 1/3 scaling behavior might occur. The colors of these curves in Fig. 2.1 are faded at the empirical location at which the two curves intersect, with the expectation of 2/7 scaling behavior at lower Ra and 1/3 behavior at larger Ra as found in previous studies. Nonetheless, it is expected from prior experiments that the transition from an $\alpha \simeq 2/7$ to an $\alpha \simeq 1/3$ scaling relation occurs near $Ra \simeq 10^{10}$,

indicating the loss of communication between thermal boundary layers with strong thermal forcing [e.g. Niemela et al. (2000), Ahlers et al. (2009), Cheng et al. (2015)]. Note that the onset of convection ($Nu = 1$), while not shown in Fig. 2.1, has a constant value of $Ra_C = 1708$ for an infinite plane layer with rigid, non-slip boundaries and $Pr \simeq 7$ [Pellew and Southwell (1940)].

2.1.2 Momentum Transfer Characterization (RBC)

A system parameter that describes momentum transfer in RBC systems is the Reynolds number, Re: the ratio of inertial advection to viscous diffusion given as:

$$Re = \frac{\text{inertial advection}}{\text{viscous diffusion}} = \frac{UH}{\nu}, \tag{2.10}$$

where U [m/s] is a characteristic system velocity. Similarly to (2.7), a scaling relation can be written between the Reynolds and Rayleigh numbers such that:

$$Re = bRa^{\gamma}, \tag{2.11}$$

where, here, b is the pre-factor and γ is the exponent. Using a free-fall velocity, $u_{\text{ff}} \sim \sqrt{\alpha g \Delta T H}$, to estimate the system scale velocity, U, in (2.10), a relationship between Re and Ra exists of the form:

$$Re \sim Ra^{1/2} \tag{2.12}$$

when $Pr \simeq 7$ [Kraichnan (1962), Grossman and Lohse (2002)]. A best fit exponent of $\gamma \simeq 0.44$ has been found experimentally by Qiu and Tong (2001a), Qiu and Tong (2001b), Xi et al. (2006), and Brown et al. (2007). Figure 2.2 shows the momentum transfer behavior of Re as a function of Ra using the best fit pre-factor, $b = 0.102$, and exponent, $\gamma = 0.447$, from Qiu and Tong (2001b). In this study, laser doppler velocimetry is used to obtain point velocities in the fluid bulk, and a time-averaged root mean square value of U is used in the calculation of Re for $5 \times 10^8 \lesssim Ra \lesssim 10^{10}$, $Pr \simeq 7$.

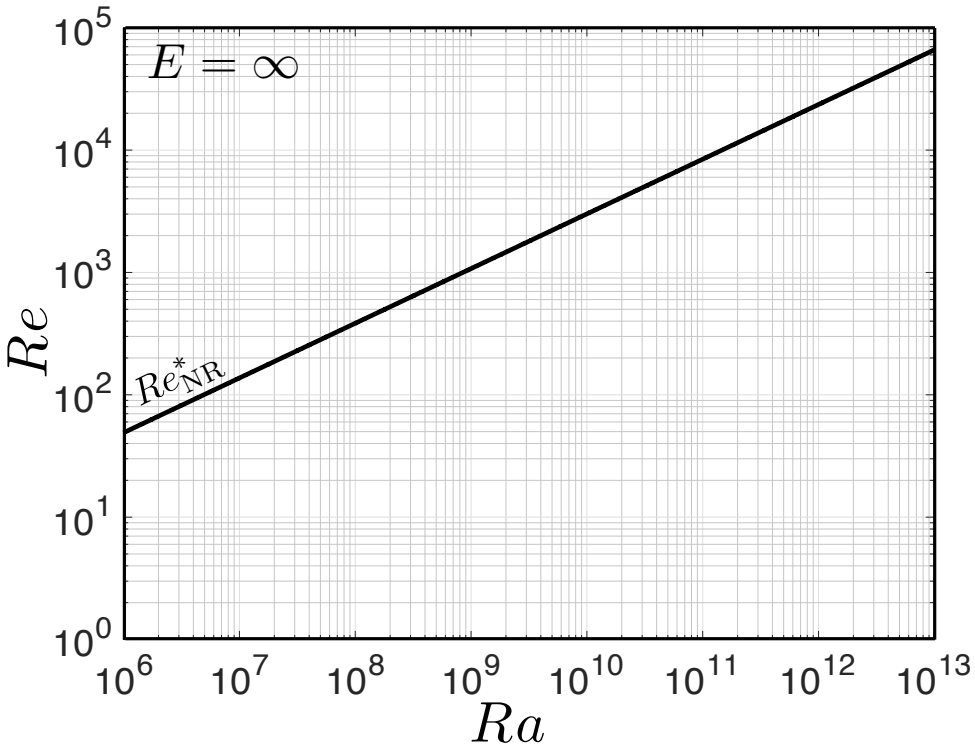

Figure 2.2: Momentum transfer, Re, versus input thermal forcing, Ra, for an RBC water system. The solid black curve is given as $Re^*_{\rm NR} = 0.102 Ra^{0.447}$ [Qiu and Tong (2001b)].

2.2 Rotating Rayleigh-Bénard Convection (RRBC)

If the RBC system described in Section 2.1 is rotated about the z-direction in a cylindrical coordinate frame, two new terms appear in the momentum equation of (2.2): the Coriolis force and a centrifugal acceleration term [Cushman-Roisin and Beckers (2011)]. The system of dimensionless equations (2.1)–(2.3) now becomes:

$$\nabla \cdot \vec{u} = 0, \tag{2.13}$$

$$\frac{D\vec{u}}{Dt} + \frac{1}{E}\hat{z} \times \vec{u} = -\nabla P + \frac{Ra}{Pr} T\hat{z} + \frac{2RaFr}{Pr\Gamma} T\vec{s} + \nabla^2 \vec{u}, \tag{2.14}$$

$$\frac{DT}{Dt} = \frac{1}{Pr}\nabla^2 T, \tag{2.15}$$

where $\vec{s}$ is a dimensionless cylindrical radius. In (2.13)–(2.15), the same non-dimensionalization is used as described in Section 2.1. The non-dimensional Coriolis force is seen as the second term on the lefthand side of (2.14), and the non-dimensional centrifugal acceleration is the third term on the righthand side of (2.14).Thus, two new resulting non-dimensional parameters are introduced to a RBC system when rotated: the Ekman number, E, and the rotational Froude number, Fr. The Ekman number, E, describes the ratio of viscous diffusion to the Coriolis force and is given as:

$$E = \frac{\text{viscous diffusion}}{\text{Coriolis}} = \frac{\nu}{2\Omega H^2}, \tag{2.16}$$

where Ω [rad/s] is rotation rate of the container bounding the fluid. The rotational Froude number, Fr, characterizes the ratio of centrifugal buoyancy to gravitational buoyancy and is given as:

$$Fr = \frac{\text{centrifugal buoyancy}}{\text{gravitational buoyancy}} = \frac{\Omega^2 R}{g}, \tag{2.17}$$

where R is the radius of the cylindrical container. Lastly, Γ in (2.14) characterizes the aspect ratio of a cylindrical container:

$$\Gamma = \frac{D}{H}, \tag{2.18}$$

where $D = 2R$ is the inner diameter of the cylindrical container.

Lastly, the Rossby number, Ro, characterizes the ratio of thermal buoyancy in the system relative to the Coriolis force as:

$$Ro = \frac{\text{inertial advection}}{\text{Coriolis}} = \frac{U}{2\Omega H}, \tag{2.19}$$

and relates to the Re and E numbers as $Ro = ReE$. A free-fall Rossby number, Ro_{ff}, which uses a free-fall velocity, $u_{\text{ff}} \sim \sqrt{\alpha g \Delta T H}$, to estimate the system scale velocity, U, is:

$$Ro_{\text{ff}} = \frac{\text{thermal buoyancy}}{\text{Coriolis}} = \frac{\sqrt{\alpha g \Delta T H}}{2\Omega H} = \sqrt{\frac{RaE^2}{Pr}} \tag{2.20}$$

[e.g. Julien et al. (1996), Horn and Shishkina (2014), Aurnou et al. (2020)]. Ro_{ff} is a

combination of the input parameters Ra, E, and Pr, and therefore does not require direct measurement of velocity. Using Ro_{ff} to estimate Ro assumes that velocities scale as the free-fall velocity, u_{ff} in which inertial advection balances buoyancy in the system. Thus, Ro_{ff} serves as an upper bounding estimate for Ro. Table 2.1 provides a summary of the non-dimensional parameters of the hydrodynamic system of study in this dissertation. The horizontal dashed line separates control parameters from output parameters, some of which can be written in terms of combinations of system input parameters. For reference, estimates of values for Earth's outer core are provided.

Parameter	Meaning	Definition	Earth's Core
Rayleigh, Ra	$\frac{\text{thermal buoyancy}}{\text{thermal \& viscous diffusion}}$	$\frac{\alpha g \Delta T H^3}{\nu\kappa}$	$\sim 10^{20} - 10^{30}$
Prandtl, Pr	$\frac{\text{viscous diffusion}}{\text{thermal diffusion}}$	$\frac{\nu}{\kappa}$	$\sim 10^{-1}$
Ekman, E	$\frac{\text{viscous diffusion}}{\text{Coriolis}}$	$\frac{\nu}{2\Omega H^2}$	$\sim 10^{-15}$
Froude, Fr	$\frac{\text{centrifugal buoyancy}}{\text{gravitational buoyancy}}$	$\frac{\Omega^2 R}{g}$	$\sim 10^{-3}$
Nusselt, Nu	$\frac{\text{total heat flux}}{\text{conductive heat flux}}$	$\frac{qH}{k\Delta T}$	$\sim 10^{2} - 10^{7}$
Reynolds, Re	$\frac{\text{inertial advection}}{\text{viscous diffusion}}$	$\frac{UH}{\nu}$	$\sim 10^{9}$
Rossby, Ro	$\frac{\text{inertial advection}}{\text{Coriolis}}$	$\frac{U}{2\Omega H} = ReE$	$\sim 10^{-6}$
free-fall Rossby, Ro_{ff}	$\frac{\text{thermal buoyancy}}{\text{Coriolis}}$	$\frac{\sqrt{\alpha g \Delta T H}}{2\Omega H} = \sqrt{\frac{RaE^2}{Pr}}$	$\sim 10^{-5} - 10^{0}$

Table 2.1: Non-dimensional parameters of a hydrodynamic RC system with estimates of values for Earth's outer core. The horizontal dashed line separates control parameters from output parameters, some of which can be written in terms of combinations of system input parameters. All symbols are defined in the text. Values used to estimate parameters for Earth's core are as follows: $\alpha \simeq 1.8 \times 10^{-5}$ 1/K [Stacey and Davis (2008)], $g \simeq 11$ m/s^2 [Turcotte and Schubert (2002)], $\Delta T \simeq 10^{-2} - 10^{5}$ mK [Buffett (2003)], $H \simeq 2300$ km [Stacey and Davis (2008)], $\nu \simeq 10^{-6}$ m^2/s [Roberts and King (2013)], $\kappa \simeq 10^{-5}$ m^2/s [Schubert and Soderlund (2011)], $\Omega \simeq 7.3 \times 10^{-5}$ 1/s [Roberts and King (2013)], $R = H \simeq 2300$ km, $q \simeq 0.0065 - 0.065$ W/m^2 [Buffett (2003)], $k \simeq 30 - 100$ W/mK [Stacey and Davis (2008), Pozzo et al. (2012)], and $U \simeq 0.1 - 1$ mm/s [Olson and Aurnou (1999), Christensen and Aubert (2006), Jones (2011)].

2.2.1 Heat Transfer Characterization (RC)

Rotation acts to suppress convection in a RRBC system [Nakagawa and Frenzen (1955)]. The acronym RRBC is henceforth shortened to RC when referring to rotating convection. The critical Rayleigh number, Ra_C, in a rotating convection system is no longer a constant for a given geometry. Instead, Ra_C depends on the non-dimensional rotation rate of the container, most commonly characterized by the Ekman number, E. Specifically, in a geometrically confined RC system, convection will first onset in the form of wall modes due to the release of the rotational constraint on the fluid by lateral boundaries [Zhong et al. (1993), Herrmann and Busse (1993), Goldstein et al. (1993)]. The criterion for the onset of wall modes in RC, under the assumption that the curvature of the cylinder can be neglected, is given as:

$$Ra_C^W = 31.8E^{-1} + 46.6E^{-2/3} \tag{2.21}$$

[Zhang and Liao (2009)]. For $Pr > 0.68$, steady, bulk-filling convection is predicted to occur in a horizontally infinite plane layer in the asymptotic limit of small E when:

$$Ra_C^S \simeq 8.7E^{-4/3} \tag{2.22}$$

[Chandrasekhar (1961)].

After the onset of steady RC, different convective regimes have been observed according to distinguishable scaling trends in heat transfer behavior and are reviewed in Cheng et al. (2018). Convection will occur in the form of long, thin isolated columns aligned with the axis of rotation when $Ra/Ra_C^S \gtrsim 2$ [e.g. Zhong et al. (1993), Sakai (1997), Sprague et al. (2006), Grooms et al. (2010), Aurnou et al. (2015)]. The cross-axial width of an RC column that develops near onset in a system with $Pr > 0.68$ is estimated as:

$$l_{\text{crit}} = 2.4E^{1/3}H \tag{2.23}$$

[Chandrasekhar (1961), Greenspan (1969a), Julien and Knobloch (1998)].

A scaling relation for the heat transfer occurring in the regime where the entire fluid layer (i.e. bulk and boundary layers) is rotationally constrained can be expressed for a water system in terms of the criticality past steady onset as:

$$Nu = (Ra/Ra_C^s)^\beta, \tag{2.24}$$

where β is the scaling exponent [e.g. Plumley and Julien (2019)]. This regime is often referred to as the 'columnar' or 'convective Taylor column' regime, though the direct tie of (2.24) to the existence of convective columns remains unclear [cf. Stellmach et al. (2014)]. As the Ekman number decreases (i.e. the rotational forcing in the system increases), β steepens in a water system ($Pr \simeq 7$) due to Ekman pumping effects, which act to boost the heat transfer for a given thermal forcing [Stellmach et al. (2014), Julien et al. (2016), Plumley et al. (2017)]. The term Ekman pumping describes the vertical momentum transport that results from a balance between viscous and Coriolis forces in the boundary layers of the fluid. Cheng et al. (2018) estimate, using the suite of laboratory and numerical data in Cheng et al. (2015), that the scaling exponent, β, depends on the Ekman number as:

$$\beta = -0.45 - 0.59 log_{10}(E). \tag{2.25}$$

The results of asymptotic models [cf. Julien et al. (2016), Plumley et al. (2016)] indicate that the impact of Ekman pumping on the exponent, β, in (2.25) eventually subsides and the exponent therefore saturates at asymptotically low E.

The heat transfer efficiency prescribed by Nu will eventually scale more weakly with Ra at higher criticalities, i.e. higher values Ra/Ra_C^S. Previous studies find that with enough thermal forcing, RC heat transfer behavior transitions to that of non-rotating RBC [e.g. Weiss et al. (2010), King et al. (2012), Cheng et al. (2015), Gastine et al. (2016), Long et al. (2020)]. One argument explaining this transition involves the dominance of either a thermal or Ekman boundary layer in the system. A detailed description of the boundary layer physics occurring to control such a transition is still under investigation [cf. Cheng et al. (2018)].

The thermal boundary layer is estimated as:

$$\delta_T \sim H/(2Nu), \tag{2.26}$$

where δ_T [m] is the thickness of a single thermal boundary layer (of which there are two) [King et al. (2009)]. King et al. (2012) verify the accuracy of this estimate, noting that the estimate is weakest (resulting in errors of the thickness estimate up to 50%) near onset in the rotationally constrained regime (i.e. $Ra < Ra_T$).

The Ekman boundary layer, δ_E [m], develops in a rotating system and is estimated as:

$$\delta_E \sim 3E^{1/2}H \tag{2.27}$$

[Greenspan (1969b)]. King et al. (2009) argue that the heat transfer behavioral transition from a regime in which the entire fluid layer is rotationally constrained to a non-rotating style regime should occur when the thermal boundary layer becomes thinner than the Ekman boundary layer. Thus, in this prediction, the heat transfer of a rotationally constrained fluid layer transitions to non-rotating style heat transfer when the Ekman layer becomes thermally unstable, i.e. when: [King et al. (2012)]

$$\delta_T/\delta_E < 1. \tag{2.28}$$

A 'transition' Rayleigh number, Ra_T, can be empirically defined in order to characterize the transition from rotationally constrained entire layer to non-rotating style heat transfer in which rotation appears to have lost any influence on the heat transfer of the fluid. Using the shallow, RBC style scaling of (2.7) and the steep RC scaling of (2.24), the empirical intersection of these two scalings define Ra_T as:

$$Ra_T = c^{1/(\beta-\alpha)}(Ra_C^S)^{\beta/(\beta-\alpha)} = 8.7^{\beta/(\beta-\alpha)}c^{1/(\beta-\alpha)}E^{4\alpha/3(\alpha-\beta)}, \tag{2.29}$$

where substitution of (2.22) is performed in the rightmost step [Cheng et al. (2015)]. Previous

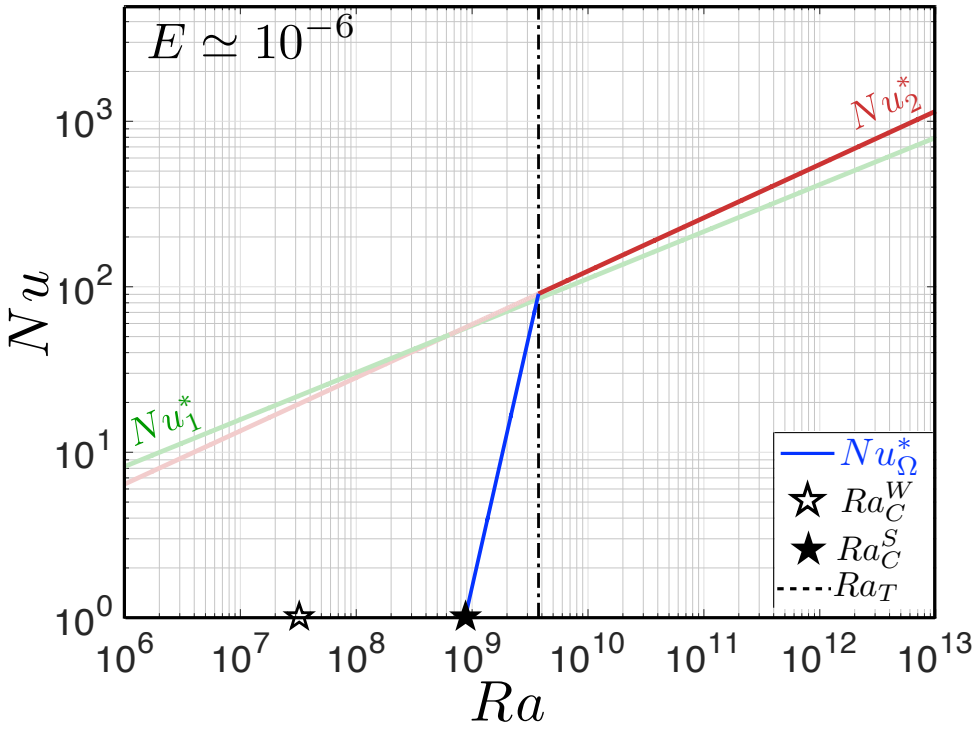

Figure 2.3: Global heat transfer efficiency, Nu, versus input thermal forcing, Ra, for an RC water system of a fixed non-dimensional rotation period of $E = 10^{-6}$. The onset of wall mode convection given by (2.21) is denoted by an open star ($Ra_C^W = 31.8E^{-1} + 46.6E^{-2/3}$, Zhang and Liao (2009)), and the onset of steady convection given by (2.22) as a solid star ($Ra_C^S \simeq 8.7E^{-4/3}$, Chandrasekhar (1961)). The solid blue line is given by (2.24), $Nu_\Omega^* = (Ra/Ra_C^S)^\beta$, where $\beta = -0.45 - 0.59log_{10}(E)$ [Cheng et al. (2018)]. Past $Ra > Ra_T$, heat transfer is expected to return to a non-rotating scaling given by (2.8), Nu_1^* (green), or by (2.9), Nu_2^*, (fuscia).

studies [e.g. King et al. (2009), Julien et al. (2012a), King et al. (2012), Ecke and Niemela (2014), Cheng et al. (2015), Gastine et al. (2016)] find that the transition from the heat transfer regime in which the entire layer is rotationally dominated to non-rotating style heat transfer occurs over a gradual region that is not well described by (2.29). A number of different ideas exist regarding this gradual transition region and are summarized in Cheng et al. (2018). As these ideas are not well understood, we implement the use of (2.29) in order to create a simple, testable framework for RC heat transfer behavior.

Figure 2.3 illustrates the heat transfer behavior of an RC water system for an arbitrary fixed non-dimensional rotation period of $E = 10^{-6}$. The schematic shown is representative of the predicted heat transfer behavior for all values of E. The onset of wall mode convection

given by (2.21) is denoted by an open star and the onset of steady convection given by (2.22) as a solid star. The heat transfer behavior near the onset of wall mode convection is not considered. As illustrated, after steady onset, the heat transfer efficiency, Nu, scales steeply with increases in Ra as given by (2.24, blue). The thermal forcing becomes strong enough to overcome the constraining effects of rotation in the system's boundary layers pasted Ra_T, given by (2.29) and shown as the vertical dashed line in Fig. 2.3. Here, the heat transfer behaves as though the system were not rotating according to (2.8) or (2.9).

2.2.2 Momentum Transfer Characterization (RC)

There exist several theoretical scaling relations in the literature to predict velocities in core dynamos based on differing assumptions of relevant, leading order force balances [cf. Aubert et al. (2001), Christensen (2010), Jones (2011), King and Buffett (2013), Jones (2015)]. These proposed velocity scalings contain a thermal wind balance at leading order and differ in an assumption of the characteristic length scale of convection in the system. Purely geostrophic flows contain, to leading order, a balance between the Coriolis force and a pressure gradient force. The Taylor-Proudman constraint (TPC) describes the independence of flow velocities on the direction of the background rotation in purely geostrophic flows and is relaxed in our system of study by the assumed next order force, the buoyancy force. Thus, the evolution of vorticity in our quasi-geostrophic (QG) system of study is described by the thermal wind relation where the buoyancy and Coriolis terms in the vorticity equation of the system balance: [cf. McWilliams (2006)]

$$2\vec{\Omega}\cdot\vec{\nabla}\vec{u} = \vec{\nabla}\times(\alpha g T\hat{z}). \tag{2.30}$$

Taking the dot product of (2.30) with the velocity vector, $\vec{u}$, and scaling the system, we obtain:

$$\frac{2\Omega U^2}{H} \sim \frac{\alpha g < u_z T >}{\delta}, \tag{2.31}$$

where δ [m] is the characteristic length scale of convection in the system, and $<\quad>$ represents a time and volume average. Re-arranging (2.31) in terms of the characteristic system velocity

of interest, U, we yield:

$$U \sim \left(\frac{\alpha g < u_z T > H}{2\Omega\delta} \right)^{\frac{1}{2}}. \tag{2.32}$$

We can further write (2.32) in terms of a dimensional convective power term, $\mathcal{P}$ [J/s], existing in the mechanical energy evolution equation of our QG system and given as: (see King and Buffett (2013))

$$\mathcal{P} = \int_V \rho_0 \vec{u} \cdot (\alpha g T \hat{z}) \partial V \sim \rho_0 \alpha g < u_z T > H^3. \tag{2.33}$$

Substituting (2.33) into (2.32) yields:

$$U \sim \left(\frac{\mathcal{P}}{2\Omega\rho_0\delta H^2} \right)^{\frac{1}{2}}. \tag{2.34}$$

Non-dimensionally, we can substitute our result in (2.34) into the Reynolds number, Re (defined in 2.10) as:

$$Re = \frac{UH}{\nu} \sim \left(\frac{\mathcal{P}}{2\Omega\rho_0\nu^2\delta} \right)^{\frac{1}{2}}. \tag{2.35}$$

To further express the righthand side of (2.35) in terms of non-dimensional numbers, we use a non-dimensional convective power term:

$$\mathcal{C} = \frac{Ra(Nu-1)}{Pr^2} = \frac{\alpha g \cancel{\Delta T} H^3}{\nu \cancel{\kappa}} \frac{< u_z T >}{\cancel{\kappa} \cancel{\Delta T}/H} \frac{\cancel{\kappa^2}}{\nu^2} = \frac{\alpha g < u_z T > H^4}{\nu^3}, \tag{2.36}$$

where $Nu - 1 = q_{conv}/q_{cond} \sim < u_z T > H/\kappa\Delta T$ [Shraiman and Siggia (1990), Grossmann and Lohse (2000), King and Buffett (2013)]. Equation (2.36) results from time and volume averaging the mechanical energy evolution equation, which produces a balance between viscous dissipation, $\epsilon_u = \nu ||\vec{\nabla}\vec{u}||^2$, and buoyancy production, given inside of the integrand in (2.33). Furthermore, comparing (2.36) to (2.33), we see:

$$\mathcal{P} = \frac{\rho_0 \nu^3}{H} \mathcal{C}. \tag{2.37}$$

Substituting (2.37) into (2.35) then yields:

$$Re \sim \left(\frac{\mathcal{P}}{2\Omega\rho_0\nu^2\delta}\right)^{\frac{1}{2}} \sim \left(\frac{\mathcal{C}\nu H}{2\Omega H^2\delta}\right)^{\frac{1}{2}} \sim \boxed{\left[\mathcal{C}E\left(\frac{H}{\delta}\right)\right]^{\frac{1}{2}}}. \tag{2.38}$$

Thus, we see that a non-dimensional velocity scaling in an RC system depends on: 1) a non-dimensional convective power, $\mathcal{C} = Ra(Nu-1)/Pr^2$, 2) the Ekman number, E, and 3) a non-dimensional dynamic length scale, δ/H, that has been proposed in several different manners.

In (2.30), the Coriolis term is balanced by a baroclinic torque. If, instead, the Coriolis term is balanced by the viscous diffusion of vorticity, we obtain:

$$2\vec{\Omega}\cdot\vec{\nabla}\vec{u} \sim \nu\nabla^2\vec{\omega}, \tag{2.39}$$

where $\vec{\omega} = \vec{\nabla}\times\vec{u}$ is the vorticity. Scaling (2.39), we see:

$$\frac{2\Omega U}{H} \sim \frac{\nu U}{\delta^3}. \tag{2.40}$$

Furthermore, re-arranging (2.40) in terms of the dynamic system length scale, δ, we obtain:

$$\frac{\delta}{H} \sim \left(\frac{\nu}{2\Omega H^2}\right)^{\frac{1}{3}} \sim E^{\frac{1}{3}}, \tag{2.41}$$

where $\delta \sim l_{\text{crit}}$ from (2.23). Thus, (2.41) is referred to as a viscous QG length scale and is the characteristic length scale of an RC system at the onset of convection according to linear theory [Chandrasekhar (1961)]. Numerous studies confirm that the horizontal width of columns existing near steady onset follows (2.41) [Jones et al. (2000), Zhang and Schubert (2000), Stellmach and Hansen (2004), Aubert (2005), Grooms et al. (2010), King et al. (2012)]. Furthermore, if we substitute (2.41) into the Reynolds scaling given by (2.38) and simplify, we find:

$$\boxed{Re_{\text{VAC}} \sim \mathcal{C}^{\frac{1}{2}}E^{\frac{1}{3}}}. \tag{2.42}$$

Equation (2.42) is referred to as a 'VAC' scaling due to the underlying assumption that a triple balance exists between the Viscous-Archimedean (buoyancy)-Coriolis forces in the system. This VAC scaling is anticipated to hold close to the onset of steady convection in an RC system [Aubert et al. (2001), Gillet and Jones (2006), Soderlund et al. (2012), King and Buffett (2013), Gastine et al. (2016), Rajaei et al. (2018)].

If the Coriolis term in (2.30) is instead balanced by an inertial advection term, we see:

$$2\vec{\Omega} \cdot \vec{\nabla}\vec{u} \sim \vec{u} \cdot \vec{\nabla}\vec{\omega}, \tag{2.43}$$

which can be scaled for our system as:

$$\frac{2\Omega U}{H} \sim \frac{U^2}{\delta^2}. \tag{2.44}$$

Re-arrangement of (2.44) yields:

$$\frac{\delta}{H} \sim \left(\frac{U}{2\Omega H}\right)^{\frac{1}{2}} \sim Ro^{\frac{1}{2}}. \tag{2.45}$$

We henceforth refer to the form of δ in (2.45) as:

$$\delta \sim l_{\text{turb}} = Ro^{1/2}H, \tag{2.46}$$

where, here, the subscript of l denotes an inertial, turbulent state. Substitution of (2.46) into (2.38) gives:

$$Re_{\text{CIA}} \sim \mathcal{C}^{\frac{1}{2}} E^{\frac{1}{2}} Ro^{-\frac{1}{4}}. \tag{2.47}$$

Furthermore, The Rossby number, Ro, can be written in terms of the Reynolds number, Re, and the Ekman number, E, as $Ro = ReE$. Substitution of this relation then eliminates Ro and yields:

$$Re_{\text{CIA}} \sim \mathcal{C}^{\frac{1}{2}} E^{\frac{1}{2}} (Re_{\text{CIA}} E)^{-\frac{1}{4}} \rightarrow \boxed{Re_{\text{CIA}} \sim \mathcal{C}^{\frac{2}{5}} E^{\frac{1}{5}}}, \tag{2.48}$$

where a triple balance between the Coriolis-Inertial-Archimedean (buoyancy) forces is as-

sumed, resulting in a 'CIA' scaling for Re [Cardin and Olson (1994), Aubert et al. (2001), Gillet and Jones (2006), Gastine et al. (2016)]. It is expected that the CIA scaling is likely to be valid farther past onset than the analogous VAC scaling due to the assumption that inertial advection, rather than viscous forces, dominates the QG flow. This inertial theory was first developed by Hide (1974) and Ingersoll and Pollard (1982). The thermal forcing needed to exceed viscous conditions at onset and reach the described inertial state is not well quantified.

Importantly, we note that when the local Reynolds number in an RC system, $Re_\delta = U\delta/\nu$, is of order unity, i.e. $Re_\delta \sim \mathcal{O}(1)$, the two scalings of δ discussed, $l_{\text{crit}} \sim E^{1/3}H$ and $l_{\text{turb}} \sim Ro^{1/2}H$, are comparable. Specifically, if we use (2.23) for δ, we can estimate the local Reynolds number as:

$$Re_\delta \simeq ReE^{1/3}. \tag{2.49}$$

Since $Ro = ReE$, then:

$$Ro \simeq (Re_\delta/E^{1/3})E \simeq E^{2/3} \tag{2.50}$$

when $Re_\delta \sim \mathcal{O}(1)$. This implies:

$$l_{\text{turb}} \sim Ro^{1/2}H \simeq (E^{2/3})^{1/2}H \simeq E^{1/3}H \sim l_{\text{crit}}. \tag{2.51}$$

Thus, the turbulent scale, l_{turb}, scales equivalently to the onset scale, $l_{\text{crit}} \sim E^{1/3}H$. Further, Sprague et al. (2006) show that (2.51) holds beyond $Re_\delta \sim \mathcal{O}(1)$ [i.e. when $Re_\delta > \mathcal{O}(1)$], so long as the local Rossby number of the system remains small, i.e. $Ro_\delta < \mathcal{O}(1)$.

Therefore, we crucially note that:

$$l_{\text{crit}} \simeq E^{1/3}H \quad \simeq \quad l_{\text{turb}} \simeq Ro^{1/2}H \tag{2.52}$$

in $Re_\delta \sim \mathcal{O}(1)$ RC systems [e.g. Calkins et al. (2015), Calkins (2018), Aubert (2019)].The difference between the VAC scaling of (2.42) and the CIA scaling of (2.47) occurs in the assumed dynamic length scale, δ. Since $l_{\text{crit}} \simeq l_{\text{turb}}$ when $Re_\delta \sim \mathcal{O}(1)$, then the VAC scaling

of (2.42) and the CIA scaling of (2.47) are comparable:

$$Re_{\text{VAC}} \simeq Re_{\text{CIA}}. \tag{2.53}$$

This magnitude equivalence is fundamental to quasi-geostrophic turbulence in which local-scale thermal wind flows dominate the bulk dynamics.

Figure 2.4 illustrates a schematic of the momentum transfer behavior in a hydrodynamic RC system for the same fixed non-dimensional rotation period shown in Fig. 2.3. This schematic is the first of its kind, and we built this 'strawman' model in order to test the theoretical velocity scalings presented herein. In Fig. 2.4, the open and solid stars again represent the onset of wall mode and steady convection, respectively. After the onset of steady convection, it is predicted that momentum transfer will follow a VAC scaling in which the Reynolds number, Re, follows the magenta curve according to (2.42). Commensurate with heat transfer behavior, it is predicted that the change from a VAC to a CIA Re scaling will occur near the thermal transition Rayleigh number, Ra_T, given by (2.29) and shown as the vertical dashed line in Fig. 2.4. This set-up follows the essential arguments of Aubert et al. (2001) and King and Buffett (2013). In order to create the magenta (green) VAC (CIA) curves in Fig. 2.4, we assume a Nu–Ra dependence given by (2.24)–(2.25) below Ra_T, and either a 2/7 or 1/3 non-rotating style scaling given by (2.8) or (2.9) above Ra_T. The RBC behavior for Re given by (2.12) is included in faded black to provide an upper bound to RC behavior of Re.

The results of the first large suite of experiments designed specifically to test the ideas underlying Fig. 2.4 are presented in Chapter 4. Specifically, the connection (or lack thereof) between the heat transfer behavior displayed in Fig. 2.3 and that of momentum transfer in Fig. 2.4 will be explored systematically, for the first time, and detailed in Chapter 4. We mention that while not included in the framework shown in Fig. 2.4, numerous studies have used the free-fall Rossby number, Ro_{ff}, of (2.20) to estimate non-dimensional velocities in the absence of direct system velocity measurements [Christensen (2002), Sprague et al. (2006), Julien et al. (2012a), Cheng et al. (2015)]. While we predict that an estimate of Ro

using (2.20) will only hold in an asymptotically large Ra diffusion-free space, we still test the accuracy of the free-fall Rossby parameter in predicting experimental values of Ro in Chapter 4. We find that Ro_{ff} does not predict our measured Ro values well. Further, our velocity data do not agree with the behavior illustrated in the 'strawman' schematic of Fig. 2.4. Instead, the CIA scaling holds excellently across the entire parameter space studied, with the VAC scaling holding adequately throughout our span of Ra as well. We also find that heat transfer behavioral transitions do not correspond to momentum transfer behavior. Furthermore, an explanation of our findings from the study discussed in Chapter 4 lies in an analysis of the theoretical length local convection scales of experiments, an additional study that we lay out in Chapter 5.

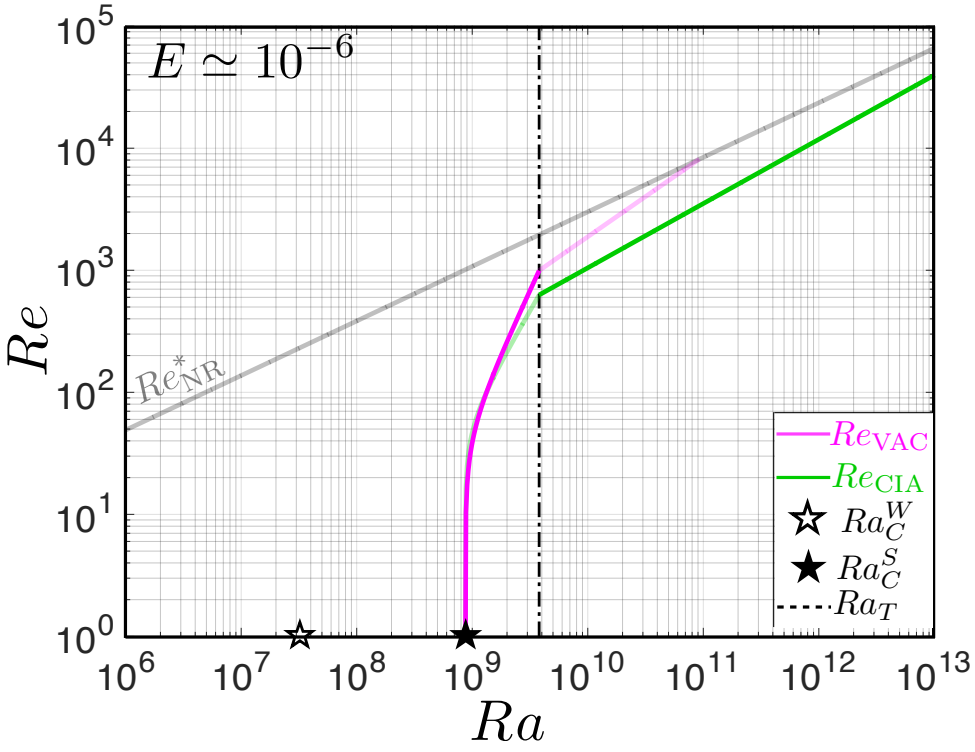

Figure 2.4: Momentum transfer, Re, versus input thermal forcing, Ra, for an RC water system of a fixed non-dimensional rotation period of $E = 10^{-6}$, consistent with Fig. 2.3. The onset of wall mode convection given by (2.21) is denoted by an open star, and the onset of steady convection given by (2.22) as a solid star. The black dashed line of Ra_T given by (2.29) displays the predicted transition from rotationally constrained to non-rotating style heat transfer. Re is predicted to follow a VAC scaling (magenta) given by (2.42) near onset until inertial advection begins to affect the system significantly, at which point a CIA scaling (neon green) given by (2.48) is expected. Specifically, The transition from VAC to CIA scalings is predicted to occur at the thermal transition Rayleigh number, Ra_T. Below $Ra \leq Ra_T$, Nu^*_Ω is assumed in the calculation of Re, and above $Ra > Ra_T$, Nu^*_1 or Nu^*_2 is assumed. Pre-factors of unity are used in (2.42) and (2.48). The non-rotating behavior of Re given by (2.11) as shown in Fig. 2.2 is included opaquely in black as an upper bound to the behavior of Re in this RC system.

CHAPTER 3

Experimental Device: NoMag

In this chapter, I describe the NoMag laboratory device at the UCLA Spinlab. In Section 3.1, I provide an overview of the device that includes a description of the broad non-dimensional parameter space that can be explored using the device. In Section 3.2, I describe the basic operation and assembly of the device and its multiple components. In Section 3.3, I detail the operation of the Laser Doppler Velocimetry (LDV) method employed in conjunction with the NoMag apparatus. A glimpse of the NoMag device in motion is provided via the Youtube film:

- https://www.youtube.com/watch?v=Et6mnyn9PzE (The Grandeur of NoMag).

3.1 The NoMag Device: An Overview

The NoMag device at the UCLA Spinlab is presently the world's largest rotating convection device by volume using water. Designed specifically to reach more extreme, planet-like parameters in which multi-scale dynamics can be studied, the device is capable of exploring essential features of core-style convection. In order to accurately characterize the complex physics of rotating convective turbulence, the device is constructed with a cylindrical geometry. This reduced geometrical approach is common to other rotating convection devices and numerical models, making direct comparisons with other studies possible [e.g. Kunnen et al. (2010), Stellmach et al. (2014) Cheng et al. (2015), Horn and Shishkina (2014), Cheng et al. (2018)]. As detailed in Section 1.3, the NoMag device simulates a local, polar parcel of planetary core convecting fluid under the influence of axial rotation and buoyancy forcing. Along with fellow graduate students, I oversaw the final fabrication stages of the NoMag

apparatus, which was completed in 2014. I conducted preliminary tests and data acquisition on the device, the details of which are provided in Section 3.3 and in Chapters 4 through 7.

In Section 3.1.1 below, I provide a basic description of the device and its main components. Greater details of the device components and operation of the custom experiment can be found in Section 3.2. In Section 3.1.2, I describe the reasoning for fabricating the device in the manner in which it has been constructed, and I explain the benefits of large non-dimensional parameter space that can be probed with the device. I also refer readers to Chapter 5 of J.S. Cheng, *Characterizing Convection in Geophysical Dynamo Systems*, PhD thesis, University of California–Los Angeles, 2015, for more information surrounding the design and fabrication of the NoMag device.

3.1.1 Device Description

The NoMag device is comprised of a 1.27 cm thick optically clear cylindrical acrylic sidewall (thermal conductivity $k = 0.19$ W/mK) of variable height that is bounded by two aluminum thermal blocks ($k = 167$ W/mK) that allow for the exchange of heat. The Biot number, which characterizes the 'isothermality' of the boundaries relative to that of the interior, is small in all experiments, i.e. $Bi \lesssim 0.05$. Thus, we argue that thermal boundary gradients will only be a few percent of those within the fluid. The container is filled with water ($Pr \simeq 7$) for the work presented in this dissertation, though future applications may include the use of air ($Pr \simeq 1$) and/or other gasses, as well as silicone oil with varying viscosities ($20 \lesssim Pr \lesssim 1000$).

The temperature dependent properties of water, used in the calculations of experimental parameters such as Nu and Ra, are given as: [Lide (2000)]

$$\alpha_T = -6.82 \times 10^{-5} + 1.70 \times 10^{-5} T - 1.82 \times 10^{-7} T^2 + 1.05 \times 10^{-9} T^3 \ [1/\mathrm{K}], \tag{3.1}$$

$$\rho = 999.8 + 0.1041 T - 9.718 \times 10^{-3} T^2 + 5.184 \times 10^{-5} T^3 \ [\mathrm{kg/m^3}], \tag{3.2}$$

$$\nu = \frac{6.581}{\rho (61.5 + T)^2} \ [\mathrm{m^2/s}], \tag{3.3}$$

$$\kappa = 1.312 \times 10^{-7} + 6.972 \times 10^{-10}T - 5.631 \times 10^{-12}T^2 + 2.633 \times 10^{-14}T^3 \text{ [m}^2\text{/s]}, \quad (3.4)$$

$$k = 0.5529 + 2.6621 \times 10^{-3}T - 2.3741 \times 10^{-5}T^2 + 1.1081 \times 10^{-7}T^3 \text{ [W/m K]}, \quad (3.5)$$

$$C_p = \frac{k}{\rho\kappa} \text{ [J/kgK]}, \quad (3.6)$$

where α_T is the thermal expansivity, T [°C] is the mean temperature of the fluid, ρ is the density, ν is the kinematic viscosity, κ is the thermal diffusivity, k is the thermal conductivity, and C_p is the specific heat capacity.

In order to generate convection, a fixed heat flux is passed through the bottom thermal block to the fluid layer by a custom fabricated OEM silicon non-inductively wound electrical resistance heating pad in direct contact with the bottom block. The fluid layer is cooled from above by a custom-built double-wound spiral heat exchanger in the top aluminum thermal block that is maintained at a fixed temperature by a ThermoNESLAB HX150 air-cooled precision thermal bath. The entire container and it's aluminum structural frame are rotated about a vertical axis by a Danaher gearhead motor (DT90-010) with a Yaskawa speed reducer (SGMPH-04AAE41D). This allows for uniform rotation of the container varying from 0 to 60 rpm, or revolutions per minute.

Figure 3.1a) shows a schematic of the NoMag device with our tallest tank of height $H \simeq 1.85$ m. The present diagnostic capabilities of the device are also shown in the schematic. Temperature measurements of the fluid layer are collected by 16 custom fabricated Amphenol thermistors located within 1 cm of the fluid layer inside the top (blue) and bottom (red) boundaries, providing accurate measurement of the vertical temperature difference across the fluid layer. These waterproof thermistors can also be placed at various depths directly inside the fluid layer (purple) via ports in the top thermal block in order to capture internal dynamics of the system. A custom calibration of all sensors has been performed such that the precision of temperature measurements is to within ±50 mK, or miliKelvin.

An MSE UltraLDV (green) is mounted in the rotating frame to conduct laser doppler velocimetry (LDV) and can be placed at various heights and radial locations to collect point velocity measurements. The details of this instrument and its functionality are described

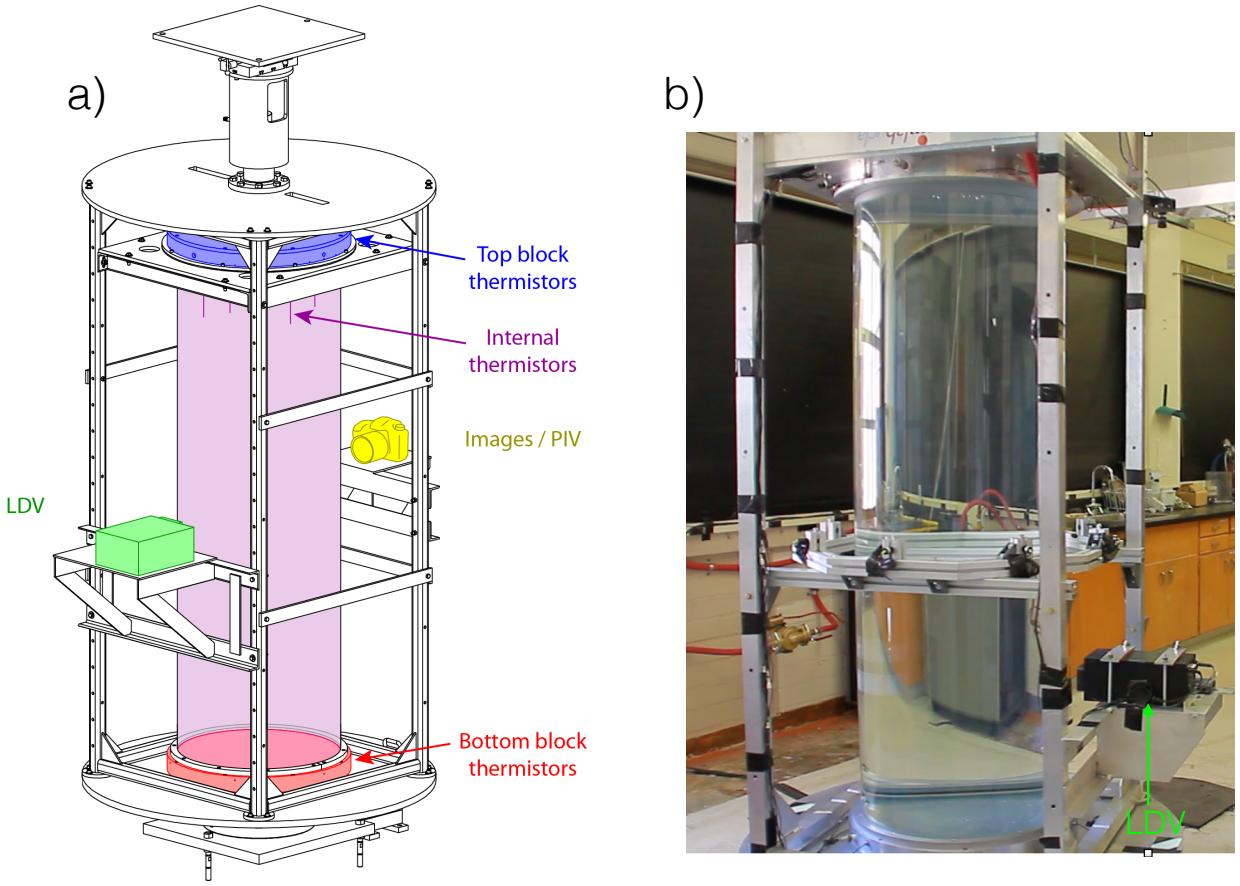

Figure 3.1: a) Schematic of the NoMag laboratory device with our $H \simeq 1.85\ m$ acrylic container. Diagnostic capabilities of the device include: 1) temperature measurements at the top (blue) and bottom (red) of the fluid boundaries, 2) direct internal fluid temperature measurements (purple), 3) point velocity measurements via laser doppler velocimetry (LDV) (green), and 4) future length scale, vorticity, and axial helicity measurements via particle image velocimetry (PIV) (yellow). Schematic courtesy of Jonathan Cheng. b) An image of the device with the tallest tank in place using water as the working fluid. The LDV instrument is mounted in the rotating frame of the device and is labeled in green.

in Section 3.3. The last diagnostic in Fig. 3.1a) is indicated by a camera icon (yellow) to represent the use of particle image velocimetry (PIV). This diagnostic tool has not been fully implemented to date and thus will not be used in the work presented in this dissertation. Future applications of the NoMag device, beyond the scope of the results herein, will make use of PIV in order to characterize length scales of RC, as well as direct measurements of vorticity and axial helicity. Figure 3.1b) displays an image of the device with the tallest tank in place using water as the working fluid. The LDV instrument is mounted in the rotating frame of the device and labeled in green.

3.1.2 Parameter Space

It is possible to use container sidewalls of different heights on the device. All containers used in the work presented in this dissertation possess a fixed inner diameter of $D_i = 0.586$ m, and possible tank heights include: $H \simeq 0.025$ m ($\Gamma \simeq 24$), $H \simeq 0.05$ m ($\Gamma \simeq 12$), $H \simeq 0.1$ m ($\Gamma \simeq 6$), $H \simeq 0.2$ m ($\Gamma \simeq 3$), $H \simeq 0.4$ m ($\Gamma \simeq 1.5$), $H \simeq 0.8$ m ($\Gamma \simeq 0.75$), and $H \simeq 1.85$ m ($\Gamma \simeq 0.33$). Note that we have fabricated containers with a smaller diameter of $D_i \simeq 0.20$ m and associated accommodators to hold such containers in place on the device that will be of use in future studies. These $D_i \simeq 0.20$ m diameter acrylic containers have varying heights of $H \simeq 0.05$ m ($\Gamma \simeq 4$), $H \simeq 0.1$ m ($\Gamma \simeq 2$), $H \simeq 0.2$ m ($\Gamma \simeq 1$), $H \simeq 0.4$ m ($\Gamma \simeq 0.5$), $H \simeq 0.8$ m ($\Gamma \simeq 0.25$), and $H \simeq 1.60$ m ($\Gamma \simeq 0.125$).

The design of the device incorporates this ability to span a wide range of container heights in order to access a broad range of non-dimensional parameter space. In fact, the range of parameters described below is one of the largest ranges of any comparable laboratory device using water to date. The input thermal forcing of the system can be expressed in terms of the Rayleigh number, Ra, and is directly dependent on height to the cubic power as prescribed in (2.4). Similarly, the non-dimensional rotation of the system is characterized by the Ekman number, E, which is inversely proportional to the height of the container squared as per (2.16). Thus, small increases to the height of the fluid container increase Ra significantly (cubically) while simultaneously decreasing E significantly. In addition, Ra in Earth's core, for example, is estimated to range between $Ra \sim 10^{20} - 10^{30}$, indicating that the thermal forcing is very strong, i.e. turbulent [see Table 2.1 in Chapter 2]. Furthermore, E of the Earth is roughly $E \sim 10^{-15}$, indicating that the Coriolis force, or rotational strength, on fluid motions in the geodynamo generating region is also very strong. Thus, in order to model this high Ra and low E, i.e. rapidly rotating and convectively turbulent, system, the NoMag device reaches some of the highest values of Ra and simultaneously low E of any of the most extreme planetary models (numerically and experimentally) to date.

The estimated ranges of non-dimensional parameters in the NoMag device using water are provided in Table 3.1, a replica of Table 2.1 with the addition of the rightmost column

Parameter	Meaning	Definition	Earth's Core	NoMag
Rayleigh, Ra	$\frac{\text{thermal buoyancy}}{\text{thermal \& viscous diffusion}}$	$\frac{\alpha g \Delta T H^3}{\nu\kappa}$	$\sim 10^{20} - 10^{30}$	$\sim 10^{5} - 10^{13}$
Prandtl, Pr	$\frac{\text{viscous diffusion}}{\text{thermal diffusion}}$	$\frac{\nu}{\kappa}$	$\sim 10^{-1}$	~ 7
Ekman, E	$\frac{\text{viscous diffusion}}{\text{Coriolis}}$	$\frac{\nu}{2\Omega H^2}$	$\sim 10^{-15}$	$\sim 10^{-8} - 10^{-2}$
Froude, Fr	$\frac{\text{centrifugal buoyancy}}{\text{gravitational buoyancy}}$	$\frac{\Omega^2 R}{g}$	$\sim 10^{-3}$	$10^{-4} - 1$
Nusselt, Nu	$\frac{\text{total heat flux}}{\text{conductive heat flux}}$	$\frac{qH}{k\Delta T}$	$\sim 10^{2} - 10^{7}$	$\sim \mathcal{O}(1) - 5 \times 10^{3}$
Reynolds, Re	$\frac{\text{inertial advection}}{\text{viscous diffusion}}$	$\frac{UH}{\nu}$	$\sim 10^{9}$	$\sim 10 - 10^{4}$
Rossby, Ro	$\frac{\text{inertial advection}}{\text{Coriolis}}$	$\frac{U}{2\Omega H} = ReE$	$\sim 10^{-6}$	$\sim 10^{-5} - 10^{2}$
free-fall Rossby, Ro_{ff}	$\frac{\text{thermal buoyancy}}{\text{Coriolis}}$	$\frac{\sqrt{\alpha g \Delta T H}}{2\Omega H} = \sqrt{\frac{RaE^2}{Pr}}$	$\sim 10^{-5} - 10^{0}$	$\sim 10^{-6} - 10^{3}$

Table 3.1: Table 2.1 reproduced with an added rightmost column of estimated parameters of the NoMag experimental apparatus using water. Details of the calculated ranges in the rightmost column for the NoMag device are provided in the text.

for the NoMag estimates. In terms of control parameters, the range of Ra that we are capable of spanning via the NoMag device is set by the minimum and maximum heat fluxes applied to the system. With our current laboratory equipment, a minimum of 30 W and a maximum of 1200 W heating power can be applied to the bottom thermal block via the heating pad that sits beneath it. We note that we are currently implementing changes to our heating and cooling systems to accommodate a heating power of up to 10kW in the future. Non-dimensionally, our control parameter is a flux Rayleigh number defined as:

$$Ra_F = \frac{\text{buoyancy flux}}{\text{viscous \& thermal diffusion}} = \frac{\alpha g H^4 q}{\rho C_p \kappa^2 \nu A} = NuRa, \tag{3.7}$$

where q [W] is the heating power, ρ [kg/m^3] is the mean density of the fluid, C_p [J/kgK] is the specific heat capacity, and A [m^2] is the active surface area of the bottom aluminum boundary. Note that the flux Rayleigh number can be written in terms of the product of the Rayleigh and Nusselt numbers. Thus, if we assume an appropriate relation between Nu and Ra such as those of (2.8), (2.9), and/or (2.24), we can solve for the Ra range corresponding

to a given heat flux (i.e. Ra_F) range. The details of such calculations are provided in the discussion of Figure 3.2 below.

The Prandtl number of water, $Pr \simeq 7$, is considered to be moderate in magnitude relative to that of Earth's outer core. Nonetheless, as explained in Section 1.2, the device is designed to replicate large-scale flows expected in planetary cores. Lastly, the Ekman number is set by the dimensional range of rotation rates at which the NoMag device can rotate. Our range of rotation rates varies from 1.0 to 60 rpm at present. At present, below 1.0 rpm, instabilities in the servomotor driving become significant. It is possible that further future tuning of the servo may allow steady rotation below 1.0 rpm. Accounting for all possible container heights, our range of E thus spans from $\sim 10^{-8} - 10^{-2}$.

In terms of the output parameter estimates in Table 3.1, using (3.7) we estimate that we can reach near to the onset of convection at $Nu \sim \mathcal{O}(1)$, out to $Nu \sim 5000$ far beyond onset. In terms of the Reynolds number, we have experimentally determined that this range using water on the NoMag device lies between $\sim 10 \lesssim Re \lesssim 10^4$. Thus, we estimate that the Rossby number range on the device is $\sim 10^{-5} \lesssim Ro \lesssim 10^2$, and a free-fall Rossby number estimate yields a range of $\sim 10^{-6} \lesssim Ro_{\text{ff}} \lesssim 10^3$.

We display in Figure 3.2 the E-Ra space that we estimate the NoMag device is capable of spanning with the $D_i = 0.586$ m wide containers of varying heights using water. For simplicity and because they are not used in this dissertation work, the $H \simeq 0.025$ m and $H \simeq 0.05$ m tanks, our two shortest tanks, are not included. Even so, as shown in Fig. 3.2, the various container heights on the NoMag device allow us to span nearly six orders of magnitude in Ra and four orders in E. In order to estimate Ra on the x-axis of Fig. 3.2, we use an input heating power range of 30–1200 W and assume a Nu-Ra relation of (2.24) until intersection with either the (2.8) or the (2.9) Nu-Ra curves occur according to (2.29). For reference, the achievable range of the temperature difference, ΔT, that can be applied across the fluid layer using this heating power range corresponds to a total range of 1–25 K.

Furthermore, Fig. 3.2 also displays the transition predictions for several different behavioral regimes of a RC system as dashed lines. The gold dashed line displays the onset of wall

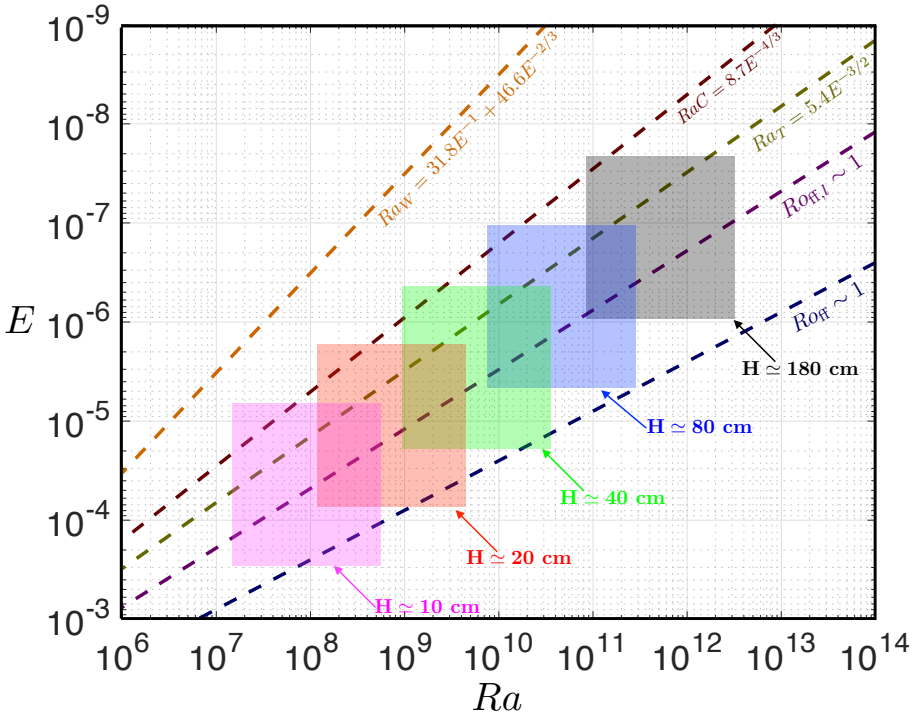

Figure 3.2: Regime diagram of RC parameters E and Ra for the experimental device, NoMag, using the magenta $H \simeq 0.1$ m ($\Gamma \simeq 6$), red $H \simeq 0.2$ m ($\Gamma \simeq 3$), green $H \simeq 0.4$ m ($\Gamma \simeq 1.5$), blue $H \simeq 0.8$ m ($\Gamma \simeq 0.75$), and black $H \simeq 1.85$ m ($\Gamma \simeq 0.33$) tall tanks with a fixed inner diameter of $D_i = 0.586$ m. The dashed lines indicate theorized behavioral transitions of a RC system as follows: gold is the onset of wall mode convection for an infinite plane layer in water, burgundy is the onset of steady convection for an infinite plane layer in water, olive is the transition from columnar to weakly rotating convection found in Cheng et al. (2015), and plum/navy is the local/global estimate of a free-fall Rossby number, Ro_{ff}, of order unity in which buoyancy begins to dominate over rotational forces.

mode convection for an infinite plane layer given by (2.21) and is not accessible in water in any of the containers shown. The onset of steady convection in water for an infinite plane layer given by (2.22) is shown by the burgundy dashed line. The olive dashed line represents the empirical transition from columnar to non-rotating style convection found in Cheng et al. (2015). The plum and navy dashed lines represent estimates for a local and global free-fall Rossby number of order unity, respectively. The plum line uses a local length scale estimate for Ro_{ff} based on the characteristic width of a convective column, $l \sim E^{1/3}H$ [Chandrasekhar (1961), Greenspan (1969b), Julien and Knobloch (1998)]. Thus, the plum/navy dashed lines represent where locally/globally thermal buoyancy begins to dominate the convection and overcome the effects of rotation past the columnar regime in a RC system. We conclude that

the inclusion of the containers shown in Fig. 3.2 should allow us to probe several different behavioral regimes of a RC system, reaching that which is theoretically closest to a planet at our highest Ra and lowest E.

3.2 Operation of the NoMag Device

The details of key components of the NoMag device are provided in subsections as follows: Section 3.2.1 includes a description of the overall structure of the apparatus, Section 3.2.2 contains a description of the heating and cooling systems of the device, Section 3.2.3 is a description of the components needed to assemble an experimental tank of fluid on the device, and Section 3.2.4 details the control, measurement, and data acquisition capabilities of the device. For further details, confer to documentation on the Spinlab website (`https://spinlab.ess.ucla.edu/`). In addition, I plan to upload a time-lapsed video demonstrating the assembly of an experimental container on the device. The video will also contain other important operational details including the present storage locations of experimental parts.

3.2.1 Structural Frame

I begin by noting that many of the design components of NoMag are comparable to its predecessor, RoMag. The design drawing package of the NoMag apparatus and its parts is located in the Spinlab foyer. An electronic version of the design package can be obtained from PI Jon Aurnou. Figure 3.3 shows the list of all parts itemized on the first page of the design package. For detailed descriptions of the RoMag device, readers are referred to the theses of Eric King [King (2009)] and Alexander Grannan [Grannan (2017)]. I focus here on describing the notable differences in the two device designs. NoMag's framework consists of a lower deck, main experimental deck/frame, and an upper deck, all made of 6061-T6 aluminum. The round bottom table has a diameter of 1.32 m and is coated in black LizardSkin^{TM} thermally insulating ceramic spray on paint to minimize thermal losses. The bottom table sits above a bearing that is attached, via a drive belt, to a pulley that is in contact with the servomotor of the device, as illustrated in Figure 3.4. Both the bottom and

ITEM NO.	PART NUMBER	DESCRIPTION	QTY.
1	UC 3101	BASE PLATE	1
2	UC 3102	LEVELING SCREW	3
3	UC 3103	BEARING ADAPTER	1
4	UC 3104	PULLEY	1
5	UC 3105	CROWNED PULLEY	1
6	UC 3106	LOWER TABLE	1
7	UC 3107	HEATER RING	1
8	UC 3108	MOTOR MOUNTING PLATE	1
9	UC 3109	MOTOR MOUNT	1
10	UC 3110	NUT 3/4-32	6
11	UC 3111	HEATER COMPRESSER	1
12	UC 3112	BOTTOM THERMAL BLOCK	1
13	UC 3113	SSS RING HALF	4
14	UC 3114	MAIN FRAME WELDMENT	1
15	UC 3115	69" HIGH TANK	1
16	UC 3116	46" HIGH TANK	1
17	UC 3117	23" HIGH TANK	1
18	UC 3118	11.5 HIGH TANK	1
19	UC 3119	TOP THERMAL BLOCK	1
20	UC 3120	TOP THERMAL BLOCK COVER	1
21	UC 3121	GASKET	1
22	UC 3122	UPPER CHASSIS	1
23	UC 3123	TOP THERMAL BLOCK MOUNTING PLATE	1
24	UC 3124	UPPER TABLE	1
25	UC 3127	UPPER BEARING MOUNT MACHINING	1
26	UC 3128	X-Y-LEVELING PLATE	1
27	UC 3129	SLIP RING MOUNT	1
28	UC 3130	TOP BEARING HOUSING	1
29	UC 3131	DOPPLER PLATFORM	1
30	UC 3132	COUNTERWEIGHT PLATFORM	1
31	UC 3134	POSITION STOP	1
32	UC 3135	BOTTOM ACCOMMODATOR	1
33	UC 3136	TOP ACCOMMODATOR	1
34	UC 3137	2m ROMAG TANK	1
35	UC 3138	1m ROMAG TANK	1
36	UC 3139	.5m ROMAG TANK	1
37	UC 3140	2m HIGH TANK	1
38	UC 3141	SLIP RING ANTI-ROTATOR	1
39	UC 3145	CROSS BAR	6
40	6651K4	TURNTABLE (McMASTER cARR)	1
41	BELT	BELT	1
42	DT90-010	MOTOR (DANAHER)	1
43	SGMPH-04AAE41D	SPEED REDUCER (YASKAWA)	1
44	36103	X-Y TABLE (PALMGREN)	1
45	GP-221	ROTARY UNION (DST)	1
46	830	SLIP RING (MERCOTAC)	1
47	ULTRA LDV	LDV (MSE)	1

ITEM NO.	PART NUMBER	DESCRIPTION	QTY.
48	K001592	HEAT PAD (0EMHEATERS)	1
49	1222	BEARING (SKF)	1
50	U-06080-20	CARBOY (COLE PARMER)	1
51	1986K5	SPRING (McMASTER CARR)	5
52	9452K365	O-RING (Mc MASTER CARR)	2
53	9452K368	O-RING (Mc MASTER CARR)	1
54	9452K496	O-RING (McMASTER CARR)	2
55	9452K495	O-RING (McMASTER CARR)	2
56	9452K497	O-RING (McMASTER CARR)	1
57	4830K136	PIPE NIPPLE (McMASTER CARR)	2
58	4830K214	PIPE NIPPLE (McMASTER CARR)	2
59	91594A310	HITCH PIN (McMASTER CARR)	1
60	91309A644	HSCS (McMASTER CARR)	3
61	-	SHCS 1/4-20 x 1/2	2
62	-	SHCS 5/16-18 x 5/8	9
63	-	SHCS 5/16-18 x 1	39
64	-	SHCS 5/16 x 1 1/4	4
65	-	SHCS 5/16-18 x 2 1/2	8
66	-	SHCS 3/8-16 x 1	12
67	-	SHCS 3/8-16 x 1 1/4	16
68	-	SHCS 3/8-16 x 2 1/2	8
69	-	SHCS M6x1.0 x 20	4
70	-	HHMS 5/16-18 x 1	4
71	-	HHCS 3/8-16 x 1 1/2	8
72	-	HHCS 3/8-16 x 2 3/4	1
73	-	HHCS 3/8-16 x 3	24
74	-	HHCS 1/2-13 x 2 1/2	30
75	-	HHCS 5/8-11 x 1 1/2	8
76	-	HEX HD WASHER SCR 10-24 x 1/2	3
77	-	HEX NUT 3/8-16	37
78	-	CUP PT SET SCREW 8-32 x 1/4	2
79	-	SOCKET SET SCREW 10-32 x 7/8	1
80	-	FLAT WASHER 5/16	8
81	-	FLAT WASHER 3/8	45
82	-	LOCK WASHER 1/2"	30

spinlab ucla
SIMULATED PLANETARY INTERIORS LAB

NO MAG ROTARY TABLE

10/31/12 UC 3100

Figure 3.3: Parts list (Page 1) of the NoMag Design Package created by Joel Neal.

top bearings need to be frequently re-greased using Shell lithium complex grease in order to prevent extra torques on the motor. I have found that if continuously running rotating experiments, it is best to re-grease the top and bottom bearings at least once every other week. After the device has been stationary for an extended period of time, also re-grease before the first instance of rotation. In general, if the device becomes louder than usual while spinning, that is typically a sign to re-grease. The lower frame supports the weight of all experimental components, and is leveled manually using thin metal shims.

The tall main deck in which experimental containers are placed and secured is structurally reinforced and connects the bottom and top decks via four hollow welded aluminum pieces, each with a height of 2.26 m [cf. Fig. 3.1]. The round upper table also has a diameter of 1.32 m and supports the weight of electronics in the rotating frame above it, as described in

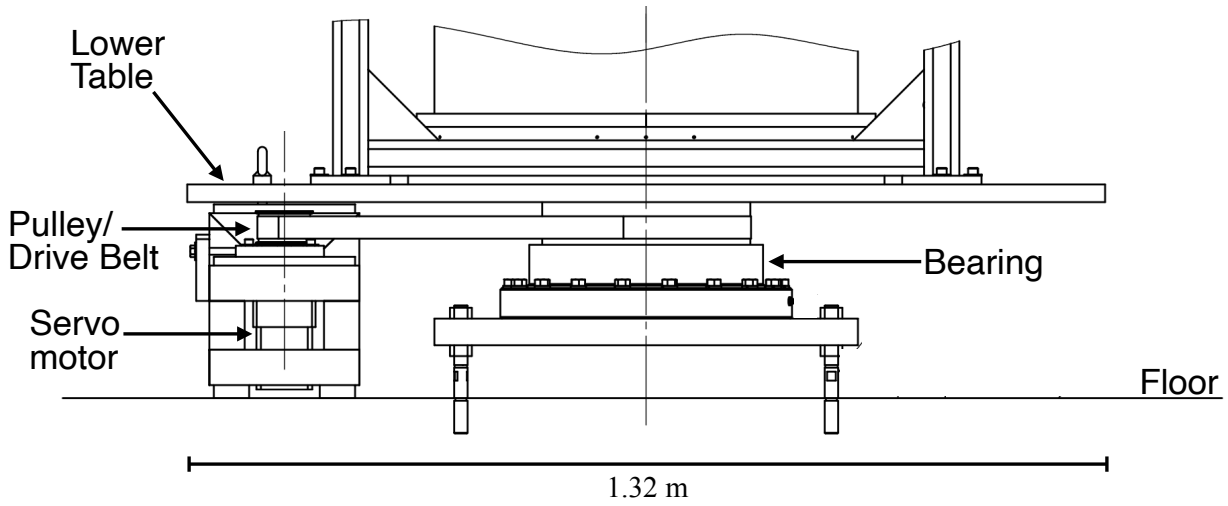

Figure 3.4: Side view drawing of the NoMag lower deck with labeled components. The diameter of the lower round turntable is 1.32 m. Drawing by Joel Neal.

subsection 3.2.4. Water is passed into/out of the rotating frame via a rotary union that is affixed above the upper turntable, and electrical signals are passed into/out of the rotating frame via slip rings, also affixed above the upper turntable [cf. subsection 3.2.4].

3.2.2 Heating and Cooling Systems

A custom fabricated OEM silicon non-inductively wound electrical resistance heating pad is placed in direct contact beneath the bottom thermal block of the convection tank in order to provide heating power for experiments. Our NoMag heating pads are custom fabricated due to their large diameter (roughly the diameter of the bottom block). Their electrical resistance at room temperature is approximately 18 Ω. A direct current is passed through the heat pad via a Sorenson DCS150-8E power supply. This power supply is impedance matched to the OEM heating pad resistance such that it is capable of delivering up to 150 V at 8 A, or up to 1200 W of heating power. The Sorenson power supply is powered by single phase 120V facility power and is in the stationary lab frame, while the heat pad is in the rotating experimental frame in contact with the convection tank. Heating current is passed through electrical slip rings into the rotating frame. The NoMag slip ring unit is a Mercotac Model 830 with eight channels, two at 4 A and six at 30 A. The Mercotac unit sits above

the fluid rotary union atop the electronics deck in the upper frame and passes electrical signals from the stationary lab frame to the rotating frame. A power supply with greater heating power has been recently purchased to replace the Sorensen unit used in this work. The new power supply is a TDK Lambda GEN 300-17 programmable DC power supply, also impedance matched to our heat pads to deliver up to 300V at 17A, or up to 5100 W.

Heat is removed from the convection tank by a water-cooled aluminum heat exchanger built into the top thermal block. The design of our custom heat exchanger is similar to that of the RoMag cooling lid and is comprised of two double wound spiral flow channels, as illustrated in Figure 3.5. The double spiral flow path is designed such that as the water flows through the cooling block and heats up, the general pattern of temperature will be roughly uniform across the top boundary. Cool water is passed through the inlet (blue) of the heat exchanger and warms up via the removal of heat from the convection tank, thus exiting the heat exchanger at the outlet (red) with a slightly warmer temperature than at the inlet. The capability of thermistor placement directly into the lid block and not in direct contact with the heat exchanger channels is also displayed in Fig. 3.5. Six thermistors can be inserted into the lid block to 0.5R, one to 0.25R, and one to 0.75R, where R is the radius of the round lid block. The bottom thermal block has the same thermistor location configuration in order to measure fluid boundary temperatures of the convection tank.

Water is pumped in a closed loop through the heat exchanger in the top thermal block via a CP-55 pump in our Thermo NESLAB HX-150 air-cooled precision thermal bath. This chiller resides in the lab frame, uses 220 V single phase facility power, and contains water at a thermostated temperature to within 0.1 C. The flow rate of the chiller in line in our entire cooling loop on NoMag is of order 10 gallons per minute. The chiller is capable of extracting up to 5,000 W of heating power at maximum efficiency. It also has a 2.5 kW heater. We deliver chilled water from the lab frame chiller to the cooling block, which resides in the rotating frame. To accomplish this, we utilize a DSTI GPS-221 two channel fluid rotary union that is affixed above the electronics deck in the upper rotating frame of the device. All hosing is rubber and all metal parts in this closed fluid cooling loop are made of stainless steel in order to prevent rusting. We use de-ionized (DI) water in this loop to

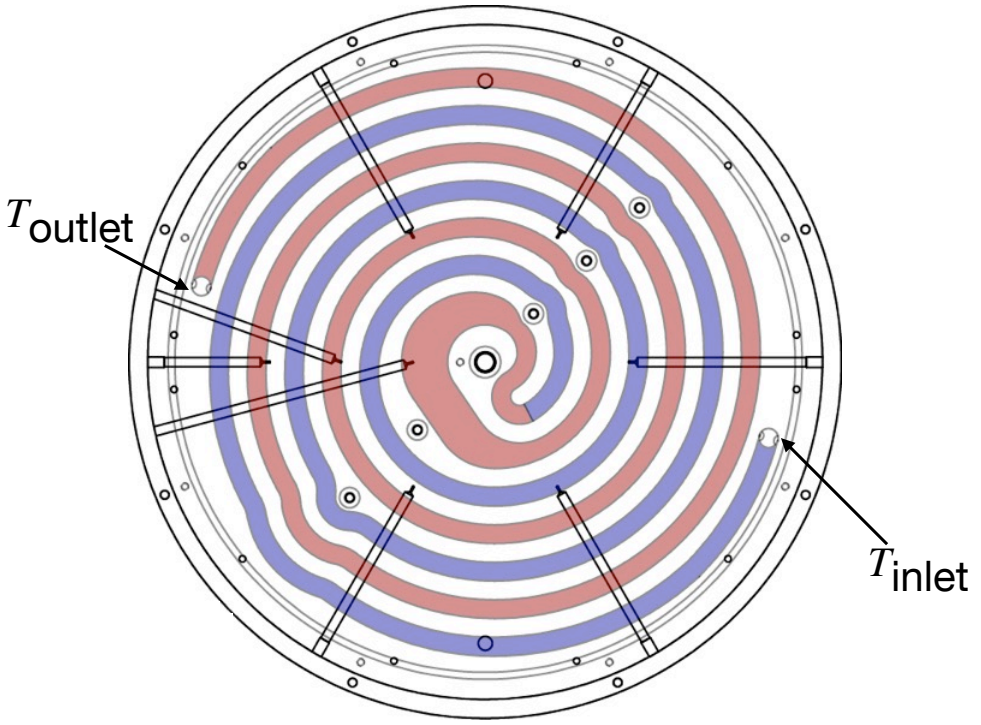

Figure 3.5: Top-down view drawing of the NoMag top thermal cooling block with two double wound spiral flow channels. The configuration of thermistors inserted into the lid block and not in contact with the heat exchanger in order to measure fluid boundary temperatures of the convection tank is also illustrated. Six thermistors can be inserted into the lid to 0.5R, one to 0.25R, and one to 0.75R, where R is the radius of the round lid. Drawing by Joel Neal and Jonathan Cheng.

further minimize corrosion, and we add a small amount of Polyscience Polyclean Clarifier solution, a lab algicide, to inhibit any biological growth (see instructions on container). When experiments are not being conducted, it is important to drain and dry the chiller reservoir and the cooling loop to further inhibit any instances of corrosion and/or bacterial growth. We note that we recently purchased a new, current-day version of the Thermo NESLAB series chiller to upgrade the cooling capabilities of NoMag. Future experiments will make use of a Thermo Fisher ThermoFlex TF10000 programmable water-cooled chiller in order to extract up to 10,000 W of heating power. This chiller requires three-phase facility power.

3.2.3 Tank Assembly

In this section, I will describe the convection tank from the ground up. Typically, the bottom thermal block is kept secured to the lower turntable and is not removed due to its weight.

While the top thermal block has heat exchanger channels cut inside, the bottom block is solid aluminum and has an estimated weight of ∼95 lbs. A minimum of two people are needed to lift and carry the thermal blocks. The only reason to remove the bottom block would be to access the heat pad beneath it. Beneath the bottom thermal block, a layer of Pacor Cryogel Aerogel insulation sits atop the lower table coated in black LizardSkin^{TM} paint. A stainless steel, thin round disk sits above the layer of insulation. The diameter of this disk is nearly that of the bottom block, ∼0.6 m. The OEM heat pad sits above this disk. A layer of Aremco Heat-Away 640 copper thermal grease is added only to the top of the heat pad, which is placed in direct contact with the bottom of the bottom thermal block. Care must be taken to ensure that strong thermal coupling exists between the heat pad and bottom block via the thermal grease layer, and we have found this bottom insulation is necessary in order to minimize heat loss out the bottom of the device.

Next, an o-ring greased with Dow Coring high vacuum grease is placed in the groove of the bottom lid. A sidewall of choice can then carefully be placed on top of this o-ring over the grooved region. Our NoMag acrylic sidewalls are custom fabricated by Reynolds Polymer Technology Inc. Care must be taken to avoid scratching these optically clear tanks. Rubber lab gloves are required to avoid leaving any fingerprints on the tank during installation. Once the tank is sat on the first o-ring in the bottom thermal block groove, another o-ring is placed on the outer diameter of the tank and moved all the way down to the bottom of the tank. This second o-ring is an extra guard against any leaks, and a 'super sidewall sealer' (SSS) is used to secure this o-ring (described below).

The top thermal block gets attached to a custom square frame and carefully inserted above the acrylic sidewall. The round top block is secured to its square frame via long threaded rods. Five people are needed to move this frame and lid unit into place. One person stands on each of the four sides of the square frame, and the group slowly moves the frame-lid unit into position. Together, the frame-lid unit is rather heavy, and it would be disastrous if dropped over any of the custom acrylic tanks. This is why it is crucial to have the minimum number of recommended people for this procedure. The fifth person is needed to insert the 9/16" bolts that attach the frame-lid unit to the 4 rectangular welded tall frame

struts permanently installed on the device. Nuts and crescent wrenches are used to tightly secure the frame-lid unit to the NoMag welded struts via the inserted coupling bolts. It is highly recommended that future NoMag operators watch the operational video that will be posted on the Spinlab website for this procedure. I also remark that this procedure is considerably more difficult for the taller tanks, as the height to which the frame-lid unit must be placed becomes higher.

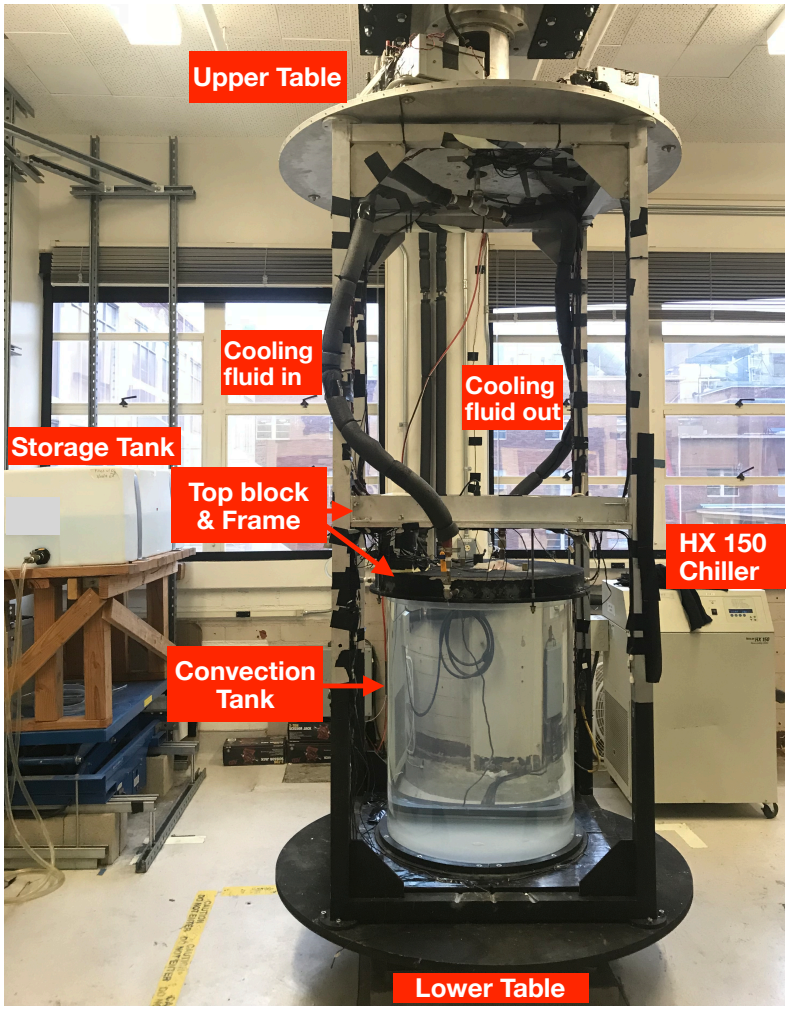

Figure 3.6: Photograph of the NoMag apparatus and a few associated parts. On the left, the plastic storage tank is shown partially filled with DI water. The clear fill hosing with quick disconnect fittings is attached to the storage tank at the bottom of the tank. The tank is secured to wooden framing that sits securely atop the blue lift that can be used to customize the height of the storage tank relative to the convection tank. The NoMag device with the convection tank installed using the 80 cm sidewall is shown in the center of the image. The lower and upper tables are labeled, as well as the top block, which is attached to its custom square frame via threaded rods visible in the image. On the right, the Thermo NESLAB HX 150 lab chiller can be seen.

Next, the lid can now be slowly lowered onto the acrylic tank. This is done by turning the threaded rods that couple the square frame and the top thermal block (see instructional video). One must make sure that the lid remains level throughout this step. Further, one must also be sure to check that a greased o-ring has been placed in the groove of the top thermal block before lowering it onto the sidewall container. As the lid is slowly lowered onto the tank, it will seat and somewhat of a popping sound can be heard, indicating that the o-rings are sealed. The top block and its square frame, both connected by threaded rods, can be seen in their final positions in the photograph in Figure 3.6. The outer portions of the lid have been coated in LizardSkin^{TM} to minimize heat loss to the surrounding room. Once the top block is properly seated onto the acrylic sidewall, the SSS can be placed at the base of the tank. The SSS is two stainless ring halves that are bolted into the bottom thermal block to provide an extra seal for the tank. The SSS and the outer portions of the bottom block have also been coated with the LizardSkin^{TM} paint to minimize heat losses.

At this point, the tank is now constructed and nearly ready to fill. There are several threaded through holes in both thermal blocks that need appropriate fittings/plugs. On the bottom thermal block, there are two side fill ports, one that extends near the edge of the inner diameter of the fluid area, and one that extends to the center. Quick disconnects are used in these ports to connect to hosing to fill the tank. These fittings must be installed, as well as the plugs in the top block before filling. In the top thermal block, there are a total of 6 ports that need plugs from a top-down view of the block, and can be seen in the drawing of Fig. 3.5. These ports exist so that internal thermistors can be inserted in them with proper custom plugs. I machined a set of solid brass plugs for the 5 off-center ports, and a delrin center plug for the larger central through hole. In addition, similar to the bottom block, two through holes exist on the sides of the block. One of the two identical holes is used to connect to the expansion tank of the device, and the other can be plugged with a quick disconnect or can be used with a custom plug for internal sidewall thermistors. These through holes in the top block are all separated from the channels cut for the heat exchanger.

The expansion tank is a $\sim$0.5 gallon round plastic container that gets secured above the top thermal block and remains permanently open to overflow from the convection tank.

Thus, the expansion tank serves as a reservoir for excess working fluid resulting from thermal expansion during convection experiments. The convection tank is therefore open to the atmosphere such that pressurization issues do not arise. Further, the expansion tank plays a key role in removing bubbles from the convection tank (described below).

The convection tank is filled with degassed DI water that is stored in a nearby plastic storage tank, as shown in Fig. 3.6. The NoMag storage tank is filled with DI water from the line in the Spinlab foyer. To eliminate bubbles existing in the water, it is recommended to leave the DI water in the storage tank for at least one week to degas before transferring to the main convection tank for experimentation. When full, the storage tank holds enough water to fill the 80 cm sidewall volume. Two fills of the storage tank are required to entirely fill the ∼185 cm sidewall volume, and proper time must be allocated for this procedure. It is important to use DI water only in the convection tank to minimize micro-pitting to the aluminum blocks. We have found that even with the DI water in our lab, micro-pitting does still slowly occur over time if the tank sits idly and filled for too long, but this undesired process occurs much faster with regular tap water. The storage tank must sit at a height above the height of the convection tank in order to use Bernoulli's pressure principle to fill the tank. The storage tank is secured to a mechanical lift so that the storage tank can be adjusted to a desired height. A clear hose at the bottom of the storage tank has quick disconnect fittings that connect to the fill ports in the sides of the bottom thermal block. We fill the tank from the bottom, keeping a close eye on when it becomes full. The water will begin to fill the expansion tank once the main convection tank becomes full. We fill the expansion tank roughly halfway, and then shut off the fill valves.

Inevitably, bubbles will form on the top lid during the filling process. Too many bubbles can affect heat transfer measurements if there are significant air gaps across the top boundary. To eliminate bubbles, we rotate the device until the fluid is fully spun up, and then abruptly shut off the rotation. Upon spin down, the bubbles will conglomerate at the center of the tank. The center plug in the top thermal block can then be opened to push out all air until water begins to overflow, thus eliminating all bubbles. Sometimes spinning up to ∼40 rpm is required to eliminate all bubbles. Before starting any rotating experiments, ensure that

the expansion tank is filled at least halfway. If the water level in the expansion tank is too low, bubbles can undesirably re-enter the main tank through the expansion tank port when the device is spun. We refer readers to Section 4.2 of Chapter 4 for the details of the manner in which the convection tank is insulated (primarily the acrylic sidewall).

Attention and care to the lids and acrylic sidewalls of the convection tank is necessary in order to preserve these parts. It is not recommended to leave the tank stationary/idling and full of DI water for longer than a week in order to minimize micro-pitting of the aluminum lids. Even rotating the tank to spin up/mix the fluid or generating thermal convection periodically can help. After experimentation and once the tank is drained into the central drain in the main lab using hosing connected to the fill ports in the bottom block, the sidewall and blocks must be well-dried and cleaned. The 6 plugs in the top thermal block should be removed and cleaned too, otherwise there is a risk of these threaded plugs seizing if left over time. The acrylic sidewall is cleaned thoroughly using Novus Plastic Clean and Shine solution and a microfiber cloth. The lids are thoroughly cleaned by applying a uniform layer of WD-40 lubricant and scrubbing vigorously with scotch-brite pads in several iterations. The original, uniformly clean shine of the aluminum will be restored after several iterations. To ensure that the WD-40 is then removed from the surfaces of the blocks, several layers of acetone and/or isopropyl alcohol on a cloth are applied until no grey residue of the lubricant shows up on the cleaning cloths. If new micro-pits have noticeably formed (usually occurring on the bottom block), very small amounts of Cotronics Corp. Epox-eez Duralco 132 thermally conductive epoxy filler (check expiration dates) can be used to carefully fill the holes while keeping an overall flat surface on the block. It may be necessary to uniformly sand the block with fine sandpaper after using the filler.

Lastly, if using titanium dioxide (TiO_2) solution for LDV during experimentation (more details in Section 3.3 below), extra care must be taken with the convection tank. The TiO_2 is just slightly more dense than the roughly room temperature DI water in the convection tank and thus will sink slowly over time. Spinning the tank can re-mix some of the TiO_2 solution, but it is often required to incrementally add small amounts to the tank in order to obtain a sufficient data rate for our LDV instrument. If continually running convection

experiments, I have found it necessary to add ∼5–10 mL at a time of ∼2 g/L concentration solution every other day (shake well before inserting via a syringe through one of the ports in the top thermal block). I have found that with such continuous operation, eventually the white TiO_2 particles will build up on the floor of the tank, and are suspected to further contribute to micro-pitting on the bottom thermal block. I have found it best to drain, flush, and refill the tank roughly once every month if running continuous experiments, or once a cumulative of ∼200 mL of the solution has been ejected in the tank. The cleaning instructions above are particularly important with the use of any solution added to the DI water in the convection tank, including the use of kalliroscope or rheoscopic fluid for flow visualization.

3.2.4 Data Acquisition

A National Instruments (NI) PXI computer system is responsible for the majority of measurements collected on the NoMag device. The NoMag PXI is a model 1042Q, and is the main chassis that contains an embedded controller, a NI PXI 8105, and a communication module, a NI PXI 6221. The communication module connects to a NI SCXI 1000 Box, which is a digitizing module chassis. Our SCXI 1000 contains three modules:

- Module 1: NI SCXI 1581 32-Channel Analog Output Current Excitation Module with a NI SCXI 1300 Terminal Block
- Module 2: NI SCXI 1102C 32-Channel Analog Voltage Input Module with a NI SCXI 1303 Isothermal Terminal Block
- Module 3: NI SCXI 1102C 32-Channel Analog Voltage Input Module with a NI SCXI 1303 Isothermal Terminal Block

The modules in the SCXI 1000 Box convert analog voltage signals into digital readings. The digital readings are then transmitted via a SCXI data cable to the PXI chassis. Using NI's software, LabVIEW, we collect, monitor, and record data at rates capable of exceeding 1000 Hz if desired. The PXI-SCXI system permits the multiplexing of measurements oc-

curring at equally spaced time intervals simultaneously on all channels, which is crucial for spectral analysis using Fourier transform methods and for comparative statistics like cross-correlations. A Gefen Wireless Communication device is used to transmit video signals from the PXI to a lab frame monitor.

Modules 1 and 2 are used to read 32 custom fabricated waterproof Amphenol NTC thermistors encased in thin stainless steel housing. 16 of these thermistors are inserted into the top and bottom thermal blocks of the convection tank in order to accurately measure the temperature difference across the tank. The other 16 sensors can be used to characterize temperatures at the sidewalls, room temperature, etc. to accurately describe the overall heat transfer of the system. The thermistors themselves connect to a custom made 32-channel BNC Box, allowing for quick disconnect. The two sense connections of each of the 32 BNC channel connections are connected to one channel in the 1581 current excitation module, and one channel in the 1102C voltage input module. The current excitation channels in Module 1 each provide a 100 mA current in order to properly read the $\sim$11 kΩ thermistors, read by the channels in Module 2.

Module 3 can be used to read additional thermistors or analog voltage signals, also borrowing the current excitation from Module 1 in order to do so as needed. There is no custom built BNC Box for the 32 channels in Module 3 at present, so signals must be directly connected to the 1303 terminal block of Module 3. Beyond the 32 custom thermistors, we have purchased additional, narrower custom waterproof Amphenol sensors to be used as internal thermistors directly in the convection tank. Cheaper, off-the-shelf Amphenol SC50F103V NTC thermistors or Adafruit Waterproof 3950 NTC thermistors can also be used for thermometry as desired. We perform a custom calibration of all thermistors used in a set of experimentation to ensure that all thermometry is calibrated to within $\pm$50 mK resolution.

At present, the PXI-SCXI system is used to collect all thermometry data throughout the duration of convection experiments. Top and bottom sensors are placed inside of custom fabricated aluminum rods that are inserted directly into the top and bottom thermal blocks (cf. the NoMag design package). The wires of all thermistors must be safely secured (via

duct tape and zip ties) prior to rotation. We have found it necessary to coat the aluminum rods that house the block thermistors with a layer of Permatex aluminum anti-seize lubricant in order to prevent any seizing within the aluminum thermal blocks. The thermistors, in particular the custom NoMag Amphenol sensors, are fragile and require attention and care with handling.

The PXI-SCXI system also accurately measures input heating power provided to the base of the convection tank beyond the precision of the front panel reading of the Sorenson power supply. The PXI-SCXI can only measure small voltages. Thus, it is necessary to reduce the voltage applied to heat pad to a readable level. A shunt resistor with a small, well-known resistance is used, and the the voltage drop across the shunt is measured in order to compute the resulting current passing through the shunt resistor and thus the heat pad. The resistors in this voltage divider circuit, where we henceforth refer to the circuit as the Power Measurement Unit (PMU), are $R_1 = 200$ kΩ, $R_2 = 10$ kΩ, and $R_3 = 2.5$ kΩ. The current shunt has a fixed resistance of $R = 0.01$ Ω. In our PMU circuit, the voltage divider voltage is given by:

$$V_{\text{div}} = \left(\frac{R_1 + R_2 + R_3}{R_2 + R_3} \right) V_{\text{read}} = 17.0 V_{\text{read}}, \tag{3.8}$$

where V_{read} is the measured voltage of across the resistors used to voltage divide. Thus, the total power measured that is provided to the heat pad is calculated as:

$$P_{\text{heatpad}} = I_{\text{shunt}} V_{\text{div}} = \left(\frac{V_{\text{shunt}}}{0.01\Omega} \right) (17.0 V_{\text{read}}) = 1700 V_{\text{shunt}} V_{\text{read}}, \tag{3.9}$$

where V_{shunt} is measured and read via the PXI-SCXI just like V_{read}.

Separately, a dell PC is also mounted to the metal electronics deck atop the upper table on the NoMag device. This PC is used to obtain velocity measurements using LDV. MSE software is installed on the computer and used to collect all velocimetry data, as detailed in Section 3.3 below. A separate dell PC exists in the lab frame to remotely control the rotation of the NoMag device via a NI SensorDAQ analog output signal and LabVIEW. At present, the heat pad power supplied by the Sorenson power supply is controlled manually, as well as the temperature of the HX 150 thermal bath. Future efforts to fully automate experimen-

tation will aim to remotely control these components by making use of the programming capabilities of the new heat pad power supply (TDK Lambda GEN 300-17) and new lab chiller (ThermoFlex TF10000). In addition, wireless signals can be used to communicate between the lab frame controls computer and the rotating frame PXI-SCXI main chassis via LabVIEW such that users only need to log in to one computer to monitor and control all experimental components. We refer readers to Sections 4.2 and 6.2.1 for further details on the operation of convection experiments on the NoMag device.

3.3 The Laser Doppler Velocimetry (LDV) Method

In this section, we detail our methodology for using the laser doppler technique to characterize bulk convective velocities. Further details on the post-processing of such data are provided in Chapter 4. We have verified this method with a set of spin up experiments described briefly below in Section 3.3.1. We also provide an analysis of the experimental error of obtained velocity measurements using our LDV instrument and method in Section 3.3.2. The results of a detailed study on the fluid spin up process with both smooth and rough boundaries is provided in Chapter 7.

The LDV method enables the acquisition of accurate point velocity measurements with small space and time resolution and with virtually no disturbance of the flow [Yeh and Cummins (1964), Warn-Varnas et al. (1978), Noir et al. (2009), Noir et al. (2010)]. A small amount of Titanium Dioxide (TiO_2) seeding particles ($\sim$2 g/L concentration) are used as optical scattering sources and are added to water in the experimental tank in order to ensure accurate flow traceability. A Measurement Science Enterprise (MSE) UltraLDV instrument is mounted to the rotating frame of the NoMag device and aligned axially in order to measure vertical convective flow velocities.

Figure 3.7 displays a schematic of the LDV method described herein as used with the NoMag device. Two orientations are possible in order to measure azimuthal (left) or axial (right) point velocities. The details of the processing of optically scattered particle light are as follows. Particle velocities are measured as a 130 mW red split laser beam is passed

through a lens in the instrument and then through one side of the $\sim$ 1.3 cm thick acrylic cylindrical wall and finally into water inside of the experimental tank. The split laser beam converges at a fixed distance of 8.4 cm in the water inside of the acrylic tank when measured from the edge of the tank. This point of intersection of the LDV instrument's split laser beam is known as the probe volume location, and it is the small volume through which a particle passes and subsequently reflects a signal back to the instrument through the lens where it is then recorded. The probe volume location is more than three times the thickness of the Stewartson layer, the thin vertical boundary layer occurring along the sidewalls of the experimental cylinder, for any given experimental tank and rotation rate (scaling as $E^{1/4}$ and ranging in thickness from $\sim 1-3$ cm) and is therefore indicative of the bulk fluid movement [Smith (1987), Kunnen et al. (2011)].

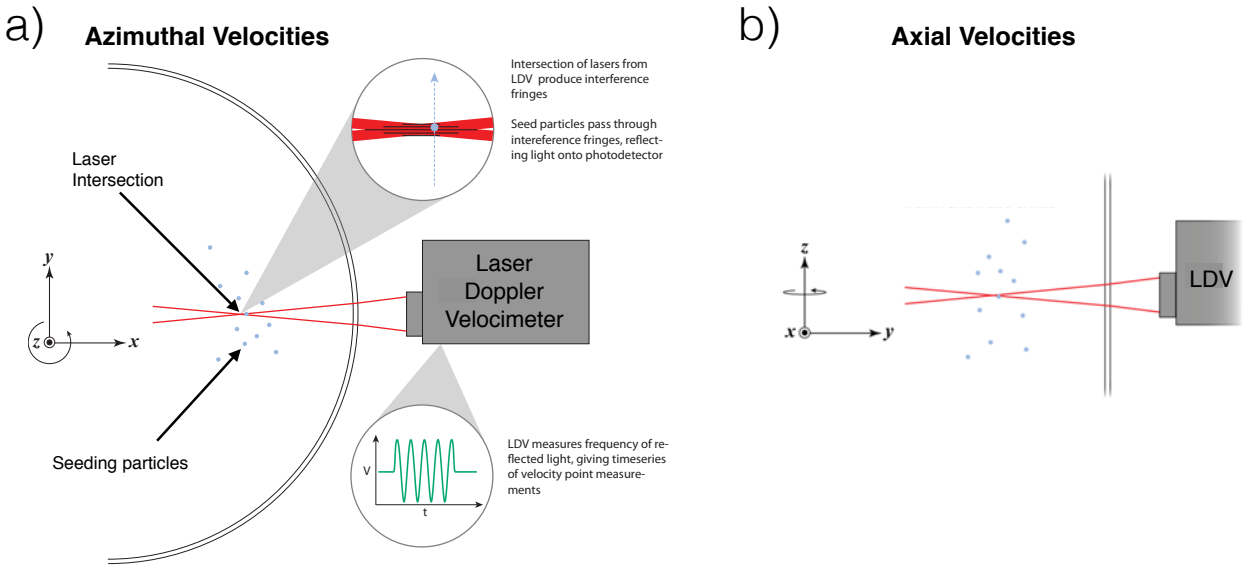

Figure 3.7: Schematic of the LDV method used to measure point velocities in the fluid either a) azimuthally (top-down view) or b) axially (side view). As detailed in a), our LDV instrument records, via a photodetector, the frequency of reflected light of neutrally buoyant optical seeding particles as they pass instantaneously through the interference fringes of the intersection of two laser beams emitted from the instrument. The instrument converts the frequency of reflected light to provide a time series of point velocities as described herein. The LDV method is used in an axial orientation in Chapter 4 in order to measure vertical bulk convective velocities and in an azimuthal orientation in Chapter 7 to measure horizontal velocities during the spin up process. Schematic courtesy of Jonathan Cheng.

The intersection of the split laser beam produces a fringe pattern due to interference at the

probe volume location. The fringe spacing is determined by the wavelength and angle of the split laser beam [Noir et al. (2010)]. A photomultiplier within the LDV instrument detects and records the frequency of light reflected by a particle passing through the probe volume. The LDV instrument converts this light frequency value, obtained by the photomultiplier, to a particle velocity by multiplying this detected frequency by the distance between the fringes of the split laser beam within the probe volume. Note that a geometric correction factor must be used to obtain proper fluid velocities from the LDV instrument due to the fact that the split laser beam must pass through one sidewall of the ~ 1.3 cm thick acrylic tank. Refraction is introduced into this measurement system as the split laser beam of the LDV instrument passes through the acrylic sidewall, causing the angle and location of the split laser beam intersection to be altered. Specifically, in order to obtain correct velocity values, two corrections to account for: 1) the location of the probe volume and 2) the fringe spacing within the probe volume itself must be applied to velocity values obtained by the LDV instrument during the post processing of such data. Snell's law is used to determine the proper probe volume location and Bragg's law is used to determine the correct fringe spacing within the probe volume. For details of such optical corrections to the velocities obtained by the LDV instrument, see Noir et al. (2009) and Noir et al. (2010).

3.3.1 Calibration of the LDV Method: Spin Up Experiments

In order to calibrate the use of the LDV method on the NoMag device, a set of spin up experiments were conducted and compared with the well-established theory of the impulsively generated linear spin up of a homogenous fluid in an axisymmetric container bounded by two smooth parallel disks [Greenspan and Howard (1963), Benton and Clark (1974)]. The detailed results of these experiments, as well as a number of spin up experiments conducted using rough boundaries, can be found in Chapter 7. According to theory, the characteristic spin up time, τ, can be expressed in terms of the Ekman number, E, and the initial rotation rate, Ω_i, as:

$$\tau = (8E)^{-1/2}\Omega_i^{-1} \tag{3.10}$$

[Greenspan and Howard (1963)]. Furthermore, the azimuthal velocity determined in the rotating reference frame is characterized as:

$$u_\phi = s_0 \Delta\Omega e^{(t-t_0)/\tau}, \tag{3.11}$$

where $t - t_0$ is the time after an incremental change in rotation rate, $\Delta\Omega$, and s_0 is the radius of the cylinder [Brito et al. (2004)].

The time series of azimuthal point velocities were experimentally recorded using the LDV instrument and method described in Section 3.3 for the entire duration of a set of experiments on the NoMag device in order to compare with theoretical profiles given by (3.11). Tank height, initial rotation, and incremental changes in rotation were varied in order to robustly confirm agreement with well-established spin up theory, thus validating the use of our method on the NoMag device. For each experiment, the LDV instrument was mounted in the rotating frame and oriented as shown in Fig. 3.7b) in order to record azimuthal point velocities. Upon the detection of zero relative fluid velocities by the LDV instrument, indicating solid body rotation at Ω_i, the rotation rate of the cylinder was changed by $\Delta\Omega$ and fluid velocities were recorded until zero relative velocities were attained and solid body rotation was re-established, indicating the completion of the spin up process.

Figure 3.8 shows the resultant velocity profile time series of an experiment conducted using our $H \simeq 0.2$ m tall tank with an initial rotation rate of $\Omega_i = 20$ rpm and an incremental change in rotation of $\Delta\Omega = 4$ rpm. The resultant profile of the experiment displayed in Fig. 3.8 is reflective of the profiles obtained in other experiments with smooth boundaries detailed in Chapter 7. The azimuthal velocity on the y-axis of Fig. 3.8 is normalized by $\Delta\Omega s_0$ and the time on the x-axis by τ in order to highlight the resultant exponential profile expected from (3.11). The solid dashed line represents the theoretical profile of u_ϕ given by (3.11), which appears in excellent agreement with the experimental profile shown in blue.

Furthermore, the experimental spin up time for the results shown in Fig. 3.8 relative to

relative to the theoretical time for this set of parameters, given by 3.10, is:

$$\frac{\tau_{\text{meas}}}{\tau} = \frac{74.48 \text{ s}}{74.14 \text{ s}} = 1.0005 \tag{3.12}$$

The experimental time, τ_{meas}, is determined by the time to which the velocity profile takes to decay by one e-folding, as highlighted by the magenta dashed line in Fig. 3.8. Thus, the experimental spin up time for the case discussed agrees with a theoretical estimate to within $\sim \pm 1\%$, highlighting the high resolution of our LDV instrument. For all other experiments, measured spin up times agree with their respective theoretical estimates given by (3.10) to within $\sim \pm 5\%$. Thus, the excellent agreement amongst spin up theory and experiments using the LDV instrument and method described verify its use on the NoMag device.

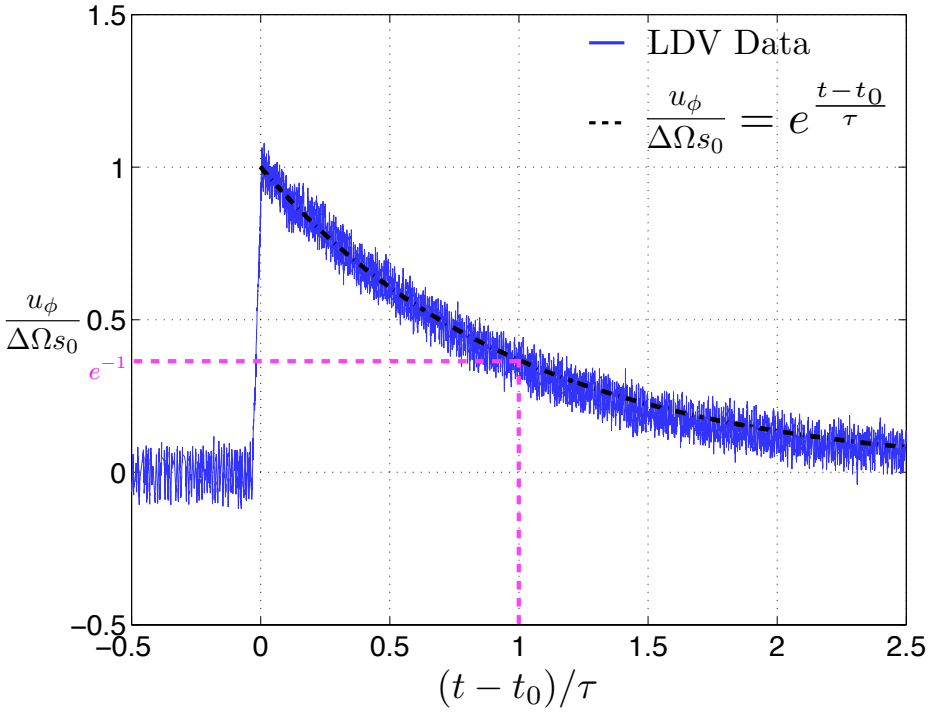

Figure 3.8: Experimental profile (blue) of the azimuthal point velocity, u_ϕ, vs. time during a spin up experiment on the NoMag device, where $H \simeq 0.2$ m, $\Omega_i = 20$ rpm, and $\Delta\Omega = 4$ rpm. The y-axis is normalized by $\Delta\Omega s_0$ and the x-axis by τ to highlight the exponential decay profile expected from (3.11). The black dashed line represents the theoretical profile given in (3.11), and the magenta dashed lines highlight the time, τ, to which the profile decays by one e-folding. The experimental spin up time for the (blue) profile shown is found to be $\tau = 74.18$ s while the theoretical time is calculated as $\tau = 74.14$ s by (3.10), in excellent agreement with one another.

3.3.2 Error Analysis of LDV Velocity Data

In this section, the experimental error in velocity measurements obtained using the Measurement Science Enterprise (MSE) UltraLDV is discussed. Specifically, the collected velocity time series of spin up experiments are analyzed in order to determine the standard error of measurements. We determine that the standard error is propagated to yield an error of $S.E. = \sigma/\sqrt{n} = \pm 10^{-4}$ m/s in velocity measurements for our applications as described, where the standard deviation is $\sigma = 3.4$ mm/s and the number of data points is $n = 1300$ in an experiment analyzed.

Figure 3.9 shows the same normalized experimental velocity time series of the spin up experiment shown in Fig. 3.8 but here, the entire time series is displayed long before and after the generated impulse. The two orange boxes in Fig. 3.9 labeled a) and b) correspond to the portions of data analyzed in the discussion of Figure 3.10 below. We note for reference that the point velocity measurements of the spin up experiment displayed in Fig. 3.8 were acquired at a non-dimensional location of $h \simeq 0.44H$ and $r \simeq 0.84R$. We find that our homogenous spin up experimental measurements and their associated error calculations described below are independent of the location of the point measurements collected in the fluid bulk.

There are two instances in which we can examine the error in acquired velocities using the time series shown in Fig. 3.9. First, during spin up experiments when the fluid is fully spun up, our LDV instrument attempts to measure 'zero' relative fluid velocities because it is placed in the rotating frame of the experiment. This occurs both prior to the generated impulse as well as several e-foldings after solid body rotation is re-established post-impulse. It is during these instances of spun up fluid that we can examine the worst-case-scenario resolution of velocities of the LDV instrument for our applications since the instrument essentially records the system noise. Figure 3.10a) shows the portion of data highlighted by the leftmost orange box in the experiment shown in Fig. 3.9b) before the impulse was generated. The y-axis is dimensionalized to display the magnitude of instantaneous velocities in mm/s, and the x-axis remains non-dimensional and identical to that of Fig. 3.9 in order to display the portion of data examined from the spin up experiment. Dimensionally, the

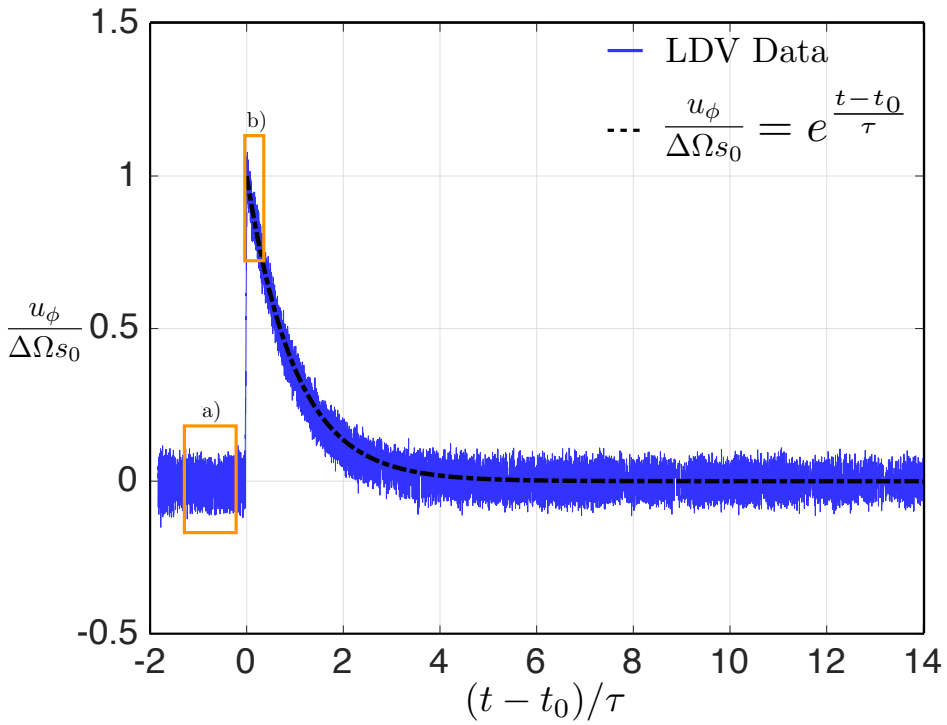

Figure 3.9: The same normalized velocity experimental time series (blue) and theoretical profile (black dashed line) as is shown in the spin up experiment of Fig. 3.8 but here, the entire time series of collected data for the experiment is displayed. The orange boxes labeled a) (leftmost) and b) (rightmost) highlight the portions of data used in the analysis presented in Fig. 3.10 below.

amount of data shown and analyzed corresponds to 1.5 minutes (prior to impulse). The standard deviation of the data shown in Fig. 3.10a) is $\sigma = 4.0$ mm/s, and the standard error is $S.E. = \sigma/\sqrt{n}$ =0.07 mm/s $\simeq$ 0.1 mm/s when rounded, where n is the number of data points, $n = 3300$. We elaborate on this result below.

Secondly, we can also examine velocity values shortly after impulse when the spin up process begins. Immediately after impulse, the LDV instrument rotates at a new speed along with the fluid container. However, the fluid itself will not immediately recognize the change in rotation that has occurred. Thus, a difference in velocity exists between the fluid and the instrument, which differs from that of Fig. 3.10a) in which the fluid and instrument co-rotate. In order to further analyze the error in point velocity measurements using our LDV instrument, we can subtract the well-established theoretical exponential profile of spin up behavior, the black dashed curve in Fig. 3.9, from the measured profile. We choose to do such an analysis between $0(t-t_0)/\tau$ (impulse) and $0.33(t-t_0)/\tau$, i.e. 1/3 of an e-

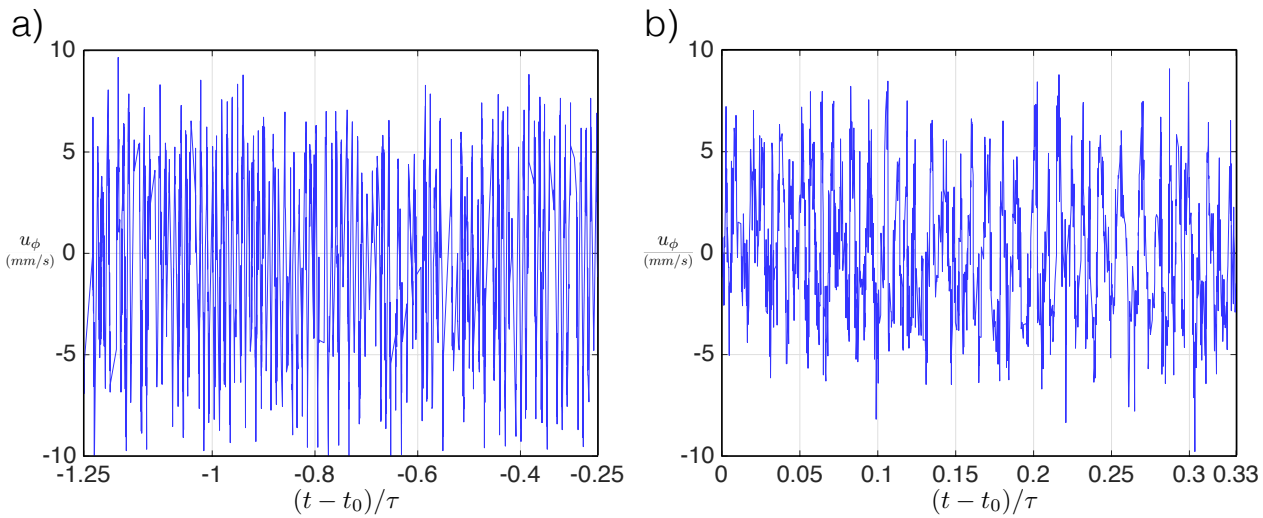

Figure 3.10: a) Azimuthal velocity, u_ϕ in mm/s vs. normalized time, $(t-t_0)/\tau$, during solid body rotation and before impulse corresponding to the leftmost orange box outlined in Fig. 3.9. b) Azimuthal velocity, u_ϕ in mm/s vs. normalized time, $(t-t_0)/\tau$, shortly after impulse when the spin up process first begins, corresponding to the rightmost orange box demarcated in Fig. 3.9. Here, the expected, theoretical exponential profile for velocity is subtracted from measured data in order to analyze the error in the data. When comparing a) and b), note the difference in the length of data displayed. The data rate is non-constant and lower in a) due to the existence of solid-body rotation, so we have chosen to analyze a longer portion of that data. Aside: the oscillatory behavior shown in b) are inertial oscillations expected during the spin up process [Benton and Clark (1974)].

folding, as shown by the rightmost orange box in Fig. 3.9. Dimensionally, this corresponds to ~ 50 seconds of data. Figure 3.10b) shows the measured azimuthal velocity in mm/s vs. normalized time for the described time period after impulse and with the expectant exponential profile subtracted from the measured data. Here, the standard deviation of the data is $\sigma = 3.4\ mm/s$, and the standard error is $S.E. = \sigma/\sqrt{n} = 0.09$ mm/s $\simeq 0.1$ mm/s, with $n = 1300$ data points. Note that we expect that this portion of data will yield a slightly smaller standard deviation, σ, than that of Fig. 3.10a) since a) primarily contains the measurement of system noise, and indeed it does.

From the described analysis, we conclude that a reasonable estimate of the error in velocity measurements via standard error analysis is ± 0.1 mm/s, or $\pm 10^{-4}$ m/s. Note that a number of additional comparable spin up experiments were conducted with varied parameters including tank height, LDV probe location, initial velocity, and incremental velocity change. For these comparable experiments, using the error analysis method described yields similar/nearly identical results to the case shown and analyzed. Lastly, we note that con-

vective velocities measured on the NoMag device range from $\sim 1 - 10$ mm/s, yielding a maximum of $\sim 10\%$ error for the lowest velocity measurements.

CHAPTER 4

Geostrophic Turbulence in Laboratory Models of Planetary Core Convection

Modified from E. K. Hawkins, J. S. Cheng, T. Pilegard, S. Stellmach, K. Julien, and J. M. Aurnou. *Geophys. J. Int.* (2020) In review.

4.1 Motivation

The characteristic velocities and length scales of flows producing planetary magnetic fields remain poorly quantified at present. These two quantities describe the overarching dynamics of core flows, and it has been long assumed that characteristic length and velocity scales are directly coupled to the heat transfer behaviors of the system. As such, heat transfer is typically used in order to infer these dynamical system characteristics, especially in laboratory based work. Temperature sensors are used with relative ease in laboratory experiments in order to characterize heat transfer [e.g. Rossby (1969), Glazier et al. (1999), Ahlers and Xu (2001), Funfschilling et al. (2005), Aurnou (2007), King et al. (2010), Ecke (2015)]. Furthermore, numerical modeling efforts also focus on the study of heat transfer in order to compare to laboratory experiments [e.g. Kerr and Herring (2000), Verzicco and Sreenivasan (2008), Weiss et al. (2010), Bailon-Cuba et al. (2010), Choblet (2012), Julien et al. (2012a), Stellmach et al. (2014), Horn and Shishkina (2014)]. Thus, the majority of studies assume that global heat transfer dynamics will also describe the bulk velocity dynamics. However, numerous studies find that convective heat transport is controlled by the dynamics occurring in the boundary layers of the system [e.g. King et al. (2009), Julien et al. (2012b), Stellmach et al. (2014), Cheng et al. (2018)]. It remains unclear as to whether or not flow regimes

that are indicated by the study of heat transfer alone are indeed representative of the bulk dynamical behavior of convection systems. In order to address this, direct measurements of bulk system velocities are needed.

Other studies have considered the balance between buoyant energy production and dissipation in convection systems in order to more directly examine system bulk dynamics [e.g. Grossmann and Lohse (2000), Aubert et al. (2001), Christensen and Aubert (2006), Schmitz and Tilgner (2010), King and Buffett (2013), Stevens et al. (2013b), Gastine et al. (2015)]. Such considerations result in exact relations between the system characteristic velocity and heat transfer that hold for all control parameters and all (impenetrable) boundary conditions [Christensen (2010), Jones (2011)]. We note that these dissipation relations are dominated by dynamics in the bulk. Thus, the dissipation relations provide a powerful tool for understanding connections between heat transfer and bulk dynamics.

In this work, convective velocities and heat transfer are simultaneously measured, and the balance between buoyant energy production and dissipation is considered. We couple laboratory experiments to a novel set of direct numerical simulations (DNS) to study system behaviors from the onset of convection to strongly supercritical rotating convective turbulence. The laboratory experiments in this work implement a commonly used reduced geometry of a right cylinder, identically to that of all studies in this dissertation as described in Section 1.2. Thus, any effects of spherical curvature are removed. To illustrate our model system once more, Figure 4.1 displays a schematic of the northern hemisphere of Earth's core region. The cylinder located at high latitude and aligned with the rotation axis represents one of the laboratory containers used in this work. Thus, we simulate a local, polar parcel of planetary core convecting fluid under the influence of axial rotation and buoyancy forcing. The interior of the cylinder is filled with an illustrative subset of the visualization of a geostrophically turbulent laboratory experiment ($E \simeq 5 \times 10^{-6}$, $Ra \simeq 2 \times 10^{10}$, $Pr \simeq 7$).The bottom (top) edges of the cell are red (blue) to represent warm (cold) fluid under the presence of convection, in parallel with the warmer/red inner core boundary (cooler/blue core mantle boundary).

The outer core region in Fig. 4.1 is occupied by a meridional slice of the instantaneous

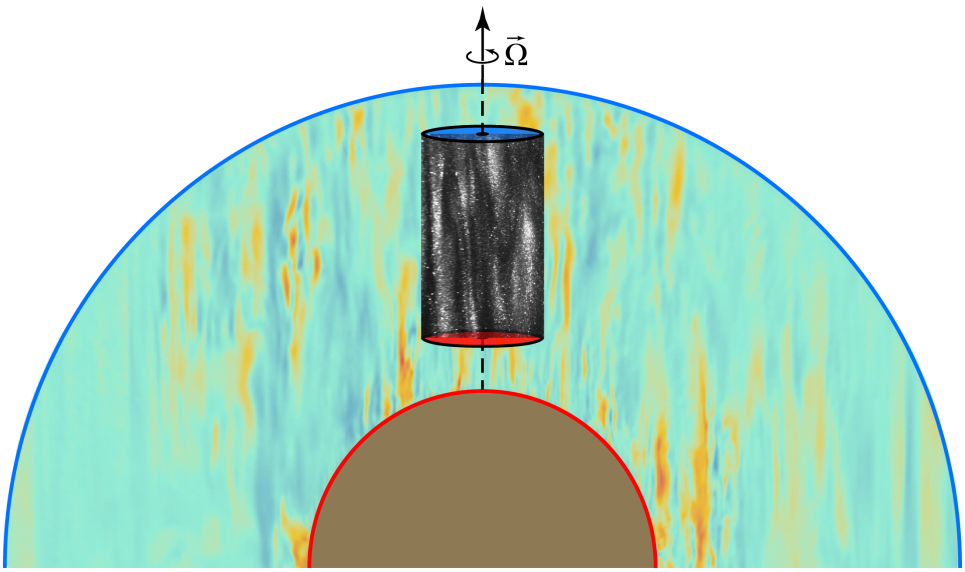

Figure 4.1: Schematic of the northern hemisphere of Earth's core region, with a solid inner core (tan colored) of radius $r = 0.35R_{\text{core}}$, rotating about the z-axis (dashed line) at rate $\vec{\Omega}$. The cylinder located at high latitude and aligned with the rotation axis is representative of the laboratory containers used in this work. The interior of the cylinder is filled with an illustrative subset of the visualization of a geostrophically turbulent laboratory experiment ($E \simeq 5 \times 10^{-6}$, $Ra \simeq 2 \times 10^{10}$, $Pr \simeq 7$). The bottom (top) edges of the experimental cell are red (blue) to represent warm (cold) fluid under the presence of convection, in parallel with the inner core boundary (core mantle boundary). A meridional slice of the instantaneous radial velocity from a dynamo simulation ($E = 3 \times 10^{-7}$, $Ra \simeq 2 \times 10^{10}$, $Pr = 1$, $Pm = 0.05$) adapted from Sheyko et al. (2018) occupies the outer core region. Orange (teal) indicates radially outward (inward) motions.

radial velocity of a dynamo simulation ($E \simeq 3 \times 10^{-7}$, $Ra \simeq 2 \times 10^{10}$, $Pr = 1$, $Pm = 0.05$, where $Pm = \nu/\eta$ is the magnetic Prandtl number and η [m^2/s] is the magnetic diffusivity) adapted from Sheyko et al. (2018). From this meridional slice, we see that fluid motions are largely aligned with the rotation axis. Furthermore, these fluid motions, which are generated in the presence of a magnetic field and in a spherical shell geometry, compare qualitatively well to the visualization of the purely hydrodynamic cylindrical laboratory experiment shown in Fig. 4.1. The schematic in Fig. 4.1 illustrates the comparison of results from numerical and laboratory models, which is crucial for gaining a detailed understanding of the convective dynamics involved in dynamo generation.

Detailed in Section 4.5, our rotating velocity data appear to follow diffusion-free scalings, indicating that quasi-geostrophic turbulence (QGT) is reached even when heat transfer still depends on diffusive processes occurring in the fluid boundary layers. The theoretical system parameters and scaling behaviors relevant to this work can be found in Chapter 2. In

Section 4.2, we describe our methodologies including the the configuration of system diagnostics on the NoMag device. The details of the novel DNS performed for this study are presented in Section 4.3. Non-rotating convection results are described in Section 4.4, and rotating convection results are presented in Section 4.5. Lastly, a discussion of this work and implications for planetary dynamo systems is provided in Section 4.6.

4.2 Configuration of the NoMag Device

For a general description of the NoMag device, refer to Section 3.1. In order to span the E-Ra space shown in Fig. 3.2 for the $H \simeq 0.2$ m (red), $H \simeq 0.4$ m (green), and $H \simeq 0.8$ m (blue) tanks, the NoMag device is spun dimensionally at a rate varying from 0 to 55 revolutions per minute (rpm). As detailed in Section 3.1, a heat flux is passed through the bottom thermal block of the experiment to the fluid layer while the top temperature of the fluid layer remains constant by a precision thermal bath in order to generate convection. Thus, in order to vary Ra, our control parameter is a flux based Rayleigh number in which:

$$Ra_F = \frac{\text{buoyancy flux}}{\text{viscous \& thermal diffusion}} = \frac{\alpha g H^4 q}{\rho C_p \kappa^2 \nu A} = NuRa, \tag{4.1}$$

where q [W] is the heating power, ρ [kg/m^3] is the mean density of the fluid, C_p [J/kgK] is the specific heat capacity, and A [m^2] is the active surface area of the bottom aluminum boundary. We vary q from a range of 30 to 1150 Watts for sets of fixed rotation rates (i.e. fixed E) in order to achieve a unique value of Ra in each experiment, as our thermal control parameter, q, which controls Ra_F, indirectly sets a unique ΔT, which controls Ra per (2.4). A minimum of 30 Watts was used due to the difficulty in controlling thermal losses out the large experimental containers below such a value. As such, the onset of convection in RC is not reached in this study, though the rotationally constrained regime is probed in a number of experiments. The heat transfer behavior of convection at and near onset in an RC cylindrical or plane layer system has been well constrained in past by studies including those of Rossby (1969), Funfschilling et al. (2005), Zhang and Liao (2009), King et al. (2012), Stellmach et al. (2014), and Ecke and Niemela (2014). The exact control parameters for

each experiment and all other experimental values can be found in data Tables 4.1 and 4.2 in Appendix 4.7.

The relatively large diameter fluid containers used in these experiments requires careful treatment of potential thermal losses through the ~ 1 cm thick acrylic sidewalls. The temperature of the room is set as closely as possible to the mean temperature of the fluid in order to minimize such potential losses. The sidewalls are also wrapped in several layers of insulation: first, in a ~ 0.3 cm thick layer of foam insulation with a conductivity of 0.036 W/mK, next in a layer of mylar to minimize any potential radiative losses, and finally in a layer of ~ 2 cm thick closed-cell foam with a conductivity of 0.036 W/mK. To further separate the fluid temperature from any potential influence by the ambient room, the outermost foam layer was surrounded by a ~ 10 cm thick layer of insulating styrofoam packing peanuts enclosed by plastic wrap. Horizontal conductive heat losses across the acrylic sidewall are calculated using recorded values of the room and mean fluid temperatures for each experiment. Losses account for less than $\sim$5% of the total input heating power for all cases.

Each experiment was allowed to equilibrate thermally until the mean temperature on each thermal sensor did not change by more than approximately 1 percent over the course of 2 hours. This process took between 8–14 hours for each experiment. Equilibrated data was then recorded for an additional 6–8 hours on average at a rate of 10 samples per second. Thus, each experiment was run for approximately 14–22 hours on average (the range of this average depends on the tank height and rotation rate for a given case). The vertical thermal diffusion time of the system, $\tau_\kappa = H^2/\kappa$, ranges between approximately 3–50 days amongst all three containers used. Thus, while the total experimental time is small relative to the thermal diffusion time of our system, the time series of the portion of data analyzed always reached a statistically steady state as described. In addition, over the 6–8 hours of equilibrated data analyzed, a minimum of $\sim$1000 free-fall times exist.

In terms of system diagnostics in these experiments, the radial locations of the 16 lid thermistors used to measure the top and bottom fluid layer temperatures and described in section 3.1 vary. Specifically, 6 thermistors are placed at $0.5R$, one is placed at $0.25R$, and one is placed at $0.75R$ in each of the two boundaries as shown in Figure 4.2. Such a place-

ment allows for the examination of changes in horizontal temperature difference information with changes in rotation. The large diameter of the NoMag device can give rise to strong centrifugal acceleration during rapid rotation which may affect vertical convective dynamics. Centrifugal buoyancy is argued to play a weak role in planetary core convection as estimates of the rotational Froude number remain small, i.e. $Fr \lesssim 10^{-2}$ in planetary dynamo systems. Nonetheless, the effects of centrifugation on RC are not well studied at present. In experiments using the NoMag device, centrifugal buoyancy cannot be removed. A better characterization of such potential effect(s) is the focus of Chapter 6.

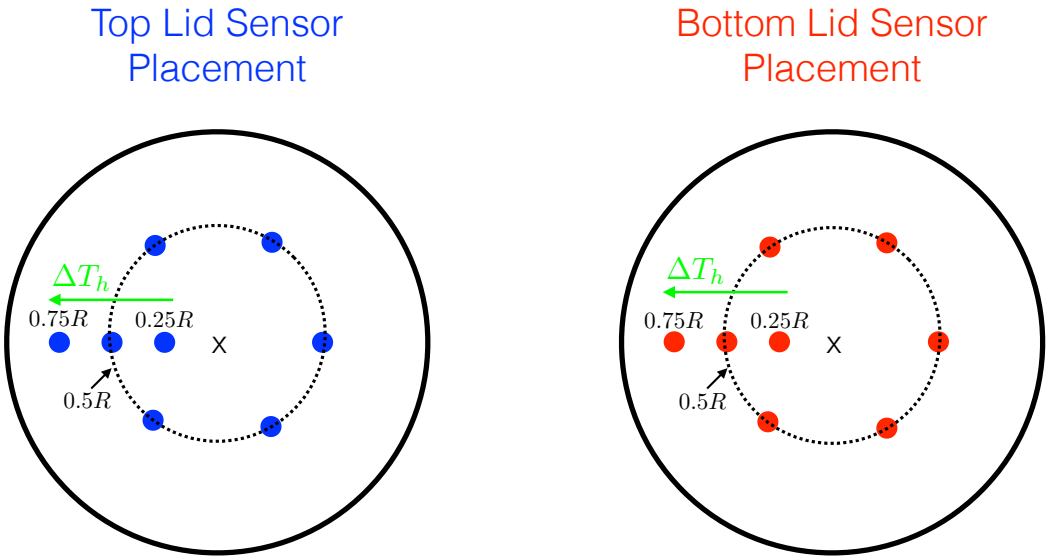

Figure 4.2: Schematic of the placement of the 16 temperature sensors located inside the top and bottom aluminum boundaries near the fluid layer. 6 thermistors are located at $0.5R$, one is located at $0.25R$, and one is located at $0.75R$ within each boundary, both having identical placements as shown. Green arrows denote the horizontal difference measured from $0.25R$ to $0.75R$.

In this study, we examine the magnitude of any horizontal temperature differences that may develop at the fluid boundaries using ΔT_h as defined in Fig. 4.2 as well as the magnitude of the Froude number itself as defined in (2.17) in order to determine whether or not centrifugal acceleration may affect the overall dynamics studied herein. Note that ΔT_h, shown by the green arrows in Fig. 4.2, corresponds to the total measurable horizontal difference between 0.25R and 0.75R at the top or bottom of the fluid layer. According to Horn and Aurnou (2018), heat transfer measurements are not significantly altered by centrifugal buoyancy until $Fr \gtrsim \Gamma/2$, i.e. when the rotational Froude number exceeds half the aspect

ratio of the cylindrical container used. In this study, this constraint is only exceeded in our most extreme dataset, where $E \simeq 1.27 \times 10^{-7}$ and $\Gamma \simeq 0.75$ (see the data tables of Appendix 4.7). The potential effect of the large centrifugal buoyancy force in this dataset is discussed in Section 4.5.

The time series of axial point velocities are collected using the LDV instrument for all RBC and RC experiments in this study. A vertical root mean square (rms) velocity, w_{rms}, is calculated for each experiment using the LDV velocity time series as:

$$w_{\mathrm{rms}} = \sqrt{\frac{1}{N}\sum_{n=1}^{N} |w_n|^2}, \tag{4.2}$$

where w_n (m/s) is the vertical velocity time series. Measured Reynolds numbers reported herein are computed as:

$$Re = \frac{w_{\mathrm{rms}} H}{\nu}. \tag{4.3}$$

A fixed location for point velocity data collection in the fluid bulk is chosen for each experimental container. In all $\Gamma \simeq 3$ experiments, data is collected at a non-dimensional location in the fluid bulk of $h_{\mathrm{LDV}} \simeq 0.33H$, $r_{\mathrm{LDV}} \simeq 0.84R$, where R is the inner radius of container, i.e. $R = D_i/2$. For all experiments in both the $\Gamma \simeq 1.5$ and $\Gamma \simeq 0.75$ tanks, the non-dimensional location of velocity measurements is $h_{\mathrm{LDV}} \simeq 0.57H$, $r_{\mathrm{LDV}} \simeq 0.84R$. The shorter, $\Gamma \simeq 3$ tank requires a different non-dimensional height location due to the difficulty of mounting of the LDV instrument in the rotating frame of the experiment. Once thermal equilibration is determined, a minimum of 2–4 hours of data for rotating cases and a minimum of 4–6 hours of data for non-rotating cases are recorded. The LDV data rate is non-constant; on average, rates are a minimum of ∼5 samples per second.

Figure 4.3 shows the Reynolds numbers for three RBC ($E = \infty$, crosses) and three RC ($E \simeq 3 \times 10^{-6}$, open squares) experiments at different non-dimensional locations. These six experiments were conducted in the $H \simeq 0.4\ m$ tall tank at a fixed input heating power of $q \simeq 400\ W$ ($Ra_F = 1.25 \times 10^{12}$). The three locations tested by these six experiments are $h_{\mathrm{LDV}} \simeq 0.16H$, $h_{\mathrm{LDV}} \simeq 0.57H$, and $h_{\mathrm{LDV}} \simeq 0.77H$, as shown on the x-axis. All experiments

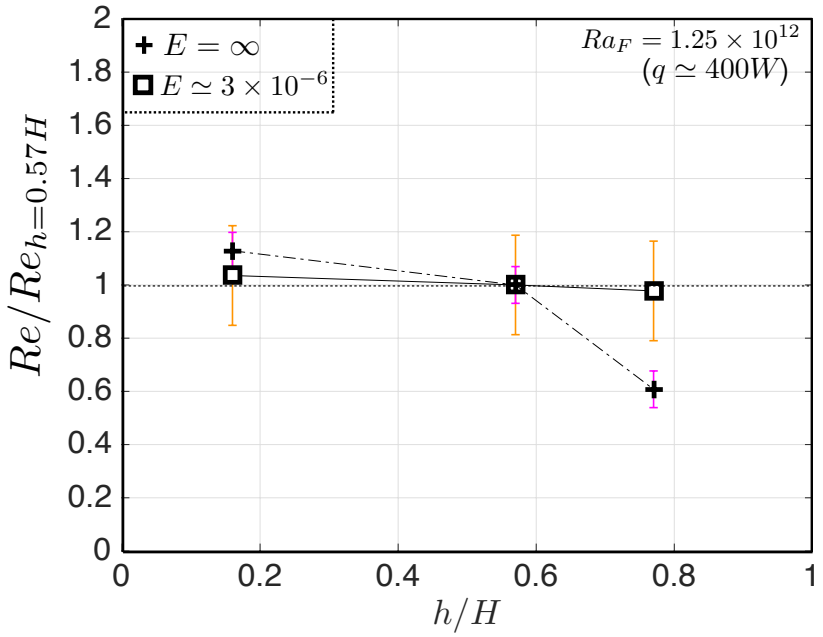

Figure 4.3: Normalized Re vs. the non-dimensional height location of the LDV measurement for 6 experiments: 3 RBC ($E = \infty$, crosses) and 3 RC ($E \simeq 3 \times 10^{-6}$, open squares) cases, where the y-axis is normalized by the value of Re at the mid-plane height, $Re_{h\simeq 0.57H}$. All 6 experiments were conducted in the $H \simeq 0.4$ m tall tank at a fixed input heating power of $q \simeq 400$ W ($Ra_F = 1.25 \times 10^{12}$). The three height locations tested are $h_{\mathrm{LDV}} \simeq 0.16H$, $h_{\mathrm{LDV}} \simeq 0.57H$, and $h_{\mathrm{LDV}} \simeq 0.77H$, as shown on the x-axis. The radial location is fixed for all cases at $r_{\mathrm{LDV}} \simeq 0.84R$. Re values for RBC cases are affected by the choice of height by up to $\sim 40\%$; the Re values of RC cases are not affected by more than $\sim$5%. Magenta colored y-error bars correspond to the 3 RBC cases shown and do not exceed an error of $\pm$6%. Orange colored vertical error bars correspond to the 3 RC cases shown and do not exceed an error of $\pm$18%.

were collected at a fixed non-dimensional radius of $r_{\mathrm{LDV}} \simeq 0.84R$. The value of Re on the y-axis in Fig. 4.3 is normalized by the Re value at the location near the mid-plane height, $Re_{h\simeq 0.57H}$. As shown, the values of Re for the non-rotating cases, connected by a dash-dot line, appear to vary by location (height) by up to $\sim 40\%$. We hypothesize that this is due to the point of the large-scale circulation (LSC) cell that develops in RBC probed. This phenomenon will be discussed further in Section 4.4. Importantly, Fig. 4.3 indicates that the values of Re for the RC cases, connected by a solid line, do not vary by more than $\sim$5% at different height locations. Thus, we argue that our choice of non-dimensional location described for experiments conducted in different tanks does not affect the RC results discussed in Section 4.5.

Vertical error bars are included in Fig. 4.3 to provide a sense of the magnitude of propagated errors of the measured Reynolds numbers in this study. The magenta (orange) y-error bars correspond to the error in measured Reynolds numbers of RBC (RC) experiments, i.e. crosses (open squares). As shown, RBC Re values contain propagated errors that do not exceed greater than $\pm 6\%$, and the computed errors of RC Re values do not exceed $\pm 18\%$. Additionally, we note that all measured velocities in this study are well above the resolution of the LDV instrument used in this study, $u_{\min} \simeq 10^{-4}\ m/s$, with the smallest recorded velocity in the $\Gamma \simeq 3$ container ($Ra \simeq 2 \times 10^8$) of $1.78 \times 10^{-3}\ m/s$ (see Table 4.1 in Appendix 4.7 for more details). For all laboratory experiments in this study, the errors in measured Reynolds numbers fall between $\pm 5\%$ to $\pm 25\%$, with slightly smaller percent errors occurring for non-rotating cases as expected. The vertical y-error bars of measured Re values in the results presented in Sections 4.4 and 4.5 are not included for cleanliness and ease of discussion due to the overlapping nature of the Re values themselves.

We provide sample convective velocity time series of a) non-rotating ($E = \infty$, pink) and b) rotating ($E \simeq 3 \times 10^{-6}$, orange) cases in Figure 4.4. These two sample experiments were collected in the $H \simeq 0.2\ m$ ($\Gamma \simeq 3$) tank with $q \simeq 600\ W$ ($Ra_F \simeq 1.15 \times 10^{11}$). The time on the bottom x-axes is normalized by a free-fall time given by $t_{\text{ff}} = \sqrt{H/(\alpha g \Delta T)}$. In a), $t_{\text{ff}} = 2.90$ seconds, and $t_{\text{ff}} = 2.58$ seconds in b). Exactly one hour of data is shown in both time series, which is only a portion of collected data (totaling between 2—6 hours depending on the case). Thus, roughly 1200 free-fall times occur in one hour of the RBC experiment in a), and roughly 1400 free-fall times occur in one hour of the RC experiment in b).

As mentioned, thermal diffusion timescales are long in our experimental containers, ranging from ∼3 days in the $H \simeq 0.2\ m$ tall tank to ∼50 days in the $H \simeq 0.8\ m$ tank. As the $H \simeq 0.2\ m$ tall tank is used in the two experimental time series of Fig. 4.4, the thermal diffusion times for these two experiments are 3.25 days in a) and 3.23 days in b). Thus, the one hour of data displayed captures a) $t/t_\kappa \simeq 0.0124$ and b) $t/t_\kappa \simeq 0.0130$, as shown by the top x-axes of Fig. 4.4. Therefore, in the 2-6 hours of analyzed, equilibrated velocity data, roughly one tenth of a thermal diffusion time is achieved in the two experiments shown. This ratio will be even smaller for the portion of equilibrated data collected in each experiment

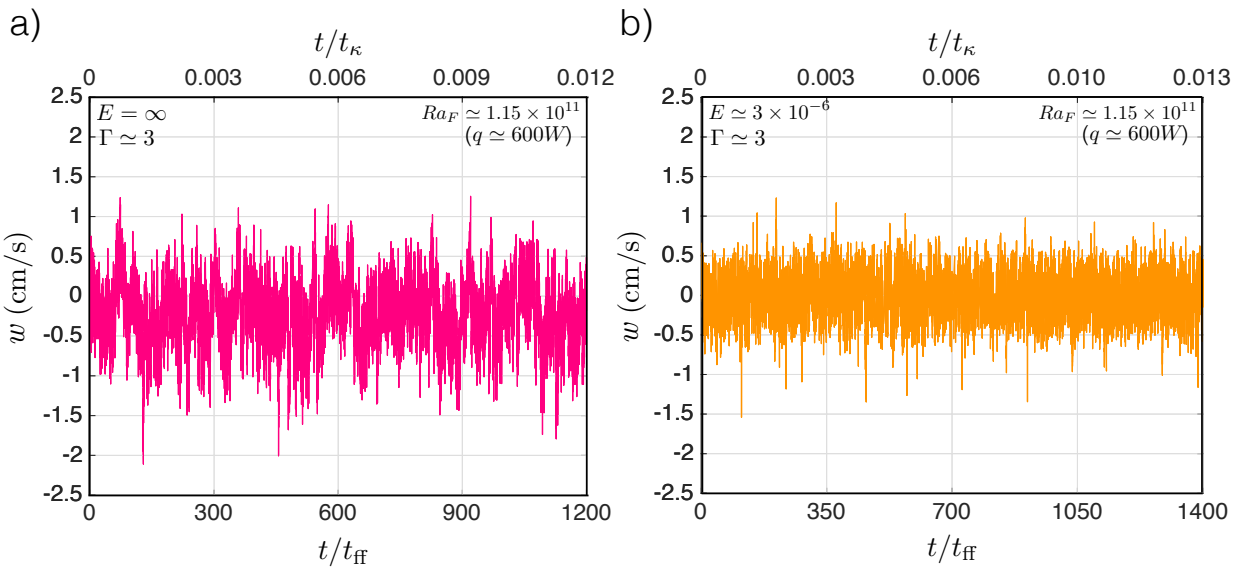

Figure 4.4: Sample laboratory velocity time series, w, of a) a non-rotating case ($E = \infty$, pink) and b) a rotating case ($E \simeq 3 \times 10^{-6}$, orange), where $H \simeq 0.2$ m ($\Gamma \simeq 3$), $Ra_F \simeq 1.15 \times 10^{11}$ ($q \simeq 600$ W), and where the time on the bottom x-axes is normalized by a free-fall time given by $t_{\rm ff} = \sqrt{H/(\alpha g \Delta T)}$ and the time on the top x-axes is normalized by a thermal diffusion time given by $t_\kappa = H^2/\kappa$. For a), $w_{\rm rms} = 4.55\ mm/s$, $t_{\rm ff} = 2.90$ seconds, $t_\kappa = 3.25$ days, and $Ra = 1.50 \times 10^9$, $Nu = 74.7$, and for b), $w_{\rm rms} = 2.40\ mm/s$, $t_{\rm ff} = 2.58$ seconds, $t_\kappa = 3.23$ days, and $Ra = 1.94 \times 10^9$, $Nu = 62.4$. Both time series display exactly one hour of equilibrated data, only a portion of collected data.

with increasing tank height because the thermal diffusion time is dependent on the tank height squared, i.e. $t_\kappa \sim H^2/\kappa$. Nonetheless, as argued, while we are unable to capture several diffusive timescales per experiment due to time constraints, we argue that all convective dynamics reach a statistically steady state as described, with thousands of measured free-fall times. We note that the inherently different overall structure of the time series in a), in which $Ra = 1.50 \times 10^9$, is typical of that of RBC in which an LSC with a slower overturning period superimposed on fast local spikes of positive (negative) convective upwellings (downwellings) exists below $Ra \simeq 10^{10}$ [e.g. Qiu and Tong (2001b), Xi et al. (2004)]. The numerous local positive (negative) overall symmetric spikes in b) correspond to observed convective upwellings (downwellings), with such symmetry expected in RC systems.

4.3 Direct Numerical Simulations (DNS)

Laboratory access of RC near steady onset (i.e. near the burgundy Ra_C^S line in Fig. 3.2) is both limited and difficult, requiring both a small input thermal forcing and a rapid rotation of the container, a setting in which it is difficult to control the thermal losses in experiments. Thus, a set of fixed $E \simeq 3 \times 10^{-6}$ DNS is conducted at lower Ra values and $Pr \simeq 6$. Details of the resultant data from these 10 DNS are provided in Table 4.3 of Appendix 4.7. These DNS model a Cartesian fluid layer and do not include centrifugal buoyancy. The code has been validated and used in prior studies [Stellmach and Hansen (2008), King et al. (2012), Stellmach et al. (2014), Cheng et al. (2015)]. The top and bottom boundaries are isothermal, rigid and non-slip, with periodic horizontal boundary conditions. Fourier expansions are implemented in the horizontal directions and Chebyshev polynomials are used in the vertical direction. The vertical resolution is set in order to maintain at least 16 grid points within the Ekman boundary layer. The box aspect ratio of simulations is set as $\Gamma = D/H \simeq 0.74$, matching the aspect ratio of the $H \simeq 0.8$ m experimental container. The onset of steady convection for these $E \simeq 3 \times 10^{-6}$ DNS is $Ra_C^S \simeq 1.84 \times 10^8$.

The reported Reynolds numbers of the DNS herein contain the volume and time averages of the rms of the total system velocity as:

$$Re = \left\langle \sqrt{\frac{1}{\mathrm{Vol}(V)} \int_V \vec{u}^2 d^3r} \right\rangle_t , \tag{4.4}$$

where V is the simulation domain, $\mathrm{Vol}(V)$ is the volume of the simulation domain, and $<>_t$ is a temporal average. It is possible that due to even the slightest misalignment of the dual laser beams in the laboratory LDV instrument, multiple components of the fluid velocity (i.e. the azimuthal direction in addition to the vertical direction) may be captured in one instantaneous measurement of each laboratory experiment. Thus, (4.4) compares well to the experimental calculation of Re given by (4.3) in this work. The number of thermal diffusion times per simulation ranges between 2.35×10^{-2} and 5.67, and the number of free-fall times captured ranges from 2.53×10^3 to 2.05×10^5.

4.4 Non-Rotating Convection Results

A set of non-rotating experiments were conducted in each of the three tanks used in this study in order to compare to the heat and momentum transfer scaling predictions presented in Sections 2.1.1 and 2.1.2 of Chapter 2. It is important to study the analogous non-rotating system results relative to the rotating results presented in the subsequent section, 4.5, not only to verify the validity of the new NoMag laboratory device itself, but to quantify the dynamics that can represent the upper bounding values of an RC system. Our RBC experimental results described below demonstrate that we recover the expected heat transfer scaling behavior described in Section 2.1.1. We also find that the momentum transfer in a RBC water system also behaves overall as anticipated, with an $\alpha \simeq 1/2$ exponent *Re*-*Ra* scaling behavior and a dependence on the location of the structure probed.

4.4.1 Heat Transfer

The entire available range of input thermal forcing (30 W $\lesssim q \lesssim$ 1150 W) was used in each of the three experimental tanks included in this study in order to span the widest range possible of *Ra*. Figure 4.5 shows our heat transfer results overplotted onto the previous results in Cheng et al. (2015), where the the y-axis is Nu, the global heat transfer efficiency, and the x-axis is *Ra*, the input thermal forcing. Pink and cyan data with black outlines represent our results obtained on the NoMag device, with symbol shape representing different tanks: circles ($H \simeq 0.2$ m, $\Gamma \simeq 3$), squares ($H \simeq 0.4$ m, $\Gamma \simeq 1.5$), and diamonds ($H \simeq 0.8$ m, $\Gamma \simeq 0.75$). The $\Gamma \simeq 3$ is distinguished in pink from data collected in the $\Gamma \simeq 1.5$ and $\Gamma \simeq 0.75$ tanks (cyan) due to the different non-dimensional location of velocity measurements in the $\Gamma \simeq 3$ tank. The open orange triangles [King et al. (2012)], and the open upside down royal purple triangles [Cheng et al. (2015)] are water data collected on UCLA's smaller diameter comparable device, RoMag.

The green line, $Nu_1 = (0.170 \pm 0.107)Ra^{(0.287\pm0.012)}$, represents the best fit to the $\Gamma \simeq 3$ data, which remains below $Ra \simeq 10^{10}$ and within the range to which we expect an agreement with the 2/7 scaling relation of (2.8). The scaling exponent, $\alpha = 0.287 \pm 0.012$, and pre-

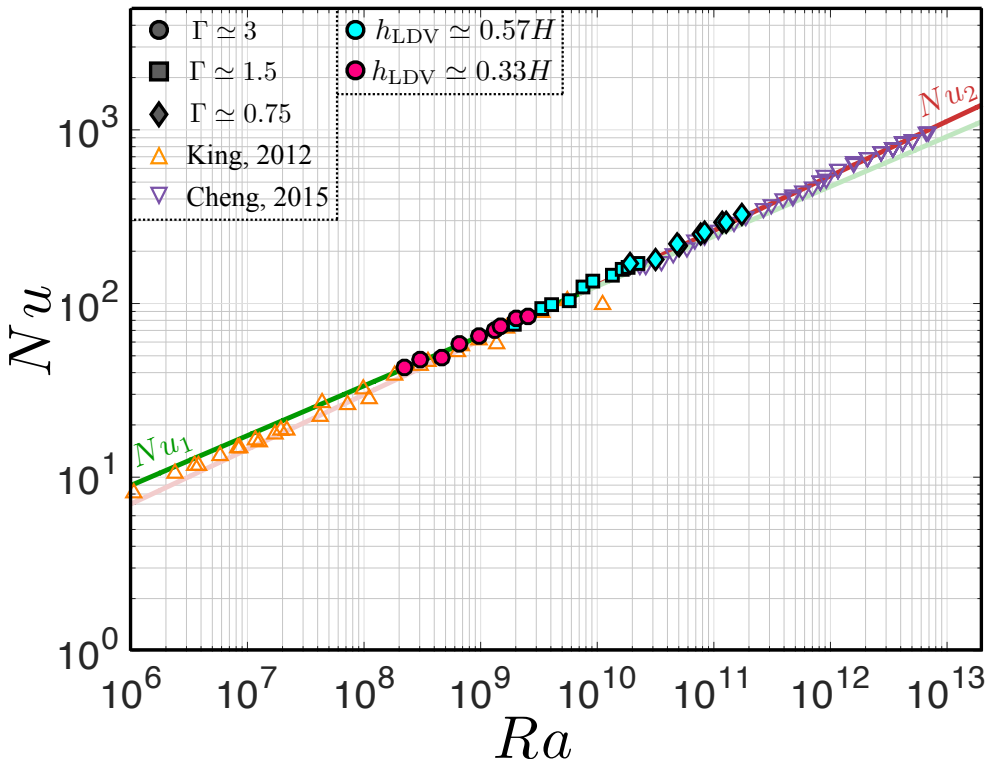

Figure 4.5: Nu vs. Ra results using the NoMag device for a cylindrical RBC water system. Pink circles with black outlines denote data from the $\Gamma \simeq 3$ tank, cyan squares with black outlines denote data from the $\Gamma \simeq 1.5$ tank, and cyan diamonds with black outlines denote data from the $\Gamma \simeq 0.75$ tank. Open orange triangles are experimental data from Cheng et al. (2015) while royal purple upside down triangles are experimental data from King et al. (2012). The green line shows empirical agreement to the theorized $\alpha \sim 2/7$ scaling exponent and is a best fit to the data below $Ra \simeq 10^{10}$, $Nu_1 = (0.170 \pm 0.107)Ra^{(0.287\pm0.012)}$. The fuchsia line shows empirical agreement to the theorized $\alpha \sim 1/3$ scaling exponent and is a best fit to the $\Gamma \simeq 0.75$ data and the data above $Ra \simeq 10^{10}$ collected in Cheng et al. (2015), $Nu_2 = (0.091 \pm 0.031)Ra^{(0.315\pm0.003)}$.

factor, $c = 0.170 \pm 0107$, are in excellent agreement with that found in Cheng et al. (2015): $\alpha = 0.284$, $c = 0.162$. The fuchsia line, $Nu_2 = (0.091 \pm 0.031)Ra^{(0.315\pm0.003)}$, represents the best fit to the $\Gamma \simeq 0.75$ data and several decades of data in Cheng et al. (2015) that are well above $Ra \simeq 10^{10}$ in which we expect the validity of the 1/3 relation of (2.9). The scaling exponent, $\alpha = 0.315 \pm 0.003$, and pre-factor, $c = 0.091 \pm 0.031$, are also in good agreement with that found in Cheng et al. (2015): $\alpha = 0.322$, $c = 0.075$. As shown, all experimental data overlay onto these best fit lines and previous data very well, indicating further confirmation of the classical 2/7 and 1/3 RBC scaling relations via the NoMag device.

4.4.2 Momentum Transfer

For the same RBC experiments shown in Fig. 4.5, the momentum transfer, Re, versus input thermal forcing, Ra, is shown in Figure 4.6. The solid black line, $Re = (0.151 \pm 0.128)Ra^{(0.434\pm0.012)}$, shows the best fit to the $\Gamma \simeq 1.5$ (squares) and $\Gamma \simeq 0.75$ (diamonds) cyan data collected at $h_{\text{ldv}} \simeq 0.57H$, $r_{\text{ldv}} \simeq 0.84R$. This fit is in good agreement with the best fit of the experimental water data of Qiu and Tong (2001b) ($Re^*_{\text{NR}} = 0.102Ra^{0.447}$, faded black dashed line).

The $\Gamma \simeq 3$ data collected at $h_{\text{ldv}} \simeq 0.33H$, $r_{\text{ldv}} \simeq 0.84R$ does not follow the same scaling behavior as in the other two experimental tanks. We purport the reason for this is largely due to the difference in the location of the large scale circulation (LSC) that is probed by our point velocity measurements. As this data falls below $Ra \simeq 10^{10}$, we expect the existence of a shear flow across the thermal boundary layer that sets up a large scale overturning circulation pattern in the fluid bulk as discussed in section 2.1.1. The velocity of the LSC structure is likely non-uniform within the fluid bulk [Shang et al. (2003), Sun et al. (2005), Ahlers et al. (2009), Zurner et al. (2019)]. It is possible that the $\Gamma \simeq 3$ data at a non-dimensional height of $h \simeq 0.33H$ is sampling a corner of the LSC structure, whereas the rest of our data at a height of $h \simeq 0.57H$, $r \simeq 0.84R$ measure velocities near the center of vertical upwellings and downwellings close to the container sidewalls.

Overall, we conclude that our RBC heat and momentum transfer measurements agree well with the results of prior studies. Further, our results indicate that a transition in heat transfer behavior occurs near $Ra \simeq 10^{10}$. However, no similar behavioral transition is indicated in our RBC momentum transfer data. The rotating convection results discussed in the following section, 4.5, further highlight the advantage to simultaneously collecting heat and momentum transfer measurements in order to gain insight into the system dynamics.

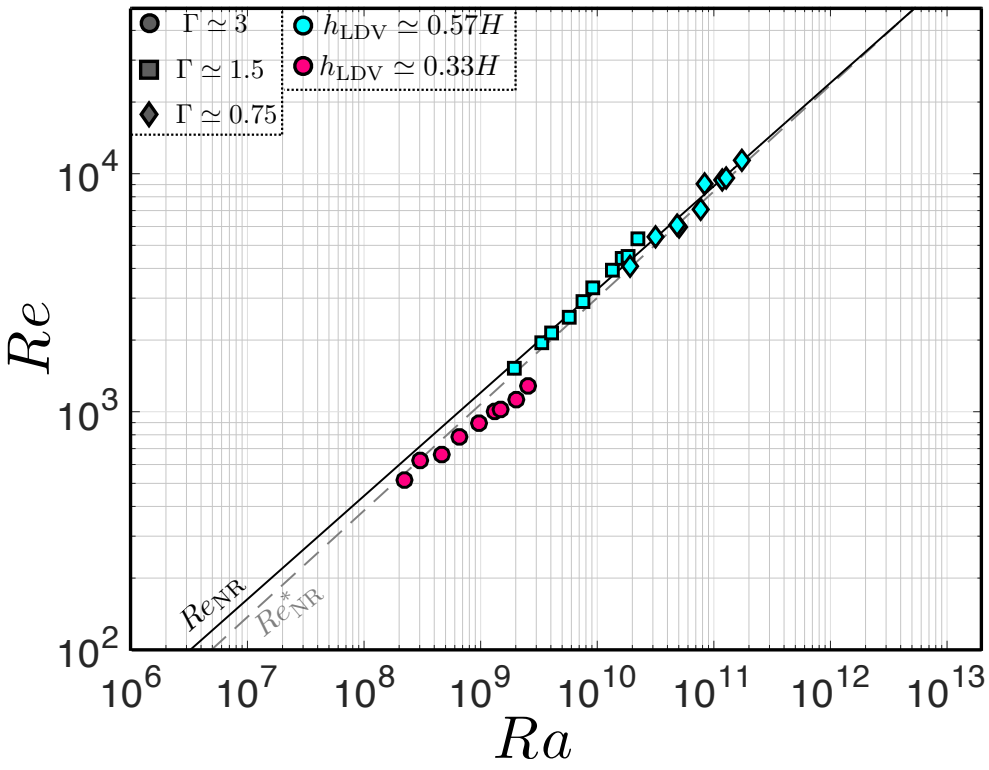

Figure 4.6: Re vs. Ra results using the NoMag device for a cylindrical RBC water system. Symbol shape and color is consistent with that of Fig. 4.5. The $\Gamma \simeq 3$ data was collected at a location of $h_{\mathrm{LDV}} \simeq 0.33H$, $r_{\mathrm{LDV}} \simeq 0.84R$, while the $\Gamma \simeq 1.5$ and $\Gamma \simeq 0.75$ data was collected at a location of $h_{\mathrm{LDV}} \simeq 0.57H$, $r_{\mathrm{LDV}} \simeq 0.84R$. The solid black line, $Re_{\mathrm{NR}} = (0.151 \pm 0.128)Ra^{(0.434\pm0.012)}$, is a best fit to data collected at the height of $h \simeq 0.57H$, in good agreement with the best fit from the water data of Qiu and Tong (2001b), $Re^{*}_{\mathrm{NR}} = 0.102Ra^{0.447}$ (faded black dashed line).

4.5 Rotating Convection Results

We performed a systematic study to simultaneously measure heat and momentum transfer across a broad parameter space in order to test the rotating convection scaling theory highlighted by Fig. 2.3 and 2.4. Direct comparison will be made to previous studies of the heat transfer a cylindrical RC water system, as compiled in Cheng et al. (2015). To our knowledge, there are no comparable studies of momentum transfer with which to compare our results detailed below. The connection (or lack thereof) between our heat and momentum transfer results will be discussed in Section 4.5.3. Finally, we discuss the implications of our overall findings from this study for planetary dynamo systems in Section 4.6.

Our results indicate that RC heat transfer measurements agree with previous studies. Similar to past studies, we find that behavioral transitions in RC heat transfer are due overall to boundary layer dynamics. In terms of RC momentum transfer, we observe a weak dependence of Ra on Re for each fixed E dataset in each container until agreement with the CIA scaling is obtained at respectively high values of Ra. The fixed E numerical dataset included in this study also agrees well with the CIA scaling theory and does not contain the weak Re dependence for respectively low Ra values that is seen in the laboratory data. Thus, we attribute the weak Re scaling seen in laboratory experiments at respectively low Ra values to be due to finite geometric effects of the cylindrical containers used that we explain in light of a few recent studies. Crucially, we find that behavioral transitions in momentum transfer do not occur where observed transitions in heat transfer behavior exist. We thus conclude that bulk velocity dynamics are not controlled by the boundary layers of the system. Robust agreement with the CIA scaling is shown in our results, including for high Ra and low E (i.e. geostrophically turbulent) experiments. Lastly, we note that the theoretical convective length scales on our data are not separable, and provide an explanation for this observation in Section 4.6.

4.5.1 Heat Transfer

The entire range of input thermal forcing (30 W $\lesssim q \lesssim$ 1150 W) was spanned in each of three experimental tanks for sets of fixed rotation rates. Specifically, non-dimensional rotation periods varied between $1.25 \times 10^{-7} \lesssim E \lesssim 3 \times 10^{-5}$ with several overlapping sets of fixed rotation for different experimental tanks. For example, $E \simeq 3 \times 10^{-6}$ can be reached within all three tanks using different dimensional rotation values and the different tank heights. At this E value, the entire range of q was spanned in each tank. Figure 4.7 shows our heat transfer results overplotted onto the previous results in Cheng et al. (2015), where the the y-axis shows Nu, the global heat transfer efficiency, and the x-axis shows Ra, the input thermal forcing. The 10 fixed $E \simeq 3 \times 10^{-6}$ DNS completed for this study are displayed in Fig. 4.7 as partially filled diamonds. Consistent with Fig. 4.5, the different solid colored symbol shapes with black outlines represent data collected in the three different experimental tanks

used in this study. Color represents a fixed non-dimensional rotation period (i.e. fixed E). The open triangles are RC laboratory data from King et al. (2012), the open upside down triangles are RC laboratory data from Cheng et al. (2015), and asterisks denote comparable direct numerical simulations from Stellmach et al. (2014).

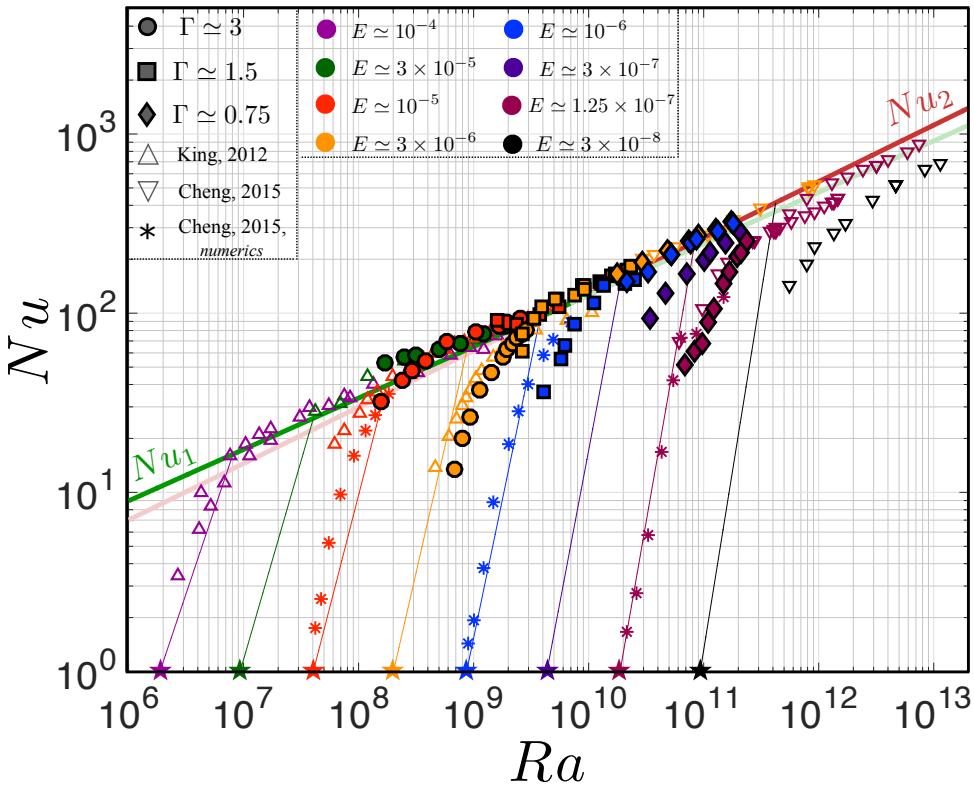

Figure 4.7: Nu vs. Ra results for a cylindrical RC water system. Circles with black outlines denote laboratory data from the $\Gamma \simeq 3$ tank, squares with black outlines denote data from the $\Gamma \simeq 1.5$ tank, and diamonds with black outlines denote data from the $\Gamma \simeq 0.75$ tank. The partially filled orange diamonds with a black outline represent the fixed $\Gamma \simeq 0.74$, $E \simeq 3 \times 10^{-6}$ DNS of this study. Open colored triangles are experimental data from Cheng et al. (2015) and open colored upside down triangles are experimental data from King et al. (2012). Asterisks denote direct numerical simulations from Stellmach et al. (2014). Color represents a fixed non-dimensional rotation period (i.e. fixed E). The onset of steady convection, given by (2.22), is shown as solid colored stars. The colored, steep sloping thin solid lines occurring past the denoted onset characterize the rotationally constrained regime predicted by (2.24),(2.25). The thick green (fuchsia) line shows the empirical findings of Fig. 4.5, $Nu_1 = 0.170 Ra^{0.287}$ ($Nu_2 = 0.091 Ra^{0.315}$).

The onset values for steady bulk convection, approximated by (2.22), are shown as solid colored stars on the x-axis. The colored, thin steep sloping solid lines occurring past the denoted onset characterize regime in which the entire fluid layer is dominated by rotation,

as given by (2.24), (2.25). As shown, the numerical simulations (asterisks and partially filled diamonds) reach nearest to convective onset and provide the most data in this regime for each fixed E branch. The thicker, solid green (fuchsia) lines again represent the non-rotating style heat transfer scaling behaviors of (2.8) [(2.9)], as verified in Fig. 4.5. Thus, we see that for a given set of fixed E experiments, say for example $E \simeq 3 \times 10^{-6}$ (orange), a steep heat transfer scaling is observed in which the entire layer is rotationally constrained, which eventually transitions to shallower, non-rotating style behavior with sufficiently strong thermal forcing.

Cheng et al. (2015) note that it is possible that their two most extreme datasets at E, i.e. $E \simeq 10^{-7}$ and $E \simeq 3 \times 10^{-8}$ might be influenced by strong centrifugal acceleration, which scales as $\Omega^2 R$, due to the rapid rotation rates these values. This notion may also hold for our (burgundy) data at $E \simeq 1.25 \times 10^{-7}$ [$Fr \gtrsim 1 \gtrsim (\Gamma/2 = 0.375)$, Horn and Aurnou (2018)]. Cheng et al. (2015) further assert that it appears that their data seem to be tending towards a 2/7 heat transfer relation when they should be tending towards a 1/3 relation at such high values of Ra and that this may be due to the effects of strong centrifugal acceleration. However, our $E \simeq 1.25 \times 10^{-7}$ data agree well with the $E \simeq 10^{-7}$ numerics of Stellmach et al. (2014) in which there is no centrifugal buoyancy. It is not obvious that the overall scaling behavior of this heat transfer data is altered in any meaningful way [cf. Horn and Aurnou (2019), Ding et al. (2020)]. The potential detailed effect(s) of centrifugation on RC heat transfer require further investigation, providing motivation for the study specially designed to explore such potential effects discussed in Chapter 6. We conclude that all of our heat transfer data agree well with past results, indicating that RC heat transfer regimes are controlled overall by horizontal boundary layer physics as discussed in Section 2.2.1.

4.5.2 Momentum Transfer

Figure 4.8 shows the resultant momentum transfer data as a function of input thermal forcing for the same sets of rotating experiments/DNS of this study shown in Fig. 4.7. Measured laboratory Reynolds numbers are calculated by (4.2) and (4.3), as detailed in Section 4.2.

The Reynolds numbers of DNS are calculated by (4.4), as described in Section 4.3. The solid faded black line is Re_{NR}, shown in Fig. 4.6, and serves as an upper bound for our rotating data. We observe a concave up curvature scaling behavior for each set of fixed E laboratory data within each experimental tank, while the fixed E DNS dataset of this study possesses a concave down pattern. The burgundy data ($E \simeq 10^{-7}$, $Fr \simeq 1$) in Fig. 4.8 do not show any observable influence of centrifugal buoyancy on vertical momentum transport.

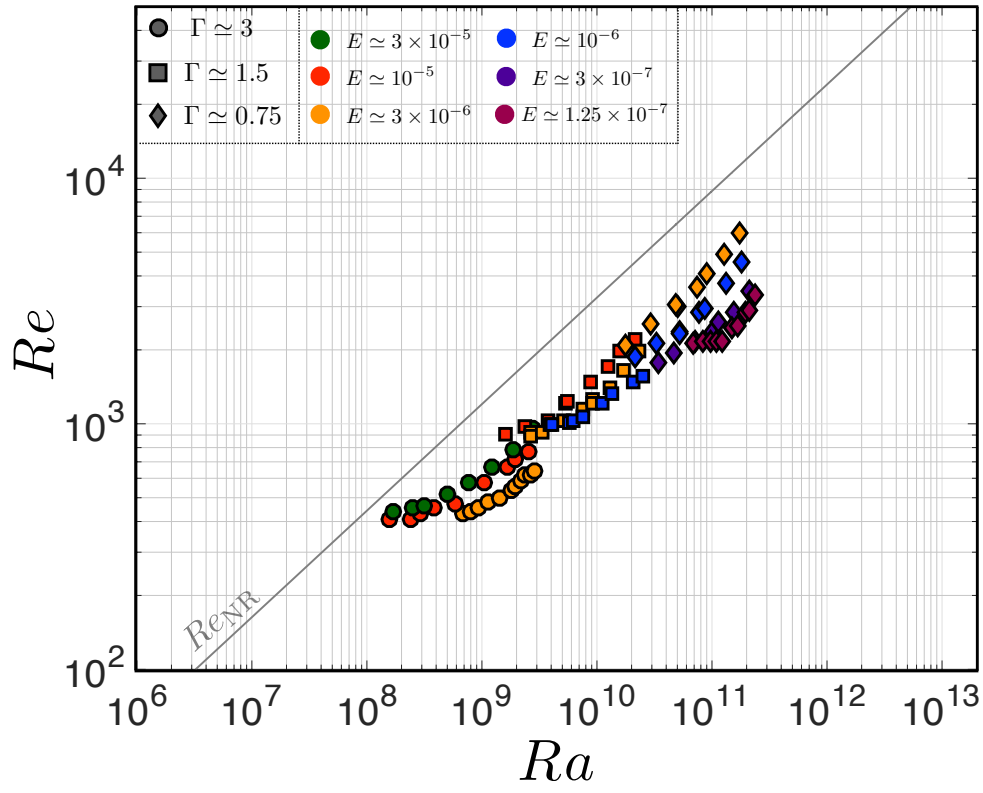

Figure 4.8: Re vs. Ra results for a cylindrical RC water system. Circles with black outlines denote laboratory data from the $\Gamma \simeq 3$ tank, squares with black outlines denote data from the $\Gamma \simeq 1.5$ tank, and diamonds with black outlines denote data from the $\Gamma \simeq 0.75$ tank. Color represents a fixed non-dimensional rotation period (i.e. fixed E). The solid faded black line is the best fit to RBC momentum transfer data shown in Fig. 4.8 and serves as an approximate upper bound for rotating data.

In Figure 4.9, we plot the measured Re values displayed in Fig. 4.8 with the scaling estimates displayed in Fig. 2.4 separately for each fixed E dataset. The empirical best fits Nu_1, Nu_2, and Re_{NR} shown in Fig. 4.7 and 4.8 are used in the computation of the theoretical Re curves of Fig. 4.9 (as opposed to the empirical scalings of prior studies, denoted with

asterisks as superscripts, i.e. Nu_1^*, and used in Fig. 2.4). Symbol shape represents the container aspect ratio, consistent with Fig. 4.8. At respectively high Ra for each E and Γ laboratory dataset, measured Reynolds numbers align well with the (green) CIA scaling estimate in which a triple balance assumption exists between the Coriolis, inertial, and buoyancy forces in the the system. For respectively lower Ra experiments, there is no obvious transition onto the (magenta) VAC curve below Ra_T. Instead, for each fixed E laboratory dataset, there is a weak dependence of Re on Ra that occurs at respectively low Ra for each E dataset in each container.

Focusing on the $E \simeq 3 \times 10^{-6}$ results in panel c) of Fig. 4.9, we see that the DNS provide information about velocity behavior near the onset of steady bulk convection. Specifically, the 10 partially filled diamond DNS show strong agreement with the theoretical Re curves. In the regime below Ra_T, the VAC (magenta) and CIA (faded green) curves overlap such that they are graphically indistinguishable. Here, the DNS overplot onto these overlapping theoretical curves well. Three DNS cases also exist past Ra_T. These points agree well with laboratory data in the same Ra range. These DNS and laboratory experiments agree qualitatively well with the green CIA theoretical scaling relation.

A concave downward trend towards the CIA scaling is observed with increasing Ra in the DNS. Contrastingly, laboratory experiments appear to have a shallow, concave up behavior trending towards the CIA scaling for respectively high Ra. This contrast suggests the existence of a potential laboratory influence on velocity behavior that does not exist in the numerical models. We hypothesize that this weak Ra scaling behavior in the laboratory data is likely due to a geometric effect of the cylindrical sidewalls. A possible explanation for this behavior is the so-called boundary zonal flow (BZF), a recently discovered phenomenon in cylindrically-confined rotating convection [de Wit et al. (2020), Zhang et al. (2020)]. The BZF is a unique mode associated with enhanced vertical transport near the sidewall of the container.

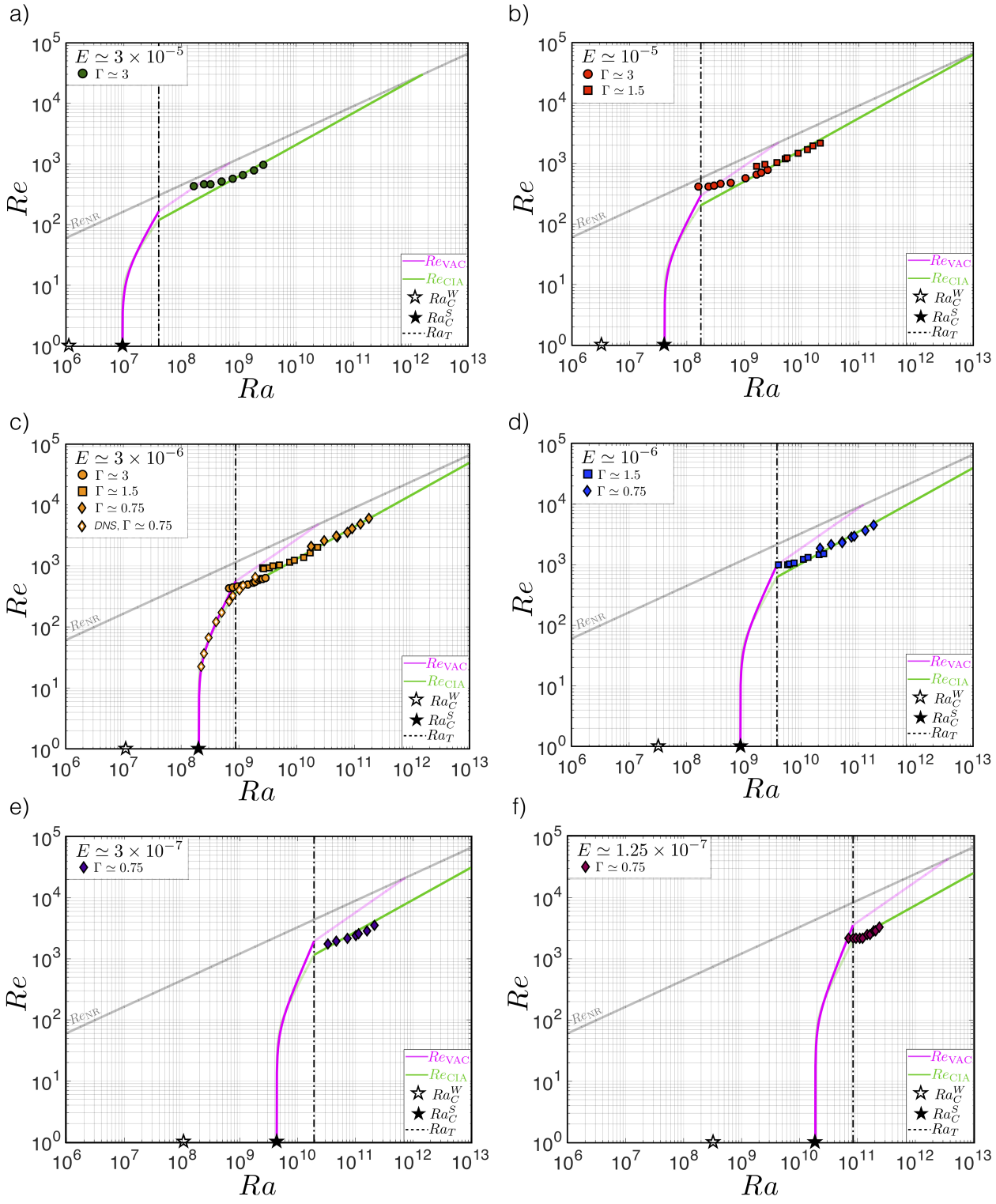

Figure 4.9: (Continued onto next page)

Figure 4.9: Re vs. Ra for each fixed E dataset collected in this study: a) $E \simeq 3 \times 10^{-5}$ (forest green), b) $E \simeq 10^{-5}$ (red), c) $E \simeq 3 \times 10^{-6}$ (orange), d) $E \simeq 10^{-6}$ (blue), e) $E \simeq 3 \times 10^{-7}$ (purple), and f) $E \simeq 1.25 \times 10^{-7}$ (burgundy). Symbol shape represents the experimental container used/simulated, consistent with Fig. 4.7. Note the inclusion of (orange) $E \simeq 3 \times 10^{-6}$ DNS in c), which reach closer to the onset of steady convection than is possible in laboratory experiments. The theoretical scaling curves from Fig. 2.4 at each respective fixed E value are plotted in each panel, where $Re_{\mathrm{VAC}} = (Ra(Nu-1)/Pr^2)^{1/2}E^{1/3}$ (magenta) and $Re_{\mathrm{CIA}} = (Ra(Nu-1)/Pr^2)^{2/5}E^{1/5}$ (green). For each fixed E laboratory dataset, we see that a weak dependence of Re on Ra occurs at respectively low Ra, eventually tending towards a strong agreement with respective Re_{CIA} estimates (green). For the DNS in panel c), we see agreement with theory at low Ra, and we see agreement with both laboratory experiments and the CIA theory past Ra_T.

A secondary circulation develops that influences vertical velocities as far into the bulk as $r \simeq 0.80R$ [de Wit et al. (2020)]. This secondary circulation strengthens as onset is approached. For $Ra/Ra_C^S \lesssim 3$, the peak z-velocity from the secondary flow occurs at $r \simeq 0.82R$ and is nearly double the mean z-velocity in the bulk. Thus, we posit that this secondary BZF circulation is responsible for the observed overshoot relative to CIA theory in laboratory measurements at respectively low Ra shown Fig. 4.9. When Ra is increased, de Wit et al. (2020) find that the secondary circulation weakens, with z-velocities at $r \simeq 0.80R$ returning to the bulk value. This finding is consistent with our velocity data, which settle toward the CIA scaling as Ra increases. Since our DNS employ doubly periodic horizontal boundary conditions, we do not expect to see the effects of the BZF in the DNS velocity data. Though the BZF is not yet well-characterized, with potential dependencies on E, Γ, and Pr unexplored, our results appear to demonstrate its influence on laboratory velocity measurements for the first time.

Figure 4.10a) shows measured Rossby numbers normalized by their associated CIA estimates versus Ra for all of our laboratory data. Symbols are hollow until experimental values come to within a 5% agreement with their associated CIA estimates for the first time (as indicated by the horizontal dashed line). Afterwards, symbols are filled in order to highlight qualitative agreement with the CIA scaling estimate (near the horizontal black line at $Ro/Ro_{\mathrm{CIA}} = 1$). The hollow symbol 'tails' for each fixed E dataset highlight the cases that are likely influenced by BZF effects.

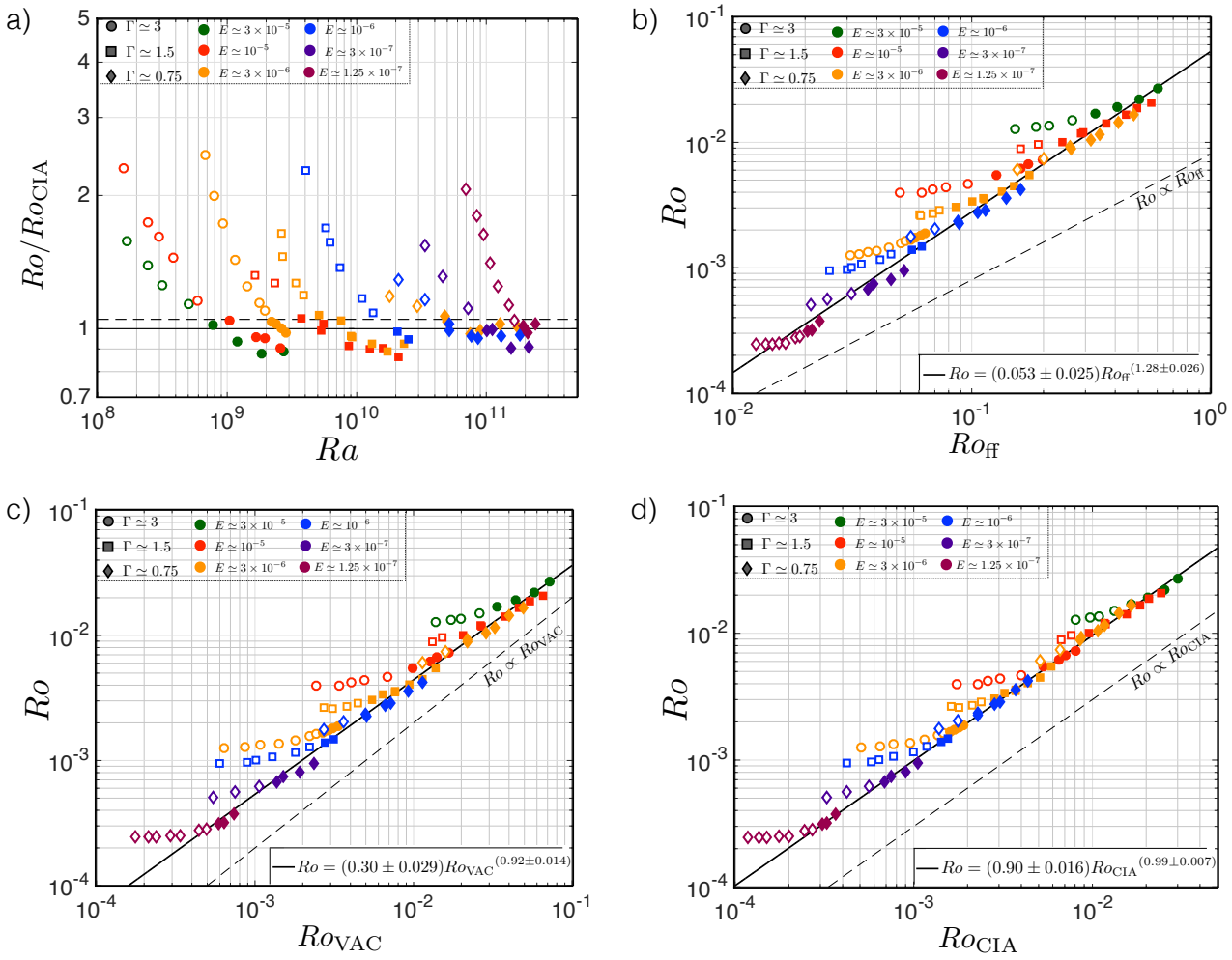

Figure 4.10: a) Measured laboratory Ro normalized by Ro_{CIA} vs. Ra, where symbols are hollow until 5% agreement with Ro_{CIA} estimates are reached for the first time (indicated by the horizontal dashed line). The use of color and symbol shape are consistent with that of Fig. 4.7, 4.8 and 4.9. b) Ro vs. Ro_{ff}, where the solid colored data from a) is used for the solid black line best fit, $Ro = (0.053 \pm 0.025) Ro_{\mathrm{ff}}^{(1.28\pm0.026)}$. c) Ro vs. Ro_{VAC}, where the solid black line best fit is given as $Ro = (0.30 \pm 0.029) Ro_{\mathrm{VAC}}^{(0.92\pm0.014)}$. d) Ro vs. Ro_{CIA}, where the solid black line best fit is given as $Ro = (0.90 \pm 0.016) Ro_{\mathrm{CIA}}^{(0.99\pm0.007)}$.

The solid symbol data of Fig. 4.10a) are subsequently used to analyze the accuracy of different global Rossby number estimates discussed in Section 2.2.2. Figure 4.10b) displays measured Ro values versus the free-fall Rossby number, Ro_{ff}. The solid black line represents a best fit to the solid colored data, $Ro = (0.053 \pm 0.025) Ro_{\mathrm{ff}}^{(1.28\pm0.026)}$. The dashed line represents an exponent of unity for reference. The VAC scaling predictions are tested in Fig. 4.10c). A best fit to the solid colored data is given as $Ro = (0.30 \pm 0.029) Ro_{\mathrm{VAC}}^{(0.92\pm0.014)}$. VAC estimates appear to give nearly linear estimates of measured Ro values, even at respectively high Ra where the CIA scaling is expected to hold. The solid data used in the

fit displayed in Fig. 4.10c) are experiments in which agreement with a CIA scaling estimate of Ro occurs as shown in Fig. 4.10a). Thus, Fig. 4.10c) suggests that the VAC and CIA scaling estimates of Ro do not differ significantly in slope.

Figure 4.10d) displays measured Ro versus Ro_{CIA}, where the best fit to solid colored data is given as $Ro = (0.90 \pm 0.016) {Ro_{\mathrm{CIA}}}^{(0.99 \pm 0.007)}$. This empirical fit shows that experiments at respectively high Ra for each dataset agree remarkably well with the CIA velocity scaling estimate, with an exponent of unity, 0.99±0.007, and a pre-factor of nearly unity, 0.90±0.016. Agreement of solid colored experiments with the CIA scaling implies that the Coriolis force, inertial advection, and buoyancy control bulk momentum transport.

Figure 4.11a) shows $\widetilde{Ro}$ versus Ra. $\widetilde{Ro}$ is defined as either measured values normalized by VAC estimates, $\widetilde{Ro} = Ro/Ro_{\mathrm{VAC}}$ (magenta), or measured values normalized by CIA estimates, $\widetilde{Ro} = Ro/Ro_{\mathrm{CIA}}$ (green). Here, the data included are the filled laboratory data of Fig. 4.10a) where $Ro/Ro_{\mathrm{CIA}} \simeq 1$. Thus, the geometrically affected 'tails' of each dataset have been removed. Symbol shape is consistent with that of Fig. 4.7, 4.8, 4.9 and 4.10. The green Ro/Ro_{CIA} points are well-centered around 1, indicating that the CIA scaling estimates the measured convective velocities well, as expected from the excellent fit of Fig. 4.10d). The magenta Ro/Ro_{VAC} points show that the VAC scaling overestimates measured values of Ro by roughly a factor of 2. We further note that the magenta VAC normalized points contain an overall flat slope, similar to that of the green CIA normalized points. This indicates that the VAC scaling also captures the velocity behavior of the system, even if off by a small, constant factor.

Overall, we conclude from Fig. 4.10 and 4.11a) that the CIA scaling predictions fit our data extremely well, in good agreement with the findings from the dynamo models in Christensen (2002) and Christensen and Aubert (2006). We note that no pre-factors are used in the calculations of CIA and VAC scaling predictions given by (2.47) and (2.42), respectively. Importantly, the VAC scaling also adequately fit our velocity data over the full range of Ra investigated. Thus, the CIA and VAC scalings appear to co-scale, with both adequately predicting our measured data. In contrast, this finding in no way supports the expectations of the theoretical framework displayed in Fig. 2.4, where the VAC scaling is

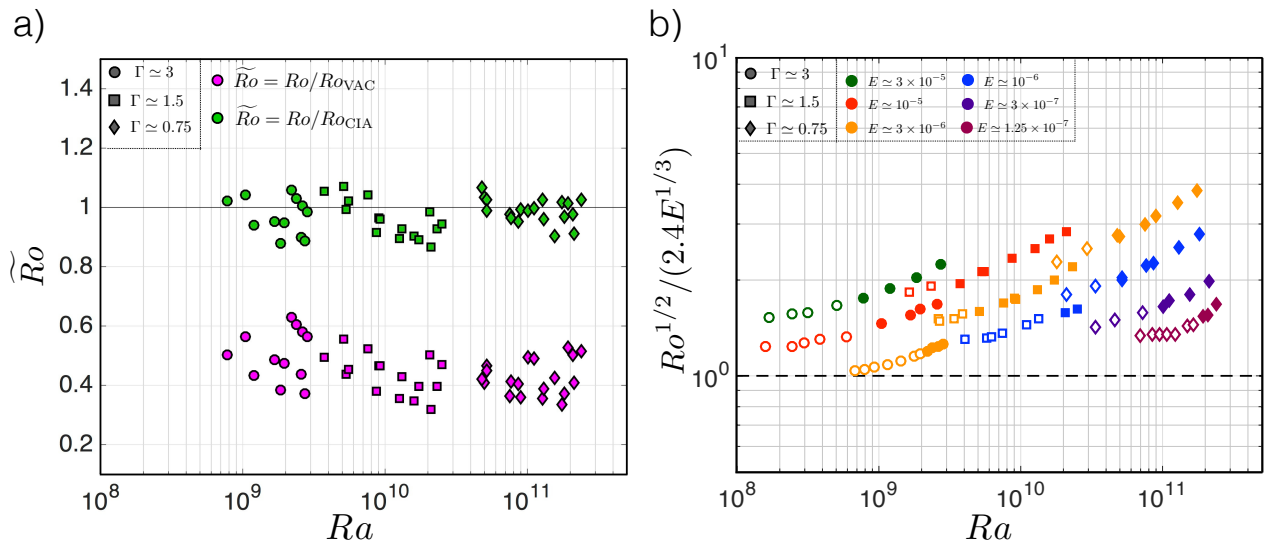

Figure 4.11: a) Normalized Rossby number, $\widetilde{Ro}$, vs. Ra, where magenta colored symbols contain a normalization on the y-axis of $\widetilde{Ro} = Ro/Ro_{\mathrm{VAC}}$, and where green colored symbols are a y normalization of $\widetilde{Ro} = Ro/Ro_{\mathrm{CIA}}$. The data included are the filled laboratory data of Fig. 4.10a) where $Ro/Ro_{\mathrm{CIA}} \simeq 1$, i.e. the geometrically affected 'tails' of each dataset have been removed. Symbol shape is consistent with that of Fig. 4.7, 4.8, 4.9, and 4.10. The green CIA normalized points are centered around 1, indicating that the CIA scaling estimates measured values well, while the magenta VAC scaling overestimates measured Ro values by roughly a factor of 2. b) $l_{\mathrm{turb}} = Ro^{1/2}H$ normalized by $l_{\mathrm{crit}} = 2.4E^{1/3}H$ vs. Ra for all laboratory data of this study. Symbols remain hollow or solid according to the method defined in Fig. 4.10a). This ratio, $l_{\mathrm{turb}}/l_{\mathrm{crit}} = Ro^{1/2}/2.4E^{1/3}$, remains roughly of order unity (horizontal dashed line) and varies by roughly only one half of an order of magnitude, meaning that the two length scale estimates yield roughly the same values for all laboratory data.

expected to exist below Ra_T and the CIA scaling is expected above Ra_T. Lastly, we argue that the parameter Ro_{ff} shown in Fig. 4.10b), with a best fit exponent of 1.28 ± 0.026, does not predict measured Ro values as accurately as the CIA or VAC scalings.

In order to explain the agreement of measured values with both the VAC and CIA scalings highlighted by Fig. 4.11a), we carry out an analysis of the theoretical length scales in our RC system of study. The convective length scale is not directly measured in this study. We estimate the local onset and local turbulent scales using (2.23) and (2.46), respectively. Figure 4.11b) shows the ratio of these two length scales, $Ro^{1/2}/(2.4E^{1/3})$, plotted versus Ra. Colored symbols are hollow or filled based on the criteria outlined in Fig. 4.10a), i.e. filled symbols indicate that laboratory data have reached agreement with CIA estimates to within 5% for the first time.

The ratio of length scales in Fig. 4.11b) only differs by up to a factor of ∼4 (i.e. roughly one half of an order of magnitude) for all of our laboratory experiments. Thus, a formal scale separation between l_{crit} and l_{turb} cannot occur in the range of laboratory parameters studied [e.g. Favier et al. (2014), Rubio et al. (2014), Calkins et al. (2015), Moffatt and Dormy (2019)]. This is also the case for the DNS of this study, though not shown graphically. We note that the local Reynolds numbers of all laboratory experiments is of order $Re_\delta \sim \mathcal{O}(10)$ using either l_{crit} or l_{turb} as the local scale. If l_{crit} and l_{turb} vary by less than an order of magnitude as shown in Fig. 4.11b), the estimates of the global Reynolds numbers using the VAC scaling of (2.42) and the CIA scaling of (2.47) will not differ significantly for all experiments. This notion explains the similarities of the best fits in Fig. 4.10c) (VAC) and Fig. 4.10d) (CIA), and Fig. 4.11a).

4.5.3 RC Behavioral Transition Tests

We examine the boundary layer physics of our laboratory data in order to further understand the connection (or lack thereof) between measurements of RC heat transfer and bulk velocities. Figure 4.12a) displays the ratio of RC boundary layer thickness estimates, δ_T/δ_E, versus Ra. The thermal boundary layer thickness, δ_T, is estimated using $\delta_T = H/(2Nu)$ given by (2.26) and the Ekman layer thickness, δ_E, as $\delta_E = 3E^{1/2}H$ given by (2.27) such that $\delta_T/\delta_E = (6NuE^{1/2})^{-1}$. Past studies have shown that heat transfer behavioral changes from a steep, rotationally constrained entire layer scaling to a shallow, non-rotating style scaling is due overall to the dominance of a thermal or Ekman boundary layer in the system [King et al. (2009), King et al. (2012), Julien et al. (2012b), Stevens et al. (2013a), Stellmach et al. (2014), Ecke and Niemela (2014), and Julien et al. (2016)]. Thus, colored symbols are solid when $\delta_T/\delta_E \leq 1$ and contain a black center when $\delta_T/\delta_E > 1$. We note that Fig. 4.12a) compares well to the results shown in Figure 4c) of King et al. (2012).

Figure 4.12b) displays measured laboratory Nusselt numbers normalized by our empirical 2/7 non-rotating style scaling, $Nu_1 = 0.170Ra^{0.287}$, plotted versus Ra. The same black center or solid colored symbol schematic as in a) is used [i.e $\delta_T/\delta_E \leq 1$ (solid) and $\delta_T/\delta_E > 1$ (black

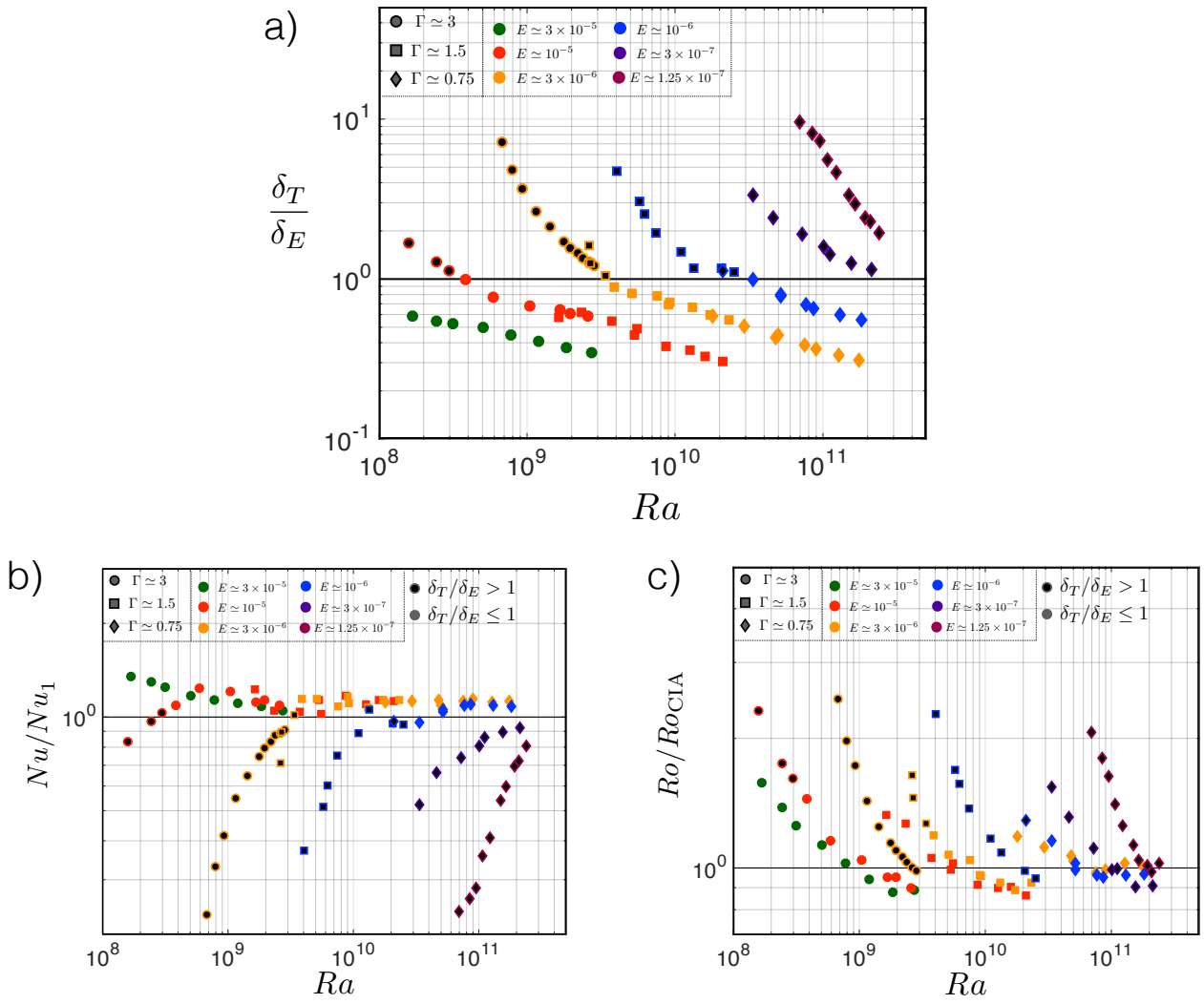

Figure 4.12: a) Estimated thermal boundary layer thickness, $\delta_T = H/(2Nu)$ [King et al. (2012)], normalized by estimated Ekman layer thicknesses, $\delta_E = 3E^{1/2}H$ [Greenspan (1969b)] vs. Ra. Colored symbols contain a black center when $\delta_T/\delta_E > 1$ and become solid when $\delta_T/\delta_E \leq 1$. b) Nu normalized by the non-rotating style scaling, $Nu_1 = 0.170Ra^{0.287}$ vs. Ra. Colored symbols have a black center or are solid based on a), i.e. $\delta_T/\delta_E \leq 1$ (solid) and $\delta_T/\delta_E > 1$ (black center). Symbols have black colored centers until $Nu/Nu_1 \simeq 1$ c) Ro normalized by Ro_{CIA} vs. Ra with the same significance for black center or solid colored symbols as in a) and b). Symbols do not necessarily remain black center filled above $Ro/Ro_{\mathrm{CIA}} > 1$ and solid where $Ro/Ro_{\mathrm{CIA}} \simeq 1$. Thus, the transition to agreement with a CIA velocity scaling is not correlated with boundary layer physics and does not necessarily occur where heat transfer transitions are observed within each dataset.

center)]. Symbols are solid when Nu/Nu_1 approaches unity, indicating that the thermal boundary layer becomes thinner than the Ekman layer in these experiments such that a non-rotating style heat transfer scaling, Nu_1, is recovered. Colored symbols contain a black center below $Nu/Nu_1 \simeq 1$, indicating that $\delta_T/\delta_E > 1$, i.e. the Ekman layer remains thin resulting

in heat transfer behavior in which the entire fluid layer is rotationally constrained. Thus, the behavioral transition in our RC heat transfer data correlates overall to the dominance of an Ekman or thermal boundary layer in the system, consistent with the results of past studies [cf. Stellmach et al. (2014), Ecke and Niemela (2014)].

Figure 4.12c) shows measured laboratory Rossby numbers normalized by their associated CIA estimates, Ro_{CIA}, versus Ra. The transition from black center to solid colored symbol type for each fixed E dataset does not coincide with the observed transition of velocity data from a weak Ra dependence (due to geometric effects) to agreement with CIA predictions (where $Ro/Ro_{\mathrm{CIA}} \sim 1$). The BZF effected 'tails' in our experimental Ro data are purposefully included in Fig. 4.12c) in order to further confirm that the observed momentum transfer behavior in this study is not tied to transitions in boundary layer physics. Thus, while observed heat transfer behavior is correlated with boundary layer dynamics, Fig. 4.12c) shows that bulk momentum transfer is not.

In Figure 4.13, we use a number of different estimates of a local Rossby number for the system, Ro_l. The difficulty in separating assumed theoretical length (l_{crit} and l_{turb}) and velocity (VAC and CIA) scalings is additionally highlighted by this analysis. Cheng et al. (2015) argue that their cylindrical rotating convection water experiments are collapsed by a Ro_l defined using the assumptions that: 1) l_{crit} accurately captures the local system length scale and 2) Re_{VAC} is an accurate estimate of the characteristic velocity in their experiments (see their Fig. 8b). In a similar fashion, we plot in Figure 4.13a) the Nusselt number normalized by the non-rotating 2/7 scaling, Nu/Nu_1, versus $Ro_{l,\mathrm{crit}} = (1/2.4)Re_{\mathrm{VAC}}E^{2/3} = 0.42Re_{\mathrm{VAC}}E^{2/3}$, i.e. a local Rossby number in which a local length scale of convective onset, l_{crit}, is assumed, and Re is estimated using a VAC scaling for all laboratory data (measured Re values are not used). These results compare nearly identically to that of Fig. 8b) in Cheng et al. (2015) with the same x and y parameters. While it appears as though data are collapsed well, we show in Fig. 4.11a) that both the VAC and CIA scalings agree well overall with measured Ro data.

Moreover, in Figure 4.13b) we plot Nu/Nu_1 versus $Ro_{l,\mathrm{crit}} = 0.42Re_{\mathrm{CIA}}E^{2/3}$, i.e. a local Rossby number in which the length scale is again assumed to be that convective onset, but

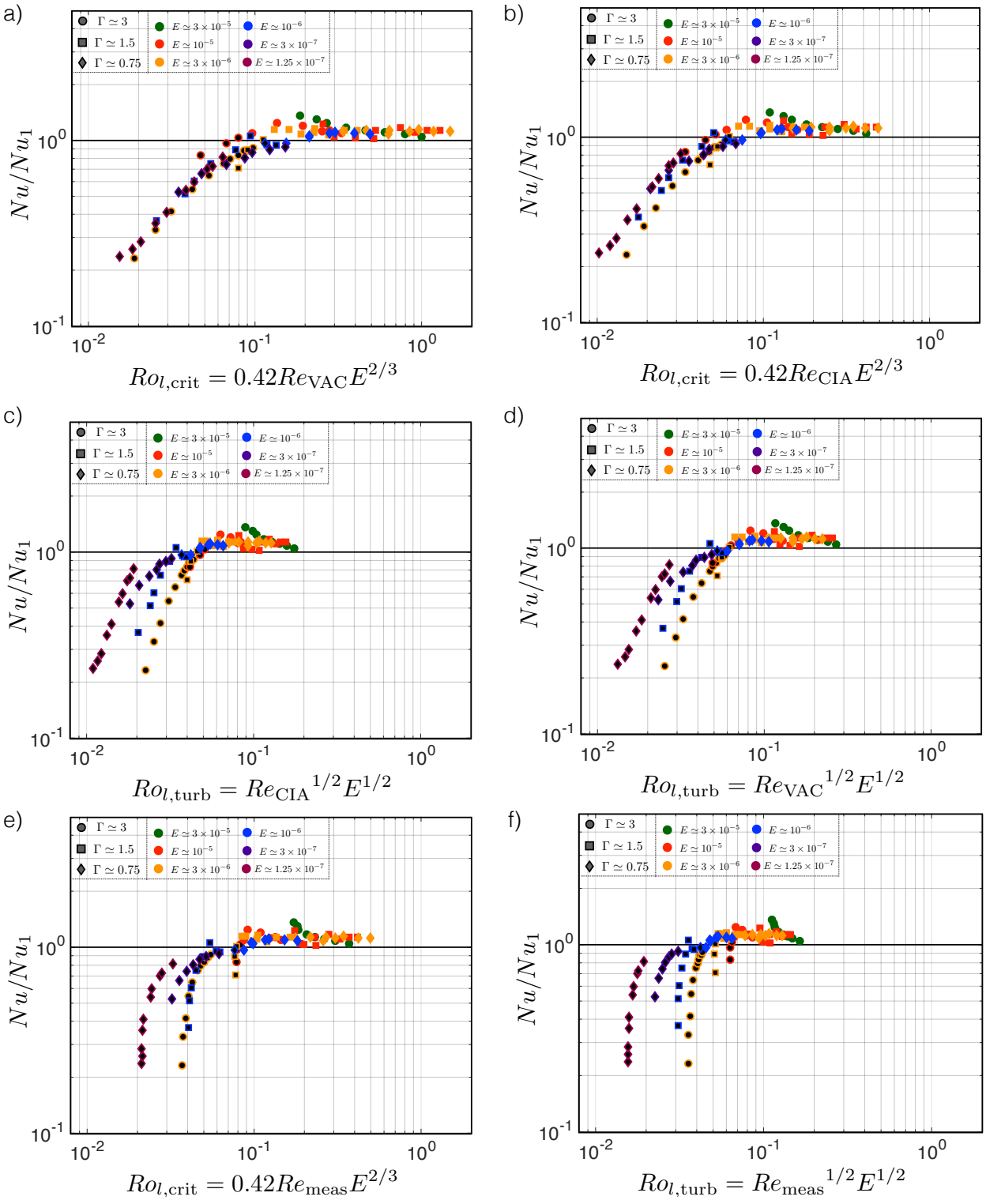

Figure 4.13: (Continued onto next page)

Figure 4.13: a) Nu/Nu_1, where $Nu_1 = 0.170Ra^{0.287}$, vs. $Ro_{l,\mathrm{crit}} = 0.42Re_{\mathrm{VAC}}E^{2/3}$, i.e. a local Rossby number in which a local length scale of convective onset, l_{crit}, is assumed and Re is estimated using a VAC scaling (measured Re values are not used). b) Nu/Nu_1 vs. $Ro_{l,\mathrm{crit}} = 0.42Re_{\mathrm{CIA}}E^{2/3}$, i.e. a local Rossby number where the length scale is again assumed to be that convective onset, but Re is instead now estimated using a CIA scaling. Note that here, essentially two different length scales are assumed at once, as the CIA scaling inherently assumes the use of l_{turb}. c) Nu/Nu_1 vs. $Ro_{l,\mathrm{turb}} = {Re_{\mathrm{VAC}}}^{1/2}E^{1/2}$, where the length scale is assumed to be the QG turbulent length scale, $l_{\mathrm{turb}} = Ro^{1/2}H$, and Re is estimated using a VAC scaling. Once again, two different length scales are assumed at once here since Re_{VAC} assumes the use of l_{crit}. d) Nu/Nu_1 vs. $Ro_{l,\mathrm{turb}} = {Re_{\mathrm{CIA}}}^{1/2}E^{1/2}$, i.e. a local Ro using l_{turb} again but using a CIA estimate of Re. e) Nu/Nu_1 vs. $Ro_{l,\mathrm{crit}} = 0.42Re_{\mathrm{meas}}E^{2/3}$, i.e. a local Ro using l_{crit} but this time using our measured Re values. f) Nu/Nu_1 vs. $Ro_{l,\mathrm{turb}} = {Re_{\mathrm{meas}}}^{1/2}E^{1/2}$, i.e. a local Ro using l_{turb} and using measured Re values. e) and f) show that measured data is rather complex, and actually neither x parameter Ro_l constructed using l_{crit} or l_{turb} actually collapses our measured laboratory heat transfer data.

Re is instead now estimated using a CIA scaling. Unsurprisingly, Fig. 4.13a) and 4.13b) yield nearly identical collapses since the two assumed velocity scalings yield similar estimates of Ro amongst all collected data, as shown in Fig. 4.11a). We note that in Fig. 4.13b), essentially two different length scales for the local characteristic scale of the fluid bulk are assumed at once, as the CIA scaling inherently assumes the use of l_{turb}. Furthermore, in Figure 4.13c) we plot Nu/Nu_1 versus $Ro_{l,\mathrm{turb}} = {Re_{\mathrm{VAC}}}^{1/2}E^{1/2}$, where the length scale is now assumed to be the QG turbulent length scale, $l_{\mathrm{turb}} = Ro^{1/2}H$, and Re is estimated using a VAC scaling. Once again, two different length scales are assumed at once here since Re_{VAC} assumes the use of l_{crit}. In Figure 4.13d) we plot Nu/Nu_1 versus $Ro_{l,\mathrm{turb}} = {Re_{\mathrm{CIA}}}^{1/2}E^{1/2}$, i.e. a local Ro using l_{turb} again but using a CIA estimate of Re. This result is similar to c).

Figure 4.13e) displays Nu/Nu_1 versus $Ro_{l,\mathrm{crit}} = 0.42Re_{\mathrm{meas}}E^{2/3}$, a local Ro using l_{crit} but using our measured Re values. Figure 4.13f) shows Nu/Nu_1 versus $Ro_{l,\mathrm{turb}} = {Re_{\mathrm{meas}}}^{1/2}E^{1/2}$, a local Ro using l_{turb} and using measured Re values. We conclude from Fig. 4.13e) and 4.13f) that neither x parameter Ro_l, constructed using l_{crit} or l_{turb}, actually collapses our laboratory heat transfer data. Overall, we conclude from Fig. 4.13 that all collapse subplots shown are qualitatively interchangeable. Thus, Re_{VAC} and Re_{CIA}, and l_{crit} and l_{turb} are not easily distinguishable in our velocity data.

4.6 Discussion

4.6.1 Implications From Simultaneous Measurements

We have presented the results of a hydrodynamic laboratory-numerical survey in which heat and momentum transfer are simultaneously measured. Our results shed light on the convection dynamics that underlie planetary magnetic field generation. Thermal measurements are collected in order to characterize convective heat transfer in conjunction with measurements of fluid bulk convective point velocities via laser doppler velocimetry (LDV). For non-rotating experiments, our results agree well with those of past studies, thus validating our convective measurements. Specifically, our non-rotating heat transfer results display the existence of a classical $\sim$'2/7' (sheared boundary layer) or $\sim$'1/3' (turbulent bulk) exponent in the Nu-Ra scaling while momentum transfer measurements exhibit a $\sim$'1/2' exponent in the Re-Ra scaling.

Rotating convection DNS and laboratory heat transfer results also confirm the findings of past studies, including that transitions in heat transfer behavior are correlated with the boundary layer dynamics of the system. We use our RC heat transfer measurements in conjunction with velocity data obtained using LDV to test the hypothesized VAC and CIA velocity scalings. Past studies suggest that the CIA scaling prediction of core velocities can be used to explain observations of planetary magnetic field intensities [e.g. Christensen and Aubert (2006), Christensen et al. (2009)]. Specifically, in Christensen and Aubert (2006), the CIA scaling is seen to hold across a dynamo survey containing columnar, dipolar cases. In their survey, the dipolarity of model fields appears to break down and become quadrupolar in high Ra cases. Nonetheless, agreement of model velocities with the CIA scaling is seen across the entire survey, even for their quadrupolar dynamos. Further, models containing columnar structures appear to correspond to cases below Ra_T, where the VAC scaling is argued to hold [cf. Aubert et al. (2001), King and Buffett (2013), Gastine et al. (2016) Long et al. (2020)]. Thus, it is not clear how the CIA scaling explains flow behavior in all of the dynamo models in Christensen and Aubert (2006).

Our simultaneous measurements of heat and momentum transfer reveal that the CIA scal-

ing holds from near convective onset to nearly ∼800 times critical (at low E, i.e. $E \simeq 3 \times 10^{-6}$). The laboratory data contain a weak Ra dependence on Re at low Ra that we attribute to sidewall boundary zonal flow (BZF) in cylindrical containers [de Wit et al. (2020), Zhang et al. (2020)]. Importantly, observed velocity behavior is not correlated with horizontal boundary layer dynamics as is the case for our heat transfer results (see Fig. 4.12). Thus, we conclude that global heat transfer and bulk dynamical regimes are not intimately tied to one another in the finite parameter space explored.

As shown in Fig. 4.11a), the ratio of measured Ro values relative to respective CIA predictions is exceptional, with $Ro/Ro_{\mathrm{CIA}} \sim 1$. This finding regarding the robustness of the CIA scaling agrees with the results of the dynamo models of Christensen and Aubert (2006). However, we also find that our velocity data are also adequately explained by the VAC scaling, with $Ro/Ro_{\mathrm{VAC}} \sim 0.5$. Fig. 4.11b) shows that the theoretical length scales, l_{crit} and l_{turb} assumed in the VAC and CIA scalings respectively, are not separable over our range of experiments and DNS. Thus, we note that our results do not support the conjecture in Guervilly et al. (2019) that the characteristic length scales, l_{crit} and l_{turb}, must be greatly scale separated in quasi-geostrophic turbulent flows.

4.6.2 Quasi-Geostrophic Scaling Arguments

The VAC and CIA scalings both adequately describe our RC velocity measurements, with the CIA scaling accurately holding both above and below all transition Rayleigh numbers and with VAC estimates approximately holding as well. How can both of these scalings simultaneously be working reasonably well?

Analysis of the vorticity equation of a hydrodynamic RC system reveals that the VAC balance cannot be a leading order balance, but rather is a magnitude equivalence. To show this, we scale the vorticity equation of our RC system [e.g. Kundu et al. (2012)] as follows:

$$\begin{gathered}\partial_t \vec{\omega} + \vec{u} \cdot \nabla \vec{\omega} - \vec{\omega} \cdot \nabla \vec{u} - 2\vec{\Omega} \cdot \nabla \vec{u} = \alpha g \nabla \times T \hat{z} + \nu \nabla^2 \vec{\omega} \\ \frac{U^2}{\delta^2} \sim \frac{U^2}{\delta^2} \sim \frac{U^2}{\delta^2} \sim \frac{2\Omega U}{H} \sim \frac{\alpha g \Delta T}{H} \sim \frac{\nu U}{\delta^3},\end{gathered} \tag{4.5}$$

where $\vec{\omega} = \nabla \times \vec{u} \sim U/\delta$ [s^{-1}] is the vorticity, U [m/s] is the characteristic velocity, and δ [m] is a local convection scale. Multiplying the second line of (4.5) by $H/(2\Omega U)$ and re-arranging produces:

$$\frac{U}{2\Omega\delta}\left(\frac{H}{\delta}\right) \sim \frac{U}{2\Omega\delta}\left(\frac{H}{\delta}\right) \sim \frac{U}{2\Omega\delta}\left(\frac{H}{\delta}\right) \sim 1 \sim \frac{\alpha g \Delta T}{2\Omega U} \sim \frac{\nu}{2\Omega H^2}\left(\frac{H^3}{\delta^3}\right). \tag{4.6}$$

In order to obtain the length scale used in the VAC scaling, l_{crit} of (2.23), the Coriolis term and the viscous diffusion term in (4.6) must balance as:

$$1 \sim \frac{\nu}{2\Omega H^2}\left(\frac{H^3}{\delta^3}\right) \longrightarrow \delta/H \sim E^{1/3}. \tag{4.7}$$

Substituting $\delta/H \sim E^{1/3}$ into (4.6), the first three terms of (4.6) simplify to order $Ro_\delta E^{-1/3}$, where Ro_δ is the local Rossby number, $Ro_\delta = U/(2\Omega\delta)$. In order for (4.6) and (4.7) to hold, it must then be true that $Ro_\delta \ll E^{1/3}$ and $\alpha g \Delta T \ll 2\Omega U$ in (4.6).

Examining the first requirement, $Ro_\delta \ll E^{1/3}$, both sides of the inequality can be multiplied by (H/ν) and re-arranged to yield:

$$\left(\frac{H}{\nu}\right) U \ll (2\Omega\delta) E^{1/3}\left(\frac{H}{\nu}\right). \tag{4.8}$$

The lefthand side (l.h.s.) of (4.8) is the global Reynolds number. The righthand side (r.h.s.) of (4.8) can be multiplied by (H/H) to produce:

$$Re \ll \left(\frac{2\Omega H^2}{\nu}\right)\left(\frac{\delta}{H}\right) E^{1/3} = E^{-1/3}, \tag{4.9}$$

where (4.7) has been substituted in for δ/H. Next, the VAC estimate of Re given by (**??**) can be substituted in for Re on the l.h.s. of (4.9) to yield:

$$Re \sim \frac{Ra^{1/2}(Nu-1)^{1/2}}{Pr} E^{1/3} \ll E^{-1/3}. \tag{4.10}$$

Re-arrangement of (4.10) implies that:

$$Ra \ll (Nu-1)^{-1} Pr^2 E^{-4/3}. \tag{4.11}$$

Near to the onset of stationary RC, the quantities $(Nu-1)^{-1}$ and Pr^2 will be roughly of order unity in a water system. Thus, (4.11) reduces to:

$$Ra \ll E^{-4/3} \sim Ra_C^S. \tag{4.12}$$

Since steady convection cannot occur for $Ra \ll Ra_C^S$, the other non-VAC terms in (4.5) cannot be subdominant. Therefore, it is not possible for the VAC scaling to be the leading order balance of the system, even at onset, where $Ra \simeq Ra_C^S$. A comparable analysis of the requirement involving the buoyancy term, $\alpha g \Delta T \ll 2\Omega U$, yields the same inequality as (4.12). Thus, in reality it must be true that $Ro_\delta \sim E^{1/3}$ and $\alpha g \Delta T \sim 2\Omega U$ so that $Ra \sim E^{-4/3}$. We note that these balances are the essential ingredients of quasi-geostrophic flow and are consistent with the findings of prior studies [e.g. Busse (1970), Sprague et al. (2006), Calkins et al. (2015), Aurnou and King (2017), Calkins (2018)]. We conclude from the above analysis that in the quasi-geostrophic turbulent (QGT) regime, the CIA scaling holds even at onset, with the VAC magnitude equivalence approximately holding as well. This approximate CIA–VAC co-scaling further supports the idea that $E^{1/3} \sim Ro^{1/2}$ in QGT flows, as found in Fig. 4.11.

4.6.3 Velocity Scales at Planetary Conditions

We summarize the key results of this study via the schematics shown in Figure 4.14. Fig. 4.14a) shows a side view of a cylindrical convection experiment in which the entire fluid layer is rotationally dominated. Here, $Nu \sim (Ra/Ra_C^S)^3$ (steep slope), and both the boundary layers (light blue) and the bulk (blue) are in quasi-geostrophic balance, with small (i.e. < 1) global Ro_H in the bulk and small local Ro_δ in the top and bottom boundary layers. Re_H scales as Re_{CIA} (and approximately as Re_{VAC}).

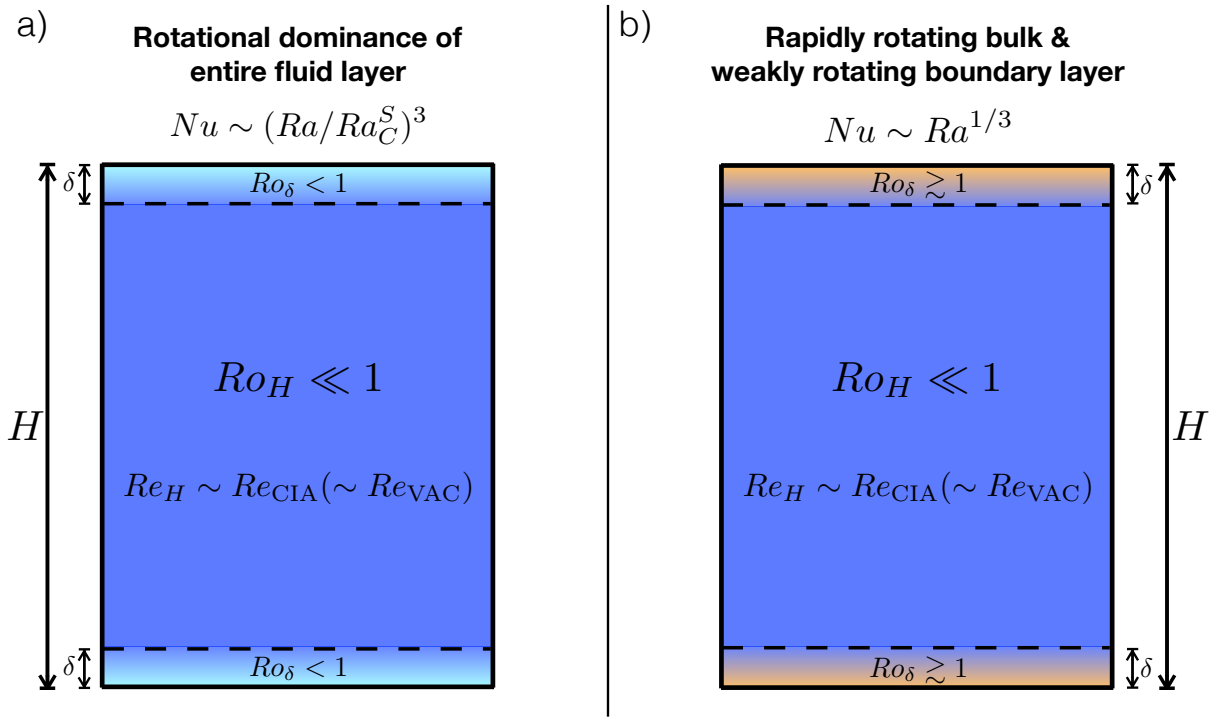

Figure 4.14: a) Schematic (side view of a cylindrical container) of the convective regime in which the entire fluid layer is rotationally dominated. Here, $Nu \sim (Ra/Ra_C^S)^3$ (steep slope), and both the boundary layers (light blue) and the bulk (blue) are controlled by the Coriolis force, with small (< 1) global Ro_H in the bulk and local Ro_δ in the boundary layers. Re_H scales as $Re_{\rm CIA}$ (and also $Re_{\rm VAC}$, though we show that the VAC scaling cannot be a leading order balance). b) Schematic of the convective regime in which the boundary layers (orange) become weakly influenced by rotation while the bulk (blue) remains dominated by the system rotation. Here, $Nu \sim Ra^{1/3}$ (non-rotating style), and Ro_δ is of order unity or larger in the boundary layer while Ro_H remains small in the bulk. Re_H scales as $Re_{\rm CIA}$, the same as in a).

Fig. 4.14b) displays the convective regime in which the boundary layers (orange) become weakly influenced by rotation while the bulk (blue) remains dominated by rotation. Here, Ro_δ is of order unity or larger in the boundary layers while Ro_H remains small in the bulk. Re_H scales as $Re_{\rm CIA}$, the same as in Fig. 4.14a). Thus, heat transfer is controlled by boundary layer dynamics such that $Nu \sim Ra^{1/3}$ (non-rotating style), while the bulk dynamics are in the QGT flow regime in which the CIA and VAC scalings approximately co-scale.

At planetary conditions with asymptotically large Ra and low E, it is expected that convective heat transfer will be throttled by the bulk and independent of system diffusivities such that:

$$Nu \sim Ra^{3/2} E^2 Pr^{-1/2} \tag{4.13}$$

[e.g. Julien et al. (2012a), Barker et al. (2014), Aurnou et al. (2020)]. While this diffusion-free RC heat transfer scaling has yet to be accessed in the laboratory, Julien et al. (2012a) and Plumley et al. (2016) recover (4.13) in asymptotically reduced models. Substituting (4.13) into the CIA scaling of (2.47) yields:

$$Ro_{\mathrm{CIA}} \sim {Ro_{\mathrm{ff}}}^2 \tag{4.14}$$

[Aurnou et al. (2020)]. Equation (4.14) implies that the CIA scaling of (2.47) asymptotes to scale as the square of the free-fall Rossby number as the system heat transfer asymptotes to (4.13). This explains the velocity transition to a ${Ro_{\mathrm{ff}}}^2$ scaling in the lowest E simulations in Guervilly et al. (2019). Further, (4.13) and (4.14) show that even when horizontal boundary processes are diffusively limiting the system heat transfer, diffusion-free geostrophic turbulence can robustly develop in the fluid bulk. Thus, we predict that (4.14) will hold at planetary conditions and can be used to estimate a characteristic core flow speed [cf. Christensen (2010)].

Heat transfer and velocity scaling behaviors are not directly coupled in the parameter space that models of planetary core dynamics are capable of exploring. Furthermore, the theoretical length scales, l_{crit} of (2.23) and l_{turb} of (2.46), and velocity scales, Re_{VAC} given by (2.42) and Re_{CIA} given by (2.47), of core convection are not scale separable in such a parameter space. Finally, the QGT flow regime develops in the bulk (even near to onset), suggesting that we can access realistic, diffusion-free bulk dynamics in models that are far from planetary core conditions.

4.7 Appendix A: Data Tables for Simultaneous Heat and Momentum Transfer Measurements

H (cm)	Ω (rpm)	Q (W)	$\overline{T_{\text{fluid}}}$ (C)	ΔT (C)	$u_{\text{z, rms}}$ (mm/s)
20.2	0	49.89	24.36	1.44	2.28
20.2	0	80.80	24.77	1.91	2.74
20.2	0	124.9	24.00	2.98	2.96
20.2	0	200.0	25.34	4.04	3.50
20.2	0	315.9	25.03	5.93	3.93
20.2	0	499.6	24.16	8.65	4.44
20.2	0	598.6	23.87	9.84	4.55
20.2	0	801.1	25.80	12.05	4.84
20.2	0	1102	24.92	16.03	5.57
40.1	0	49.75	24.33	1.56	3.42
40.1	0	102.8	24.44	2.66	4.34
40.1	0	135.0	24.07	3.36	4.77
40.1	0	199.0	24.43	4.68	5.50
40.1	0	297.9	24.86	5.88	6.39
40.1	0	403.6	25.16	7.29	7.23
40.1	0	599.4	25.24	10.21	8.65
40.1	0	797.1	25.73	12.33	9.60
40.1	0	902.5	26.02	13.67	9.64
40.1	0	1149	25.73	16.66	11.4
80.2	0	66.64	24.46	1.93	4.55
80.2	0	125.6	23.92	3.29	6.09
80.2	0	249.5	22.81	5.57	6.96
80.2	0	250.8	22.73	5.47	7.01
80.2	0	402.1	24.01	7.91	8.01

80.2	0	502.2	22.61	9.41	10.6
80.2	0	697.3	25.14	11.65	10.3
80.2	0	800.7	23.68	13.36	10.9
80.2	0	1107	25.42	16.77	12.4
20.2	3.6	49.98	25.07	1.02	1.91
20.2	3.6	75.22	24.98	1.52	2.01
20.2	3.6	99.14	24.83	1.97	2.04
20.2	3.6	163.4	24.83	3.12	2.28
20.2	3.6	272.9	24.83	4.82	2.54
20.2	3.6	447.9	25.44	7.20	2.88
20.2	3.6	731.7	26.17	10.66	3.33
20.2	3.6	1145	26.38	15.43	4.04
20.2	10.6	31.43	24.98	0.98	1.79
20.2	10.6	49.63	25.41	1.45	1.78
20.2	10.6	75.45	25.18	1.81	1.89
20.2	10.6	103.2	25.21	2.33	1.98
20.2	10.6	202.1	25.21	3.59	2.07
20.2	10.6	399.7	25.59	6.30	2.47
20.2	10.6	649.1	26.61	9.39	2.79
20.2	10.6	800.2	26.44	11.12	3.01
20.2	10.6	1099	26.78	14.21	3.27
40.1	2.7	50.10	24.40	1.32	2.02
40.1	2.7	67.28	24.45	1.88	2.18
40.1	2.7	102.6	24.46	2.55	2.29
40.1	2.7	201.2	24.81	4.16	2.68
40.1	2.7	200.4	24.41	4.49	2.72
40.1	2.7	391.6	25.10	6.79	3.24
40.1	2.7	599.1	25.09	9.85	3.75
40.1	2.7	797.3	25.64	11.96	4.27

40.1	2.7	1148	25.60	15.93	4.74
20.2	35.0	49.78	25.67	4.02	1.86
20.2	35.0	81.23	26.05	4.61	1.90
20.2	35.0	125.7	25.40	5.60	1.97
20.2	35.0	200.9	26.60	6.46	2.03
20.2	35.0	315.7	26.30	8.20	2.13
20.2	35.0	498.7	25.37	10.64	2.32
20.2	35.0	598.3	25.31	11.74	2.40
20.2	35.0	700.3	26.47	12.56	2.45
20.2	35.0	803.0	26.73	13.37	2.58
20.2	35.0	945.8	25.95	15.25	2.66
20.2	35.0	1104	25.64	16.93	2.76
40.1	9.0	51.45	25.40	1.99	2.00
40.1	9.0	67.30	24.68	2.12	1.98
40.1	9.0	103.0	24.53	2.69	2.04
40.1	9.0	134.9	25.20	3.00	2.17
40.1	9.0	201.3	24.10	4.16	2.30
40.1	9.0	296.7	25.18	5.79	2.53
40.1	9.0	398.9	25.62	6.83	2.70
40.1	9.0	402.7	24.87	7.24	2.68
40.1	9.0	599.3	25.13	10.03	3.06
40.1	9.0	801.1	27.69	11.62	3.42
40.1	9.0	1144	27.78	15.36	4.11
80.2	2.3	66.45	24.35	1.83	2.35
80.2	2.3	126.3	23.80	3.10	2.89
80.2	2.3	251.0	22.82	5.52	3.46
80.2	2.3	250.8	22.72	5.42	3.58
80.2	2.3	402.1	23.93	7.78	4.05
80.2	2.3	499.7	24.69	8.99	4.54

80.2	2.3	799.5	23.69	13.42	5.59
80.2	2.3	1107	25.47	16.76	6.45
40.1	26.7	49.12	25.37	3.10	2.15
40.1	26.7	101.5	25.63	4.33	2.18
40.1	26.7	134.7	24.99	4.81	2.22
40.1	26.7	219.3	24.39	6.04	2.39
40.1	26.7	389.9	25.92	8.14	2.88
40.1	26.7	600.9	25.16	10.22	2.53
40.1	26.7	902.4	26.50	14.79	3.13
40.1	26.7	1148	26.38	17.97	3.30
80.2	7.0	66.44	24.58	2.13	2.10
80.2	7.0	125.5	24.06	3.47	2.40
80.2	7.0	250.1	22.88	5.72	2.75
80.2	7.0	250.3	22.93	5.72	2.67
80.2	7.0	401.9	24.04	7.97	3.22
80.2	7.0	503.5	22.74	9.64	3.40
80.2	7.0	799.8	23.85	13.67	4.22
80.2	7.0	1108	25.61	17.18	4.95
80.2	23.2	66.43	25.14	3.28	1.96
80.2	23.2	126.5	24.62	4.65	2.17
80.2	23.2	251.8	24.40	7.47	2.41
80.2	23.2	402.8	25.01	9.84	2.63
80.2	23.2	502.9	24.61	11.21	2.88
80.2	23.2	799.1	24.78	15.54	3.15
80.2	23.2	1109	26.61	19.07	3.71
80.2	55.7	66.52	26.48	6.21	2.28
80.2	55.7	95.12	26.55	7.61	2.30
80.2	55.7	126.3	26.51	8.59	2.30
80.2	55.7	168.6	26.34	9.77	2.32

80.2	55.7	252.1	26.25	11.24	2.33
80.2	55.7	400.4	26.92	13.18	2.60
80.2	55.7	498.5	27.48	14.22	2.62
80.2	55.7	698.2	27.67	16.42	2.93
80.2	55.7	798.4	27.64	17.78	3.00
80.2	55.7	1097	26.87	21.08	3.53

Table 4.1: Dimensional Laboratory Parameters: Heat and Momentum Transfer Study

H is the fluid container height (which contains a fixed inner diameter of $D_i = 58.6$ cm), Ω is the dimensional rotation rate of the container, Q is the mean input heating power, $\overline{T_{\text{fluid}}}$ is the mean temperature of the fluid, ΔT is the temperature difference across the fluid layer, and $u_{\text{z, rms}}$ is the z-rms velocity in the fluid bulk. The dashed horizontal lines separate the different aspect ratio containers used.

Γ	E	Ra	Pr	Nu	Re	Ro	Ro_{ff}	Fr
2.91	∞	2.25×10^8	6.16	42.6	513.6	∞	∞	0
2.91	∞	3.07×10^8	6.10	48.0	623.2	∞	∞	0
2.91	∞	4.58×10^8	6.22	49.1	661.1	∞	∞	0
2.91	∞	6.70×10^8	6.01	59.2	780.3	∞	∞	0
2.91	∞	9.67×10^8	6.06	64.4	899.7	∞	∞	0
2.91	∞	1.34×10^9	6.20	70.7	996.5	∞	∞	0
2.91	∞	1.50×10^9	6.24	74.7	1014	∞	∞	0
2.91	∞	2.05×10^9	5.94	81.4	1126	∞	∞	0
2.91	∞	2.60×10^9	6.07	84.5	1272	∞	∞	0
1.46	∞	1.93×10^9	6.17	76.4	1535	∞	∞	0
1.46	∞	3.31×10^9	6.15	94.1	1953	∞	∞	0
1.46	∞	4.08×10^9	6.21	98.2	2127	∞	∞	0

1.46	∞	5.82×10^{9}	6.15	103	2471	∞	∞	0
1.46	∞	7.63×10^{9}	6.04	124	2918	∞	∞	0
1.46	∞	9.29×10^{9}	6.08	136	3340	∞	∞	0
1.46	∞	1.33×10^{10}	6.02	144	3961	∞	∞	0
1.46	∞	1.65×10^{10}	5.95	158	4439	∞	∞	0
1.46	∞	1.86×10^{10}	5.90	162	4492	∞	∞	0
1.46	∞	2.23×10^{10}	5.95	169	5296	∞	∞	0
0.73	∞	1.91×10^{10}	6.15	169	4089	∞	∞	0
0.73	∞	3.16×10^{10}	6.24	188	5403	∞	∞	0
0.73	∞	4.98×10^{10}	6.42	221	6014	∞	∞	0
0.73	∞	4.87×10^{10}	6.44	226	6047	∞	∞	0
0.73	∞	7.62×10^{10}	6.22	250	7120	∞	∞	0
0.73	∞	8.32×10^{10}	6.46	263	9128	∞	∞	0
0.73	∞	1.20×10^{11}	6.04	294	9350	∞	∞	0
0.73	∞	1.26×10^{11}	6.28	295	9574	∞	∞	0
0.73	∞	1.76×10^{11}	6.00	323	11400	∞	∞	0
2.91	2.90×10^{-5}	1.67×10^{8}	6.05	52.8	437.1	1.27×10^{-2}	1.53×10^{-1}	0.0042
2.91	2.91×10^{-5}	2.46×10^{8}	6.06	56.4	458.9	1.34×10^{-2}	1.85×10^{-1}	0.0042
2.91	2.92×10^{-5}	3.17×10^{8}	6.09	58.3	465.1	1.36×10^{-2}	2.11×10^{-1}	0.0042
2.91	2.92×10^{-5}	5.02×10^{8}	6.09	62.4	518.5	1.52×10^{-2}	2.65×10^{-1}	0.0042
2.91	2.92×10^{-5}	7.76×10^{8}	6.09	68.4	579.0	1.69×10^{-2}	3.30×10^{-1}	0.0042
2.91	2.88×10^{-5}	1.20×10^{9}	6.00	75.9	665.8	1.92×10^{-2}	4.07×10^{-1}	0.0042
2.91	2.83×10^{-5}	1.85×10^{9}	5.88	83.8	781.1	2.21×10^{-2}	5.02×10^{-1}	0.0042
2.91	2.82×10^{-5}	2.71×10^{9}	5.85	90.9	954.0	2.69×10^{-2}	6.07×10^{-1}	0.0042
2.91	9.77×10^{-6}	1.59×10^{8}	6.06	31.9	410.2	4.00×10^{-3}	5.01×10^{-2}	0.037
2.91	9.67×10^{-6}	2.42×10^{8}	6.00	41.8	411.7	3.98×10^{-3}	6.14×10^{-2}	0.037
2.91	9.73×10^{-6}	2.97×10^{8}	6.03	47.3	432.2	4.22×10^{-3}	6.83×10^{-2}	0.037
2.91	9.72×10^{-6}	3.84×10^{8}	6.03	54.1	455.6	4.42×10^{-3}	7.76×10^{-2}	0.037
2.91	9.72×10^{-6}	5.90×10^{8}	6.03	69.1	475.4	4.62×10^{-3}	9.61×10^{-2}	0.037

2.91	9.64×10^{-6}	1.04×10^{9}	5.97	79.3	572.5	5.52×10^{-3}	1.27×10^{-1}	0.037
2.91	9.42×10^{-6}	1.67×10^{9}	5.82	84.2	660.1	6.23×10^{-3}	1.59×10^{-1}	0.037
2.91	9.38×10^{-6}	1.96×10^{9}	5.84	89.5	715.9	6.72×10^{-3}	1.72×10^{-1}	0.037
2.91	9.45×10^{-6}	2.55×10^{9}	5.79	93.0	772.0	7.30×10^{-3}	1.98×10^{-1}	0.037
1.46	9.84×10^{-6}	1.63×10^{9}	6.18	92.2	906.0	8.89×10^{-3}	1.60×10^{-1}	0.0024
1.46	9.79×10^{-6}	2.34×10^{9}	6.15	86.7	980.3	9.60×10^{-3}	1.91×10^{-1}	0.0024
1.46	9.79×10^{-6}	3.71×10^{9}	6.15	98.4	1030	1.01×10^{-2}	2.41×10^{-1}	0.0024
1.46	9.71×10^{-6}	5.29×10^{9}	6.09	119	1213	1.18×10^{-2}	2.86×10^{-1}	0.0024
1.46	9.78×10^{-6}	5.58×10^{9}	6.16	109	1225	1.20×10^{-2}	2.94×10^{-1}	0.0024
1.46	9.64×10^{-6}	8.77×10^{9}	6.05	142	1478	1.43×10^{-2}	3.67×10^{-1}	0.0024
1.46	9.65×10^{-6}	1.27×10^{10}	6.05	149	1713	1.65×10^{-2}	4.42×10^{-1}	0.0024
1.46	9.53×10^{-6}	1.59×10^{10}	5.96	163	1974	1.88×10^{-2}	4.92×10^{-1}	0.0024
1.46	9.54×10^{-6}	2.12×10^{10}	5.97	176	2190	2.09×10^{-2}	5.68×10^{-1}	0.0024
2.91	2.91×10^{-6}	6.79×10^{8}	5.96	13.5	432.7	1.26×10^{-3}	3.11×10^{-2}	0.40
2.91	2.89×10^{-6}	7.95×10^{8}	5.90	20.2	440.7	1.29×10^{-3}	3.35×10^{-2}	0.40
2.91	2.93×10^{-6}	9.32×10^{8}	6.00	26.5	454.9	1.33×10^{-3}	3.65×10^{-2}	0.40
2.91	2.85×10^{-6}	1.15×10^{9}	5.82	37.1	482.2	1.37×10^{-3}	4.01×10^{-2}	0.40
2.91	2.87×10^{-6}	1.44×10^{9}	5.86	46.6	501.3	1.44×10^{-3}	4.50×10^{-2}	0.40
2.91	2.93×10^{-6}	1.77×10^{9}	6.00	57.3	535.1	1.57×10^{-3}	5.04×10^{-2}	0.40
2.91	2.94×10^{-6}	1.94×10^{9}	6.01	62.4	551.9	1.62×10^{-3}	5.28×10^{-2}	0.40
2.91	2.86×10^{-6}	2.22×10^{9}	5.84	68.1	591.6	1.66×10^{-3}	5.58×10^{-2}	0.40
2.91	2.84×10^{-6}	2.40×10^{9}	5.80	73.4	614.5	1.75×10^{-3}	5.79×10^{-2}	0.40
2.91	2.89×10^{-6}	2.62×10^{9}	5.92	76.0	621.3	1.80×10^{-3}	6.09×10^{-2}	0.40
2.91	2.91×10^{-6}	2.86×10^{9}	5.96	80.1	641.3	1.87×10^{-3}	6.39×10^{-2}	0.40
1.46	2.87×10^{-6}	2.62×10^{9}	5.99	61.0	918.4	2.64×10^{-3}	6.01×10^{-2}	0.027
1.46	2.92×10^{-6}	2.67×10^{9}	6.11	77.1	894.5	2.61×10^{-3}	6.11×10^{-2}	0.027
1.46	2.93×10^{-6}	3.37×10^{9}	6.14	93.7	917.9	2.69×10^{-3}	6.87×10^{-2}	0.027
1.46	2.89×10^{-6}	3.91×10^{9}	6.03	109	990.6	2.86×10^{-3}	7.35×10^{-2}	0.027
1.46	2.96×10^{-6}	5.07×10^{9}	6.03	119	1024	3.04×10^{-3}	8.58×10^{-2}	0.027

1.46	2.89×10^{-6}	7.52×10^{9}	6.21	125	1158	3.34×10^{-3}	1.01×10^{-1}	0.027
1.46	2.86×10^{-6}	9.10×10^{9}	6.00	143	1249	3.57×10^{-3}	1.11×10^{-1}	0.027
1.46	2.91×10^{-6}	9.24×10^{9}	6.08	136	1218	3.54×10^{-3}	1.13×10^{-1}	0.027
1.46	2.89×10^{-6}	1.30×10^{10}	6.04	146	1396	4.03×10^{-3}	1.34×10^{-1}	0.027
1.46	2.73×10^{-6}	1.73×10^{10}	5.66	168	1654	4.51×10^{-3}	1.51×10^{-1}	0.027
1.46	2.72×10^{-6}	2.30×10^{10}	5.65	181	1993	5.43×10^{-3}	1.74×10^{-1}	0.027
0.73	2.87×10^{-6}	1.80×10^{10}	6.17	167	2100	6.03×10^{-3}	1.55×10^{-1}	0.0018
0.73	2.90×10^{-6}	2.95×10^{10}	6.26	194	2552	7.42×10^{-3}	1.99×10^{-1}	0.0018
0.73	2.97×10^{-6}	4.95×10^{10}	6.42	217	2987	8.88×10^{-3}	2.61×10^{-1}	0.0018
0.73	2.98×10^{-6}	4.82×10^{10}	6.44	224	3082	9.19×10^{-3}	2.58×10^{-1}	0.0018
0.73	2.90×10^{-6}	7.46×10^{10}	6.23	252	3588	1.04×10^{-2}	3.17×10^{-1}	0.0018
0.73	2.84×10^{-6}	9.02×10^{10}	6.11	270	4097	1.17×10^{-2}	3.46×10^{-1}	0.0018
0.73	2.91×10^{-6}	1.27×10^{11}	6.27	292	4933	1.44×10^{-2}	4.14×10^{-1}	0.0018
0.73	2.79×10^{-6}	1.76×10^{11}	5.99	323	5962	1.66×10^{-2}	4.79×10^{-1}	0.0018
1.46	9.69×10^{-7}	4.06×10^{9}	6.00	36.1	985.3	9.55×10^{-4}	2.52×10^{-2}	0.23
1.46	9.64×10^{-7}	5.77×10^{9}	5.96	55.3	1005	9.69×10^{-4}	3.00×10^{-2}	0.23
1.46	9.78×10^{-7}	6.18×10^{9}	6.06	66.3	1021	9.99×10^{-4}	3.12×10^{-2}	0.23
1.46	9.91×10^{-7}	7.49×10^{9}	6.16	86.9	1071	1.06×10^{-3}	3.46×10^{-2}	0.23
1.46	9.57×10^{-7}	1.10×10^{10}	5.92	115	1217	1.17×10^{-3}	4.13×10^{-2}	0.23
1.46	9.74×10^{-7}	1.33×10^{10}	6.04	144	1317	1.28×10^{-3}	4.57×10^{-2}	0.23
1.46	9.45×10^{-7}	2.07×10^{10}	5.83	148	1473	1.39×10^{-3}	5.63×10^{-2}	0.23
1.46	9.48×10^{-7}	2.49×10^{10}	5.85	155	1550	1.47×10^{-3}	6.18×10^{-2}	0.23
0.73	9.45×10^{-7}	2.12×10^{10}	6.13	151	1886	1.79×10^{-3}	5.55×10^{-2}	0.016
0.73	9.57×10^{-7}	3.35×10^{10}	6.21	172	2130	2.04×10^{-3}	7.03×10^{-2}	0.016
0.73	9.83×10^{-7}	5.14×10^{10}	6.41	210	2376	2.34×10^{-3}	8.80×10^{-2}	0.016
0.73	9.82×10^{-7}	5.16×10^{10}	6.40	213	2314	2.27×10^{-3}	8.82×10^{-2}	0.016
0.73	9.57×10^{-7}	7.69×10^{10}	6.21	247	2859	2.74×10^{-3}	1.07×10^{-1}	0.016
0.73	9.87×10^{-7}	8.59×10^{10}	6.43	258	2934	2.90×10^{-3}	1.14×10^{-1}	0.016

0.73	9.61×10^{-7}	1.31×10^{11}	6.25	287	3733	3.59×10^{-3}	1.39×10^{-1}	0.016
0.73	9.23×10^{-7}	1.82×10^{11}	5.97	313	4563	4.21×10^{-3}	1.61×10^{-1}	0.016
0.73	2.82×10^{-7}	3.38×10^{10}	6.04	93.8	1784	5.04×10^{-4}	2.11×10^{-2}	0.18
0.73	2.85×10^{-7}	4.65×10^{10}	6.12	129	1955	5.58×10^{-4}	2.49×10^{-2}	0.18
0.73	2.87×10^{-7}	7.26×10^{10}	6.16	164	2161	6.19×10^{-4}	3.11×10^{-2}	0.18
0.73	2.83×10^{-7}	1.01×10^{11}	6.06	197	2387	6.76×10^{-4}	3.65×10^{-2}	0.18
0.73	2.85×10^{-7}	1.12×10^{11}	6.12	218	2596	7.40×10^{-4}	3.86×10^{-2}	0.18
0.73	2.84×10^{-7}	1.57×10^{10}	6.10	249	2848	8.10×10^{-4}	4.56×10^{-2}	0.18
0.73	2.72×10^{-7}	2.13×10^{11}	5.82	280	3497	9.53×10^{-4}	5.21×10^{-2}	0.18
0.73	1.14×10^{-7}	6.90×10^{10}	5.84	52.0	2145	2.44×10^{-4}	1.24×10^{-2}	1.02
0.73	1.14×10^{-7}	8.48×10^{10}	5.82	60.8	2168	2.46×10^{-4}	1.37×10^{-2}	1.02
0.73	1.14×10^{-7}	9.55×10^{10}	5.83	68.2	2160	2.46×10^{-4}	1.46×10^{-2}	1.02
0.73	1.14×10^{-7}	1.08×10^{11}	5.86	89.1	2170	2.48×10^{-4}	1.55×10^{-2}	1.02
0.73	1.14×10^{-7}	1.23×10^{11}	5.87	106	2182	2.49×10^{-4}	1.66×10^{-2}	1.02
0.73	1.13×10^{-7}	1.50×10^{11}	5.77	147	2467	2.78×10^{-4}	1.82×10^{-2}	1.02
0.73	1.13×10^{-7}	1.66×10^{11}	5.69	168	2520	2.80×10^{-4}	1.90×10^{-2}	1.02
0.73	1.11×10^{-7}	1.94×10^{11}	5.66	206	2829	3.13×10^{-4}	2.05×10^{-2}	1.02
0.73	1.11×10^{-7}	2.10×10^{11}	5.67	219	2883	3.21×10^{-4}	2.13×10^{-2}	1.02
0.73	1.13×10^{-7}	2.39×10^{11}	5.78	254	3347	3.77×10^{-4}	2.29×10^{-2}	1.02

Table 4.2: Non-Dimensional Laboratory Parameters: Heat and Momentum Transfer Study Γ is the aspect ratio of the cylindrical container used, E is the Ekman number, Ra is the Rayleigh number, Pr is the Prandtl number, Nu is the Nusselt number, Re is the Reynolds number, Ro is the Rossby Number, Ro_{ff} is the free-fall Rossby number given as $Ro_{\text{ff}} = \sqrt{RaE^2/Pr}$, and Fr is the Froude number. The dashed horizontal lines separate the different aspect ratio containers used.

Γ	E	Ra	Pr	Nu	Re	Ro	Ro_{ff}	Fr	N_x	N_y	N_z
0.74	2.9×10^{-6}	2.20×10^{8}	5.92	1.61	22.08	6.40×10^{-5}	1.77×10^{-2}	0	288	288	240
0.74	2.9×10^{-6}	2.50×10^{8}	5.92	2.50	36.90	1.07×10^{-4}	1.88×10^{-2}	0	288	288	240
0.74	2.9×10^{-6}	3.00×10^{8}	5.92	5.26	67.38	1.95×10^{-4}	2.06×10^{-2}	0	288	288	240
0.74	2.9×10^{-6}	4.00×10^{8}	5.92	11.7	121.9	3.54×10^{-4}	2.38×10^{-2}	0	288	288	240
0.74	2.9×10^{-6}	5.00×10^{8}	5.92	18.5	174.6	5.06×10^{-4}	2.67×10^{-2}	0	288	288	240
0.74	2.9×10^{-6}	6.80×10^{8}	5.92	30.8	265.9	7.71×10^{-4}	3.11×10^{-2}	0	288	288	240
0.74	2.9×10^{-6}	8.00×10^{8}	5.92	38.3	322.4	9.35×10^{-4}	3.37×10^{-2}	0	288	288	240
0.74	2.9×10^{-6}	1.00×10^{9}	5.92	48.8	404.5	1.17×10^{-4}	3.77×10^{-2}	0	384	384	240
0.74	2.9×10^{-6}	1.20×10^{9}	5.92	56.6	473.1	1.37×10^{-3}	4.13×10^{-2}	0	384	384	240
0.74	2.9×10^{-6}	1.95×10^{9}	5.92	73.7	662.6	1.92×10^{-3}	5.26×10^{-2}	0	384	384	384

Table 4.3: Non-Dimensional DNS Parameters: Heat and Momentum Transfer Study. Γ is the aspect ratio of the cylinder simulated, E is the Ekman number, Ra is the Rayleigh number, Pr is the Prandtl number, Nu is the Nusselt number, Re is the Reynolds number, Ro is the Rossby Number, Ro_{ff} is the free-fall Rossby number given as $Ro_{\text{ff}} = \sqrt{RaE^2/Pr}$, Fr is the Froude number, and N_x, N_y, and N_z are the number of grid points in the x, y, and z directions, respectively.

CHAPTER 5

Assessing Length Scales in Models of Planetary Core Flow

5.1 Motivation

The characteristic length scales of planetary core flows and their connection to observations of magnetic field structures remain poorly understood [cf. Aurnou et al. (2015), Jones (2015), Aurnou and King (2017), Aubert et al. (2017), Guervilly et al. (2019)]. Flux patches of the geomagnetic field, observed to exist at both high latitude and equatorial regions, scale in diameter as roughly $\mathcal{O}(500) - (1000)$ km [e.g. Bloxham and Gubbins (1985), Olson et al. (1999), Jackson (2003), Olson and Amit (2006), Roberts and King (2013)]. The results of dynamo models that are run with unrealistically large viscosities and relatively weak rotational forcing produce flow structures that, when directly mapped to Earth's core conditions, compare well to geomagnetic flux observations [e.g. Glatzmeier and Roberts (1996), Kuang and Bloxham (1997), Aubert et al. (2008), Christensen (2010), Amit et al. (2010), King and Buffett (2013)]. Specifically, the columnar flow structures existing in these viscous models scale to the size of observed geomagnetic flux patches of $\mathcal{O}(500) - (1000)$ km in width. However, if the realistic ratio of viscosity relative to the strength of rotation in Earth's core is considered (i.e. Ekman number, $E \sim \mathcal{O}(10^{-15})$, as opposed to $E \sim \mathcal{O}(10^{-4})$ of models), it is predicted that the length scales of structures would be far too small to be geomagnetically observable [cf. Nataf and Schaeffer (2015), Aurnou et al. (2015)].

The measured length scales of most current-day dynamo models [e.g. Soderlund et al. (2012), Marti et al. (2016), Yadav et al. (2016), Starchenko (2019)] *appear* to suggest that the characteristic length scale of core flows scales with the predicted width of structures

occurring at the onset of rotating convection, $l_{\text{crit}} \sim E^{1/3}H$ of (2.23), albeit with differing scaling coefficients. These length scales are perpendicular to the rotation axis. For $Pr < 0.68$, a dependence on the Prandtl number, Pr, exists for l_{crit} according to plane layer theory as:

$$l_{\text{crit}} = 2.4(E/Pr)^{1/3}H \tag{5.1}$$

[Chandrasekhar (1961), Julien et al. (1999)]. Figure 5.1 illustrates the width of a single structure, to scale, in Earth's outer core region using (5.1) for $Pr = 0.025$ and three different Ekman numbers: a) $E = 10^{-4}$ (model-like) as a red column, b) $E = 10^{-9}$ as a blue column, and c) $E = 10^{-15}$ (Earth-like) as a green column that is sub-pixel scale and thus not visible. It is highlighted visually here that for larger E values of $E = 10^{-4}$ in a) and even $E = 10^{-9}$ in b), only $\mathcal{O}(10) - (10^3)$ coherent structures are predicted to occupy Earth's outer core region, while $\sim 10^5$ structures (as prescribed in Fig. 5.1c) are realistically predicted to exist using (5.1). Thus, should these narrow structures exist in Earth's core (and comparably in other dynamo generating regions), they cannot be **directly** connected to nor used to explain present magnetic field observations [Nataf and Schaeffer (2015), Aurnou and King (2017)].

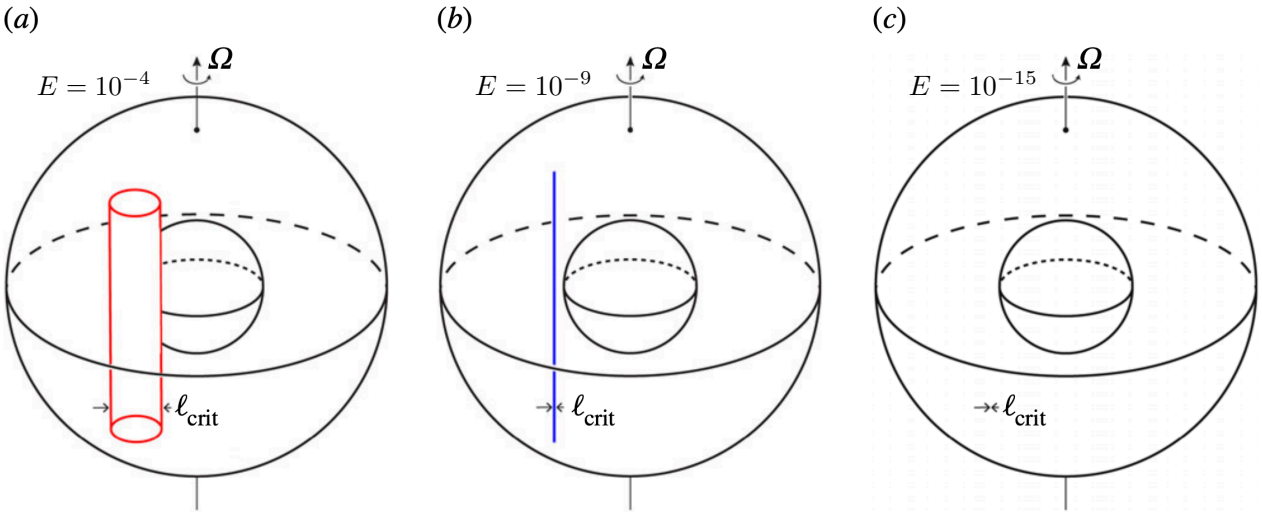

Figure 5.1: The magnitude of a single structure, to scale, in Earth's outer core region using (5.1) for $Pr = 0.025$ and three different Ekman numbers: a) $E = 10^{-4}$ as a red column, b) $E = 10^{-9}$ as a blue column, and c) $E = 10^{-15}$ as a green column that is sub-pixel scale and thus not visible. Modified from Figure 4 of Aurnou and King (2017).

Another prediction for the characteristic length scale of core flows exists and has been considered in recent studies [e.g. Schaeffer et al. (2017), Guervilly et al. (2019), Aubert (2019), Hawkins et al. (2020)]. This scale, the turbulent length scale of (2.46), $l_{\text{turb}} \simeq Ro^{1/2}H$, is thought to be relevant when rotating convective turbulence exists far past convective onset, as described in Section 2.2.2. However, Hawkins et al. (2020) [cf. Chapter 4 and Eqn. (2.52) in Chapter 2] show that the onset scale, $l_{\text{crit}} = 2.4E^{1/3}H$, scales equivalently to this turbulent scale, $l_{\text{turb}} \simeq Ro^{1/2}H$, when the local Reynolds number in the geostrophic fluid bulk is of order unity, i.e. $Re_l \sim \mathcal{O}(1)$. A natural question thus arises regarding the ability to separate these characteristic system scales in both models of core flows (for which $Re_l \sim \mathcal{O}(1)$) and planetary core flows themselves.

The precise aim of this study is to investigate the scale separation (or lack thereof) of theorized length scales of models of planetary core flows in order to ultimately better constrain the length scales of planetary core flows. We explore the two theorized hydrodynamic length scales mentioned, l_{crit} and l_{turb}. A third theorized characteristic system length scale, a magnetic length scale, l_{mag}, is not examined in order to first better understand the scales involved in QG core flows. This scale involves the importance of the magnetic Lorentz force, where $l_{\text{mag}} \sim \Lambda H$, and Λ is the magnetic Elsassar number [cf. King and Buffett (2013)].

We briefly elaborate on a few key characteristics of turbulent flows through the examination of several examples. Figure 5.2 displays several snapshots of turbulent flows, with two enhanced photographs of naturally occurring planetary turbulent flows in a) and b), and two images of flow fields originating from two-dimensional (2D) numerical models in c) and d). Turbulent motions arise in natural fluids including the oceans, atmospheres, and interiors of astrophysical bodies due to the nonlinear, coupled nature of the system of equations that govern these flows. More specifically, advection, or the movement of fluid parcels that move with the velocity field, tends to cause entanglement between neighboring parcels, thus generating disordered motions including irreversible mixing [cf. Davidson (2012), McWilliams (2017)].

Some classical characteristics of turbulence include scale variations in both time and space as well as energy and enstrophy cascades [e.g. Rhines (1979), Boer and Shepherd (1984),

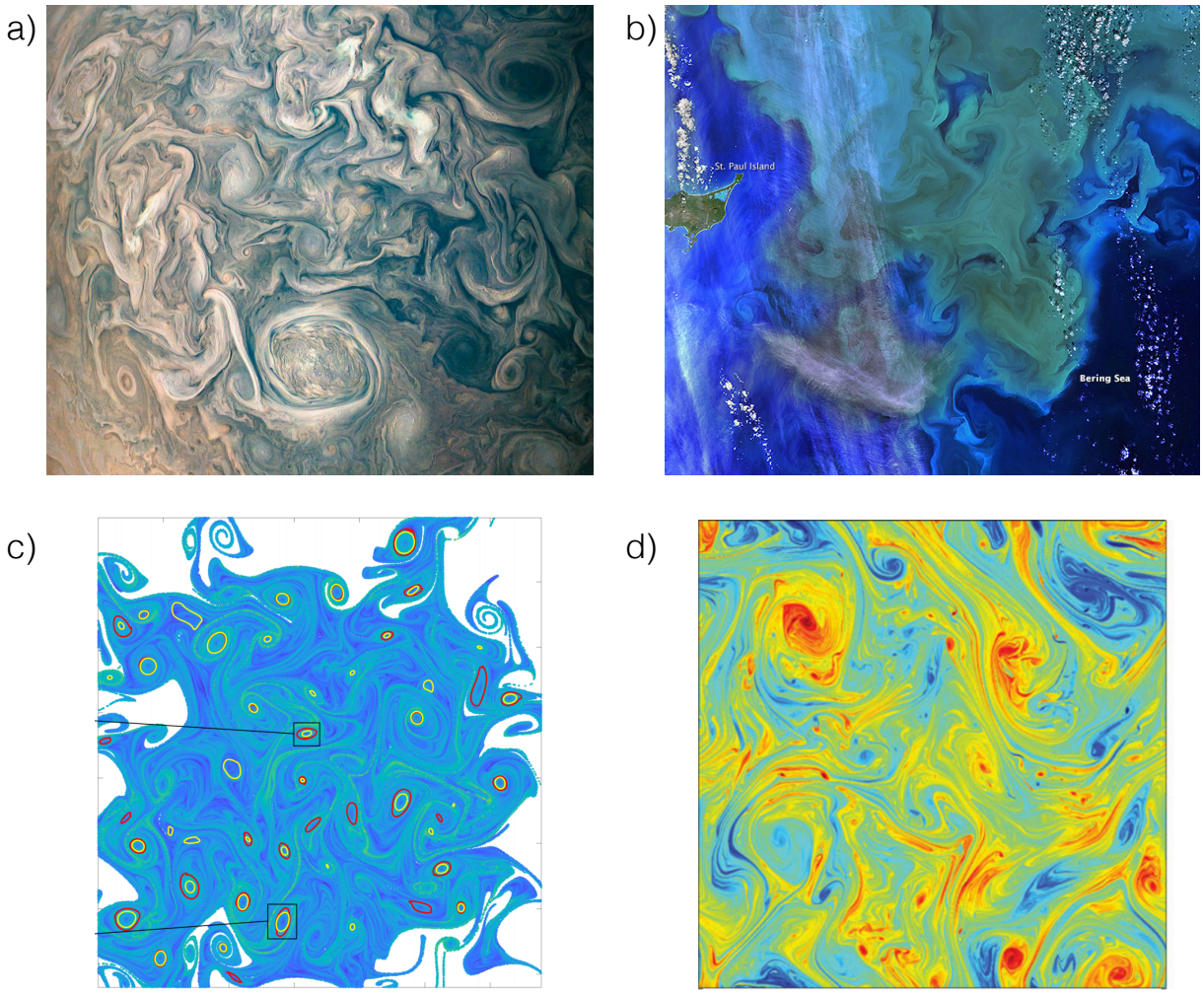

Figure 5.2: a) Turbulent gaseous flow of Jupiter's atmosphere in a portion of the northern hemisphere captured by the Juno spacecraft in May of 2018 [Image credit: NASA], b) Turbulent oceanic flow in the Bering Sea illuminated by a phytoplankton bloom captured by the Landsat 8 satellite in September of 2014 [Image credit: NASA Earth Observatory], c) Fig. 5 of Katsanoulis et al. (2020): a portion of the vorticity field of a 2D numerical model of turbulent flow, and d) Fig. 2b) of Bracco and McWilliams (2010): the instantaneous vorticity field of a 2D numerical model of homogeneous stationary turbulence.

McWilliams et al. (1994), Capet et al. (2008), Boffetta and Ecke (2012)]. Characterizations also include the existence of locally ordered (coherent) but globally disordered flow [Batchelor (1953), Prigogine and Stengers (1984), Herring and McWilliams (1989), Rubio et al. (2014)]. To provide a few visual examples of flows that contain obvious turbulent qualities, the chaotic atmospheric flow of Jupiter's northern hemisphere is shown in Fig. 5.2a), and oceanic flow illuminated by phytoplankton in Earth's Bering Sea is shown in Fig. 5.2b). Both of these

planetary surface flows have coherent, organized structures called vortices within broadly disorganized mixed flow. Furthermore, we clearly see coherent vortices amongst overall disordered flow in the 2D models shown in Fig. 5.2c) and d) [see caption for more details].

Guervilly et al. (2019) argue in their recent study that the turbulent length scale, l_{turb}, is observed in their simplified QG numerical models, which assume that axial vorticity is invariant along the rotation axis in order to reach Ekman numbers as low as $E = 5 \times 10^{-12}$. However, the radial velocities of the models displayed in Figure 2 of Guervilly et al. (2019), reproduced here as Figure 5.3, do not display structures occurring at multiple scales, or any cross-scale interactions characteristic of fluid turbulence. In fact, in Section 5.3 below, we show that their models exist below and very near to the onset of convection where turbulence has yet to develop. Specifically, Fig. 5.3 shows the radial velocities of a quarter of the spherical equatorial plane from the models of Guervilly et al. (2019) with: a) $E = 5 \times 10^{-9}$, b) $E = 5 \times 10^{-10}$, c) $E = 5 \times 10^{-11}$, and d) $E = 5 \times 10^{-12}$. Fig. 5.3e)–g) show the magnification of the boxed areas in d), where e) corresponds to the outermost box, radially, and g) corresponds to the innermost box, radially. It appears that the velocity structures are of the same scale in each of the images in Fig. 5.3e)–g). Thus, from Fig. 5.3, we argue that, qualitatively, the simulations conducted have yet to reach a turbulent state. If there is no turbulence, this begs the question as to how the measured length scales in the models of Guervilly et al. (2019) appear to agree with estimates using the turbulent scale, l_{turb}. We provide an answer to this question through our analysis and discussion of the results of a number of models in Sections 5.3 and 5.4.

Based on the results of Hawkins et al. (2020), we predict that the two length scales, l_{crit} and l_{turb}, will roughly scale equivalently in the models of Guervilly et al. (2019), indicating that they are non-separable in the parameter space investigated. We further argue that their models are not turbulent and comment on their conclusions regarding turbulent dynamics and the applicability of their models to core conditions. In Section 5.2, we provide details of the models from the publications of Soderlund et al. (2012), Guervilly et al. (2019), and Hawkins et al. (2020) analyzed in this study. We present our results in Section 5.3, which includes a look at linear onset theory, the details of which are provided in subsection 5.3.2.

Lastly, we elaborate on our findings in light of the characteristic length scales of planetary core convection and discuss our ongoing work on this topic in Section 5.4.

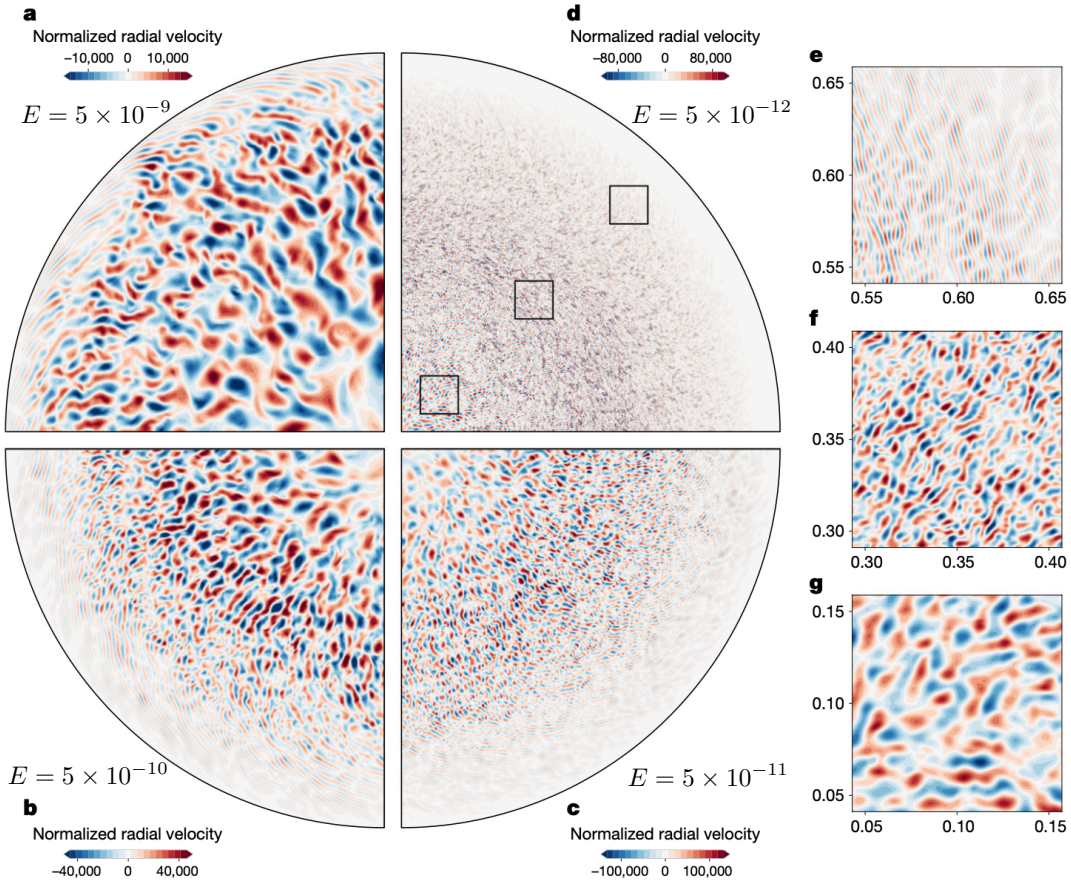

Figure 5.3: Figure 2 of Guervilly et al. (2019): The radial velocity of a quarter of the spherical equatorial plane of: a) 3D simulation with $E = 5 \times 10^{-9}$, b) QG simulation with $E = 5 \times 10^{-10}$, c) QG simulation with $E = 5 \times 10^{-11}$, and d) QG simulation with $E = 5 \times 10^{-12}$, their most extreme case. e)–g) show the magnification of the boxed areas of d), where e) corresponds to the outermost box, radially, and g) corresponds to the innermost box, radially. Radial velocities are normalized by the viscous velocity scale, ν/R, in the color scales, and the axes in e)–g) show Cartesian coordinates normalized by the sphere radius, R. For more model details, see Section 5.2, and the Supplementary Material of Guervilly et al. (2019).

5.2 Details of Models

We compare the results of Guervilly et al. (2019) with the numerical dynamo models of Soderlund et al. (2012) and the recent rotating convection laboratory experiments and direct numerical simulations (DNS) of Hawkins et al. (2020). The details of these three models

are given in order to appropriately compare them against one another. All of the models in Guervilly et al. (2019) are analyzed. There are three types of non-magnetic rotating convection models included in their study, the majority of which are a simplified QG model. The range of thermal forcing explored in the three model types is discussed in Section 5.3.1. A limited number of fully three-dimensional (3D) hydrodynamic rotating convection models by Kaplan et al. (2017) with Ekman numbers ranging from $5 \times 10^{-9} \leq E \leq 5 \times 10^{-7}$ are included and are argued to compare well with the results of the QG models. These models were conducted using the code XSHELLS, which simulates a full sphere under the presence of rotation in which convection is generated via internal heating. The thermal Prandtl number in their 3D models is small and is fixed at $Pr = 10^{-2}$.

The QG models in Guervilly et al. (2019) simulate a full sphere with internally heated convection. Instead of being 3D, it is assumed that rotation is sufficiently strong such that variations of the velocity along the axial direction are small compared with variations along the orthogonal directions. This simplification is often used in planetary core convection models [e.g. Busse (1970), Or and Busse (1987), Aubert et al. (2003), Gillet and Jones (2006), Calkins et al. (2012a)]. Pr is varied between $10^{-2} \leq Pr \leq 10^{-1}$ and E between $5 \times 10^{-12} \leq E \leq 5 \times 10^{-7}$ in the internally heated QG models that comprise the majority of the simulations in Guervilly et al. (2019). The third type of model included in their study is a modified form of their QG model in which heating occurs differentially with fixed temperature boundary conditions and an inner core of radius $R_i = 0.35$. These models were performed to test the dependence of results on the heating mode and the presence of an inner core, and no notable differences in results are reported.

The planetary dynamo simulations of Soderlund et al. (2012), with $E = 10^{-4}$ and $E = 10^{-5}$, are included in our analysis presented in Section 5.3. These models were conducted using the open source numerical code MagIC 3.38 [cf. Wicht (2002)]. The spherical shell geometry is defined by the ratio of the inner to outer shell radii as $\chi = R_i/R_o = 0.4$ (Earth's core-like), with no-slip, fixed temperature boundaries. The thermal Prandtl number in all simulations is fixed at $Pr = 1$. The Lorentz force is included in these dynamo models, and the magnetic Prandtl number, the ratio of viscous to magnetic diffusion, is fixed at

$Pm = \nu/\eta = 2$. The range of thermal forcing explored in these models is discussed in Section 5.3.1.

The last set of data analyzed in this work are the cylindrical non-magnetic laboratory experiments and cartesian DNS of Hawkins et al. (2020). The details of such models, where $Pr \simeq 6$ and $1.25 \times 10^{-7} \leq E \leq 3 \times 10^{-5}$, can be found in Chapter 4. The experiments possibly influenced by cylindrical boundary zonal flows are not included here.

Measured Reynolds numbers, Re, from each of the three studies are used to estimate the turbulent length scale for each simulation or experiment according to (2.46). The reported values of Re for the dynamo models of Soderlund et al. (2012) are calculated as $Re = \sqrt{2\varepsilon_K}$, where $\varepsilon_K \propto \vec{u} \cdot \vec{u}$ is the volume-averaged kinetic energy density of the system. In Guervilly et al. (2019), the characteristic velocity used to calculate Re is based on the root mean square (rms) of the radial velocity, $\vec{u} \cdot \hat{s}$, averaged in volume and time over at least ten convective turnover timescales. As described in Section 4.2 of Chapter 4, our laboratory Re values are obtained as the rms of the vertical convective velocity time series of a single point in the fluid bulk, $\vec{u} \cdot \hat{z}$, while our DNS Re values are computed as volume and time averages of the rms of the total system velocity. Note that Rossby numbers reported in this study are dependent upon the described Reynolds numbers as $Ro = ReE$.

5.3 Comparison of Length Scale Estimates

5.3.1 Ratio of Length Scales: The Braginsky Parameter

Based on the results of Hawkins et al. (2020) [cf. Fig. 4.11 of Chapter 4], we examine the ratio of the two hypothetical non-dimensional system length scales $l_{\text{turb}} \simeq Ro^{1/2}$ and $l_{\text{crit}} = 2.4E^{1/3}$ (with $l_{\text{crit}} = 2.4(E/Pr)^{1/3}$ for $Pr < 0.68$). The study of Guervilly et al. (2019) is the first to directly measure length scales at low E such that a best fit scaling of l_{turb} with an appropriate pre-factor is determined. They find $l_{\text{turb}} = 11Ro^{1/2}$ agrees well with their data for $E < 5 \times 10^{-10}$. We choose to examine the general scaling, $l_{\text{turb}} \simeq Ro^{1/2}$, and not use their pre-factor because their $11Ro^{1/2}$ finding appears to agree with their lowest E data

only, i.e. with their models that are the most laminar due to computational limitations. We further elaborate on their pre-factor of 11 and 1/2 slope in our discussion of the ongoing work in this study in Section 5.4.

We define the ratio between the two hypothesized characteristic length scales, l_{turb} and l_{crit}, relevant to core flows as:

$$Bg = \frac{l_{\text{turb}}}{l_{\text{crit}}} = \begin{cases} \frac{Ro^{1/2}}{2.4E^{1/3}}, & Pr > 0.68 \\ \frac{Ro^{1/2}}{2.4(E/Pr)^{1/3}}, & Pr \leq 0.68 \end{cases}, \tag{5.2}$$

which we refer to as the Braginsky parameter, Bg. We name this parameter after Stanislav I. Braginsky for his many contributions towards understanding turbulent planetary core flows [e.g. Braginsky (1965), Braginsky and Roberts (1987), Braginsky and Meytlis (1990)]. Our choice to include the 2.4 pre-factor in l_{crit} in the definition of Bg in (5.2) is somewhat arbitrary. We choose to include this pre-factor for l_{crit} and exclude any pre-factor for l_{turb} because the critical onset scale pre-factor is derived from plane layer theory, while there is no theory beyond scaling analysis for l_{turb}. By examining this ratio of hypothesized length scales, the direct measurement of length scales is not involved. Rather, Bg is dependent upon the Ekman number, E (namely the rotation period of the system), the Rossby number, $Ro = ReE$ (directly proportional to the non-dimensional velocity of the system), and the Prandtl number, Pr, when $Pr < 0.68$.

Figure 5.4 displays the Braginsky parameter versus measured Rossby number for: 1) the dynamo models of Soderlund et al. (2012) as open circles, 2) the 3D and QG models of Guervilly et al. (2019) as open upside down triangles when $Pr = 10^{-2}$ and as open triangles when $Pr = 10^{-1}$, and 3) the laboratory experiments and DNS of Hawkins et al. (2020) as filled and open squares, respectively. Color denotes the Ekman number of each model as indicated by the color bar. Nearly seven orders of magnitude are spanned in Ro on the x-axis. Interestingly, the results of all models do not vary by even a full order of magnitude in Bg and are clustered around $Bg \simeq 10^0$, indicating that the onset and turbulent length scales in each model are not scale separable [cf. Dormy and Gérard-Varet (2008), Favier et al. (2014), Calkins et al. (2015), Moffatt and Dormy (2019)].

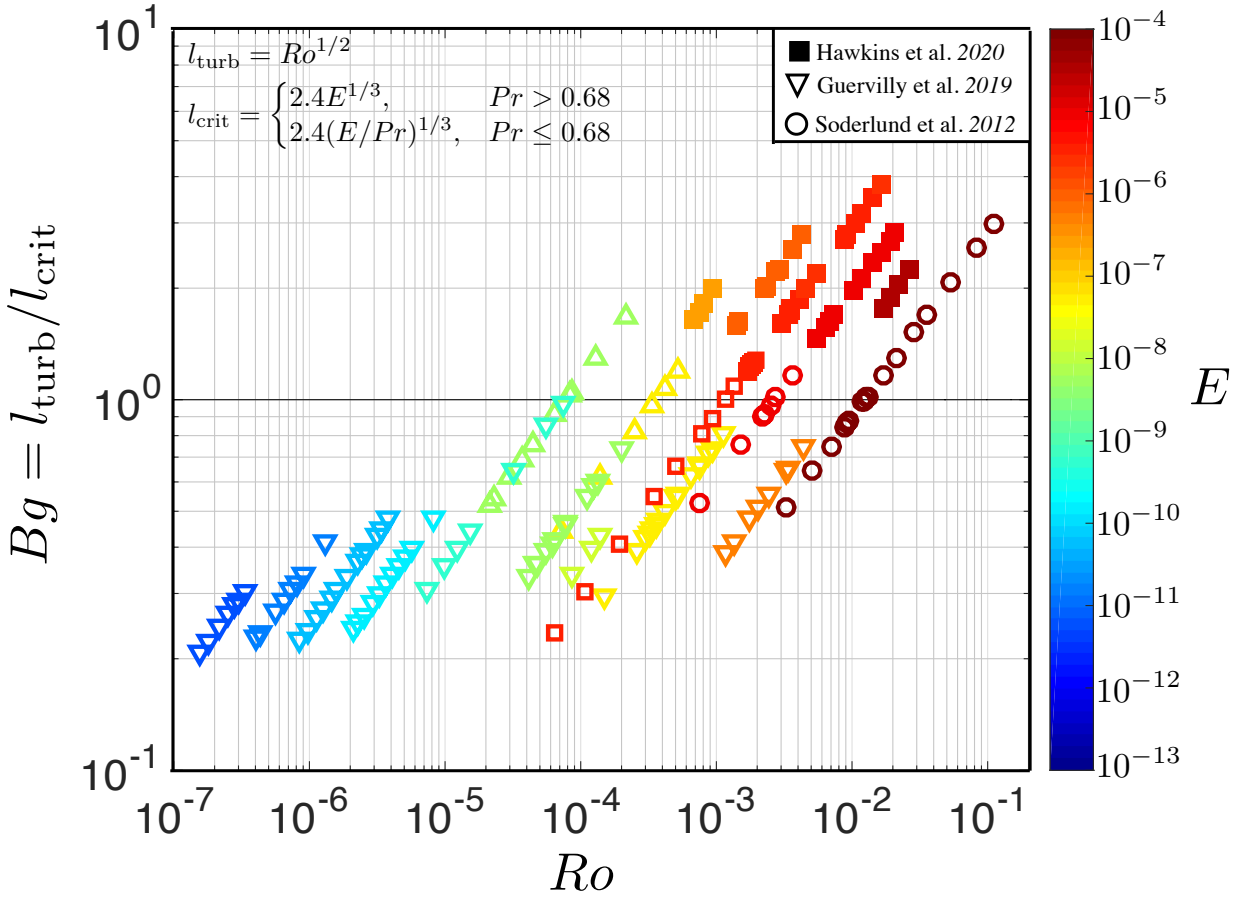

Figure 5.4: The Braginsky parameter, Bg according to (5.2), versus measured Rossby number for: 1) the dynamo models of Soderlund et al. (2012) as open circles, 2) the 3D and QG models of Guervilly et al. (2019) as open upside down triangles when $Pr = 10^{-2}$ and as open triangles when $Pr = 10^{-1}$, 3) and the experiments/DNS of Hawkins et al. (2020) as filled/open squares, respectively. Color denotes the Ekman number of each model as indicated by the color bar.

Figure 5.5 displays Bg versus convective supercriticality, Ra/Ra_C, for all of the models plotted in Fig. 5.4. Symbol shape and color is consistent with that of Fig. 5.4, and the vertical dashed line indicates the predicted onset of steady convection at $Ra/Ra_C = 1$. The supercriticality definition used for each model comes from the manner in which they are defined within each of the three respective publications. Specifically, Soderlund et al. (2012) use the critical Rayleigh number description from King et al. (2010), $Ra_C = 3.5E^{-4/3}$. We note that this is not the most accurate description of the true value of Ra_C for the initiation of steady convection in a spherical shell [e.g. Carrigan and Busse (1983), Jones et al. (2000), Dormy et al. (2004), Vidal and Schaeffer (2015)], but we use this value nonetheless for consistency with their publication. The critical Rayleigh numbers for the 3D and QG models

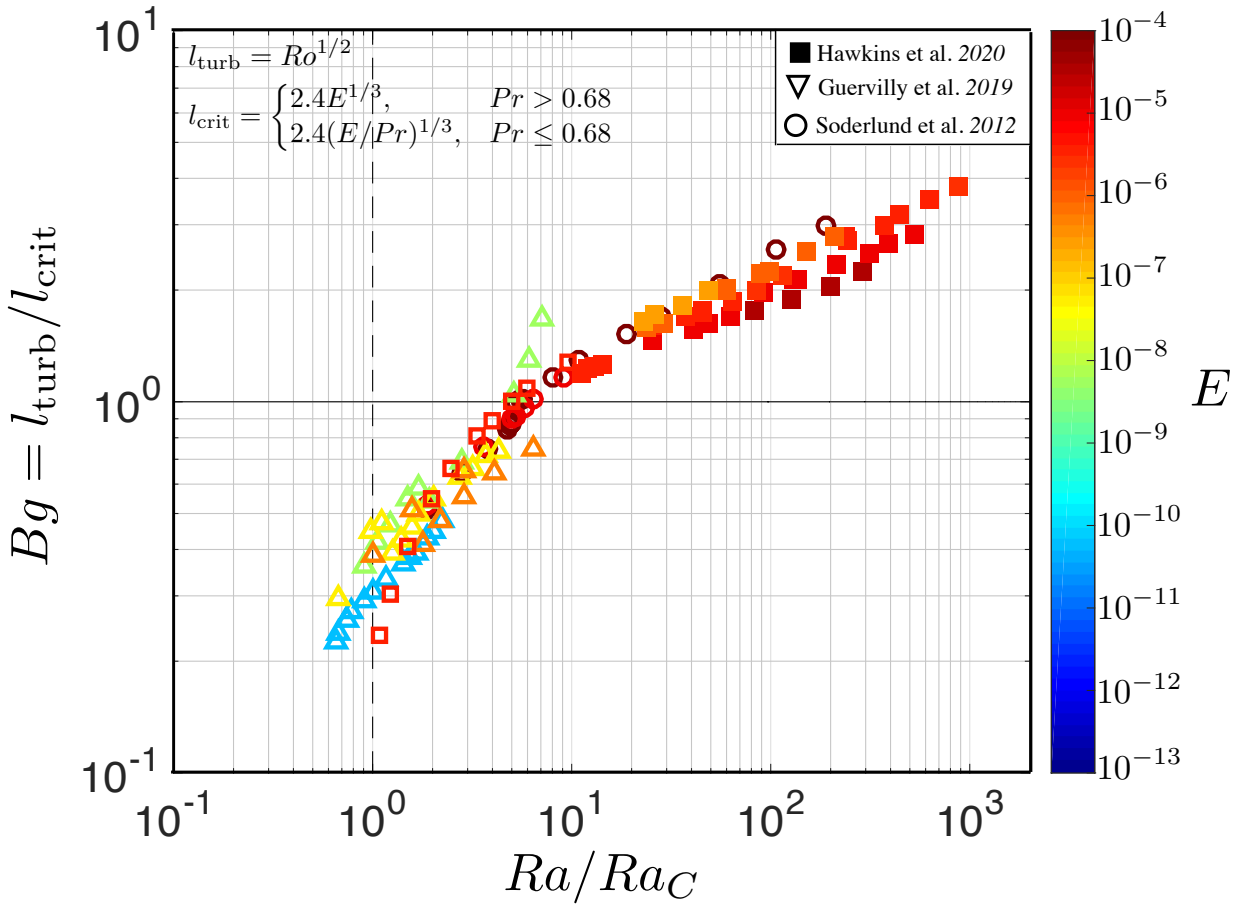

Figure 5.5: Bg vs. supercriticality, Ra/Ra_C. Symbol shape and color is consistent with that of Fig. 5.4, and the vertical dashed line indicates the onset of steady convection at $Ra/Ra_C = 1$. On the x-axis, Ra values of Soderlund et al. (2012) (circles) are normalized by $Ra_C = 3.5E^{-4/3}$ [King et al. (2010)], Ra of Guervilly et al. (2019) (triangles) are normalized by available Ra_C values obtained via private communication with C. Guervilly, and Ra of the experiments and DNS of Hawkins et al. (2020) (squares) are normalized by $Ra_C^S = 8.7E^{-4/3}$ given by (2.22).

of Guervilly et al. (2019) were only available for some of their models and were obtained via private communication with C. Guervilly. The SINGE numerical eigensolver developed by Vidal and Schaeffer (2015) was used to calculate available values of Ra_C for their models. Lastly, equation (2.22), the plane layer estimate of Ra_C^S, is used for the cartesian DNS and cylindrical experiments in Hawkins et al. (2020).

It appears there are two differing behavioral trends for all of the data plotted in Fig. 5.5, separated at a supercriticality of $Ra/Ra_C \sim 10$. A steeper trend exists for low values of Ra/Ra_C, with Bg values transitioning to a shallower trend for high supercriticalities near $Ra/Ra_C \sim 10$. The dynamo models of Soderlund et al. (2012) (open circles) plot very well

behind the data of both Guervilly et al. (2019) at low supercriticalities and Hawkins et al. (2020) at high supercriticalities despite the differences between all of these models. Crucially, we note that the QG and 3D cases of Guervilly et al. (2019) all occur near to the onset of convection, below $Ra/Ra_C \sim 10$. Particularly, the most extreme cases with the lowest E values (blue) are subcritical and fall below the dashed line line occurring at $Ra/Ra_C = 1$. These low Ra/Ra_C values for the available data of Guervilly et al. (2019) further support our contention that their models are not turbulent.

5.3.2 Linear Convective Onset Theory

We consider the classical linear stability analysis of plane layer rotating convection by Chandrasekhar (1961) in an attempt to further understand the Bg behaviors as a function of supercriticality displayed in Fig. 5.5. This linear theory predicts that convective onset is strongly suppressed in the presence of rotation. If flows are weakly non-linear, it is possible that the length scales of such flows are marginally unstable. According to equation 3.127 in Chandrasekhar (1961), the dispersion relation for steady convection in an infinite plane layer with vertical depth H and isothermal, mechanically stress-free boundaries is given in terms of the Rayleigh number as:

$$Ra = \frac{1}{k^2}\left[(\pi^2 + k^2)^3 + \frac{\pi^2}{E^2}\right], \tag{5.3}$$

where $k = \pi/l$ is the wavenumber and $l = \mathcal{L}/H$ is the non-dimensional length of a given flow structure and is taken to be half of a wavelength [cf. Aurnou and King (2017)].

The Ra–k marginal stability curves are displayed in Fig. 5.6a) for rotating convection at three Ekman numbers in a core-like liquid metal with $Pr = 0.025$. The stability curves at fixed values of $E = 10^{-9}$, $E = 10^{-15}$, and $E = 10^{-21}$, are plotted as blue, green, and purple thick lines, respectively. Each fixed E curve displays the lowest Ra value for which steady convection will occur for a given value of the wavenumber k. The marginal stability curves have a U-shape with a single global minimum Ra value as a function of k. This minimum in each curve is demarcated by a solid square and marks the critical Rayleigh number, Ra_C^S.

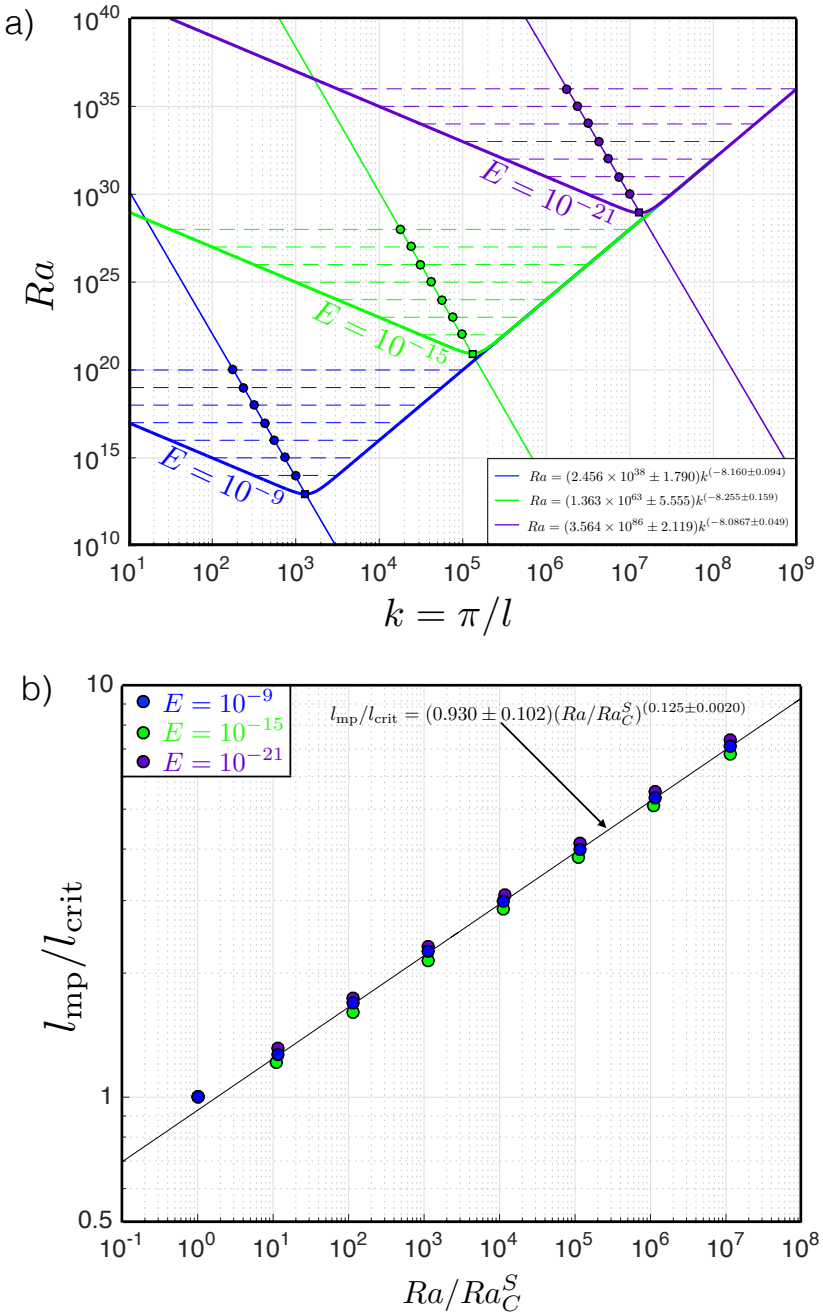

Figure 5.6: a) Ra–k marginal stability curves (thick colored lines) according to (3.127) of Chandrasekhar (1961) for steady rotating convection with $Pr = 0.025$ and $E = 10^{-9}$ (blue), $E = 10^{-15}$ (green), $E = 10^{-21}$ (purple). Colored solid squares denote the single global minimum value of Ra for each of the three E curves. Solid colored circles are the calculated midpoint values for 7 values of Ra in which $Ra > Ra_C^S$ for each of the three E curves. Horizontal colored dashed lines highlight the value of Ra that each midpoint corresponds to. b) The midpoint data of a) collapsed in $(l_{\mathrm{mp}}/l_{\mathrm{crit}})$–$(Ra/Ra_C^S)$ normalized space, with a best fit line given as $l_{\mathrm{mp}}/l_{\mathrm{crit}} = (0.930 \pm 0.102)(Ra/Ra_C^S)^{(0.125 \pm 0.0020)}$. The overlapping three E points at onset, where $Ra/Ra_C^S = 1$ and $(l_{\mathrm{mp}}/l_{\mathrm{crit}}) = 1$, are not included in this best fit line to the data.

The corresponding value on the x-axis, k_{crit}, sets the critical length scale at which convective onset will occur.

We purport that the typical wavenumber for a given $Ra > Ra_C^S$ in any of the curves shown in Fig. 5.6a) can be estimated by the midpoint between the curve. Furthermore, the marginal stability curves shown in Fig. 5.6a) are not symmetric about their minimum (k_{crit},Ra_C^S) point. In fact, the midpoint of any spot along a given curve for $Ra > Ra_C^S$ trends towards lower wavenumbers (and therefore larger length scales) with increasing Ra. To explore this asymmetry, we calculate the midpoint of the curve for 7 values of Ra in which $Ra > Ra_C^S$ for each of the three E curves. These points are displayed in Fig. 5.6a) as solid circles with horizontal dashed lines to highlight the value of Ra that each point corresponds to. For each set of calculated midpoints at the three fixed E values, we best fit the data, including the respective square onset point. The best fit line to the blue $E = 10^{-9}$ points is given as $Ra = (2.456 \times 10^{38} \pm 1.790)k^{(-8.160\pm0.094)}$, the best fit green $E = 10^{-15}$ line is $Ra = (1.363 \times 10^{63} \pm 5.555)k^{(-8.255\pm0.159)}$, and the purple $E = 10^{-21}$ line is given as $Ra = (3.564 \times 10^{86} \pm 2.119)k^{(-8.087\pm0.049)}$. Thus, a $\sim$-8 slope exists between Ra and k according to the exponents of these best fits that result from the analysis of RC marginal stability curves.

In Figure 5.6b), we collapse the best fit lines in Fig. 5.6a) as a single fit in $(l_{\text{mp}}/l_{\text{crit}})$–$(Ra/Ra_C^S)$ normalized space, where $l_{\text{mp}} = \pi/k_{\text{mp}}$ is the midpoint length scale and l_{crit} is the onset length scale given by (2.23). The best fit line is given as $l_{\text{mp}}/l_{\text{crit}} = (0.930 \pm 0.102)(Ra/Ra_C^S)^{(0.125\pm0.0020)}$. The overlapping three E points right at onset, where $Ra/Ra_C^S = 1$ and $(l_{\text{mp}}/l_{\text{crit}}) = 1$, are not included in this best fit line to the data. Thus, theory predicts that a 1/8 slope exists between the ratio of the length scale midpoint for which steady convection occurs for a given Ra relative to the steady onset length scale and the supercriticality of any plane layer steady RC model. In subsection 5.3.3 below, we test this best fit theoretical line to see if linear convective onset theory explains any of the observed behaviors of the models displayed in Fig. 5.5.

5.3.3 Reexamination of Length Scale Ratios

We re-plot the results of Fig. 5.5 in Figure 5.7, now with several best fit lines. The solid line is the fit of convective onset theory discussed in subsection 5.3.2 with a 1/8 slope, $l_{\rm mp}/l_{\rm crit} = 0.930(Ra/Ra_C)^{0.125}$, shown in Fig. 5.6b). The dashed line in Fig. 5.7 is a fit to all data above $Ra/Ra_C > 10$, $Bg = 0.763(Ra/Ra_C)^{0.220}$, primarily containing the laboratory data of Hawkins et al. (2020) but also the dynamo models of Soderlund et al. (2012). The dashed-dotted line is the best fit to all data below $Ra/Ra_C \leq 10$, including dynamo data from Soderlund et al. (2012) and the available data from Guervilly et al. (2019), minus the lime green triangles of Guervilly et al. (2019) (QG, $Pr = 0.1$, $E = 5 \times 10^{-9}$) that have the highest supercriticalities of their available data and visibly deviate from all other data. We further comment about the behavior of the lime green triangle data of Guervilly et al. (2019) in Section 5.4 below. The fit line is given as $Bg = 0.344(Ra/Ra_C)^{0.573}$. Thus, we see that onset theory does not appear to explain either of the obvious two behavioral trends of Fig. 5.5. Instead, it appears that for models near onset (i.e. below $Ra/Ra_C \leq 10$), there is a nearly 1/2 slope relationship between Bg and supercriticality, while data at higher supercriticalities out to $Ra/Ra_C = 10^3$ behave with a nearly 1/4 slope relationship between Bg and Ra/Ra_C. The fit from onset theory with the 1/8 slope appears to act as a lower bound for the $Ra > Ra_C$ data.

5.4 Discussion

A meta-analysis of length scales in models simulating planetary core convection is conducted in order to further understand the characteristic length scales of core-style flows. This work is largely motivated by the recent findings of Guervilly et al. (2019) in which it is argued that measured length scales of low E QG models agree with the hypothesized turbulent length scale thought to be relevant to dynamo generating flows. Simultaneously, Hawkins et al. (2020) show that this turbulent length scale actually scales equivalently to the steady convective onset scale when the local Reynolds number in the geostrophic fluid bulk is of

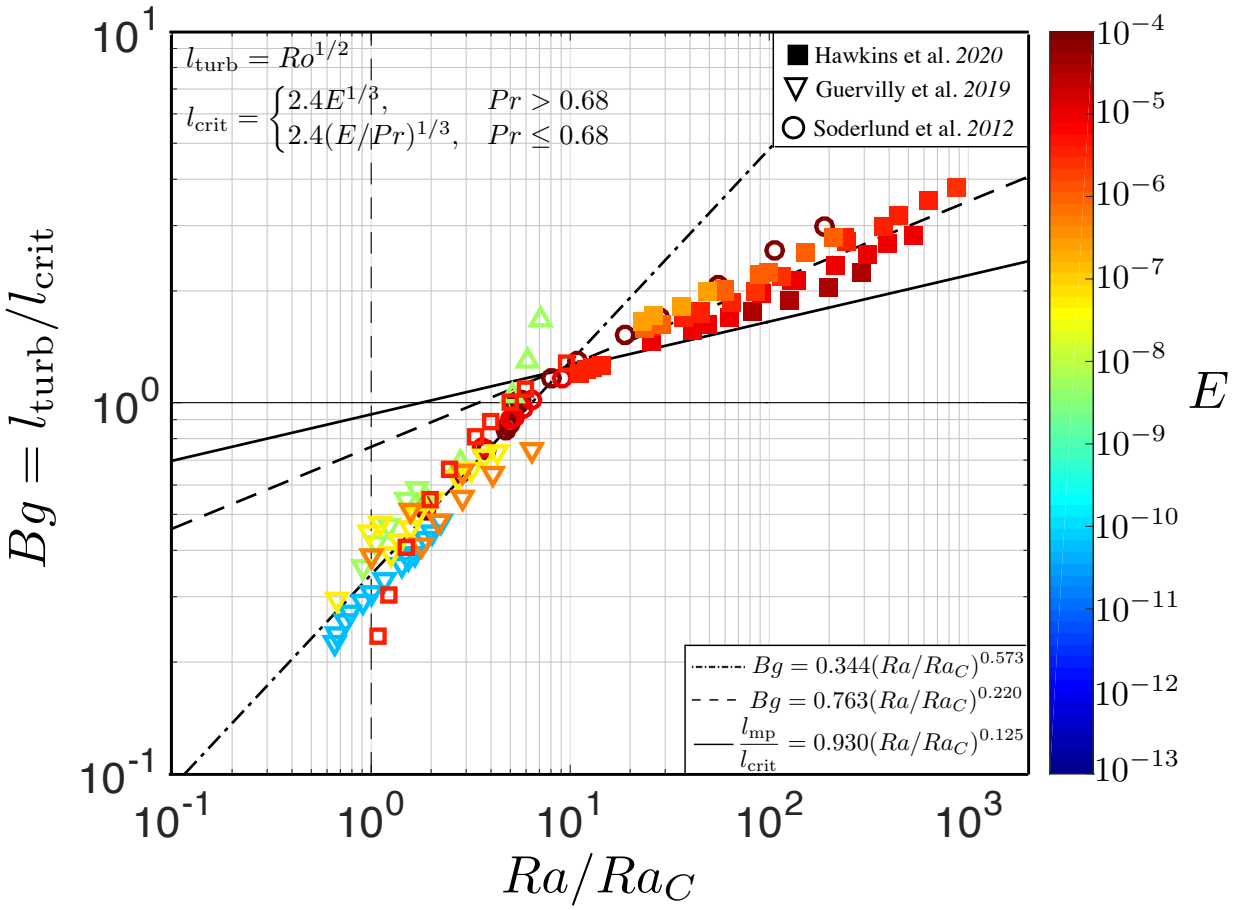

Figure 5.7: Fig. 5.5 reproduced, now with several best fit lines. The solid line is the fit of linear theory shown in Fig. 5.6b), $l_{\rm mp}/l_{\rm crit} = 0.930(Ra/Ra_C)^{0.125}$. The dashed line is a fit to data above $Ra/Ra_C > 10$, $Bg = 0.763(Ra/Ra_C)^{0.220}$. The dashed-dotted line is a fit to data below $Ra/Ra_C \leq 10$ (excluding the deviatory lime green triangle data) and is given as $Bg = 0.344(Ra/Ra_C)^{0.573}$.

order unity. Indeed, Fig. 5.4 shows, via examination of the Braginsky parameter, or the ratio of turbulent to onset scales, that these two scales are comparable such that $Ro^{1/2} \simeq E^{1/3}$ in the models of core convection analyzed.

Further, the Braginsky ratio is examined relative to the convective supercriticality of models in Fig. 5.5. Interestingly, two distinct behavioral trends exist. Near to the onset of convection, i.e. $Ra/Ra_C \leq 10$, a steep relationship between Bg and Ra/Ra_C exists, while a shallower trend between Bg and Ra/Ra_C is found when $Ra/Ra_C > 10$. Linear convective onset theory appears to act as a lower bound to the behavior above $Ra/Ra_C > 10$. We find that $Bg = 0.344(Ra/Ra_C)^{0.573}$ when $Ra/Ra_C \leq 10$, and $Bg = 0.763(Ra/Ra_C)^{0.220}$ when $Ra/Ra_C > 10$. Thus, the steeper sloping relationship near onset has an exponent near

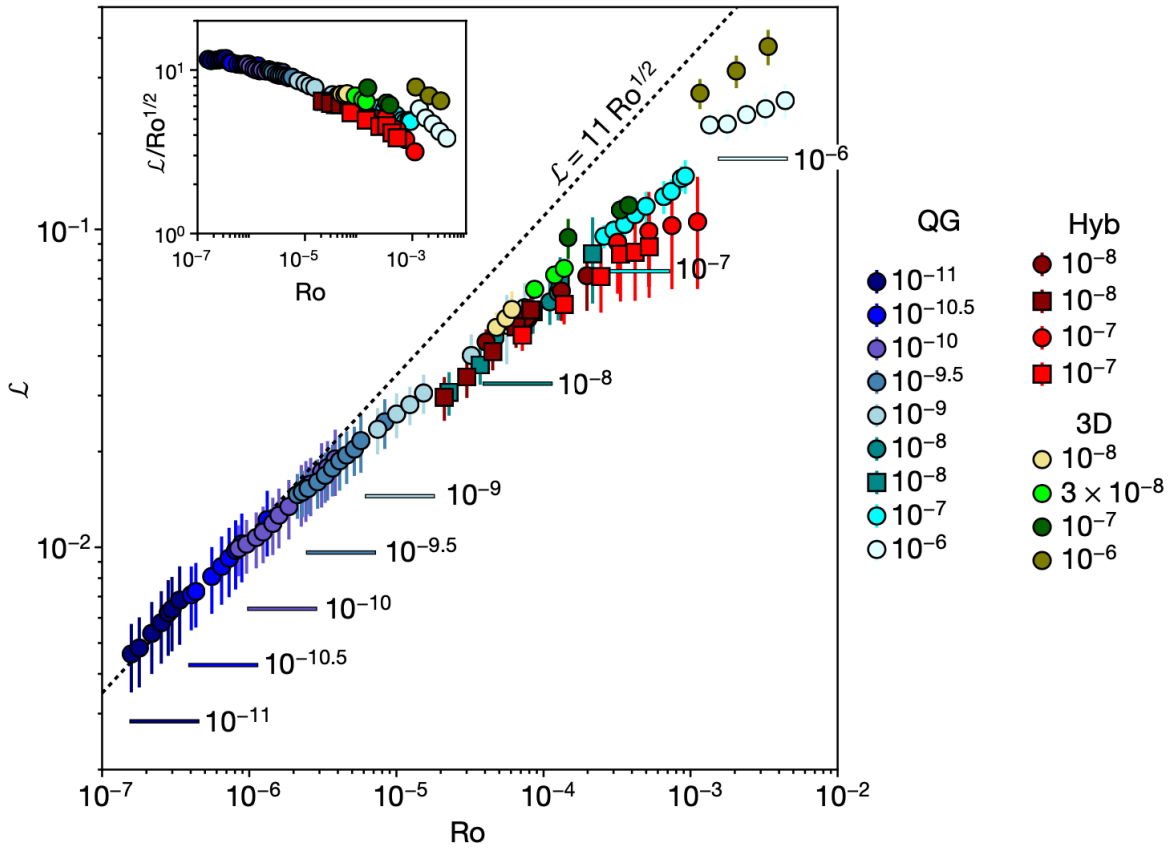

Figure 5.8: Figure 4b) of Guervilly et al. (2019): Measured length scale, $\mathcal{L}$, vs. measured Ro, where $\mathcal{L}$ is radially averaged between $0.1R$ to $0.6R$. The squares in the key on the right denote $Pr = 10^{-1}$, circles denote $Pr = 10^{-2}$. The inset in the top left corner shows measured $\mathcal{L}$ normalized by the turbulent scale, $l_{\mathrm{turb}} \simeq Ro^{1/2}$, with no pre-factor. According to Guervilly et al. (2019), the horizontal lines show the hypothetical value of the onset length scale, $l_{\mathrm{crit}} \simeq E^{1/3}$.

to 1/2, while the shallower relationship between Bg and supercriticality existing for high supercriticalities out to $Ra/Ra_C \simeq 10^3$ has a slope of nearly 1/4.

Current work is underway to elucidate the physics that underlies these relationships. Though only a few points of data, the lime green triangle data of Guervilly et al. (2019) shown in Fig. 5.7 indicate that it is possible the models of Guervilly et al. (2019) might continue to track along the ∼1/2 slope best fit line. If this is to be the case, we surmise that laboratory models must thus exist in a regime that differs from the models of Guervilly et al. (2019). An outstanding question then remains as two how these results might meaningfully extrapolate to planetary conditions. We comment that it would be interesting to continue equivalent numerical models (i.e. moderately low E) to the lime green triangle data at even

stronger supercriticalities, despite computational expense. Alternatively, fully non-linear turbulent low E RC experiments (e.g. at $E \leq 10^{-9}$) are also likely to give a more complete answer to this outstanding question.

Figure 5.8 is the reproduction Figure 4b) in Guervilly et al. (2019) in which measured length scales are displayed as a function of measured Rossby numbers for all of the models in their study. The length scales, $\mathcal{L}$, for each simulation are computed as the radial average between $0.1R$ to $0.6R$. We focus here on the inset in the top left corner of this figure, where measured $\mathcal{L}$ values are normalized by respective theorized turbulent scales, $l_{\text{turb}} \simeq Ro^{1/2}$, with no pre-factor as stated in their paper. Only the darkest blue points all the way on the left seem to be compensated as plotted. In fact, we observe a smooth, concave downward curve with increasing Ro. The next step we plan to take with this work is to create a polynomial or nonlinear fit to this data to produce a best fit with a pre-factor that is a function of Ro. We will then apply this fit to the Braginsky parameter, i.e. instead of examining $Ro^{1/2}/2.4E^{1/3}$, we will examine this fitted scaling, dependent on Ro, relative to the onset scale for all models. We hypothesize that this method might better collapse the data shown in Fig. 5.7.

We conclude by extending our current findings to Earth's core conditions. All evidence from models of planetary core convection to date indicates that $Ro^{1/2} \simeq E^{1/3}$ in planetary dynamo systems. We use the scalings between the Braginsky parameter and supercriticality in Fig. 5.7 to estimate hypothetical length scales in Earth's core. Simplifying the three scalings found in this study as $Bg = (Ra/Ra_C)^{1/8}$, $Bg = (Ra/Ra_C)^{1/4}$, and $Bg = (Ra/Ra_C)^{1/4}$, we display in Fig. 5.9 estimates of the characteristic length scales of flows in Earth's core. Specifically, by multiplying each of the Bg scalings by $l_{\text{crit}} = 2.4E^{1/3}H$, where $E = 10^{-15}$ and $H = 2,200$ km in Earth's outer core, we obtain a range of characteristic length scales possibly existing in Earth's core.

We estimate $Ra/Ra_C \sim \mathcal{O}(10^3)$ in Earth's core using the asymptotic thermal wind scaling of Ro in Aurnou et al. (2020), $Ro = Ro_{\text{ff}}^2 = RaE^2/Pr$, to obtain an estimate of Ra. Assuming $Ro \simeq 10^{-6}$ and $Pr \simeq \mathcal{O}(1)$ in Earth's core, we obtain $Ra \simeq 10^{24}$ and thus $Ra/Ra_C \simeq 10^3$. If true, the scalings of this study therefore suggest that a range of core length scales between

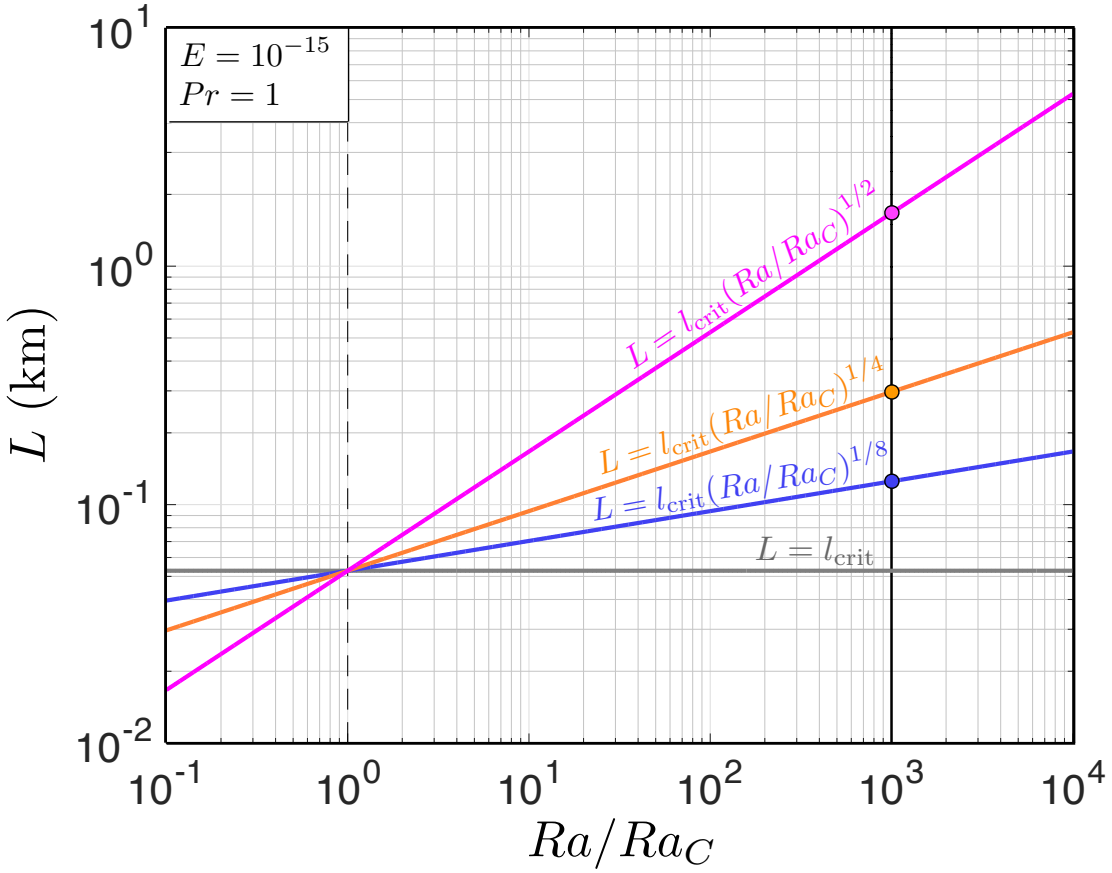

Figure 5.9: Regime diagram of estimated dimensional L in km vs. Ra/Ra_C for Earth's outer core ($E = 10^{-15}$, $Pr = 1$). The scalings found in this study are plotted as: $Bg = (Ra/Ra_C)^{1/8}$ (blue), $Bg = (Ra/Ra_C)^{1/4}$ (orange), and $Bg = (Ra/Ra_C)^{1/2}$ (pink), where $l_{\mathrm{crit}} = 2.4E^{1/3}H$ and is shown in grey. Circle colored symbols denote the length scale estimates from the three scalings for the supercriticality estimated in Earth's core, $Ra/Ra_C \simeq 10^3$ (black line) [see text for details].

$\mathcal{O}(10^{-1})$ km to $\mathcal{O}(10^{0})$ km could exist. With no pre-factors in these scalings, this variation is roughly one order of magnitude, or non scale-separable mathematically [cf. Dormy and Gérard-Varet (2008), Moffatt and Dormy (2019)]. Future work to determine realistic pre-factors to these scalings will further illuminate the accuracy of these estimates for Earth's core and other planetary dynamo systems.

CHAPTER 6

The Effects of Centrifugal Buoyancy on Rotating Convection in Water and in Liquid Metal

6.1 Motivation

A number of extreme laboratory experiments have been constructed worldwide to date in order to investigate the properties of rapidly rotating convective turbulence thought to control large scale planetary dynamo generation processes [cf. Cheng et al. (2018)]. The large diameters and heights of such devices gives rise to an external force on a rotating Rayleigh-Bénard convection (RC) system that is considered negligible in planetary dynamo systems: centrifugal buoyancy. Similarly to gravitational buoyancy, centrifugal buoyancy initiates convective motions. Rather than drive vertical motions aligned with the rotation axis in RC, centrifugal buoyancy drives colder, denser fluid radially outward away from the axis of rotation while warmer, less dense fluid simultaneously moves radially inward towards the rotation axis [Barcilon and Pedlosky (1967), Hart (2000)]. Thus, the horizontal symmetry of fluid motions in RC is broken as centrifugal buoyancy begins to affect vertical bulk convective motions driven by gravitational acceleration, the details of which are not well studied at present [Homsy and Hudson (1967), Hu et al. (1997), Hart and Ohlsen (1999)].

Planets and other astrophysical bodies are centrifugally deformed systems, i.e. the equipotential surfaces of these rotating bodies incorporate both gravitational and centrifugal acceleration. As such, direct numerical and asymptotically reduced models incorporate density variations in the gravitational buoyancy term and not in the centrifugal buoyancy term of the relevant governing equations of motion [Marques et al. (2007)]. Only a very limited number of direct models that incorporate centrifugal buoyancy in a RC system

exist, all of which focus on properties near the onset of convection [Torrest and Hudson (1974), Lopez et al. (2006), Becker et al. (2006) Lopez and Marques (2009), Curbelo et al. (2014)]. Using the results of these limited studies, present extreme laboratory studies restrict experiments to remain within an arguably arbitrary range (often characterized below $Fr =$ centrifugal buoyancy/gravitational buoyancy $\lesssim 0.1$) in which it is believed that centrifugal acceleration will safely not affect vertical convective dynamics relevant to planetary systems [e.g. Koschmieder (1967), Kunnen et al. (2010), Weiss and Ahlers (2011), Cheng et al. (2015), Cheng et al. (2018)]. However, previous studies do not account for the characterization of the effect of centrifugation in the presence of turbulence (i.e. far past convective onset), of varied fluid properties (i.e. Pr), or of varied container geometries (i.e. aspect ratio values, Γ).

Thus, we present the first set of laboratory experiments designed specifically to better characterize the properties and occurrence of centrifugally dominated convection in RC in the presence of turbulence with varied Prandtl numbers, Pr, and varied aspect ratios, Γ. This laboratory study is the first to test the recent numerical results of Horn and Aurnou (2018) and Horn and Aurnou (2019), which, if verified in a laboratory setting, have important implications for the use of such extreme devices in the study of core-style rotating turbulence. In the subsection below, we summarize the theory described in Horn and Aurnou (2018) pertinent to this study. In Section 6.2, we describe the configuration of the two laboratory devices used in this study. In Section 6.3, we discuss our present findings, and in Section 6.4, we discuss our present conclusions and the future work of this study.

6.1.1 A Further Look Into System Parameters: RC with the Inclusion of Centrifugal Buoyancy

As introduced in Section 2.2, the ratio of the strength of centrifugal buoyancy relative to that of gravitational buoyancy in RC is characterized by the rotational Froude number, Fr (see (2.17)). This system parameter, which inherently depends on the rotation of the system as well as the radius of the confining container, will naturally be of importance

in characterizing the effect of centrifugal acceleration on vertical convective dynamics that are driven by gravitational acceleration in our system of study. In order to accurately determine the effect of centrifugation in RC, Horn and Aurnou (2018) present a number of arguments that are based upon three relevant system timescales: a Coriolis timescale (τ_Ω), a gravitational buoyancy (free-fall) timescale (τ_{ff}), and a centrifugal buoyancy timescale (τ_{cb}), defined respectively as:

$$\tau_\Omega = \frac{1}{2\Omega},\ \tau_{\text{ff}} = \frac{H}{\sqrt{\alpha g \Delta T H}},\ \tau_{\text{cb}} = \frac{R}{\sqrt{\alpha \Delta T \Omega^2 R^2}}, \tag{6.1}$$

where the dimensional system parameters are described in Chapter 2, i.e. Ω $[rad/s]$, H $[m]$, R $[m]$ is the rotation rate, height, and radius of the confining container, respectively, g $[m/s^2]$ is gravitational acceleration, α $[1/K]$ is the thermal expansivity of the fluid, and ΔT $[K]$ is the temperature difference across the fluid layer.

As defined in Section 2.2, the gravitational based thermal Rossby number, Ro_{ff}, describes the ratio of the Coriolis timescale relative to that of the gravitational buoyancy timescale such that:

$$Ro_{\text{ff}} = \frac{\tau_\Omega}{\tau_{\text{ff}}} = \frac{\sqrt{\alpha g \Delta T H}}{2\Omega H} = \sqrt{\frac{RaE^2}{Pr}}. \tag{6.2}$$

Thus, we see that this parameter describing the strength of the gravitational buoyancy in the system relative to the Coriolis force can be expressed in terms of three control parameters: Ra, E, and Pr (see (2.4), (2.16), and (2.5)). Similarly, a centrifugal based thermal Rossby number, Ro_{cb}, can be defined to describe the ratio of the Coriolis timescale relative to that of the centrifugal buoyancy timescale such that:

$$Ro_{\text{cb}} = \frac{\tau_\Omega}{\tau_{\text{cb}}} = \frac{\sqrt{\alpha \Delta T}}{2} = \sqrt{\frac{2RaE^2Fr}{Pr\Gamma}}. \tag{6.3}$$

Thus, we see that this parameter describing the strength of the centrifugal buoyancy in the system relative to the Coriolis force can be expressed in terms of the same three control parameters (Ra, E, Pr) as Ro_{ff} but with a dependence on two additional control parameters: Fr and Γ. Close inspection therefore reveals that these two thermal Rossby parameters relate

to one another as the following:

$$Ro_{\mathrm{cb}} = Ro_{\mathrm{ff}}\sqrt{\frac{2Fr}{\Gamma}}. \tag{6.4}$$

Note that the ratio of the two buoyant timescales, $\tau_{\mathrm{ff}}/\tau_{\mathrm{cb}}$, yields the Froude number itself. Thus, one might hypothesize that the parameters Ro_{ff}, Ro_{cb}, and Fr should be examined in order to characterize the relevant system dynamics.

Horn and Aurnou (2018) further exert the involvement of these three system parameters by predicting transitions for which each involved timescale may become important and/or dominant in their RC water system. Using the findings of a RC water study by King et al. (2012), they predict that the transition from 'non-rotating' style 3D convection to rotationally constrained QG convection (sans centrifugation) occurs between:

$$6 \lesssim Ro_{\mathrm{ff}}^{3/2} Ra^{1/4} Pr^{3/4} \lesssim 20. \tag{6.5}$$

Similarly, Horn and Aurnou (2018) also use this prediction, (6.5), based on the likeness between the two thermal Rossby numbers of (6.2) and (6.3), to hypothesize that a transition from 'non-rotating' style convection to centrifugally constrained convection (sans Coriolis) occurs between:

$$6 \lesssim Ro_{\mathrm{cb}}^{3/2} Ra^{1/4} Pr^{3/4} \lesssim 20, \tag{6.6}$$

where Ro_{cb} can be expressed in terms of Ro_{ff} as given in (6.4). Horn and Aurnou (2018) call this centrifugally dominated regime in which centrifugal buoyancy balances a pressure gradient force to leading order a quasi-cyclostrophic (QC) regime, as opposed to a QG regime in which the Coriolis force balances a pressure gradient force at leading order. Lastly, they predict that the transition to a Coriolis-Centrifugally (CC) dominated system in which centrifugal buoyancy begins to significantly affect a QG system or the Coriolis force begins to affect a QC system should occur at the intersection between Ro_{ff} and Ro_{cb}. Thus, equating

these two parameters in (6.4) yields:

$$Ro_{\text{ff}} \simeq Ro_{\text{cb}} \longleftrightarrow Fr \simeq \Gamma/2. \tag{6.7}$$

The CC regime is also described as a regime in which a gradient wind balance occurs [Willoughby (1990)]. Despite seeming non-intuitive, according to (6.7), centrifugal buoyancy effects are most easily excited in low aspect ratio containers.

In order to test these prediction arguments, Horn and Aurnou (2018) conduct 160 direct numerical simulations (DNS) using $Pr \simeq 6.52$ (i.e. water), $Ra = 10^7, 10^8$, $0.0125 \leq Ro_{\text{ff}} \leq \infty$ ($10^{-5} \leq E \leq \infty$), $0 \leq Fr \leq 10$, and $\Gamma = 0.73$. In fact, simulations were conducted in such a manner as to provide direct comparison to experiments on the NoMag laboratory device using water ($Pr \simeq 6.5$) and the $H \simeq 0.8\ m$ tall tank, where $\Gamma \simeq 0.75$. DNS, such as those of Horn and Aurnou (2018), provide the ability to independently vary Fr and Ro_{ff}, which in turn provides the ability to separately explore the broadest space of these system parameters unlike in a laboratory setting, where these parameters are inherently coupled. Figure 6.1 shows the results of their study with the inverse gravitational thermal Rossby number $1/Ro_{\text{ff}}$ on the y-axis (meaning rotational strength increases with y), the Froude number, Fr, on the x-axis, and the anomaly in the Nusselt number, Nu, relative to that without rotation as the color bar. Specifically, the heat transfer anomaly, $(Nu - Nu_0)/Nu_0$, characterizes the change of Nu for a given ($1/Ro_{\text{ff}}$, Fr) relative to an equivalent case with $Fr = 0$, i.e. non-rotating RBC. As shown, a decrease in heat transfer efficiency (blue) is observed in the QG and CC regimes, with the strongest decrease occurring in the CC regime where both centrifugal acceleration and the Coriolis force inhibit vertical convective motions. An increase in heat transfer efficiency (pink) beyond an equivalent non-rotating value is observed in the QC regime, where a strong central upwelling develops [cf. Horn and Aurnou (2018), Horn and Aurnou (2019)]. Lastly, no anomaly (white) is observed in the 3D regime in which the effects of rotation are too weak to alter the heat transport in any significant manner.

The solid horizontal black lines below $Fr = \Gamma/2$ in Fig. 6.1 are given by (6.5) for $Ra = 10^7$ and appear to separate the 3D and QG regimes well [see also Figure 2a) in Horn and Aurnou

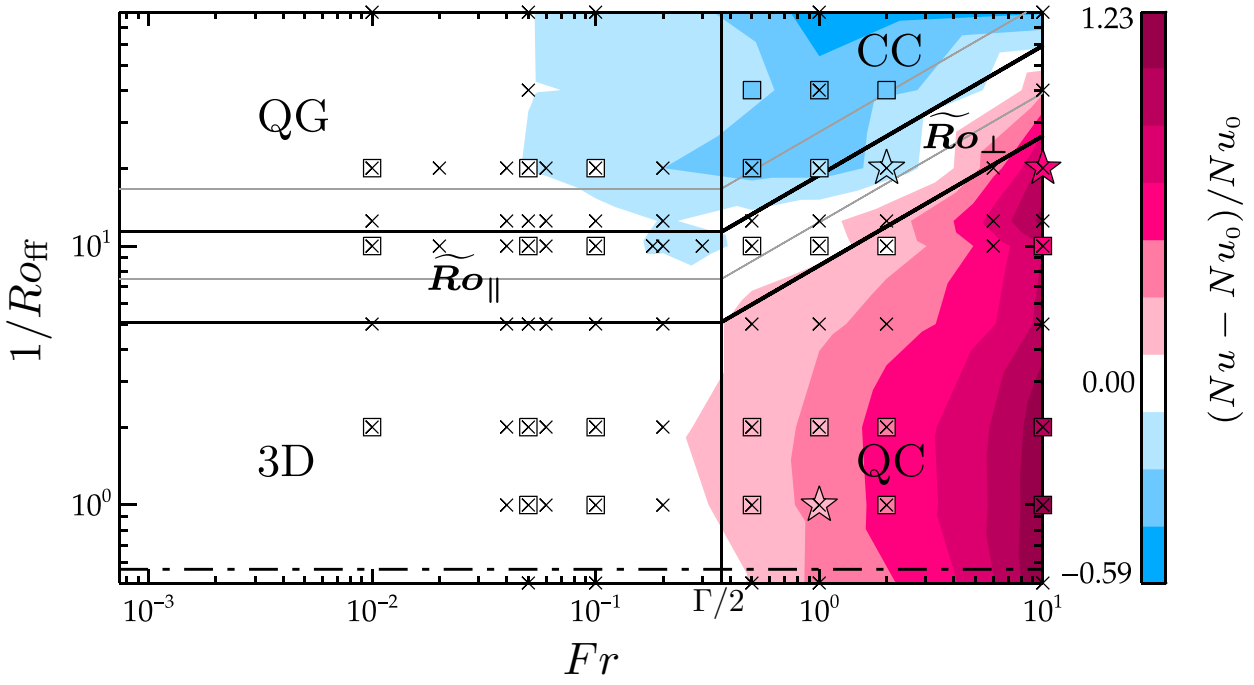

Figure 6.1: $1/Ro_{\mathrm{ff}}$ vs. Fr for a RC water system, where the color bar represents a Nusselt anomaly, $(Nu - Nu_0)/Nu_0$. Here, Nu_0 represents the heat transfer of a non-rotating RBC value; thus, this anomaly represents the deviation of a rotating case from its respective non-rotating version. Four behavioral regimes are labeled: 3D (weak Coriolis effect, weak centrifugal buoyancy effect), QG (strong Coriolis effect, weak centrifugal buoyancy effect), QC (weak Coriolis effect, strong centrifugal buoyancy effect) and CC (strong Coriolis effect, strong centrifugal buoyancy effect). The solid black vertical line represents the transition prediction of (6.7), and the solid horizontal lines below $Fr = \Gamma/2$ represent the prediction of (6.5), while the linear black lines above $Fr = \Gamma/2$ represent the prediction of (6.6). $\tilde{Ro}_{\parallel}$ denotes the transition region controlled by Ro_{ff}, while $\tilde{Ro}_{\perp}$ demarcates that which is controlled by Ro_{cb}. Refer to Figure 2b) in Horn and Aurnou (2018) for additional details. Modified from Horn and Aurnou (2018).

(2018)]. Note that $\tilde{Ro}_{\parallel}$ and $\tilde{Ro}_{\perp}$ in Fig. 6.1 signify the transition Ro_{ff} and Ro_{cb} in (6.5) and (6.6). The solid linear black lines above $Fr = \Gamma/2$ are given by (6.6) for $Ra = 10^7$ and appear to separate the QC and CC regimes well. In addition, the vertical solid black line, which represents the transition prediction of (6.7), appears to well signify the transition from the 3D/QG regimes, where centrifugal buoyancy does not significantly affect the system, to the QC/CC regimes, where centrifugal acceleration cause a strong increase (QC) or decrease (CC) in heat transfer efficiency. Thus, it appears that the transition arguments presented herein agree well with the DNS of Horn and Aurnou (2018).

The results of Fig. 6.1, while yet to be verified in a laboratory setting, imply that most

of the extreme laboratory experiments built at present do not need to be as restricted in rotation as previously thought [cf. Cheng et al. (2018)]. Thus, these devices can potentially be used to reach even more extreme parameters (i.e. lower E) without a concern for the alteration of relevant core-style dynamics due to centrifugal buoyancy. As mentioned, the results of Horn and Aurnou (2018) need to be verified in a laboratory environment with a variety of settings in order to prove their applicability to various devices that contain differences in their constraints on system parameters including Pr and Γ. Thus, we conduct, for the first time, a set of experiments in water ($Pr \simeq 6.5$) and separately in liquid metal ($Pr \simeq 0.025$) with different Γ values that test the results of Horn and Aurnou (2018). In low Prandtl liquid metal convection, we expect the same relevant system parameters, namely Ro_{ff}, Ro_{cb}, and Fr. We predict, using the results of the laboratory experiments of King and Aurnou (2015), that for a $Pr \simeq 0.025$ liquid metal RC system, the transition from 3D 'non-rotating' style convection to QG rapidly rotating convection will occur when:

$$Ro_{\text{ff}} \simeq 1. \tag{6.8}$$

Similarly to the arguments put forth by Horn and Aurnou (2018) for a water system, we argue that the transition from 3D 'non-rotating' style convection to QC centrifugally constrained convection occurs at:

$$Ro_{\text{cb}} \simeq 1. \tag{6.9}$$

These arguments will be tested and discussed in Section 6.3.2.

6.2 Configuration of NoMag and RoMag Devices

In this section, we discuss the experimental configurations of the NoMag (Section 6.2.1) and RoMag (Section 6.2.2) laboratory devices specific to this study. A detailed general description of the NoMag device is provided in Chapter 3, and a detailed description of the RoMag device at the UCLA Spinlab can be found in the theses of former Ph.D. students Eric King [King (2009)] and Alexander Grannan [Grannan (2017)].

6.2.1 Nomag Experimental Setup

The $H \simeq 0.8\ m$, $\Gamma \simeq 0.75$ tall tank was used with water on the NoMag device in order to directly compare to the DNS of Horn and Aurnou (2018) at the same $Pr \simeq 6.5$ and Γ. Our experimental range of Fr does not span quite as large of a range as is capable with DNS; our maximum rotation rate of 55 rpm corresponds to $Fr \simeq 1$. In order to examine the transitions between the regimes discussed in Horn and Aurnou (2018), a set of fixed Ra_F experiments were conducted in which the rotation rate was varied in each case, thus varying E and Fr and hence Ro_{ff} and Ro_{cb}. A total of three sets of fixed heating power were used: 125 Watts ($Ra_{F,0} \simeq 5.7 \times 10^{12}$), 250 Watts ($Ra_{F,0} \simeq 1.1 \times 10^{13}$), and 625 Watts ($Ra_{F,0} \simeq 2.9 \times 10^{13}$), totaling roughly thirty experiments. The exact dimensional and non-dimensional values of all experiments can be found in Tables 6.1 and 6.2 of Appendix A in Section 6.5, respectively.

The collection of data in terms of equilibration time, length of collection, etc. resembles that which is discussed in Section 4.2. Similarly, the use of thermal insulation and treatment of heat loss through the acrylic sidewall of the experimental container is also identical to the details provided in Section 4.2. In terms of system diagnostics for this study, velocimetry is not used. Instead, we choose to focus on the collection and analysis of temperature data with the use of sensors placed both at the fluid boundaries to obtain global system information, and at various locations inside of the fluid to analyze local system dynamics. Identically to that which is described in Section 4.2, 16 thermistors are placed in the lids of the container to measure top and bottom fluid layer temperatures as described. The horizontal temperature difference within each lid was examined and determined to be negligible on the measurement of the global heat transfer efficiency described by the Nusselt number, Nu. In other words, the averaging of sensors in each lid that exist at different radial locations does not affect the accurate characterization of Nu, even at high values of Fr.

Figure 6.2 shows a schematic of the internal sensor placement for this study. Specifically, a number of our high precision thermistors described in Chapter 3 are each inserted directly into the fluid via small ports in the top lid and secured to remain in one location throughout the study despite instances of rapid rotation. As shown, 4 sensors are placed precisely at the

center of the experimental container (i.e. at $r = 0R_i$) along a very thin ($\sim$ 1 cm thick) sturdy metal rod at non-dimensional heights of $h \simeq 0.25H$, $h \simeq 0.5H$, $h \simeq 0.75H$, and $h \simeq 0.95H$ in the fluid bulk. Additionally, an array of 5 sensors are placed along the inner sidewall of the container (i.e. at $r = R_i$) at the same non-dimensional heights as those located at the center of the tank, with an additional sensor at $h \simeq 0.05H$. These sensors, mounted to the inner sidewall, are oriented such that they extend past the thin sidewall boundary layer ($\sim$ 3 cm thick at most) and into the fluid bulk. Due to experimental implementation, the sensors along the inner sidewall are Adafruit 3950 NTC thermistors. A custom calibration was conducted prior to the start of this study to ensure all thermistors were properly calibrated to within ± 50 mK agreement with one another. A discussion of initial analyses performed using these internal sensors is discussed in Section 6.3.1.

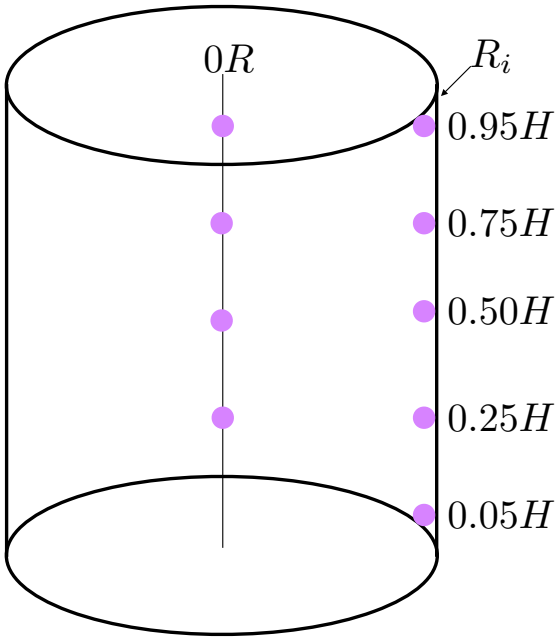

Figure 6.2: Schematic of the internal sensor placement in the NoMag device in this study using the $\Gamma \simeq 0.75$ tank. 4 custom Amphenol thermistors are placed in the center of the tank directly into the fluid (accessed through a port in the top aluminum lid) at non-dimensional heights of $h \simeq 0.25H$, $h \simeq 0.5H$, $h \simeq 0.75H$, and $h \simeq 0.95H$. 5 Adafruit thermistors are affixed to the inner sidewall in the fluid at heights of $h \simeq 0.05H$, $h \simeq 0.25H$, $h \simeq 0.5H$, $h \simeq 0.75H$, and $h \simeq 0.95H$. These sensors are oriented so as to extend into the fluid bulk as described herein. A custom calibration was performed to ensure all thermometry agreed to within a ± 50 mK resolution.

6.2.2 Romag Experimental Setup

The UCLA Spinlab experimental device 'RoMag', the predecessor to the new NoMag device, was first constructed in 2004 and was designed to study the effects of rotation, convection, and/or magnetic forces on fluid motions in both water (i.e. moderate Pr) and liquid metal (i.e. low Pr). As such, it possesses the overall structure of the NoMag device described in Chapter 3 on an overall smaller scale. The use of the conducting liquid metal gallium allows for the study of the effects of magnetic forces, a component to planetary dynamo generation processes in addition to rotating convective turbulence [see Chapter 1 for details]. Liquid gallium possesses similar properties (i.e. $Pr \simeq \mathcal{O}(10^{-2})$) to that of liquid metals found in planetary cores, such as the liquid metal iron of which the Earth's outer core is comprised. It is used over other liquid metals due to its convenient melting temperature ($\sim 30°C$), non-toxicity, and affordability. As gallium is roughly six times more dense than water, we restrict its usage to the smaller containers configured for the RoMag device, which also possesses an installed external electromagnet that can be lowered over the entire experimental container to apply a vertically aligned magnetic field to the fluid. This electromagnet and thus magnetic forces will not be used or considered in this study. A schematic of the RoMag device that is adapted from King et al. (2012) is shown in Figure 6.3a) for reference. We invite readers to explore the theses of King (2009) and Grannan (2017) and the recent publications of Aurnou et al. (2018) and Vogt et al. (2018) for an understanding of additional applications of the versatile RoMag device.

The properties of liquid gallium, some of which are temperature dependent, are used in the calculation of experimental values such as Nu and Ra. They are given as: [cf. Aurnou et al. (2018)]

$$\alpha_T = 1.25 \times 10^{-4} \text{ [1/K]}, \tag{6.10}$$

$$\rho(T) = \rho_{mp}(1 - \alpha_T(T - T_{mp})) \text{ [kg/m}^3\text{]}, \tag{6.11}$$

$$C_p = 397.6 \text{ [J/kgK]}, \tag{6.12}$$

$$k = 31.3 \text{ [W/m K]}, \tag{6.13}$$

$$\kappa(T) = k/(\rho C_p) \text{ [m}^2\text{/s]}, \tag{6.14}$$

$$\mu(T) = \nu\rho = \mu_0 exp\left(\frac{E_a}{RT_{ab}}\right) \text{ [kg/m s]}, \tag{6.15}$$

where α_T is the thermal expansivity [Brandes and Brook (1992)], ρ is the density [Assael et al. (2012)], $\rho_{mp} = 6.09 \times 10^3$ kg/m^3 is the density at the melting point, $T_{mp} = 29.8$ C [Spells (1936)], C_p is the specific heat capacity [Brandes and Brook (1992)], k is the thermal conductivity [Aurnou and Olson (2001), Aurnou et al. (2018)], κ is the thermal diffusivity, μ is the dynamic viscosity, ν is the kinematic viscosity, $\mu_0 = 4.6 \times 10^{-4}$ PaS is the dynamic viscosity coefficient, $E_a = 4000$ J/mol is the activation energy, $R = 8.3144$ J/(mol K) is the gas constant, and T_{ab} is the absolute temperature [Andrade and Da (1934), Aurnou et al. (2018)].

The cylindrical experimental container used on the RoMag device in this study contains a diameter of $D \simeq 0.2$ m and a height of $H \simeq 0.2$ m, giving $\Gamma \simeq 1$. A photograph of the experiment with this container and no thermal insulation is shown in Figure 6.3b). The sidewall is made of ~ 1.3 cm thick stainless steel ($k \simeq 16$ W/mK), while the top (bottom) bounding thermal blocks are made of ~ 4 cm (~ 1.5) cm thick copper ($k \simeq 390$ W/mK), neither of which interact with gallium. Similarly to the NoMag device, a non-inductively wound heater provides a heating power to the bottom copper block while heat is removed from the system by a double-spiral wound heat exchanger placed above the top copper block and maintained at a constant temperature by a ThermoNESLAB HX-300 precision thermal bath. Six thermistors are inserted into each of the the copper lids within 2 mm of the fluid layer, and the Biot number is small in all experiments (i.e. $Bi \lesssim 0.2$), indicating the 'isothermality' of the boundaries relative to that of the fluid. Furthermore, the top and bottom fluid temperatures are corrected to include conduction occurring in the copper boundaries. Nine thermistors are placed at various depths and radii directly in the fluid layer through small ports in the copper top boundary. A schematic of the non-dimensional locations of these sensors is displayed in Figure 6.3c). Sensor locations are chosen based upon the availability of sensors used on the RoMag device (custom fabricated waterproof Amphenol NTC thermistors encased in thin stainless steel housing). Nonetheless, these

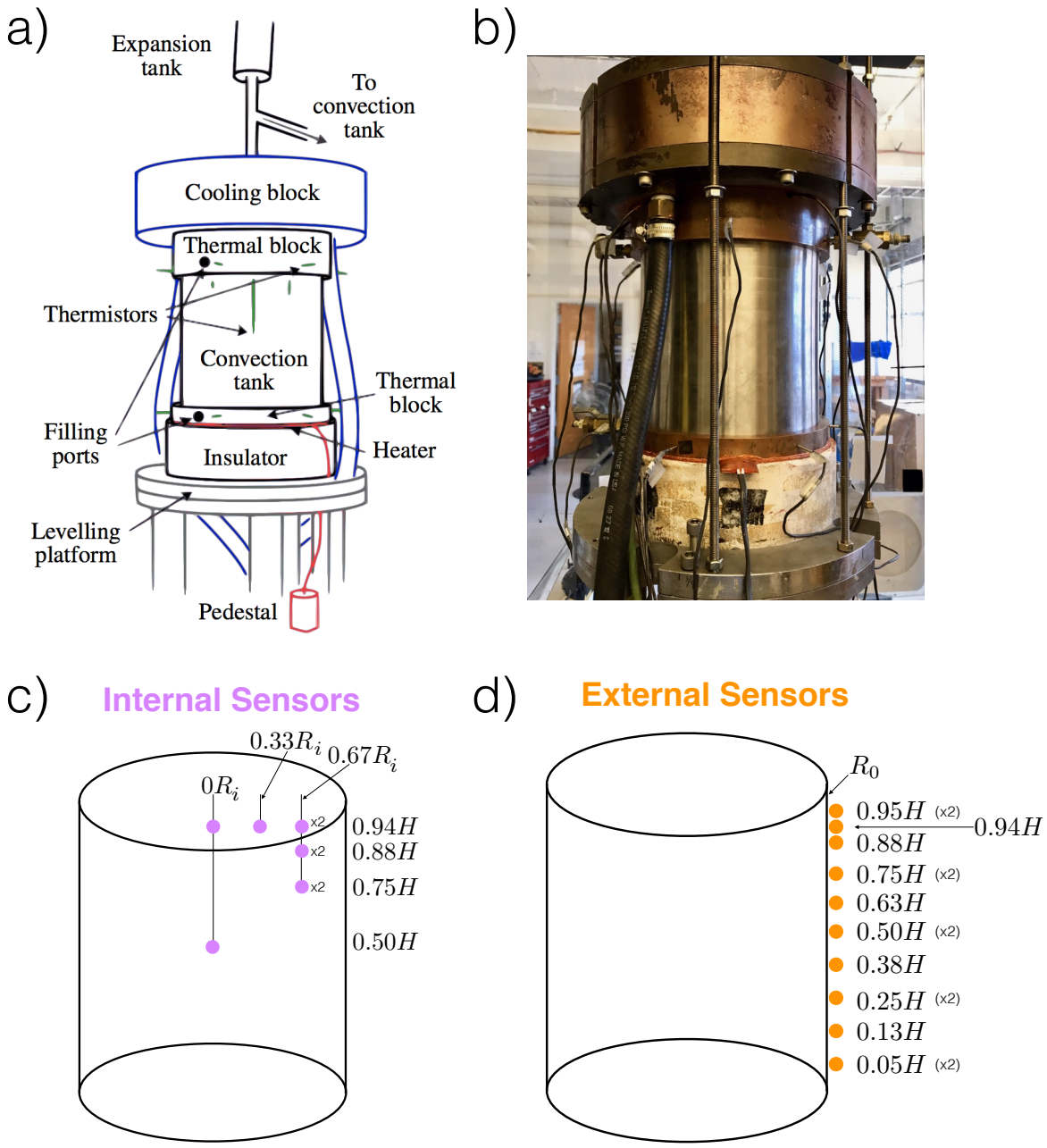

Figure 6.3: a) Schematic of the RoMag Device adapted from King et al. (2012) b) Photograph of the experimental container used in this study ($\Gamma \simeq 1$) with no thermal insulation in place c) Schematic of the locations of the 9 internal sensors (purple) used in this study. At the center of the tank, $r \simeq 0R_i$, one sensor is placed at $h \simeq 0.5H$ and another is placed at $h \simeq 0.94H$. At $r \simeq 0.33R_i$, one sensor is placed at $h \simeq 0.94H$. At $r \simeq 0.67R_i$, two sensors are placed at $h \simeq 0.75H$, two are placed at $h \simeq 0.88H$, and another two are placed at $h \simeq 0.94H$ at different azimuthal locations. Any azimuthal dependencies are not presently considered for the analysis presented herein. d) Schematic of the 15 K-type thermocouples (orange) placed at various heights on the external sidewall. As shown, sensors are spaced apart overall by roughly $h \simeq 0.1H$. Duplicate sensors are placed 180° apart for 5 of the locations.

internal sensors still allow us to infer internal system dynamics at a variety of locations. 15 K-type thermocouple temperature sensors are placed externally on the stainless steel sidewall at various heights in order to capture temperature information at the fluid sidewall, i.e. at $r = R_0$. A schematic for the placement of these sensors is provided in Figure 6.3d).

The maximum rotation rate of the RoMag device in this study is 60 rpm, corresponding to $Fr = 0.40$. Three fixed values of Ra_F were used to create three different datasets in which the rotation was varied for each case, thus varying E and Fr and hence Ro_{ff} and Ro_{cb}. These three fixed heat values were: 200 Watts ($Ra_{F,0} \simeq 1.1 \times 10^8$), 800 Watts ($Ra_{F,0} \simeq 4.5 \times 10^8$), and 1600 Watts ($Ra_{F,0} \simeq 9.4 \times 10^8$), totaling roughly thirty two experiments. Dimensional and non-dimensional values of all liquid metal experiments can be found in Tables 6.3 and 6.4 of Appendix A in Section 6.5, respectively. In terms of equilibration time for these liquid metal experiments, similarly to our water experiments, the system is assumed to have equilibrated when the mean temperature on each thermistor does not change by more than 1% during the previous 30 minutes. Equilibrated data is then recorded for ∼3 hours on average at a rate of 10Hz. In order to minimize heat loss through the stainless steel experiment sidewall, we first insulate the sidewall with a $\sim$ 10 cm thick inner layer of closed cell foam and then with an outer layer of $\sim$ 5 cm thick Insulfrax fibrous insulation. Temperature sensors placed between these insulation layers provide an estimate for sidewall heat losses. Additionally, heat loss due to vertical conduction in the stainless steel sidewall itself is also accounted for.

6.3 Experimental Results

For ease of discussion, we present below the initial results of the water study on the NoMag device in Section 6.3.1 separately from the liquid metal study on the RoMag device, which we discuss in Section 6.3.2. Each respective study will be compared to the theory and results of the numerical water studies presented in Horn and Aurnou (2018) and Horn and Aurnou (2019). We conclude with a synthesized discussion of the implications of the results of both laboratory studies and discuss the future work remaining on this study in Section 6.4.

6.3.1 NoMag Water Study

For direct comparison to the DNS results of Horn and Aurnou (2018) shown in Fig. 6.1, the ∼30 experiments collected on the NoMag device using water are plotted in a similar fashion in Figure 6.4. Shown as a scatter plot, data are plotted with Fr on the x-axis, $1/Ro_{\text{ff}}$ on the y-axis, and the Nusselt anomaly, $(Nu - Nu_0)/Nu_0$ as the color bar. Here, Nu_0 corresponds to the value of the Nusselt number for the equivalent non-rotating case. Symbol shape represents the three different sets of data, each collected at a fixed value of Ra_F. Note the slight difference in the axes values of Fig. 6.4 in comparison to Fig. 6.1, as well as the difference in range of the color bar. Nonetheless, our water data collected on the NoMag device with $\Gamma \simeq 0.75$ appear to agree well overall to the predictions and results of Horn and Aurnou (2018).

Specifically, we see that little to no anomaly (white) in the heat transfer efficiency of the system occurs at low Fr and low $1/Ro_{\text{ff}}$ as expected. The solid horizontal black lines below $Fr = \Gamma/2$ represent the predicted transitional range, denoted as $\tilde{Ro}_{\|}$, from the 3D to QG regimes of (6.5) for a chosen value of $Ra = 3 \times 10^{10}$. This Rayleigh number corresponds to the value of Ra_0 for the non-rotating case of $Ra_{F,0} \simeq 5.7 \times 10^{12}$ (125 Watts). Other values of Ra, such as those for the non-rotating cases of the other two fixed Ra_F cases, can be used, yielding very similar predicted lines that shift ever so slightly in the y-direction. A decrease in the heat transfer efficiency is observed as the QG regime is entered, indicating that the constraining Coriolis force begins to inhibit vertical convective transport. The dashed vertical black line at $Fr = \Gamma/2 = 0.365$ indicates the initiation of centrifugation, either from a 3D to a QC regime, or from a QG to a CC regime, as predicted by (6.7). The solid linear black lines above $Fr = \Gamma/2$ represent the transition region prediction of (6.6) also for $Ra_0 = 3 \times 10^{10}$, denoted as $\tilde{Ro}_{\perp}$. Though only moderately probed, we see that our most extreme data enters the CC regime at high Fr and high $1/Ro_{\text{ff}}$ in which strong rotational effects, that is both the Coriolis force and the centrifugal buoyancy in the system, inhibit vertical convection. The Nusselt anomalies here show the strongest decrease in heat transfer efficiency (dark blue), in good agreement with the results of Horn and Aurnou (2018).

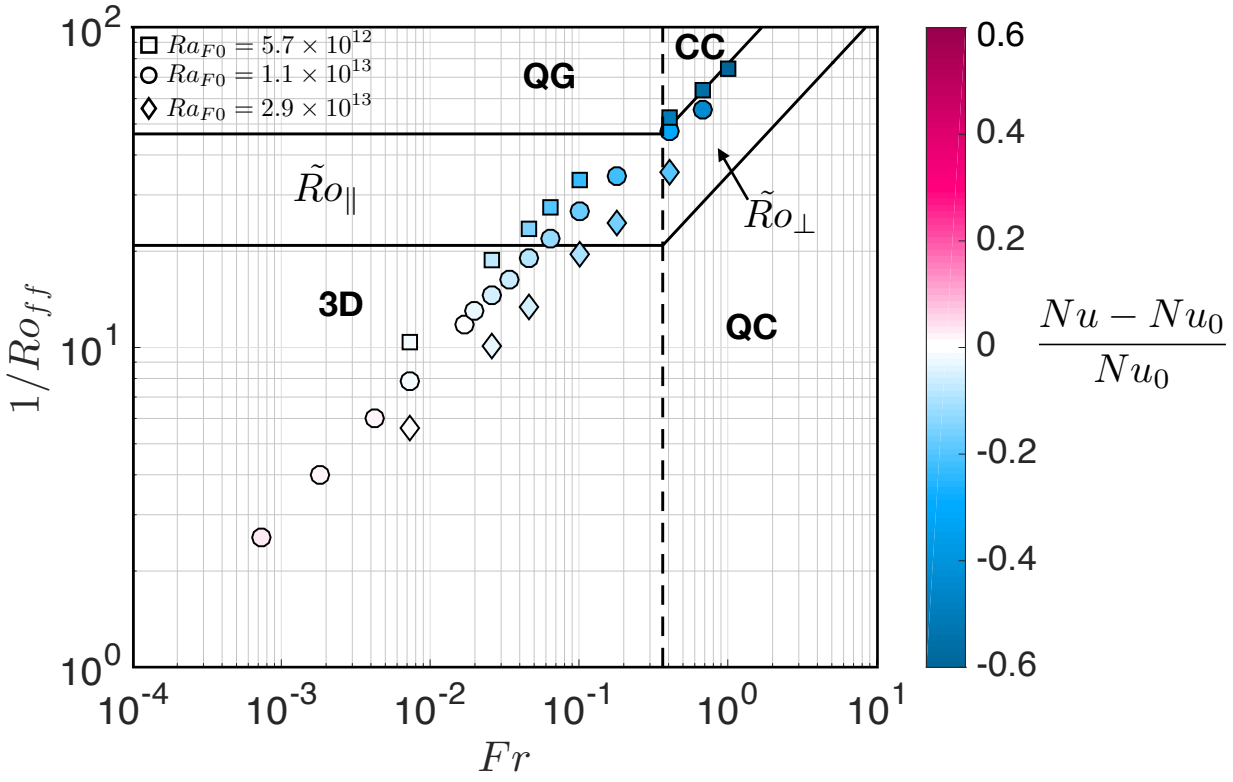

Figure 6.4: A scatter plot of experimental data collected on the NoMag device using water and the $\Gamma \simeq 0.75$ tank, where $1/Ro_{\text{ff}}$ is shown on the y-axis, Fr is shown on the x-axis, and the color bar represents the Nusselt anomaly, $(Nu - Nu_0)/Nu_0$. Nu_0 corresponds to the value of the Nusselt number for the equivalent non-rotating case. The symbol shape of each experiment corresponds to the fixed Ra_F value as denoted in the legend of the upper left corner. The four predicted regimes of Horn and Aurnou (2018) are labeled: 3D, QG, QC, and CC. The solid horizontal black lines below $Fr = \Gamma/2$ represent the predicted transitional range, denoted as $\tilde{Ro}_{\|}$, of (6.5) for $Ra_0 = 3 \times 10^{10}$ ($Ra_{F,0} \simeq 5.7 \times 10^{12}$). The dashed vertical black line at $Fr = \Gamma/2 = 0.365$ represents the transition prediction of (6.7). The solid linear black lines above $Fr = \Gamma/2$ represent the transition region prediction of (6.6) also for $Ra_0 = 3 \times 10^{10}$, denoted as $\tilde{Ro}_{\perp}$. Note the slight difference in axes ranges and the color bar range when comparing to Figure 6.1.

Due to experimental limitations, it is difficult for any experiments on the NoMag device or any other comparable device to probe the QC regime. This is largely due to the inherently coupled nature of Fr and $1/Ro_{\text{ff}}$, both coupled dimensionally by Ω, the rotation of the container. In other words, in order to reach high values of $Fr \propto \Omega^2$, simultaneously high values of $1/Ro_{\text{ff}} \propto \Omega$ are reached, causing our experiments to exist in the CC regime beyond $Fr = \Gamma/2$ but not the QC regime. Nonetheless, we systematically explore, for the first time, the transition from QG to CC convection in order to understand which experiments remain relevant to planetary dynamo systems (i.e. those in the QG regime and not in the CC

regime). To further investigate this transition, we analyze the temperature profiles directly inside of the fluid using the internal sensors mapped in Fig. 6.2. The color bar in Figure 6.5 shows the the mean local internal temperature normalized by the mean temperature of the fluid as determined from the sensors at the fluid boundaries, T_{mixing}, for: a) the temperature at the center of the tank, i.e. $r \simeq 0R_i$, $h \simeq 0.5H$, denoted as T_{center}, and b) the temperature at the mid-plane on the internal edge of the tank, i.e. $r \simeq R_i$, $h \simeq 0.5H$ and denoted as T_{edge}. Note that the data collected at $Ra_{F,0} \simeq 1.1 \times 10^{13}$ (250 Watts, shown as circles) did not have internal temperature information.

In Fig. 6.5a), we see agreement (white) between the estimated mean fluid temperature (i.e. at the mid-plane) from boundary measurements, T_{mixing}, and the direct measurement of the center temperature, T_{center}, in the 3D regime as expected. Here, centrifugal buoyancy is extremely weak and does not cause any temperature anomalies in the fluid bulk. We observe a similar result for the comparison of T_{mixing} with T_{edge} at $r \simeq R_i$ in this regime as well, as shown in Fig. 6.5b). However, once the predicted transition of $Fr = \Gamma/2$ is crossed, indicated by the vertical dashed line, we observe a significant enhancement of the central temperature relative to the estimated mean in a) (dark pink) and a simultaneous decrease in the mid-plane temperature at the sidewall relative to the mean in b) (blue). These results indicate that the increase in the strength of centrifugal acceleration in the system acts to develop a horizontal dependence on temperature. These findings are also behaviorally consistent with the results described in Horn and Aurnou (2018), that is a strong central upwelling appears to develop with an anomalously hot center and a simultaneously cool outer downwelling in the CC regime. Thus, we argue that our initial analysis of our water experiments conducted on the NoMag device yield results that confirm the recent findings of Horn and Aurnou (2018) in a laboratory setting. A discussion of further analysis to be conducted on this data, including further investigation of the internal temperature profiles of such experiments, will be discussed in Section 6.4.

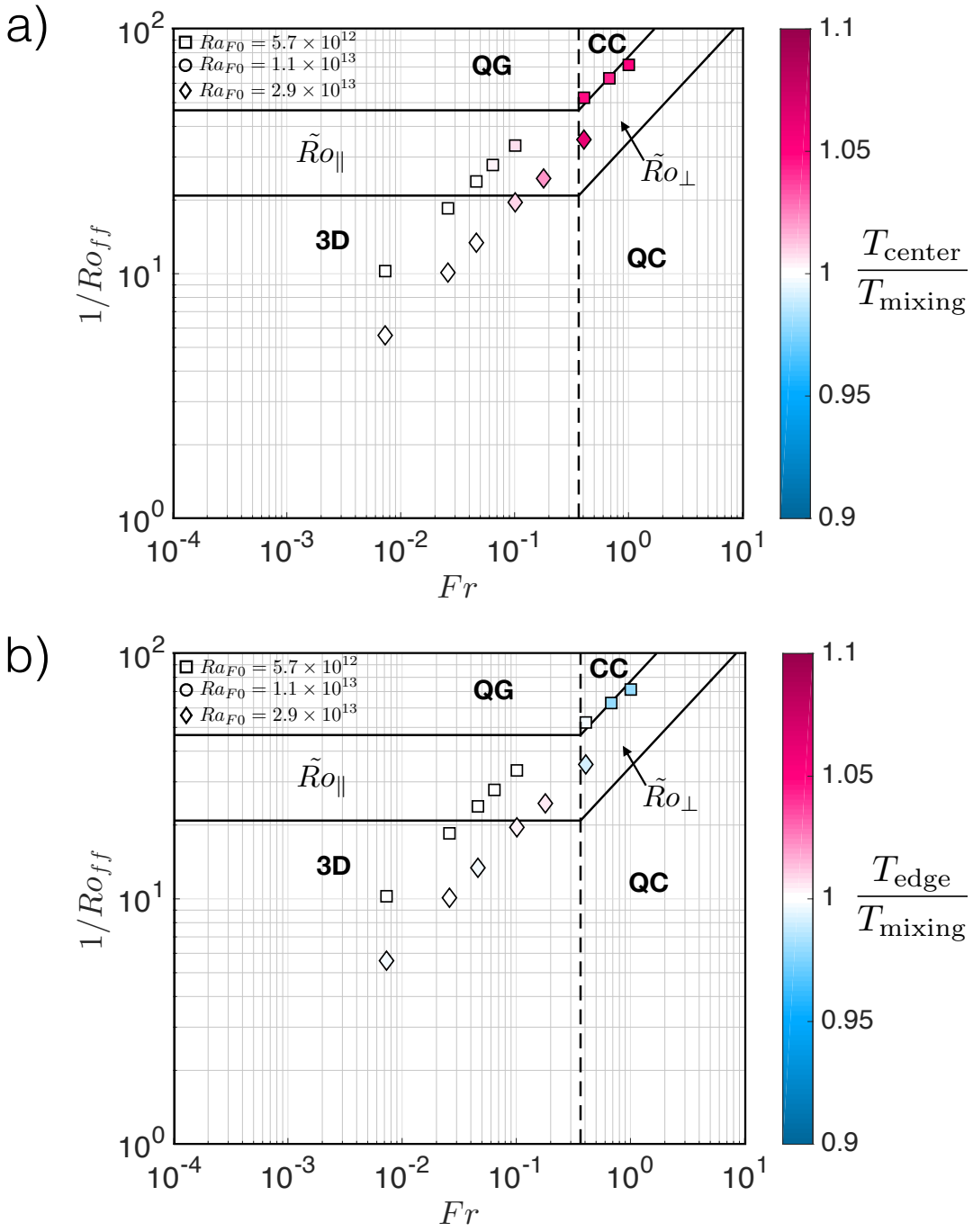

Figure 6.5: a) A scatter plot created using local temperature information, where $1/Ro_{\text{ff}}$ is shown on the y-axis, Fr is shown on the x-axis, and the color bar is the normalized center temperature, T_{center}, measured at $r \simeq 0R_i$, $h \simeq 0.5H$, relative to the mean temperature of the fluid estimated by the sensors at the fluid boundaries, T_{mixing}, and b) the same scatter plot but with the color bar representing the edge temperature at the mid-plane internal sidewall, i.e. at $r \simeq R_i$, $h \simeq 0.5H$, also normalized by T_{mixing}. Symbol shape again represents the fixed Ra_F dataset, and we refer readers to Fig. 6.4 for the definitions of the solid and dashed lines demarcating regime transitions.

6.3.2 RoMag Liquid Metal Study

The 32 experiments collected using liquid gallium ($Pr \simeq 0.025$) on the RoMag device are shown in Figure 6.6 for comparison with experimental results using water ($Pr \simeq 6.5$) as shown in Fig. 6.4 and with DNS using water as shown in Fig. 6.1. In the scatter plot of Fig. 6.6, $1/Ro_{\text{ff}}$ is shown on the y-axis, Fr is shown on the x-axis, and the color bar denotes the Nusselt anomaly, $(Nu - Nu_0)/Nu_0$, relative to the equivalent non-rotating case, denoted as Nu_0. Symbol shapes represent the three fixed heating values used: 200 Watts ($Ra_{F,0} \simeq 1.1 \times 10^8$), 800 Watts ($Ra_{F,0} \simeq 4.5 \times 10^8$), and 1600 Watts ($Ra_{F,0} \simeq 9.4 \times 10^8$). As shown, even in the QG regime, the heat transfer efficiency decreases by close to 90% of its non-rotating value in our most extreme cases. We purport that this is the case in a liquid metal as the low viscosity of the fluid allows for the Coriolis force to control the fluid even more easily than for a water system of moderate fluid viscosity. The solid horizontal black line below $Fr = \Gamma/2$ in Fig. 6.6 displays the predicted transition from a 3D to QG regime of (6.8) for a liquid metal system. As shown, experimental data appear to agree with such a transition to leading order, as significant Nusselt diminution does not appear to occur until the QG regime is established (blue-dark blue). The ease of reaching the QG regime from the 3D regime is further displayed by this relatively low transition prediction of $1/Ro_{\text{ff}} \sim 1$.

The vertical dashed line in Fig. 6.6 highlights the predicted transition for which centrifugal buoyancy should noticeably begin to affect the system of (6.7), i.e. when $Fr = \Gamma/2$. Note that this prediction occurs independently of the value of Pr. The linear solid black line above $Fr = \Gamma/2$ displays our prediction given in (6.9), i.e. $1/Ro_{\text{cb}} \sim 1$. For the given aspect ratio tank used on the RoMag device, $\Gamma \simeq 1$, the transition to which centrifugal buoyancy should begin to affect the system, either entering the QC or CC regimes, occurs at a value of $Fr = \Gamma/2 \simeq 0.5$. At our highest dimensional rotation rate of 60rpm, we are able to reach $Fr \simeq 0.4$; thus, we are unable to extend into a regime in which the effects centrifugal buoyancy can be observed. Nonetheless, we argue that these initial results behave as expected. We further hypothesize that extending beyond this transition (dashed line) will lead to further decreases in the Nusselt number, perhaps past 100% of the equivalent

non-rotating value. As these experiments occur closer to the onset of convection and contain Ra and Nu values comparable to that of Horn and Aurnou (2018), we conjecture that convection could become entirely suppressed due to the constraining Coriolis and centrifugal acceleration forces in the CC regime if we were able to conduct experiments in this regime.

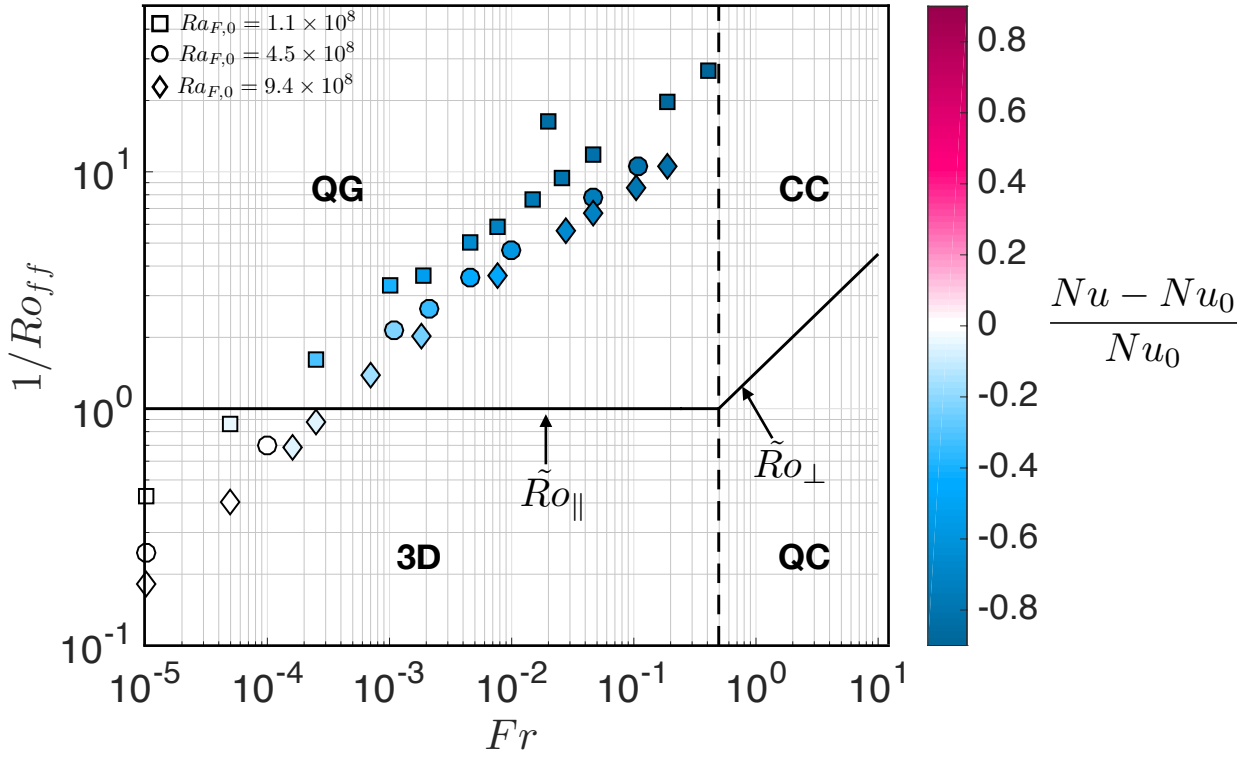

Figure 6.6: A scatter plot of experimental data collected on the RoMag device using liquid gallium ($Pr \simeq 0.025$) and the $\Gamma \simeq 1$ tank, where $1/Ro_{\text{ff}}$ is shown on the y-axis, Fr is shown on the x-axis, and the color bar represents the Nusselt anomaly, $(Nu - Nu_0)/Nu_0$. Nu_0 corresponds to the value of the Nusselt number for the equivalent non-rotating case. The symbol shape of each experiment corresponds to the fixed Ra_F value as denoted in the legend of the upper left corner. The four predicted regimes of Horn and Aurnou (2018) are labeled: 3D, QG, QC, and CC. The solid horizontal black line below $Fr = \Gamma/2$ represents the predicted transitional range, denoted as $\tilde{Ro}_{\parallel}$, of (6.8). The dashed vertical black line at $Fr = \Gamma/2 \simeq 0.5$ represents the transition prediction of (6.7). The solid linear black lines above $Fr = \Gamma/2$ represent the transition region prediction of (6.9). Note the differences in axes ranges and the color bar range when comparing to the water system results shown in Figure 6.1 and Figure 6.4.

Note that the same experimental difficulty in probing the QC regime as described in section 6.3.1 also applies on the RoMag device due to the inherently couple nature of Fr and $1/Ro_{\text{ff}}$ (or, equivalently, $1/Ro_{\text{cb}}$) in a laboratory setting. The further difficulty in using this device to probe the CC regime is due to the use of a smaller diameter container ($D \simeq 0.2$

m for all containers on the RoMag device, as opposed to $D \simeq 0.6\ m$ for all containers at present on the NoMag device). Thus, future experiments could make use of smaller aspect ratio containers (i.e. with heights greater than $H \simeq 0.2\ m$) in order to probe the CC regime. Nonetheless, an initial examination of the internal temperature profiles of the experiments conducted thus far on the RoMag device further reinforces agreement with the theory of Horn and Aurnou (2018) presented in Section 6.1.1.

Specifically, Figure 6.7a) displays a similar scatter plot to that of Fig. 6.6 but with a color bar in which the center temperature measured at $R \simeq 0R_i$, $h \simeq 0.5H$, T_{center}, is normalized by the mean fluid temperature as estimated from measurements at the fluid boundaries, T_{mixing}. Further, Fig. 6.7b) shows the same data but with a color bar in which the temperature at the external sidewall, i.e. $R \simeq R_0$, $h \simeq 0.5H$, T_{edge}, is normalized by T_{mixing}. The conducting nature of the stainless steel sidewall as well as the use of several layers of thermal insulation allows for the accurate characterization of the mid-plane temperature at the sidewall using external sensors affixed to the sidewall and coupled using thermal conducting grease. There does not appear to exist any notable changes in the center or edge temperatures relative to the estimated mean for any of the experiments conducted, as shown by the overall white coloring of all symbols. This finding implies that there exists no altercation of temperature as a function of radii due to radial centrifugal forces. This is to be expected for our data, which lie either in the 3D or QG regimes. Thus, from Fig. 6.5 and Fig. 6.7, we conclude that the examination of temperature internally in the fluid at various non-dimensional locations allows for further examination of the direct effects (or lack thereof) of centrifugal buoyancy in addition to the examination of heat transfer anomalies. Future analysis, discussed in greater detail in the subsequent section, will be conducted on the available sensor data at additional locations.

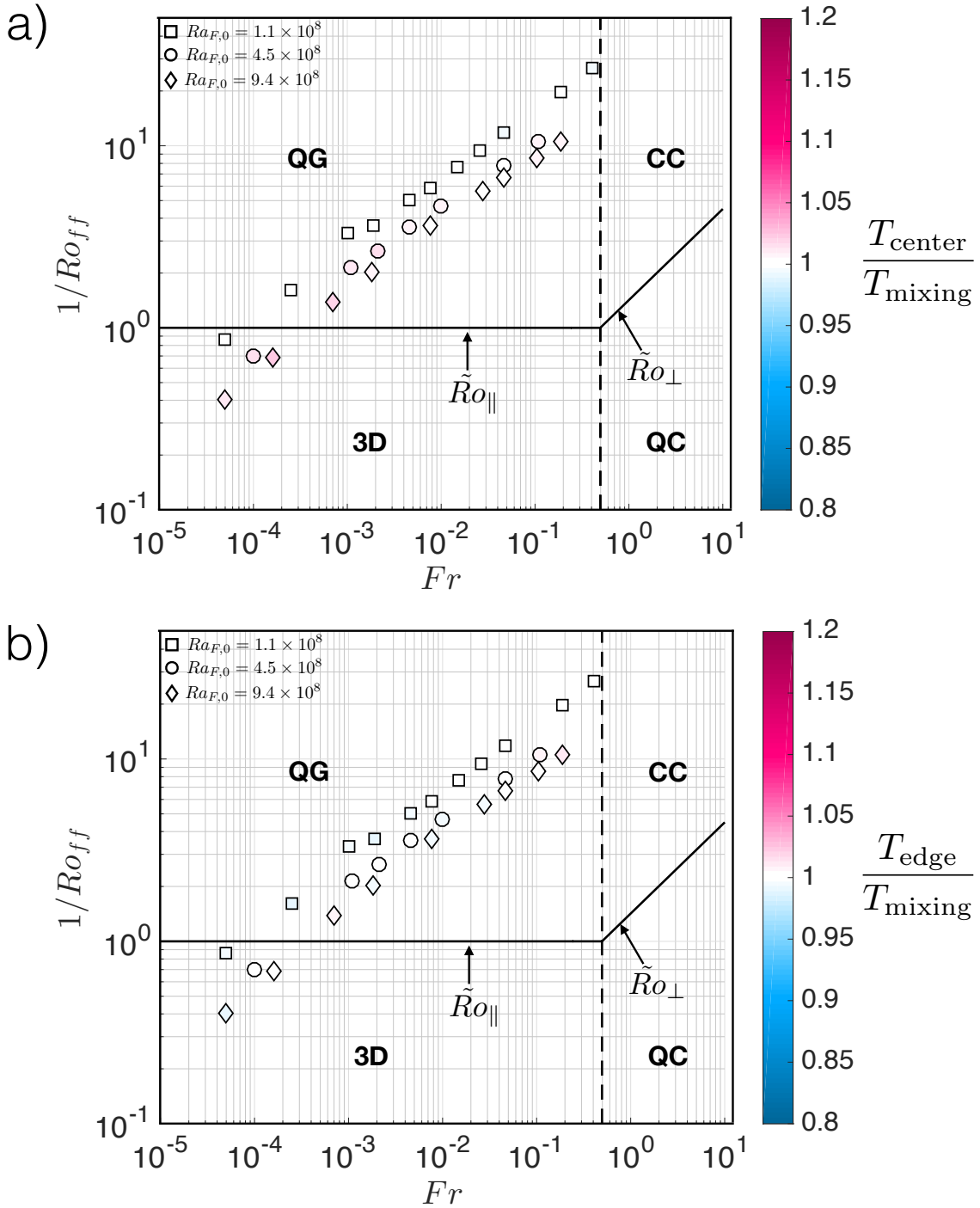

Figure 6.7: a) A scatter plot created using local temperature information, where $1/Ro_{\text{ff}}$ is shown on the y-axis, Fr is shown on the x-axis, and the color bar is the normalized center temperature, T_{center}, measured at $r \simeq 0R_i$, $h \simeq 0.5H$, relative to the mean temperature of the fluid estimated by the sensors at the fluid boundaries, T_{mixing}, and b) the same scatter plot but with the color bar representing the edge temperature at the mid-plane external sidewall, i.e. at $r \simeq R_0$, $h \simeq 0.5H$, also normalized by T_{mixing}. Symbol shape again represents the fixed Ra_F dataset, and we refer readers to Fig. 6.6 for the definitions of the solid and dashed lines demarcating regime transitions.

6.4 Discussion

The first set of laboratory experiments to test and verify the predictions and results of Horn and Aurnou (2018) and Horn and Aurnou (2019) regarding the transition to centrifugally dominated convection in RC have been completed. Specifically, a set of experiments on the NoMag device using water ($Pr \simeq 6.5$) and a $\Gamma \simeq 0.75$ aspect ratio container were conducted for direct comparison with the DNS of Horn and Aurnou (2018) and the additional study of results in the presence of turbulence (i.e. strong thermal forcing). In addition, a set of experiments were conducted on the RoMag device using liquid metal ($Pr \simeq 0.025$) and a $\Gamma \simeq 1$ aspect ratio container in order to further examine any potential dependence of the behavioral regimes of RC with the presence of centrifugal buoyancy on fluid properties. Our initial findings for both Pr systems appear to agree with and verify the theory and results of Horn and Aurnou (2018). Similarly to this study, we find that centrifugation effects on vertical convective dynamics are found above a system transition constrained by $Fr = \Gamma/2$.

Specifically, in our water study, we observe a significant decrease in the heat transfer efficiency, characterized by the Nusselt number, relative to an equivalent non-rotating case once centrifugal acceleration begins to constrain vertical convective motions in a regime described as Coriolis-centrifugal (CC) convection. Coincident with this observation, we notice the development of a horizontal dependence on temperature in which an anomalous strong central upwelling and a simultaneous outer downwelling develops, also consistent with the findings of Horn and Aurnou (2018). We argue that the observation of the development of a horizontal temperature dependence in the system is an important indicator of the transition from the quasi-geostrophic (QG) regime to the CC regime, as no horizontal temperature dependence should exist and is not observed in our experiments in the QG regime. We note that our experimental results confirm the theory of Horn and Aurnou (2018) far past the onset of convection for the first time.

The findings of our initial analyses on our liquid metal experiments conducted on the RoMag device further confirm the recent theory of Horn and Aurnou (2018), despite the difference in Prandtl number. While the CC regime is not probed in this set of experiments,

our findings show that no observable effects of centrifugal buoyancy exist in the 3D and QG regimes explored as expected. Together, our initial experimental results, along with the DNS of Horn and Aurnou (2018), indicate that laboratory devices may be used in the study of core-style convection with less restrictions on rotation than previously thought [e.g. Cheng et al. (2018)]. Thus, these extreme experiments may now be able to justifiably reach parameters (i.e. lower Ekman numbers) even closer to planets than previously imagined, making them an even more crucial tool for the dynamo community.

We plan to conduct further analysis on the data collected and presented herein. Specifically, we plan to examine the full vertical profiles at different radii of our internal sensors for a more in depth characterization of temperature changes due to the influence of centrifugal buoyancy in the system. We will compare our profiles to the limited models developed previously with careful consideration of the applicability of such models [e.g. Hart and Ohlsen (1999)]. In terms of global system information, we note that it is difficult to observe the influence of centrifugal buoyancy on vertical convection in RC if examining global heat transfer alone, i.e. if examining the Nusselt number relative to the Rayleigh number of the system as is commonly done. While we find that examining the Nusselt number anomaly as a function of (Fr, $1/Ro_{\text{ff}}$) as suggested by Horn and Aurnou (2018) allows for the observation of the transition from the QG regime (relevant to planetary dynamo systems) to the CC regime, we plan to explore any and all other avenues by which this transition can be more easily understood and observed. This analysis will include close inspection of different ways in which to best represent data given all system input parameters.

Lastly, there are several laboratory datasets that have already been collected which can be added to the analysis presented herein. Specifically, a good number of the experiments discussed in Chapter 4 on the NoMag device in the $\Gamma \simeq 3$, $\Gamma \simeq 1.5$, and $\Gamma \simeq 0.75$ tanks will be useful for examination in this study. Although not previously mentioned, internal temperature profile data was collected in the $\Gamma \simeq 3$ and $\Gamma \simeq 0.75$ tanks for the experiments conducted in the study of Chapter 4 in a manner that is nearly identical to the mapping shown in Fig. 6.2. Further, we plan to harvest the data of the water experiments collected in the $\Gamma \simeq 0.25$ and $\Gamma \simeq 0.125$ tanks on the RoMag device of Cheng et al. (2015) in order to

examine the potential effects of centrifugal buoyancy in these experiments in detail for the first time in light of the new methodology presented herein. We plan to create a composite analysis of all of this data, some of which will lie in the CC regime, thus providing us with more data to analyze in this regime. The addition of such data is likely to reinforce our findings, and perhaps even enhance and illuminate further details regarding them.

6.5 Appendix A: Data Tables for Centrifugation Study

H	D_i	$\overline{Q_{input}}$	Q	Ω	$\overline{T_{fluid}}$	T_{center}	T_{edge}	ΔT_v	t_{total}	$t_{analyzed}$
(m)	(m)	(W)	(W)	(rpm)	(C)	(C)	(C)	(C)	(hr)	(hr)
0.802	0.586	124.94	124.94	0	23.49	23.48	23.45	3.10	23.23	10.7
0.802	0.586	124.93	124.93	4.71	23.53	23.51	23.48	3.15	23.74	3.74
0.802	0.586	124.50	124.50	8.88	23.60	23.63	23.59	3.32	23.95	9.55
0.802	0.586	124.95	124.95	11.8	23.78	23.81	23.77	3.65	23.39	10.4
0.802	0.586	124.30	124.30	14.1	23.86	23.94	23.85	3.81	23.77	5.00
0.802	0.586	124.16	124.16	17.7	23.96	24.10	23.94	4.00	23.53	10.0
0.802	0.586	124.82	124.82	35.4	24.90	26.06	24.82	6.10	23.57	3.57
0.802	0.586	126.59	124.45	45.4	25.53	26.63	24.99	7.12	17.72	2.88
0.802	0.586	124.37	124.43	55.5	25.96	27.28	25.44	8.29	16.40	1.00
0.802	0.586	249.01	248.69	0	22.27	–	–	5.49	56.20	33.6
0.802	0.586	250.05	249.73	1.50	22.17	–	–	5.35	22.24	4.74
0.802	0.586	248.52	248.20	2.36	22.15	–	–	5.38	23.31	3.31
0.802	0.586	250.69	250.37	3.56	22.27	–	–	5.46	24.47	10.0
0.802	0.586	250.11	249.79	4.71	22.38	–	–	5.61	19.47	6.00
0.802	0.586	250.69	250.37	7.12	22.30	–	–	5.58	22.55	2.55
0.802	0.586	248.67	248.35	7.90	22.33	–	–	5.66	23.33	10.0
0.802	0.586	248.21	247.89	8.88	22.34	–	–	5.76	30.18	5.00

0.802	0.586	249.49	249.17	10.2	22.52	–	–	5.89	18.38	4.00
0.802	0.586	248.45	248.13	11.9	22.44	–	–	6.00	21.65	4.00
0.802	0.586	248.02	247.70	14.1	22.58	–	–	6.27	25.37	5.37
0.802	0.586	250.01	249.69	17.7	22.81	–	–	6.67	23.12	5.00
0.802	0.586	249.25	248.93	23.7	23.02	–	–	7.11	22.73	4.50
0.802	0.586	249.11	248.79	35.3	23.60	–	–	8.06	14.00	4.00
0.802	0.586	249.07	248.75	45.4	24.42	–	–	9.63	16.41	4.41
0.802	0.586	625.17	625.17	0	23.45	23.46	23.46	10.9	33.70	9.11
0.802	0.586	624.46	624.46	4.74	23.49	23.45	23.41	11.0	23.43	6.00
0.802	0.586	625.05	625.05	8.88	23.63	23.65	23.61	11.3	22.96	5.60
0.802	0.586	623.94	623.94	11.9	23.71	23.76	23.67	11.5	23.89	6.50
0.802	0.586	625.18	625.18	17.9	24.04	24.26	24.10	12.1	23.88	13.88
0.802	0.586	626.33	626.33	23.7	24.44	24.95	24.57	13.0	25.53	5.00
0.802	0.586	623.37	623.37	35.4	24.73	26.23	24.52	13.6	21.59	6.50

Table 6.1: NoMag Water Study Dimensional Experimental Values: H is the fluid container height, D_i is the inner fluid container diameter, Q_{input} is the measured mean input heating power, Q is the heating rate calculated to be applied to the device after accounting for horizontal conductive losses, Ω is the rotation rate of the fluid container, $\overline{T_{fluid}}$ is the mean fluid temperature, T_{center} is the local fluid temperature at $h \simeq 0.5H$ and $r \simeq 0R$, T_{edge} is the local fluid temperature at $h \simeq 0.5H$ and $r \simeq R$, ΔT_v is the vertical temperature difference, t_{total} is the total experimental time, and $t_{analyzed}$ is the portion of time over which equilibrated data is analyzed. Single solid horizontal lines separate fixed applied heat cases for clarity.

$\frac{Ra_F}{10^8}$	$10^7 E$	$10^2 Pr$	$\frac{Ra}{10^8}$	$\widetilde{Ra}$	Nu	$\frac{Nu}{Nu_{E=\infty}}$	Fr	$\frac{\Gamma}{2}$	Ro_{ff}	Ro_{cb}
0.57	∞	6.31	2.90	∞	199	1.00	0	0.73	∞	∞
0.58	1.4	6.30	2.95	4.79×10^2	195	0.98	0.00073	0.73	0.098	0.014
0.58	0.76	6.29	3.12	2.17×10^2	184	0.92	0.026	0.73	0.054	0.014
0.58	0.57	6.26	3.47	1.64×10^2	168	0.84	0.046	0.73	0.042	0.015

0.58	0.48	6.25	3.63	1.35×10^2	160	0.80	0.065	0.73	0.036	0.016
0.59	0.38	6.23	3.84	1.05×10^2	153	0.77	0.10	0.73	0.030	0.016
0.62	0.19	6.08	6.19	6.50×10^1	100	0.50	0.41	0.73	0.019	0.020
0.65	0.14	5.98	7.49	5.45×10^1	87.1	0.44	0.67	0.73	0.016	0.021
0.66	0.11	5.91	8.94	4.71×10^1	73.4	0.37	1.01	0.73	0.014	0.022
1.06	∞	6.52	4.75	∞	224	1.00	0	0.73	∞	∞
1.06	4.7	6.53	4.60	3.58×10^3	231	1.03	0.00074	0.73	0.39	0.018
1.05	3.0	6.54	4.61	1.97×10^3	228	1.02	0.0018	0.73	0.25	0.018
1.06	2.0	6.52	4.72	1.16×10^3	227	1.01	0.0042	0.73	0.17	0.018
1.07	1.5	6.50	4.88	8.22×10^2	220	0.98	0.0073	0.73	0.13	0.018
1.07	0.98	6.51	4.83	4.70×10^2	222	0.99	0.017	0.73	0.084	0.018
1.06	0.88	6.50	4.91	4.16×10^2	216	0.96	0.020	0.73	0.077	0.018
1.06	0.79	6.50	5.00	3.62×10^2	212	0.95	0.026	0.73	0.069	0.018
1.07	0.68	6.47	5.17	3.12×10^2	209	0.93	0.034	0.73	0.061	0.019
1.07	0.59	6.49	5.24	2.57×10^2	204	0.91	0.046	0.73	0.053	0.019
1.07	0.49	6.46	5.52	2.14×10^2	195	0.87	0.065	0.73	0.045	0.019
1.10	0.39	6.42	5.97	1.69×10^2	185	0.83	0.10	0.73	0.037	0.020
1.11	0.29	6.39	6.44	1.24×10^2	173	0.77	0.18	0.73	0.030	0.020
1.14	0.19	6.29	7.57	8.38×10^1	152	0.68	0.41	0.73	0.021	0.022
1.20	0.15	6.15	9.51	7.33×10^1	127	0.57	0.67	0.73	0.018	0.025
2.87	∞	6.31	10.2	∞	282	1.00	0	0.73	∞	∞
2.87	1.4	6.31	10.3	1.66×10^3	279	0.99	0.00073	0.73	0.18	0.025
2.90	0.76	6.28	10.6	7.39×10^2	273	0.97	0.026	0.73	0.099	0.026
2.91	0.57	6.27	10.9	5.11×10^2	267	0.95	0.046	0.73	0.075	0.027
2.97	0.37	6.22	11.7	3.16×10^2	253	0.90	0.10	0.73	0.051	0.027
3.04	0.28	6.15	12.9	2.36×10^2	236	0.84	0.18	0.73	0.041	0.028
3.08	0.19	6.10	13.6	1.45×10^2	225	0.80	0.41	0.73	0.028	0.030

Table 6.2: NoMag Water Study Non-Dimensional Experimental Values: Ra_F is the flux Rayleigh number, E is the Ekman number, Pr is the Prandtl number, Ra is the Rayleigh number, $\widetilde{Ra}$ is the reduced Rayleigh number given as: $\widetilde{Ra} = RaE^{\frac{4}{3}}$, Nu is the Nusselt number, $Nu/Nu_{E=\infty}$ is a normalized Nusselt number where $Nu_{E=\infty}$ is the Nusselt value of the RBC case, Fr is the Froude number, $\Gamma/2$ is a half of the aspect ratio of the experimental container where $\Gamma = D/H$, Ro_{ff} is the free-fall Rossby number given by $Ro_{\text{ff}} = \sqrt{RaE^2/Pr}$, and Ro_{cb} is the centrifugal Rossby number given by $Ro_{\text{cb}} = \sqrt{2RaE^2Fr/Pr\Gamma}$.

H	D_i	$\overline{Q_{input}}$	Q	Ω	$\overline{T_{fluid}}$	T_{center}	T_{edge}	ΔT_v	t_{total}	$t_{analyzed}$
(m)	(m)	(W)	(W)	(rpm)	(C)	(C)	(C)	(C)	(hr)	(hr)
0.2017	0.199	209.27	197.90	0	45.62	45.72	45.84	4.14	3.52	0.14
0.2017	0.199	209.56	198.97	0.68	44.59	45.76	44.30	4.33	2.48	1.48
0.2017	0.199	209.53	198.40	1.50	45.52	45.58	45.15	6.08	2.46	1.00
0.2017	0.199	209.49	197.94	3.00	45.83	45.99	45.52	6.99	2.25	0.84
0.2017	0.199	209.49	197.32	4.11	46.73	46.75	46.32	8.85	2.62	1.62
0.2017	0.199	209.33	196.41	6.50	47.84	47.88	47.62	11.9	2.70	0.70
0.2017	0.199	209.23	195.82	8.39	49.53	49.48	49.44	14.1	1.79	0.90
0.2017	0.199	209.21	194.66	11.8	50.18	50.06	50.02	17.0	2.66	0.66
0.2017	0.199	208.17	191.84	15.5	53.37	53.18	53.29	20.1	2.16	0.52
0.2017	0.199	207.94	190.90	20.8	54.91	54.67	54.95	22.6	2.53	0.33
0.2017	0.199	208.05	188.38	41.4	58.62	58.63	58.77	30.4	2.62	0.28
0.2017	0.199	209.01	188.91	60.0	59.33	59.04	59.39	36.2	2.42	0.20
0.2017	0.199	811. 84	799.63	0	45.86	46.33	45.70	12.7	2.74	1.24
0.2017	0.199	808.65	796.35	0.96	45.48	46.10	45.36	12.7	1.34	0.54
0.2017	0.199	807.87	794.28	3.10	46.98	47.41	47.10	16.3	2.70	1.20
0.2017	0.199	808.00	793.93	4.40	48.62	49.29	48.77	19.2	1.53	0.33
0.2017	0.199	807.53	792.16	6.50	49.62	49.91	49.62	23.4	1.94	1.94

0.2017	0.199	806.73	788.67	9.60	53.70	53.94	53.47	30.2	2.32	0.82
0.2017	0.199	805.27	781.62	20.8	61.13	61.30	61.06	48.5	2.81	0.81
0.2017	0.199	804.11	766.87	31.0	67.47	67.88	67.84	68.0	1.71	0.40
0.2017	0.199	1601.40	1584.31	0	57.00	57.62	57.24	20.3	2.48	0.88
0.2017	0.199	1597.60	1580.60	0.68	58.37	59.55	58.37	20.6	2.27	1.00
0.2017	0.199	1598.32	1580.88	1.20	56.74	57.94	56.60	21.7	2.51	0.51
0.2017	0.199	1595.52	1577.64	1.50	–	–	–	21.4	1.79	1.00
0.2017	0.199	1597.25	1578.91	2.50	58.23	59.26	58.52	24.6	1.46	0.46
0.2017	0.199	1593.77	1574.89	4.11	62.38	62.86	61.99	26.9	1.50	1.00
0.2017	0.199	1593.74	1570.71	8.39	67.22	67.26	66.69	37.8	4.05	1.55
0.2017	0.199	1589.94	1560.52	15.9	74.54	74.53	73.95	57.0	2.51	1.01
0.2017	0.199	1587.65	1555.25	20.8	80.99	81.14	80.71	67.3	3.24	1.00
0.2017	0.199	1581.94	1542.16	31.0	90.54	90.99	90.60	90.9	1.93	0.75
0.2017	0.199	1580.00	1535.01	41.4	96.92	97.62	98.04	108	2.10	1.10

Table 6.3: RoMag Metal Study Dimensional Experimental Values: H is the fluid container height, D_i is the inner fluid container diameter, Q_{input} is the measured mean input heating power, Q is the heating rate calculated to be applied to the device after accounting for horizontal conductive losses, Ω is the rotation rate of the fluid container, $\overline{T_{fluid}}$ is the mean fluid temperature, T_{center} is the local fluid temperature at $h \simeq 0.5H$ and $r \simeq 0R$, T_{edge} is the local fluid temperature at $h \simeq 0.5H$ and $r \simeq R$, ΔT_v is the vertical temperature difference, t_{total} is the total experimental time, and $t_{analyzed}$ is the portion of time over which equilibrated data is analyzed. Single solid horizontal lines separate fixed applied heat cases for clarity.

$\frac{Ra_F}{10^8}$	$10^7 E$	$10^2 Pr$	$\frac{Ra}{10^8}$	$\widetilde{Ra}$	Nu	$\frac{Nu}{Nu_{E=\infty}}$	Fr	$\frac{\Gamma}{2}$	Ro_{ff}	Ro_{cb}
1.11	∞	2.06	0.11	∞	9.89	1.00	0	0.50	∞	∞
1.11	490	2.08	0.12	2.08×10^1	9.51	0.96	5.0×10^{-5}	0.50	1.16	0.012
1.11	220	2.07	0.16	1.01×10^1	6.76	0.68	0.00025	0.50	0.62	0.014
1.11	100	2.05	0.19	4.07×10^0	5.86	0.59	0.0010	0.50	0.31	0.014

1.11	80.0	2.06	0.24	3.84×10^{0}	4.62	0.47	0.0019	0.50	0.27	0.017
1.11	50.0	2.04	0.32	2.78×10^{0}	3.41	0.34	0.0046	0.50	0.20	0.019
1.12	39.0	2.02	0.39	2.37×10^{0}	2.89	0.29	0.0077	0.50	0.17	0.021
1.11	27.0	2.02	0.47	1.76×10^{0}	2.38	0.24	0.015	0.50	0.13	0.023
1.11	20.0	1.98	0.56	1.42×10^{0}	1.98	0.20	0.026	0.50	0.11	0.024
1.12	15.0	1.97	0.64	1.09×10^{0}	1.75	0.18	0.047	0.50	0.085	0.026
1.12	7.50	1.93	0.88	6.00×10^{-1}	1.28	0.13	0.19	0.50	0.051	0.031
1.12	1.50	1.92	1.04	4.25×10^{-1}	1.08	0.11	0.40	0.50	0.038	0.034
4.48	∞	2.06	0.34	∞	13.1	1.00	0	0.50	∞	∞
4.45	350	2.07	0.34	3.93×10^{1}	12.9	0.99	0.00010	0.50	1.43	0.020
4.47	100	2.05	0.44	9.51×10^{0}	10.1	0.78	0.0011	0.50	0.46	0.022
4.50	74.0	2.03	0.53	7.57×10^{0}	8.59	0.66	0.0021	0.50	0.38	0.025
4.55	50.0	2.02	0.64	5.50×10^{0}	7.07	0.54	0.0046	0.50	0.28	0.027
4.59	33.0	1.98	0.85	4.17×10^{0}	5.40	0.41	0.010	0.50	0.22	0.031
4.71	15.0	1.91	1.41	2.43×10^{0}	3.33	0.26	0.047	0.50	0.13	0.040
4.82	9.50	1.85	1.83	1.71×10^{0}	2.64	0.20	0.11	0.50	0.095	0.045
9.37	∞	1.95	0.58	∞	16.2	1.00	0	0.50	∞	∞
9.44	260	1.93	0.59	9.50×10^{1}	15.9	0.98	5.0×10^{-5}	0.50	2.50	0.025
9.33	200	1.95	0.62	4.77×10^{1}	15.0	0.93	1.6×10^{-4}	0.50	1.47	0.026
9.46	120	1.91	0.62	3.37×10^{1}	15.3	0.95	2.5×10^{-4}	0.50	1.14	0.026
9.39	100	1.93	0.71	1.94×10^{1}	13.3	0.82	6.9×10^{-4}	0.50	0.73	0.027
9.55	76.0	1.89	0.79	1.18×10^{1}	12.1	0.75	0.0018	0.50	0.49	0.030
9.74	35.0	1.85	1.13	6.03×10^{0}	8.59	0.53	0.0077	0.50	0.27	0.034
10.0	18.0	1.79	1.77	3.86×10^{0}	5.67	0.35	0.028	0.50	0.18	0.043
10.3	13.3	1.73	2.15	3.14×10^{0}	4.78	0.30	0.047	0.50	0.15	0.046
10.6	8.60	1.66	3.01	2.47×10^{0}	3.51	0.22	0.11	0.50	0.12	0.054
10.8	6.30	1.62	3.66	1.98×10^{0}	2.95	0.18	0.19	0.50	0.095	0.058

Table 6.4: RoMag Metal Study Non-Dimensional Experimental Values: Ra_F is the flux Rayleigh number, E is the Ekman number, Pr is the Prandtl number, Ra is the Rayleigh number, $\widetilde{Ra}$ is the reduced Rayleigh number given as: $\widetilde{Ra} = RaE^{\frac{4}{3}}$, Nu is the Nusselt number, $Nu/Nu_{E=\infty}$ is a normalized Nusselt number where $Nu_{E=\infty}$ is the Nusselt value of the RBC case, Fr is the Froude number, $\Gamma/2$ is a half of the aspect ratio of the experimental container where $\Gamma = D/H$, Ro_{ff} is the free-fall Rossby number given by $Ro_{\text{ff}} = \sqrt{RaE^2/Pr}$, and Ro_{cb} is the centrifugal Rossby number given by $Ro_{\text{cb}} = \sqrt{2RaE^2Fr/Pr\Gamma}$.

CHAPTER 7

The Spin Up of a Fluid in a Cylindrical Container Using Smooth and Rough Boundaries

7.1 Introduction

To date, the theory involving the fluid mechanical process of an impulsively generated linear spin up of a homogenous fluid in an axisymmetric container confined by smooth boundaries has been well-verified, both numerically and experimentally [e.g. Warn-Varnas et al. (1978), Duck and Foster (2001)]. Such spin up processes, alongside thermal convection, are thought cause viscous coupling between planetary fluid cores and mantles [Brito et al. (2004), Roberts and Aurnou (2012a)]. Earth's ocean floor is characterized as a rough boundary over which seawater flows and spin up processes occur. Furthermore, a detailed understanding of the spin up processes occurring over the small-scale topography of the ocean floor in relation to the turbulent mixing of the ocean is not well-characterized to date [e.g. Kunze and Smith (2004)]. Small-scale roughness is also believed to play a role in the spin up process occurring at the core mantle boundary [e.g. Mouël et al. (2006)].

Well-accepted theory involving the spin up process of a homogeneous fluid confined by rough boundaries has yet to be established. As a result, there exists a lack of numerical simulations and experiments involving such a physical process [cf. Burmann and Noir (2018)]. While numerous experiments have been conducted in order to study the role of thermal convection in rapidly rotating systems [cf. Aubert et al. (2001), Stellmach et al. (2014), Cheng et al. (2015), Aurnou et al. (2018)] as well as the effect of small-scale topography on rapidly rotating convection [e.g. Calkins et al. (2012b)], the spin up process over roughness in such rotating systems with possible planetary applications is not well-studied. We present results

characterizing the spin up of a homogenous fluid in an axisymmetric container confined by both smooth and rough boundaries in order to ultimately gain a greater understanding of the spin up process of a fluid with rough boundaries. In Section 7.2, the theoretical framework for linear spin up of a fluid confined by smooth boundaries is detailed. The experimental method is described in Section 7.3, and experimental results are presented in Section 7.4. Our present conclusions and the future work of this study are discussed in Section 7.5.

7.2 Theoretical Formulation

A well-accepted linear theory exists to characterize the hydrodynamics involved during the process of an impulsively generated spin up of a rotating, axisymmetric cylindrical container of homogeneous fluid bounded by two parallel smooth disks [Greenspan and Howard (1963); Benton and Clark (1974); Weidman (1976)]. Suppose that such a cylinder and fluid rotate together with a uniform initial angular velocity, Ω_i, about the symmetry axis until the angular velocity of the cylinder is suddenly increased by an incremental value, $\Delta\Omega$, and is maintained at this new value, $\Omega_i + \Delta\Omega$. Initially, the bulk of the fluid away from any boundaries remains unperturbed and geostrophic, meaning that the flow field remains nearly two-dimensional, with little variation along the direction of the rotation axis [Brito et al. (2004)]. Layers of fluid near horizontal boundaries begin to rotate faster due to viscous stress [Benton and Clark (1974)]. Fluid in such horizontal layers is subsequently driven radially outward due to the dominance of the centrifugal force over the pressure gradient in these layers.

The strength of viscous forces relative Coriolis forces in rotating systems is measured by the Ekman number, $E = \frac{\nu}{2\Omega_i h^2}$. The thin layer of fluid in which there exists a force balance between viscous forces and the Coriolis force is known as the Ekman boundary layer, which has a thickness that is described as $\delta_E \sim \sqrt{\frac{\nu}{2\Omega_i}}$ [Cushman-Roisin and Beckers (2011)]. In a process known as Ekman suction, replacement fluid from the interior is sucked into the boundary due to mass conservation, creating a field of secondary circulations such that interior fluid is transported towards the axis of rotation. Furthermore, this replacement fluid retains its angular momentum such that fluid rings concentric with the cylinder's axis

of symmetry spin faster as their radii decrease [Benton and Clark (1974)].

The described spin up process is complete once all of the fluid inside of the cylinder reaches the angular velocity of the cylinder itself. The characteristic spin up time can be expressed in terms of the Ekman number, E, as:

$$\tau = (8E)^{-1/2}\Omega_i^{-1} \tag{7.1}$$

[Greenspan and Howard (1963)]. This characteristic spin up time, τ, holds for low Ekman and low Rossby numbers, or the strength of inertial forces over the Coriolis force, and has been verified both numerically and experimentally using homogenous fluids in axisymmetric cylinders with smooth, parallel boundaries [e.g. Brito et al. (2004)]. As shown by the Ekman dependence in (7.1), the spin up time depends on the height of fluid columns aligned parallel to the rotation axis due to the fact that a portion of the bulk fluid remains unperturbed and geostrophic during the spin up process [Pedlosky (1987)]. Thus, a longer column requires a longer time for the fluid within the column to cycle through the viscous (Ekman) boundary layer by way of Ekman suction [Busse and Carrigan (1976)]. Furthermore, the azimuthal velocity determined in the rotating reference frame is characterized as:

$$u_\phi = s\Delta\Omega e^{\frac{-\Delta t}{\tau}}, \tag{7.2}$$

where Δt is the time after an incremental change in rotation rate, $\Delta\Omega$, and s is the radius of the cylinder [Brito et al. (2004)].

As stated by Greenspan and Howard (1963), the Ekman spin up time, $\tau \sim E^{-1/2}$, controls the re-establishment of solid body rotation rather than the slower viscous diffusion time, $\tau_\nu \sim E^{-1}$. To understand this phenomenon, we note that after only two radians of system rotation upon impulse, i.e. $\Omega t \approx 2$, radial outflow that is accelerated from rest by centrifugal imbalance generated by the impulse induces a three-dimensional axial flow from the interior towards each boundary to satisfy mass conservation requirements [Benton and Clark (1974)]. This three-dimensional axial flow becomes fully-developed and quasi-steady within the Ek-

man boundary layer. Superimposed on such a quasi-steady axial flow are inertial oscillations occurring at 2Ω, or twice the frequency of rotation. These inertial oscillations are excited by the impulse and propagate into the interior bulk fluid and are deemed "unimportant" to the overall spin up process by Greenspan and Howard (1963) due to their small amplitudes, on the order of $E^{1/2}$. The small nature of these inertial oscillations is due, in part, to the fact that they feed on the vorticity supplied by the rotation of the bulk interior fluid, thus causing the amplitudes of the inertial oscillations themselves to gradually decrease in time as the spin up process completes [Benton and Clark (1974)].

7.3 Experimental Methodology

The UCLA NoMag device is used in this study, with the MSE UltraLDV instrument mounted in the rotating frame of the apparatus to collect laser doppler velocimetry (LDV) measurements. The LDV instrument is oriented so as to obtain azimuthal point velocity time series during spin up experiments. Azimuthal point velocity measurements are obtained at a non-dimensional radius of $r \simeq 0.84s$ for all experiments and are independent of the height placement of the instrument. The experimental results presented in Section 7.4 are the first experiments to be conducted on the NoMag device since its construction. The agreement between measurements obtained using this experimental apparatus of the well-studied spin up process of a fluid confined by smooth boundaries with well-established theory validates the use of the device and the LDV method for future studies.

In order to effectively measure the spin up process of a homogeneous fluid, a cylindrical tank of $D = 60$ cm diameter and a variable height of $h = 40$ or 185 cm was filled with water (with a small amount of added TiO_2 for flow traceability) and spun to solid body rotation at several different rotation rates. Two aluminum cylindrically shaped plates serve as boundaries to fluid inside the cylinders and are placed on the ends of the experimental cylinder. Both smooth and rough plates have been machined for usage as boundaries. In the case of a smooth boundary, no pyramidal roughness exists and the boundary is made of machined flat, smooth aluminum. Figure 7.1 shows a sketch of our rough boundary plate

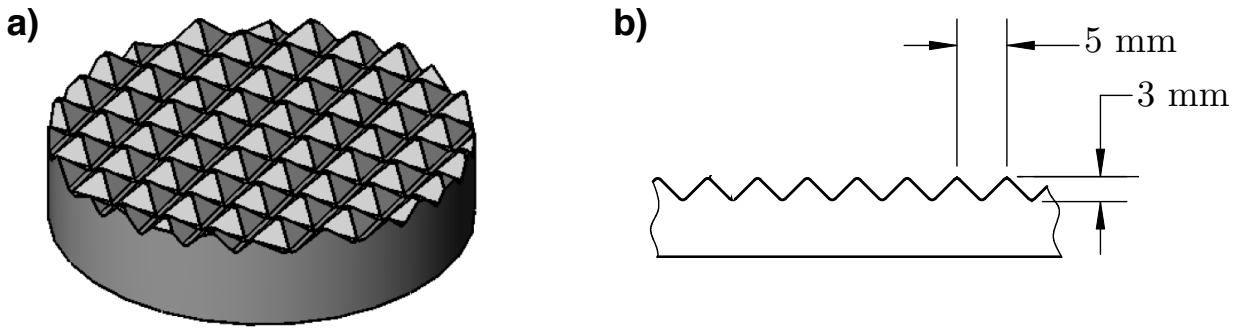

Figure 7.1: a) A drawing of the cylindrical aluminum rough plate used as a boundary to fluid inside the central acrylic cylinder on the UCLA NoMag device. b) An enhanced side view of the rough plate where roughness is created by 3 mm tall aluminum pyramids spaced 5 mm apart. Not shown is a smooth cylindrical aluminum plate, also used as a fluid boundary on this device.

in which 3 mm tall aluminum triangular pyramids spaced 5 mm apart serve as the surface of the boundary in contact with the interior fluid. Note that the use of two different tank heights allows for experimental verification of the predicted directly proportional relationship between tank height and spin up time given in (7.1).

Initial rotation rates at which solid body rotation was first established of $\Omega_i = 10$, 20, 30, and 40 rpm were used, and changes in rotation rate of $\Delta\Omega = 1$, 2, and 4 rpm were used for each initial rotation rate. For each case, the LDV measurement system in the rotating frame was used to record fluid velocities. Upon the detection of zero relative fluid velocities by the LDV instrument, indicating solid body rotation at Ω_i, the rotation rate of the cylinder was changed by $\Delta\Omega$ and fluid velocities were recorded until zero relative velocities were attained and solid body rotation was re-established, indicating the completion of the spin up process. The dimensional and non-dimensional values of all experimental parameters are provided in Tables 7.1 and 7.2 of Appendix A in Section 7.6, respectively.

7.4 Experimental Results

7.4.1 Linear Homogeneous Spin Up Using Smooth Boundaries

Figure 7.2 shows the azimuthal velocity time series of several smooth boundary spin up cases, where the azimuthal velocity is normalized by $s\Delta\Omega$ on the y-axis, while time on the x-axis is normalized by τ as given in (7.1). Dashed black lines in each velocity profile correspond to theoretical spin up velocity curves described by (7.2). The profiles of four different smooth boundary spin up cases with varied values for Ω_i, $\Delta\Omega$, and h are shown in order to display the overall robustness of the spin up process and strong agreement with theory despite these varied parameters. Greenspan and Howard (1963) assert that the insignificance of excited inertial oscillations is largely due to their small amplitudes, i.e initially on the order of $E^{1/2}$. Nonetheless, the high resolution of the LDV instrument used to obtain the profiles shown in Fig. 7.2 enables the observation of these inertial oscillations throughout the spin up process within measured azimuthal velocity profiles.

Specifically, while the LDV instrument is capable of accurately measuring fluid velocities at values as low as 10^{-4} m/s [cf. Section 3.7], the initial amplitudes of inertial oscillations in the fluid velocities of spin up cases for both the $h = 0.4$ m and $h = 1.85$ m containers range between 5 x 10^{-4} to 10^{-3} m/s. Figure 7.3 shows the fast Fourier transforms (FFT) of two cases shown in b) and c) of Fig. 7.2, where $h = 0.4$ m. Parts i. and iii. of Fig. 7.3 show a portion of the normalized velocity-time profiles of these two cases in which oscillatory motion is evident. Further, FFTs of the profiles shown in i. and iii., taken after detrending and interpolating the data, are shown in ii. and iv., respectively, in which frequency on the x-axis is normalized by the initial rotation rate, Ω_i. Parts ii. and iv. of Fig. 7.3 clearly show a primary peak at Ω, corresponding to the rotation rate of the container, while a distinct secondary peak at 2Ω also exists, corresponding to the impulse generated inertial oscillations occurring at twice the initial rotation rate [Greenspan and Howard (1963)].

In order to further examine the agreement between the experimental and theoretical velocity profiles displayed in Fig. 7.2, an experimental spin up time, which we denote as τ_{meas} as opposed to $\tau_{\text{theory}} = \tau$ given by (7.1), was determined. Specifically, taking the natural

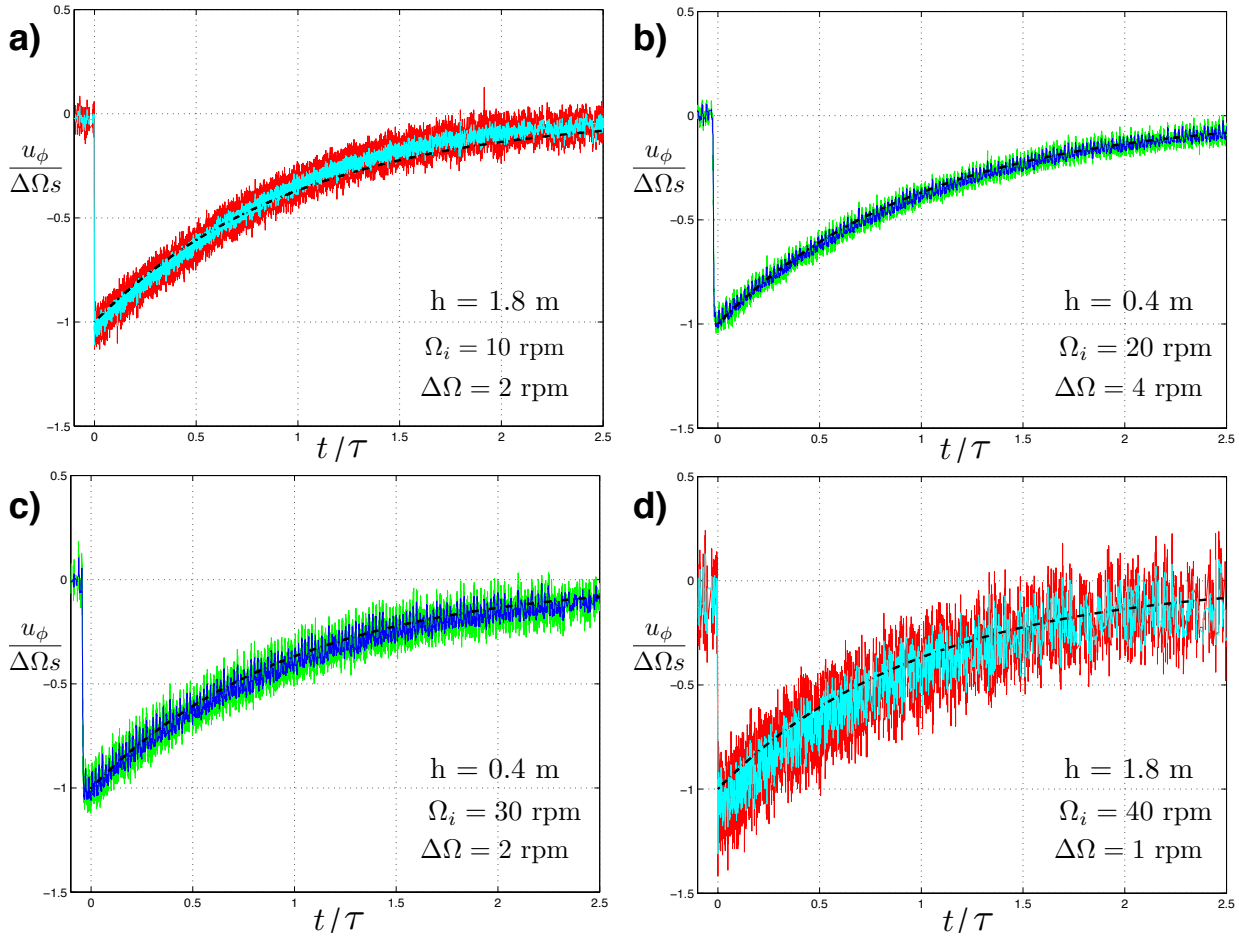

Figure 7.2: Normalized azimuthal velocity, u_ϕ, vs. normalized time profiles of four different spin up cases with varied values for Ω_i, $\Delta\Omega$, and h. Azimuthal velocity is normalized by dividing by $s\Delta\Omega$, while time is normalized by dividing by τ. Un-averaged and 10 point windowed averaged data for $h = 1.85$ m data are shown in red and cyan, respectively, while un-averaged and 10 point window averaged data for $h = 0.4$ m are shown in green and blue, respectively. Black dashed lines correspond to theoretical spin up curves described by (7.2). a) $\Omega_i = 10$ rpm, $\Delta\Omega = 2$ rpm $h = 1.85$ m; b) $\Omega_i = 20$ rpm, $\Delta\Omega = 4$ rpm $h = 0.4$ m; c) $\Omega_i = 30$ rpm, $\Delta\Omega = 2$ rpm $h = 0.4$ m; d) $\Omega_i = 40$ rpm, $\Delta\Omega = 1$ rpm $h = 1.85$ m.

logarithm of (7.2) after normalization results in the following:

$$ln\left(\frac{u_\phi}{s\Delta\Omega}\right) = \frac{-\Delta t}{\tau}, \tag{7.3}$$

where u_ϕ is the velocity measured by the LDV. The slope of a linear fit of (7.3) is therefore proportional to $\frac{-1}{\tau_{\text{meas}}}$. Thus, the experimentally measured spin up time, τ_{meas}, is the time to which the velocity profile takes to decay by one e-folding. Figure 7.4 displays $\frac{\tau_{\text{meas}}}{\tau_{\text{theory}}}$ versus initial rotation rate in rpm for all smooth boundary spin up cases for $\Omega_i = 10$, 20, 30, and

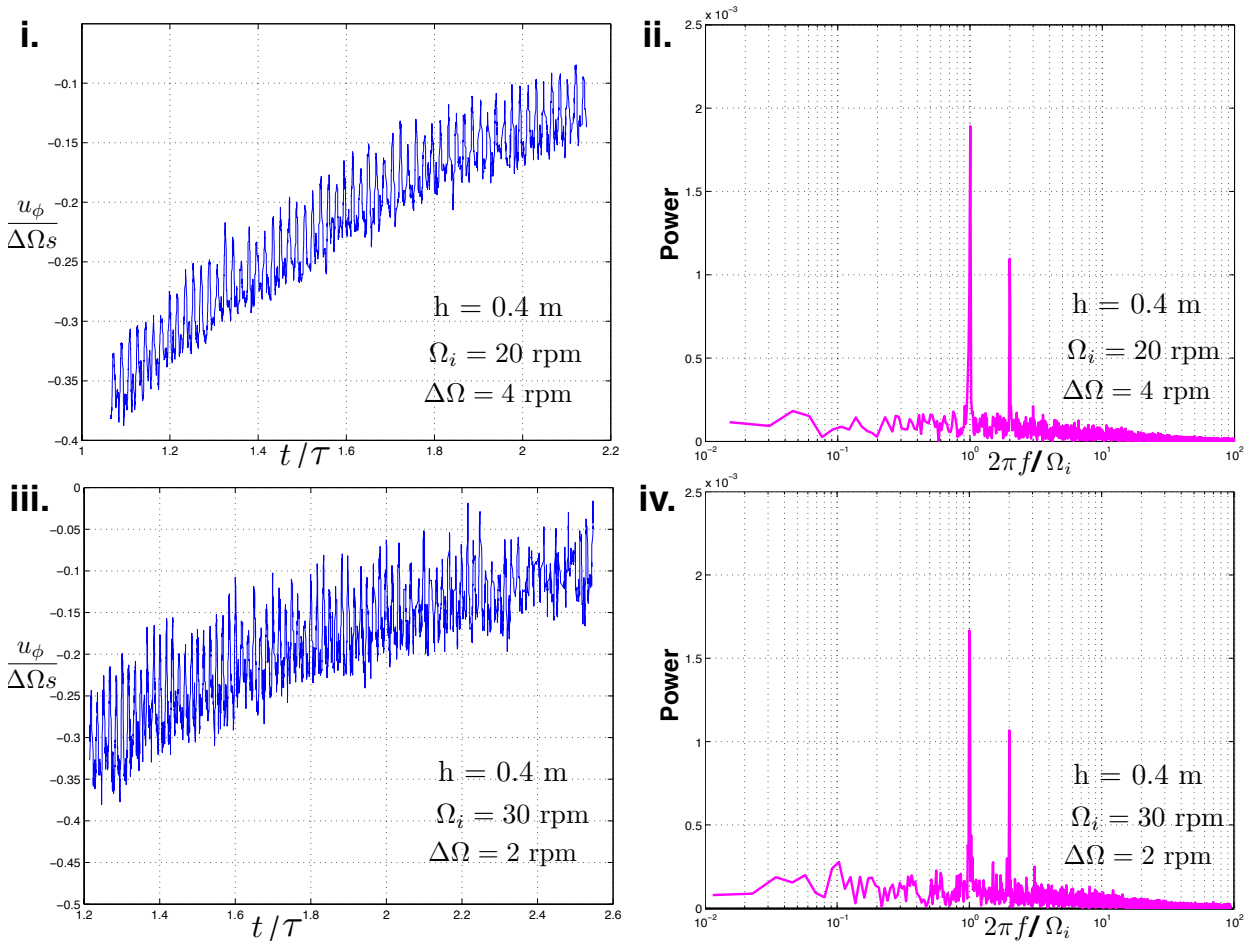

Figure 7.3: i. Portion of a normalized velocity-time profile shortly after impulse for $\Omega_i = 20$ rpm, $\Delta\Omega = 4$ rpm $h = 0.4$ m; ii. FFT of data shown in i. after detrending and interpolating the profile, where the x-axis is normalized by rotation rate, Ω_i; iii. Portion of a normalized velocity-time profile shortly after impulse for $\Omega_i = 30$ rpm, $\Delta\Omega = 2$ rpm $h = 0.4$ m; iv. FFT of data shown in iii. after detrending and interpolating the profile, where the x-axis is normalized by rotation rate, Ω_i. Plots ii. and iv. show a distinct peak at 1 corresponding to the rotation rate of the container, as well as a peak a 2, corresponding to the inertial oscillations occurring at twice the rotation rate of the container.

40 with $\Delta\Omega = 1$, 2, and 4 rpm for each Ω_i for both $h = 0.4$ m (circles) and $h = 1.85$ m (squares). The diameter of each symbol is proportional to the Rossby number, i.e. a larger circular or cubic diameter at each Ω_i corresponds to a larger value of $\Delta\Omega$. A resulting linear fit, indicated by the solid black line, to all data in this figure shows a very small slope ($\sim 10^{-4}$) in which all data converge approximately to a value of unity, meaning measured experimental spin up times match theoretical values well.

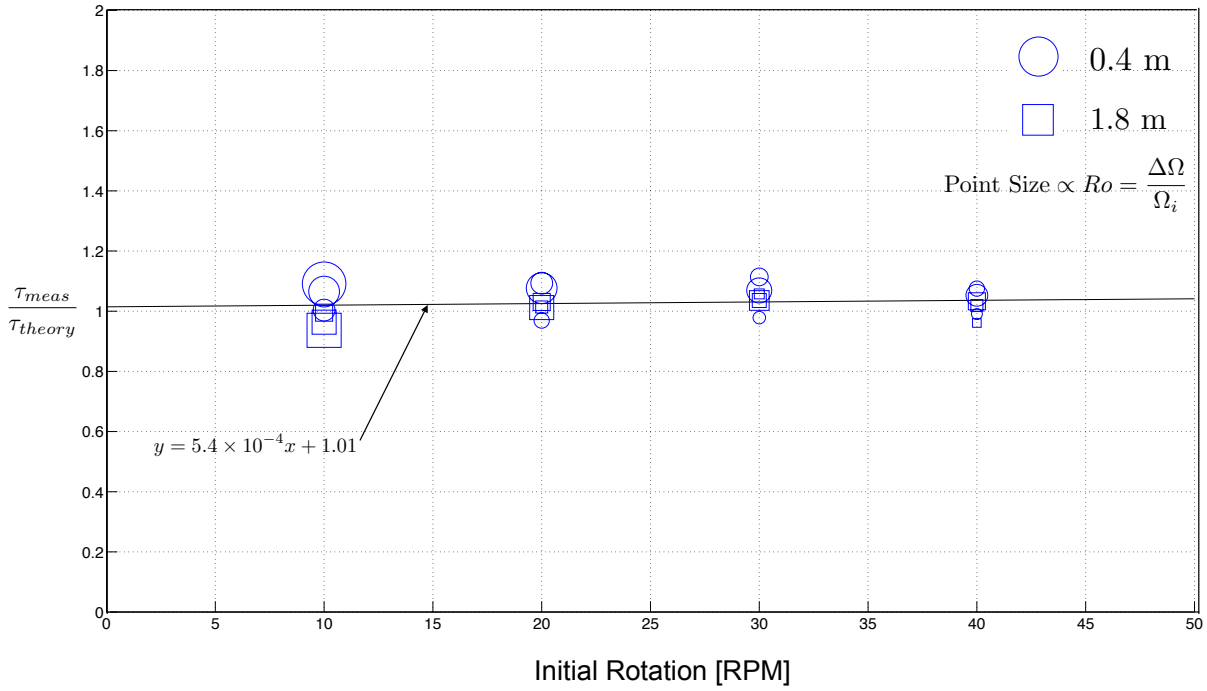

Figure 7.4: $\frac{\tau_{meas}}{\tau_{theory}}$ vs. initial rotation rate in rpm for all smooth boundary spin up cases for Ω_i = 10, 20, 30, and 40 with $\Delta\Omega$ = 1, 2, and 4 rpm for each Ω_i for both h = 0.4 m (circles) and h = 1.85 m tanks (squares). The diameter of each symbol is proportional to the Rossby number, i.e. a larger circular or cubic diameter at each Ω_i corresponds to a greater value of $\Delta\Omega$. A resulting linear fit, indicated by the solid black line, to all data in this figure shows a very small slope in which all data converge approximately to a value of unity, meaning measured experimental spin up times match theoretical values.

7.4.2 Homogeneous Spin Up Using Rough Boundaries

The rough plate shown in Fig. 7.1 was placed as the bottom boundary in both the h = 0.4 m and h = 1.85 m containers in order to test the effects of a rough boundary on the spin up process. All smooth boundary cases shown in Fig. 7.4 were repeated. While well-accepted theory surrounding the spin up process using rough boundaries is not established to date, one might reasonably expect that a rough boundary enhances the turbulent motions occurring during Ekman suction throughout the spin up process, resulting in the time it takes for the fluid to enter solid body rotation to occur more quickly. Figure 7.5 shows the normalized azimuthal velocity versus normalized time profiles of four different spin up cases with a rough bottom boundary with varied values for Ω_i, $\Delta\Omega$, and h. Black dashed lines, corresponding to theoretical spin up curves described by (7.2), show the difference in the spin up process

with the existence of a rough bottom boundary from the predicted process using two smooth boundaries. In each case shown in Fig. 7.5, the exponential velocity curve appears steeper than the smooth boundary prediction characterized in (7.2), meaning the spin up process does indeed complete more quickly.

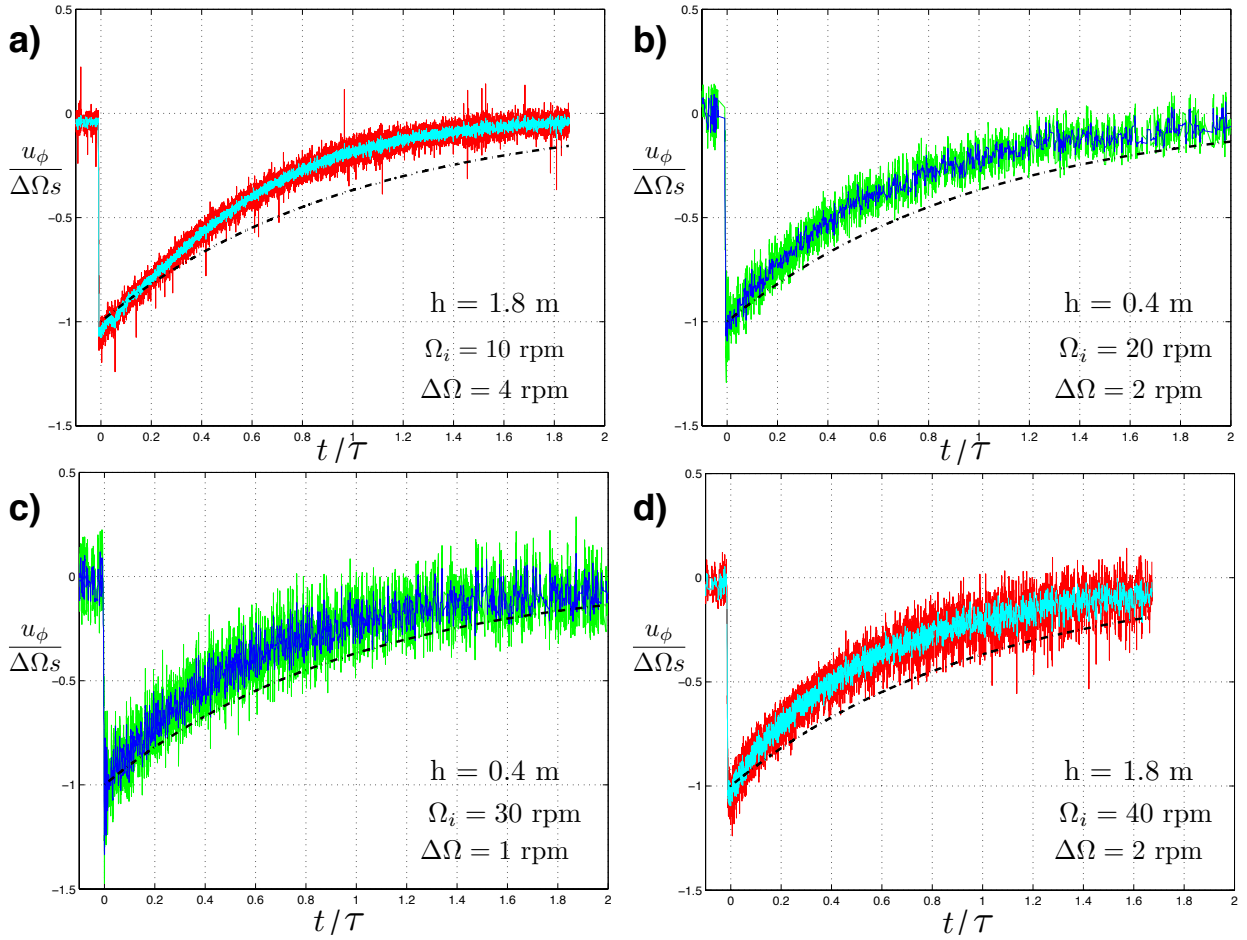

Figure 7.5: Normalized azimuthal velocity vs. normalized time profiles of four different spin up cases with a rough bottom boundary with varied values for Ω_i, $\Delta\Omega$, and h. Azimuthal velocity is normalized by dividing by $s\Delta\Omega$, while time is normalized by dividing by τ. Un-averaged and 10 point windowed averaged data for $h = 1.85$ m data are shown in red and cyan, respectively, while un-averaged and 10 point window averaged data for $h = 0.4$ m are shown in green and blue, respectively. Black dashed lines correspond to theoretical spin up curves described by (7.2). a) $\Omega_i = 10$ rpm, $\Delta\Omega = 4$ rpm $h = 1.85$ m; b) $\Omega_i = 20$ rpm, $\Delta\Omega = 2$ rpm $h = 0.4$ m; c) $\Omega_i = 30$ rpm, $\Delta\Omega = 1$ rpm $h = 0.4$ m; d) $\Omega_i = 40$ rpm, $\Delta\Omega = 2$ rpm $h = 1.85$ m.

One might also expect that the existence of two rough boundaries imposed upon a homogeneous fluid might further expedite the spin up process. Figure 7.6 shows normalized azimuthal velocity versus time for two cases in which two rough boundaries were used. Black

dashed lines representing theoretical spin up profiles with smooth boundaries show an even greater difference in steepness with experimental profiles shown in blue (un-averaged data) and green (averaged data). Furthermore, a comparison of a) and b) in Fig. 7.6, respectively, with those in Fig. 7.5 shows an even more dramatic change in the exponential nature of the azimuthal velocity over time throughout the spin up process, indicating the completion of the spin up process occurs even faster with the inclusion of two rough boundaries.

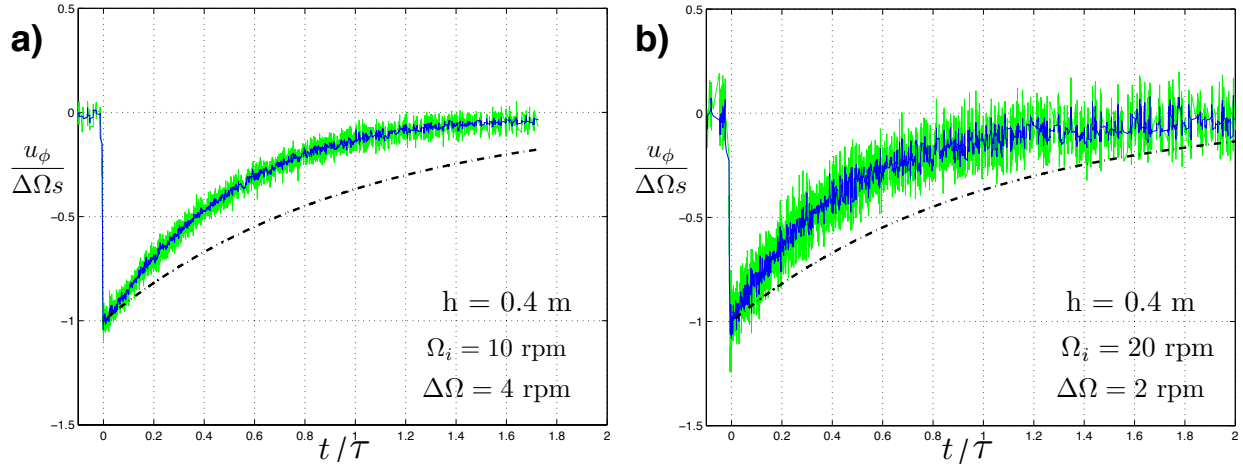

Figure 7.6: Normalized azimuthal velocity, u_ϕ, vs. normalized time profiles of four different spin up cases with two rough bottom boundaries with varied values for Ω_i, $\Delta\Omega$, and h. Azimuthal velocity is normalized by dividing by $s\Delta\Omega$, while time is normalized by dividing by τ. Un-averaged and 10 point windowed averaged data for $h = 0.4$ m are shown in green and blue, respectively. Black dashed lines correspond to theoretical spin up curves described by (7.2). a) $\Omega_i = 10$ rpm, $\Delta\Omega = 4$ rpm $h = 0.4$ m; b) $\Omega_i = 20$ rpm, $\Delta\Omega = 2$ rpm $h = 0.4$ m.

Inertial oscillations generated shortly after impulse for each respective spin up case using a rough bottom boundary and two rough boundaries also appear to be evident in data shown in both Fig. 7.5 and 7.6. Figure 7.7 shows the FFT profiles of two cases shown in b) and d) of Fig. 7.5. Parts i. and iii. of Fig. 7.7 show a portion of the normalized velocity-time profiles of these two cases in which oscillatory motion can be observed. Further, FFTs of the profiles shown in i. and iii. after detrending and interpolating the data are shown in ii. and iv., respectively, in which frequency on the x-axis is normalized by the initial rotation rate, Ω_i. Parts ii. and iv. of Fig. 7.7 clearly show a peak at Ω, corresponding to the rotation rate of the container, while a distinct peak at 2Ω also exists, corresponding to the impulse generated inertial oscillations occurring at twice the initial rotation rate as described by

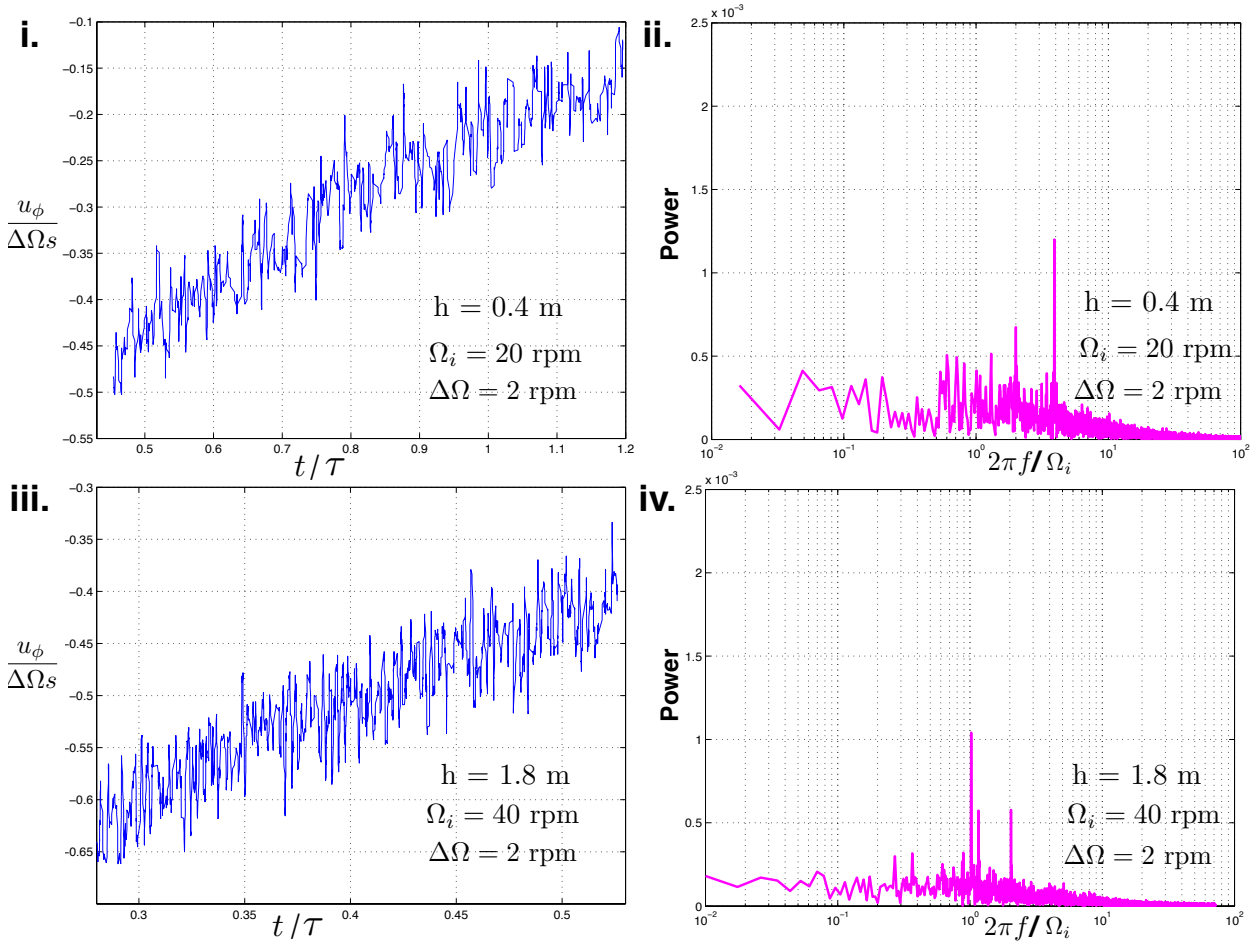

Figure 7.7: i. Portion of a normalized velocity-time profile shortly after impulse for $\Omega_i = 20$ rpm, $\Delta\Omega = 2$ rpm $h = 0.4$ m; ii. FFT of data shown in i. after detrending and interpolating the profile where the x-axis is normalized by rotation rate, Ω_i; iii. Portion of a normalized velocity-time profile shortly after impulse for $\Omega_i = 40$ rpm, $\Delta\Omega = 2$ rpm $h = 1.85$ m; iv. FFT of data shown in iii. after detrending and interpolating the profile where the x-axis is normalized by rotation rate, Ω_i. Plots ii. and iv. show a distinct peak at 1 corresponding to the rotation rate of the container, as well as a peak a 2, corresponding to the inertial oscillations occurring at twice the rotation rate of the container. Other discernible peaks correspond to subharmonics.

Greenspan and Howard (1963). We purport that other discernible peaks in ii. and iv. of Fig. 7.7 correspond to several subharmonics of the rotation rate of the container. While the velocity profiles shown in i. and iii. of Fig. 7.7 do not appear to have oscillatory motion as evident as that shown in i. and iii. of Fig. 7.3 and the FFT profiles shown in ii. and iv. of Fig. 7.7 contain several other discernible peaks other than those at Ω and 2Ω, the relatively large amplitude of the peaks existing at Ω and 2Ω in ii. and iv. of Fig. 7.7 suggest that inertial oscillations do occur and are still evident in the spin up process when using rough

boundaries. Very similar FFT profiles to those shown in ii. and iv. of Fig. 7.7 also exist for two rough boundary cases shown in Fig. 7.6.

The theory developed by Greenspan and Howard (1963) for the linear spin up of a homogeneous fluid with two smooth boundaries can be applied to experimental data using rough boundaries in order to examine evident differences in the spin up processes with the different boundary types. Figure 7.8 shows $\frac{\tau_{meas}}{\tau_{theory}}$ versus initial rotation rate in rpm for all rough boundary spin up cases (red corresponds to a rough bottom boundary; green corresponds to two rough boundaries) with $h = 0.4$ m data represented as circles and $h = 1.85$ m represented as squares, similarly to that of Fig. 7.4. The same process described using (7.3) is used in order to determine an experimental spin up time, τ_{meas}. Fig. 7.8 shows that experimentally measured spin up times are consistently faster than theoretical values for smooth boundaries. Furthermore, linear fits to both rough bottom and two rough boundary data, denoted as solid black lines, show a clear linear relationship between rotation rate and normalized spin up times, i.e. for higher rotation rate cases, the effect of the rough boundary is even more evident in decreasing the spin up time.

An argument using the container's aspect ratio, defined as $\Gamma = D/h$ where D is the diameter and h is the height of the cylinder, can be made in order to explain the differences between rough bottom boundary and two rough boundary data shown in Fig. 7.8. Figure 7.9a) shows the different values of Γ for the $h = 0.4$ m and $h = 1.85$ m containers. Fig. 7.9b) shows the expected difference in the fluid circulation patterns due to Ekman suction for a rough bottom boundary and two rough boundary spin up cases. As shown in the rightmost image in Fig. 7.9b), it is predicted that there are twice as many circulation cells when using two rough boundaries rather than one rough bottom boundary in which the bottom roughness dominates the Ekman suction process with two large cells. Furthermore, according to Fig. 7.9, the perimeter, P, of these circulation cells with a rough bottom boundary can be written as:

$$P_{1rough} = 2\frac{D}{2} + 2h = h\left(\Gamma + 2\right), \tag{7.4}$$

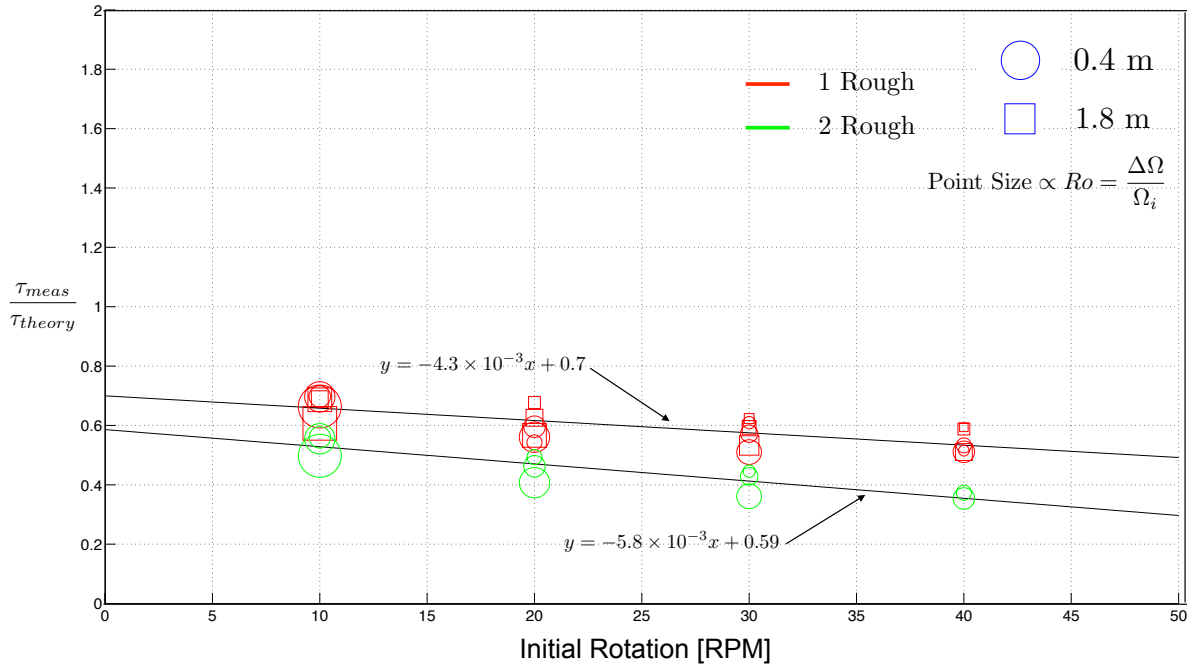

Figure 7.8: $\frac{\tau_{meas}}{\tau_{theory}}$ vs. initial rotation rate in rpm for all rough bottom boundary spin up cases (red) and two rough boundary cases (green) for $\Omega_i = 10$, 20, 30, and 40 with $\Delta\Omega = 1$, 2, and 4 rpm for each Ω_i for both $h = 0.4$ m (circles) and $h = 1.85$ m (squares). The diameter of each symbol is proportional to the Rossby number. Solid black lines correspond to linear fits to one rough and two rough boundary cases. The slopes of such linear fits are one order of magnitude larger than in Fig. 7.4 and indicate a possible linear trend in data for both boundary situations. As $\frac{\tau_{meas}}{\tau_{theory}}$ is less than 1 in all cases, experimental spin up times occur faster than theory predicts for smooth boundaries, as expected.

whereas the perimeter of the circulation cells with two rough boundaries is written as:

$$P_{2rough} = 2\frac{D}{2} + 2\frac{h}{2} = h\left(\Gamma + 1\right). \tag{7.5}$$

The spin up time is directly proportional to the perimeter of an Ekman circulation cell. Thus, using (7.4) and (7.5), the relation between the spin up time using a rough bottom boundary and two rough boundaries can be written as:

$$\frac{\tau_{2rough}}{\tau_{1rough}} = \frac{2+\Gamma}{1+\Gamma}. \tag{7.6}$$

As shown in Fig. 7.9, $\Gamma = 3/2$ for the $h = 0.4$ m tank and $\Gamma = 1/3$ for the $h = 1.85$ m tank. Hence, according to (7.6), $\tau_{2rough} = \frac{7}{5}\tau_{1rough}$ for the $h = 0.4$ m tank and $\tau_{2rough} = \frac{7}{4}\tau_{1rough}$

for the $h = 1.85$ m tank. Two rough boundary data was only collected using the $h = 0.4$ m tank in this set of experiments.

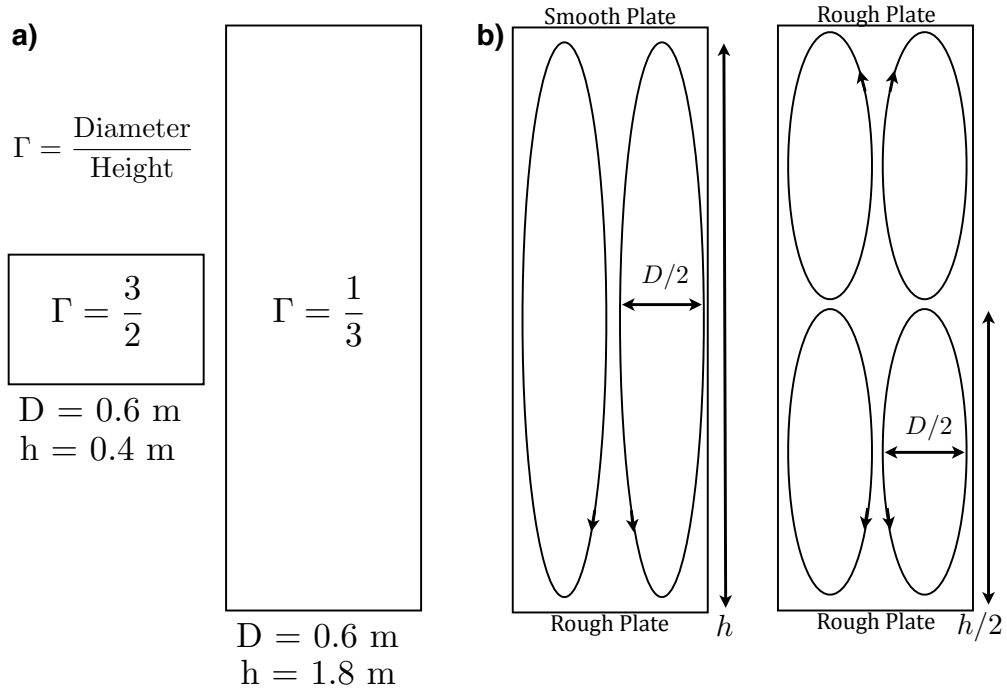

Figure 7.9: a) Relatively scaled diagrams of the two different tanks used in spin up experiments with given aspect ratios defined as $\Gamma = D/h$. b) The expected difference in fluid circulation patterns for a rough bottom boundary versus two rough boundaries using the $h = 1.85$ m tank as an example.

Figure 7.10 shows $\frac{\tau_{meas}}{\tau_{theory}}$ versus initial rotation rate in rpm for all spin up cases including two smooth boundaries (blue), rough bottom and smooth top boundaries (red), as well as two rough boundaries (green), with $h = 0.4$ m data represented as circles and $h = 1.85$ m represented as squares. The relationship between the spin up times for rough bottom and two rough boundary data given by (7.6) has been applied to data shown in Fig. 7.10 such that two rough boundary data is now collapsed with rough bottom data. As shown by Fig. 7.10, rough bottom and two rough boundary data now align well, with a linear equation of fit (solid black line) displaying an overall linear trend between spin up time and rotation rate in rough boundary data. Contrarily, smooth boundary data (blue) show a very small slope and indicate values align well such that experimentally measured spin up times match theoretical values characterized by (7.1).

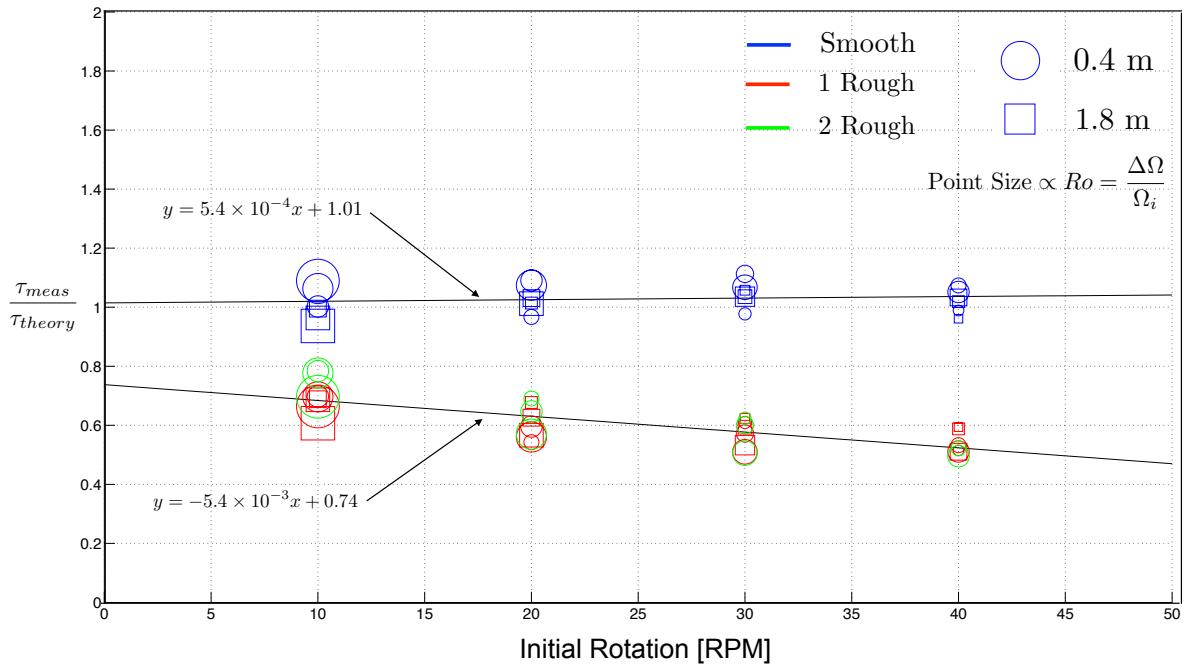

Figure 7.10: $\frac{\tau_{meas}}{\tau_{theory}}$ vs. initial rotation rate in rpm for all smooth spin up cases (smooth, rough bottom, and collapsed two rough boundaries) for Ω_i = 10, 20, 30, and 40 with $\Delta\Omega$ = 1, 2, and 4 rpm for each Ω_i = for both h = 0.4 m (circles) and h = 1.85 m (squares). The diameter of each symbol is proportional to the Rossby number. Two rough boundary data is now collapsed with rough bottom boundary data using outlined aspect ratio and circulation pattern arguments. While a linear fit (solid black line) to smooth boundary data show a small slope and indicate a strong agreement between theoretical and measured spin up times, a linear fit to rough boundary data shows a possible linear trend in data with measured spin up times that occur faster than is predicted by theory for smooth boundaries.

7.4.3 The Convergence of Smooth and Rough Boundary Spin Up Results

We make several attempts to further collapse the rough boundary data shown in Fig. 7.10 in order to explain the effects of rough boundaries on spin up time. First, boundary roughness height (d = 0.003 m) was compared to Ekman layer height in order to test whether or not effect of the dominance of the physical height of the rough boundary over the Ekman layer might explain the faster spin up times displayed in Fig. 7.10. Specifically, Figure 7.11 shows $\frac{\tau_{meas}}{\tau_{theory}}$ versus a parameter defined as:

$$\chi = \frac{\text{roughness height}}{\text{Ekman layer height}} = \frac{d}{\delta_E}. \tag{7.7}$$

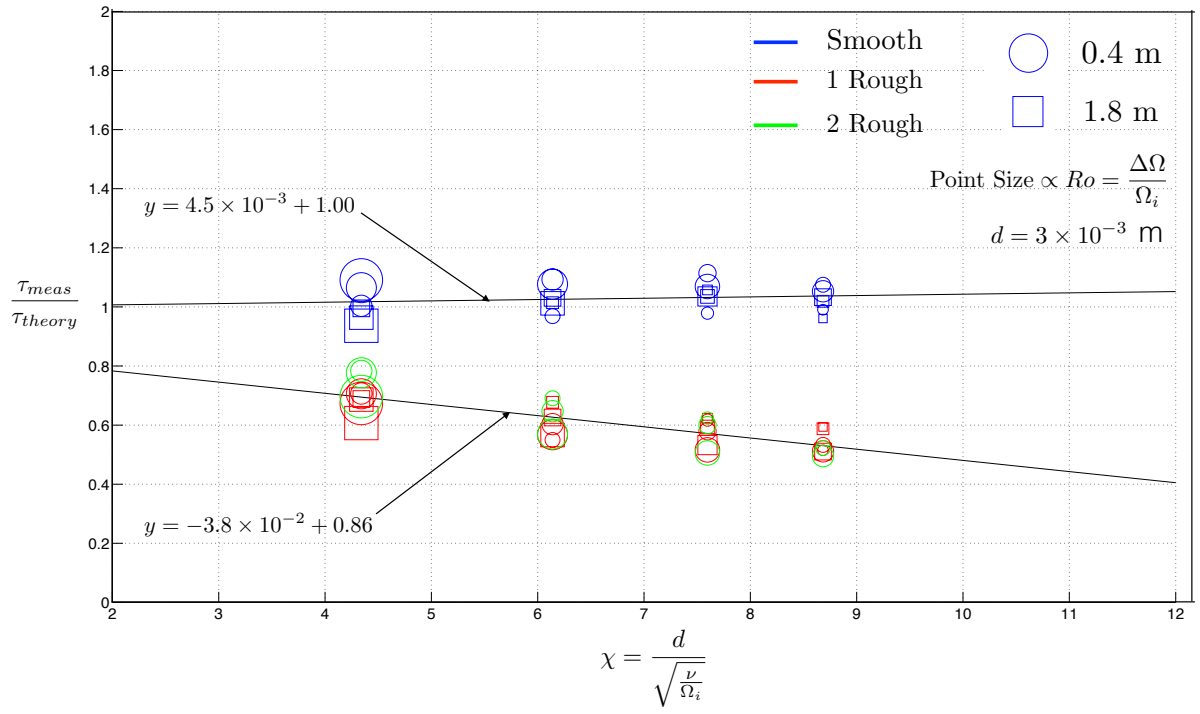

Figure 7.11: $\frac{\tau_{meas}}{\tau_{theory}}$ vs. χ, defined as roughness height divided by Ekman layer height. Scaling the x-axis by this defined parameter, χ, is directly proportional to scaling the x-axis by rotation rate, as shown in figure 7.10.

Note that τ_{theory} used to normalize the y-axis is still given by (7.1) and is based off the use of smooth boundaries. Plotting $\frac{\tau_{meas}}{\tau_{theory}}$ versus the defined parameter χ is directly proportional to plotting versus rotation rate as shown by the similarity to Fig. 7.10. Furthermore, Fig. 7.11 therefore suggests that the decrease in measured spin up times with rough boundaries is also linearly proportional to our defined parameter χ. Thus, the influence of the physical roughness height over the Ekman layer alone cannot explain the observed decrease in spin up times when using rough boundaries.

While the parameter χ is plotted on the x-axis for all spin up data in Fig. 7.11, the roughness height, d, does not apply to smooth boundary data. Thus, a perhaps more

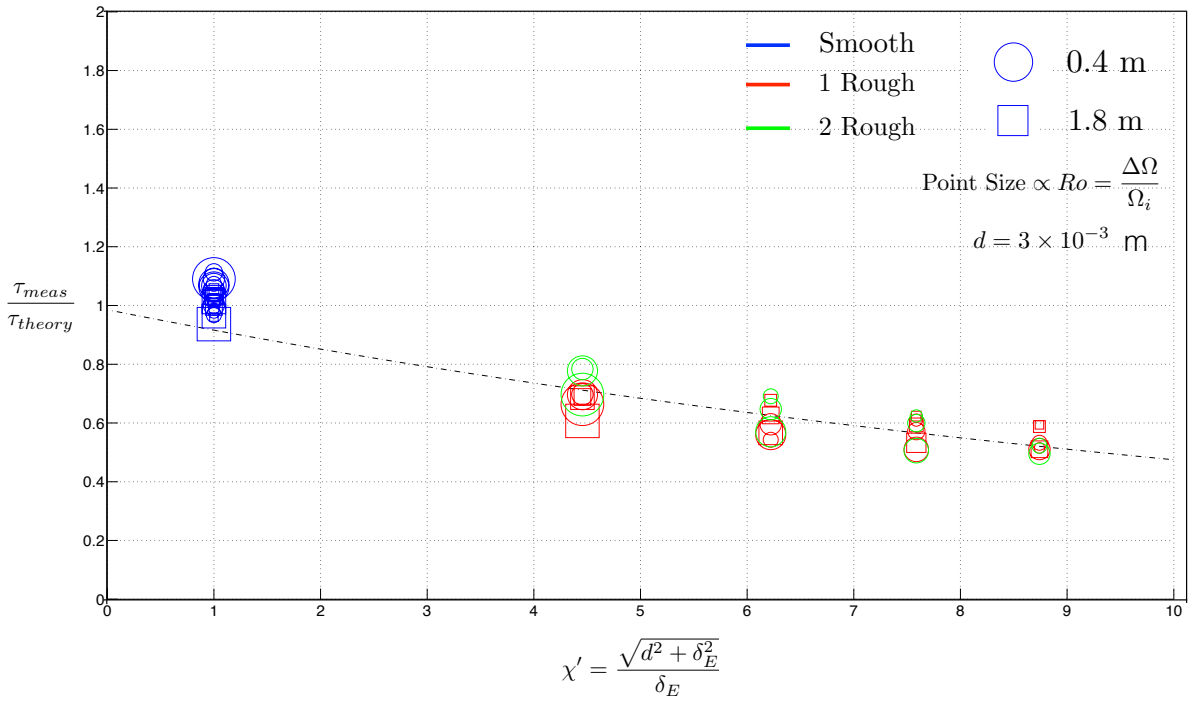

Figure 7.12: $\frac{\tau_{meas}}{\tau_{theory}}$ vs. $\chi' = \frac{\sqrt{d^2+\delta_E^2}}{\delta_E}$ where δ_E is the Ekman layer height. Using this x-axis scaling, all smooth boundary data is collapsed as shown. There appears to be a possible exponential correlation between data as shown by the dashed line.

accurate parameter to use on the x-axis of such plots is given by:

$$\chi' = \frac{\sqrt{d^2 + \delta_E^2}}{\delta_E}. \tag{7.8}$$

Hence, when using smooth boundaries (roughness height d = 0 m) this parameter then reduces to unity. Therefore, all smooth boundary spin up data should collapse to unity on both the x and y axes when plotting with this new parameter. Figure 7.12 shows $\frac{\tau_{meas}}{\tau_{theory}}$ versus χ' for all spin up cases. As expected, all smooth boundary data collapses to unity on both axes. Furthermore, it appears in Fig. 7.12 that there might be an exponential trend in the data. Nonetheless, the use of this new parameter more accurately attempts to use

roughness height dominance over Ekman layer height in order to explain the reduction in spin up times using rough boundaries, an attempt does not appear to work either. Thus, we can conclude that the reason for the reduction in spin up times using rough boundaries is more than the simple effect of the dominance of roughness height over Ekman layer height.

An additional attempt was also made in order to explain the reduction in spin up times using rough boundaries by accounting for the turbulent diffusivity, defined as $\nu_\tau = d^2\Delta\Omega$, introduced to the system with the use of rough boundaries. We define a new spin up time, which we call $\tau_{\text{theorynew}}$, to normalize y-axis data by first simplifying the expression given in (7.1). Re-writing (7.1) in terms of dimensional parameters, h, ν, and Ω yields:

$$\tau_{theory} = \frac{h}{\sqrt{2\nu\Omega}}. \tag{7.9}$$

In order to account for turbulent diffusivity effects, the molecular viscosity, ν, can be re-written to include the turbulent diffusivity, ν_τ, as $\sqrt{\nu^2 + \nu\tau^2}$. Further, a newly defined spin up time, $\tau_{theorynew}$ can be expressed based on (7.9) as:

$$\tau_{theorynew} = \frac{h}{\sqrt{\sqrt{\nu^2 + \nu_\tau^2}2\Omega}}. \tag{7.10}$$

Figure 7.13 shows the y-axis, the measured spin up time, now normalized by (7.10) versus rotation rate in rpm for all spin up cases. As shown, while values begin to converge towards unity, it is clear that accounting for the effect of turbulent diffusivity alone in the spin up time formula given by (7.10) when using rough boundaries does not properly account for the reduction in measured spin up times when using rough boundaries. Thus, we have exhausted the use of this simple turbulent model in our attempt to explain the effects of rough boundaries on the spin up process.

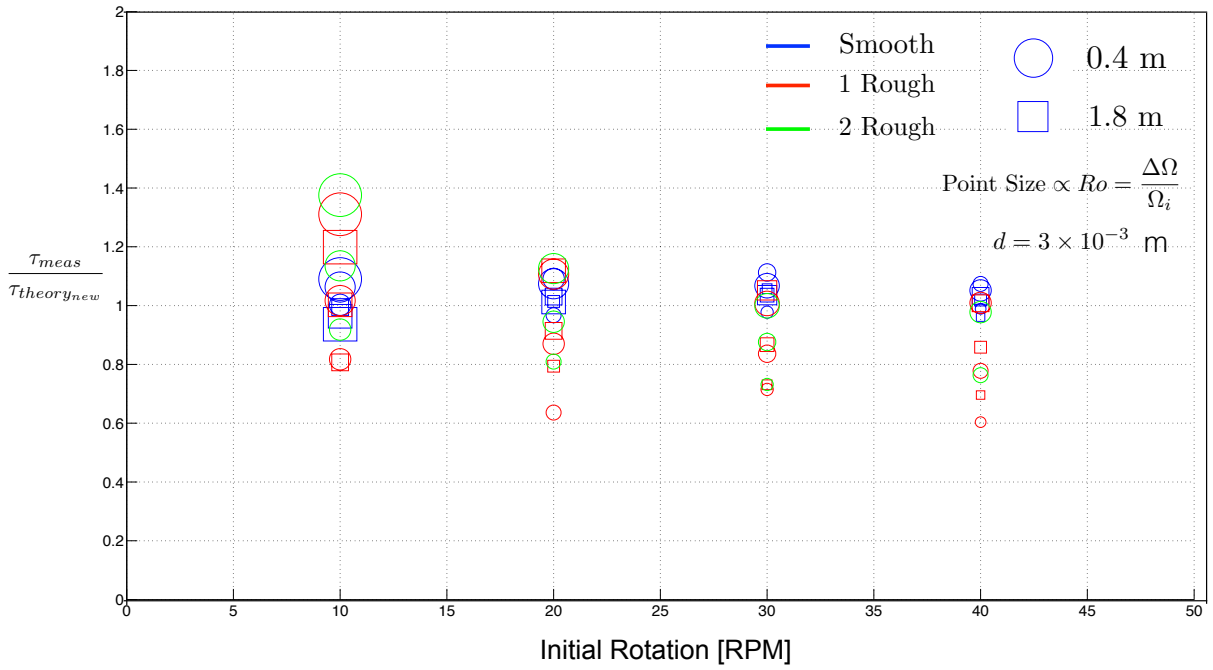

Figure 7.13: $\frac{\tau_{meas}}{\tau_{theorynew}}$ vs. rotation rate in rpm, where $\tau_{\text{theorynew}}$ accounts for turbulent diffusivity introduced by a rough boundary. While values on the y-axis for all cases begin to converge towards a value of unity, this method of accounting for turbulent diffusivity with $\tau_{theorynew}$ alone does not explain the difference in spin up times occurring when rough boundaries are used.

7.5 Discussion

Experimental measurements of azimuthal fluid velocities throughout the spin up process obtained using LDV on the UCLA NoMag device have been completed. The strong agreement between well-established theory surrounding the linear spin up of a homogeneous fluid in an axisymmetric container confined by smooth boundaries and experimental measurements validates the the use of the LDV technique on the NoMag device. Experimentally obtained results of the spin up process of a fluid bounded by small-scale roughness show that the spin up process occurs significantly faster (i.e. by approximately 40% for rough bottom cases and by approximately 60% for two rough boundary cases) when compared to well-characterized

theory for the use of smooth boundaries. Furthermore, it appears as though there might be a linear correlation between the decrease in spin up times and the rotation rate of the container, Ω_i.

While a number of simple models to account for the induced turbulence by the pyramidal rough boundaries used in experimental cases have been applied to presented results, it does not appear as though the decrease in spin up times can be fully explained by such simple turbulence models. Nonetheless, the results presented in this study that highlight the differences in the spin up process of a homogeneous fluid in an axisymmetric container between smooth boundaries and pyramidal rough boundaries are the first to date. Further work must be done in order to provide a more thorough explanation for the difference in the physical processes that occur with the use of small-scale topographic boundaries leading to a faster spin up. Such a detailed explanation will provide a more comprehensive understanding of several physical processes in which the fluid dynamical spin up over roughness is relevant, possibly including viscous coupling existing at Earth's core mantle boundary as well as turbulent mixing in the global ocean.

7.6 Appendix A: Data Tables for Spin Up Experiments

Case	Boundaries	H (m)	Ω_i (rad/s)	$\Delta\Omega$ (rad/s)	τ_{meas} (s)	τ_{theory} (s)
1	2 smooth	0.4	10	1	195.93	195.44
2	2 smooth	0.4	10	2	207.77	195.44
3	2 smooth	0.4	10	4	213.073	195.44
4	2 smooth	0.4	20	1	133.65	138.20
5	2 smooth	0.4	20	2	150.76	138.20
6	2 smooth	0.4	20	4	148.47	138.20
7	2 smooth	0.4	30	1	110.31	112.84
8	2 smooth	0.4	30	2	125.56	112.84

9	2 smooth	0.4	30	4	120.46	112.84
10	2 smooth	0.4	40	1	96.64	97.72
11	2 smooth	0.4	40	2	104.93	97.72
12	2 smooth	0.4	40	4	102.77	97.72
13	2 smooth	1.85	10	1	875.23	879.48
14	2 smooth	1.85	10	2	847.53	879.48
15	2 smooth	1.85	10	4	823.56	879.48
16	2 smooth	1.85	20	1	630.66	621.89
17	2 smooth	1.85	20	2	640.99	621.89
18	2 smooth	1.85	20	4	629.41	621.89
19	2 smooth	1.85	30	1	537.03	507.77
20	2 smooth	1.85	30	2	525.85	507.77
21	2 smooth	1.85	30	4	525.82	507.77
22	2 smooth	1.85	40	1	422.47	439.74
23	2 smooth	1.85	40	2	448.08	439.74
24	2 smooth	1.85	40	4	454.24	439.74
25	rough bottom	0.4	10	1	136.30	195.44
26	rough bottom	0.4	10	2	136.08	195.44
27	rough bottom	0.4	10	4	129.71	195.44
28	rough bottom	0.4	20	1	75.00	138.20
29	rough bottom	0.4	20	2	82.31	138.20
30	rough bottom	0.4	20	4	77.44	138.20
31	rough bottom	0.4	30	1	68.79	112.84
32	rough bottom	0.4	30	2	64.60	112.84
33	rough bottom	0.4	30	4	57.56	112.84
34	rough bottom	0.4	40	1	50.31	97.72
35	rough bottom	0.4	40	2	52.06	97.72
36	rough bottom	0.4	40	4	49.94	97.72
37	rough bottom	1.85	10	1	605.35	879.48

38	rough bottom	1.85	10	2	603.65	879.48
39	rough bottom	1.85	10	4	533.83	879.48
40	rough bottom	1.85	20	1	421.24	621.89
41	rough bottom	1.85	20	2	389.14	621.89
42	rough bottom	1.85	20	4	352.23	621.89
43	rough bottom	1.85	30	1	316.49	507.77
44	rough bottom	1.85	30	2	301.40	507.77
45	rough bottom	1.85	30	4	270.41	507.77
46	rough bottom	1.85	40	1	261.02	439.74
47	rough bottom	1.85	40	2	258.45	439.74
48	rough bottom	1.85	40	4	224.44	439.74
49	2 rough	0.4	10	1	153.14	195.44
50	2 rough	0.4	10	2	151.91	195.44
51	2 rough	0.4	10	4	136.15	195.44
52	2 rough	0.4	20	1	95.46	138.20
53	2 rough	0.4	20	2	89.42	138.20
54	2 rough	0.4	20	4	78.78	138.20
55	2 rough	0.4	30	1	70.40	112.84
56	2 rough	0.4	30	2	67.68	112.84
57	2 rough	0.4	30	4	57.09	112.84
58	2 rough	0.4	40	1	–	97.72
59	2 rough	0.4	40	2	51.07	97.72
60	2 rough	0.4	40	4	48.39	97.72

Table 7.1: Dimensional Values for Spin Up Experiments: Boundaries are either two smooth, one rough bottom with a smooth top, or two rough. H is the tank height in (m), Ω_i is the initial rotation rate of the container in (rad/s), $\Delta\Omega$ is the incremental change in rotation rate in (rad/s), τ_{meas} is the measured experimental spin up time in (s), and τ_{theory} is the theoretical spin up time according to (7.1) in (s).

Case	Boundaries	Γ	E	Ro	$\tau_{\text{meas}}/\tau_{\text{theory}}$
1	2 smooth	1.5	2.98×10^{-6}	0.1	1.00
2	2 smooth	1.5	2.98×10^{-6}	0.2	1.06
3	2 smooth	1.5	2.98×10^{-6}	0.4	1.09
4	2 smooth	1.5	1.49×10^{-6}	0.05	0.97
5	2 smooth	1.5	1.49×10^{-6}	0.1	1.09
6	2 smooth	1.5	1.49×10^{-6}	0.2	1.07
7	2 smooth	1.5	9.95×10^{-7}	0.033	0.98
8	2 smooth	1.5	9.95×10^{-7}	0.066	1.11
9	2 smooth	1.5	9.95×10^{-7}	0.133	1.07
10	2 smooth	1.5	7.46×10^{-7}	0.025	0.99
11	2 smooth	1.5	7.46×10^{-7}	0.05	1.07
12	2 smooth	1.5	7.46×10^{-7}	0.1	1.05
13	2 smooth	0.33	1.47×10^{-7}	0.1	1.00
14	2 smooth	0.33	1.47×10^{-7}	0.2	0.96
15	2 smooth	0.33	1.47×10^{-7}	0.4	0.94
16	2 smooth	0.33	7.37×10^{-8}	0.05	1.01
17	2 smooth	0.33	7.37×10^{-8}	0.1	1.03
18	2 smooth	0.33	7.37×10^{-8}	0.2	1.01
19	2 smooth	0.33	4.91×10^{-8}	0.033	1.06
20	2 smooth	0.33	4.91×10^{-8}	0.066	1.04
21	2 smooth	0.33	4.91×10^{-8}	0.133	1.04
22	2 smooth	0.33	3.68×10^{-8}	0.025	0.96
23	2 smooth	0.33	3.68×10^{-8}	0.05	1.02
24	2 smooth	0.33	3.68×10^{-8}	0.1	1.03
25	rough bottom	1.5	2.98×10^{-6}	0.1	0.70
26	rough bottom	1.5	2.98×10^{-6}	0.2	0.70
27	rough bottom	1.5	2.98×10^{-6}	0.4	0.66

28	rough bottom	1.5	1.49×10^{-6}	0.05	0.54
29	rough bottom	1.5	1.49×10^{-6}	0.1	0.60
30	rough bottom	1.5	1.49×10^{-6}	0.2	0.56
31	rough bottom	1.5	9.95×10^{-7}	0.033	0.61
32	rough bottom	1.5	9.95×10^{-7}	0.066	0.57
33	rough bottom	1.5	9.95×10^{-7}	0.133	0.51
34	rough bottom	1.5	7.46×10^{-7}	0.025	0.51
35	rough bottom	1.5	7.46×10^{-7}	0.05	0.53
36	rough bottom	1.5	7.46×10^{-7}	0.1	0.51
37	rough bottom	0.33	1.47×10^{-7}	0.1	0.69
38	rough bottom	0.33	1.47×10^{-7}	0.2	0.69
39	rough bottom	0.33	1.47×10^{-7}	0.4	0.61
40	rough bottom	0.33	7.37×10^{-8}	0.05	0.68
41	rough bottom	0.33	7.37×10^{-8}	0.1	0.63
42	rough bottom	0.33	7.37×10^{-8}	0.2	0.57
43	rough bottom	0.33	4.91×10^{-8}	0.033	0.62
44	rough bottom	0.33	4.91×10^{-8}	0.066	0.59
45	rough bottom	0.33	4.91×10^{-8}	0.133	0.53
46	rough bottom	0.33	3.68×10^{-8}	0.025	0.59
47	rough bottom	0.33	3.68×10^{-8}	0.05	0.59
48	rough bottom	0.33	3.68×10^{-8}	0.1	0.51
49	2 rough	1.5	2.98×10^{-6}	0.1	0.78
50	2 rough	1.5	2.98×10^{-6}	0.2	0.78
51	2 rough	1.5	2.98×10^{-6}	0.4	0.70
52	2 rough	1.5	1.49×10^{-6}	0.05	0.69
53	2 rough	1.5	1.49×10^{-6}	0.1	0.65
54	2 rough	1.5	1.49×10^{-6}	0.2	0.57
55	2 rough	1.5	9.95×10^{-7}	0.033	0.62
56	2 rough	1.5	9.95×10^{-7}	0.066	0.60

57	2 rough	1.5	9.95×10^{-7}	0.133	0.51
58	2 rough	1.5	7.46×10^{-7}	0.025	–
59	2 rough	1.5	7.46×10^{-7}	0.05	0.52
60	2 rough	1.5	7.46×10^{-7}	0.1	0.50

Table 7.2: Non-Dimensional Values for Spin Up Experiments: Boundaries are either two smooth, one rough bottom with a smooth top, or two rough. Γ is the aspect ratio of the experimental container used, E is the Ekman number using the initial rotation rate, Ω_i, Ro is the Rossby number calculated as $\Delta\Omega/\Omega_i$, and $\tau_{\text{meas}}/\tau_{\text{theory}}$ is the measured experimental spin up time normalized by the theoretical spin up time given by (7.1).

CHAPTER 8

Conclusion

I have conducted laboratory experiments to better constrain the characteristic velocities and length scales of rotating convective turbulence relevant to planetary core flows. Specifically, I have explored the properties of quasi-geostrophic turbulence (QGT) at some of the most extreme laboratory conditions possible to date by conducting the first studies on the UCLA large-scale rotating convection device, NoMag. The results of my study to simultaneously measure the heat and momentum transfer behaviors of accessible rotating convective regimes reveal, for the first time, that heat transfer and system velocity behaviors do not directly couple in the parameter space explored as previously assumed. Instead, I demonstrate that heat transfer is largely controlled by the dynamics of boundary layers of the system, while the QGT velocity regime develops in the fluid bulk–even near to the onset of convection. Further, through the comparison between my laboratory data and the results of numerical models of core-style flows, I conclude that all evidence to date suggests that the theorized characteristic length scales of planetary dynamo systems co-scale with one another and are thus non-separable.

The majority of studies of convection system dynamics focus on the parameterization of global heat transfer and assume that heat transfer dynamics will also describe bulk velocity dynamics of the system. Detailed in Chapter 2, two theoretical scalings exist primarily for the characteristic length scales of rotating convective (RC) flows–the convective onset and turbulent scales. These two length scales underlie the two main velocity scaling predictions for core-style flows–the 'VAC' and 'CIA' scalings, respectively. Meanwhile, the results of many RC heat transfer studies show evidence of two main behavioral regimes in the range of parameters assessed: a regime occurring nearer to the onset of convection in which heat

transfer is dependent on the system rotation, and separately, a regime that resembles non-rotating heat transfer behavior [cf. Rossby (1969), King et al. (2012), Cheng et al. (2015), Gastine et al. (2016)]. While RC length and velocity scaling behaviors are not nearly as well-studied as that of heat transfer, one might predict that the onset length scale and associated VAC velocity scaling will exist in the rotation dependent heat transfer regime existing near onset, whereas the turbulent length scale and CIA velocity scaling will coincide with the non-rotating style heat transfer regime [cf. Fig. 2.3 and 2.4].

This prediction of the correlation between heat transfer and velocity behaviors is directly tested in my laboratory study of Chapter 4. I utilize laser doppler velocimetry (LDV) to obtain point measurements of bulk axial velocities with the simultaneous collection of temperature measurements for the characterization of system heat transfer. I show that heat transfer behavior is largely controlled by boundary layer dynamics, consistent with the results of past studies. However, I find that behavioral transitions in my RC velocity data do not occur where transitions in heat transfer behaviors exist. I instead show that my velocity data agree well with both the VAC and CIA velocity scaling predictions over the range of parameters studied. An explanation of this result lies in the examination of the theoretical length scales of the system. In addition, scaling theory shows that the VAC balance cannot be a leading order balance, but rather is a magnitude equivalence [cf. Section 4.6.2]. Overall, I conclude that while heat transfer and velocity scaling behaviors are not directly coupled in the finite parameter space explored, what can be described as the QGT flow regime develops in the bulk, even near to convective onset. In this flow regime, the CIA scaling holds, with the VAC magnitude equivalence approximately holding as well. Crucially, these findings thus suggest that it is possible to access realistic bulk dynamics in models that remain far from planetary core conditions.

I examine the ratio of estimated convective onset to turbulent length scales for my laboratory data and for the data of the core flow models of Soderlund et al. (2012) and Guervilly et al. (2019) in Chapter 5. I find that for all of the models analyzed, the ratio of onset to turbulent length scales is of order unity, indicating that the two hypothesized length scales are non-separable. Scaling analysis shows that the onset and turbulent length scale estimates

will scale equivalently when the local Reynolds in the geostrophic fluid bulk is of order unity. When the behavior of these equivalent length scales relative to the supercriticality (Ra/RaC) of each model is examined, the data is collapsed by two discernible behavioral trends. The behavior of the ratio of length scales for models near to the onset of convection appears to depend on the supercriticality as nearly $l_{\text{turb}}/l_{\text{crit}} \sim (Ra/Ra_C)^{1/2}$. Farther past onset (i.e. $Ra/Ra_C > 10$) and out to $Ra/Ra_C \sim 10^3$ where the most extreme models lie, data appear to follow a nearly $l_{\text{turb}}/l_{\text{crit}} \sim (Ra/Ra_C)^{1/4}$ scaling, with a $l_{\text{turb}}/l_{\text{crit}} \sim (Ra/Ra_C)^{1/8}$ scaling resulting from linear convective onset theory acting as a lower bound. Future work must be done to discern how each of these three scaling behaviors between the ratio of length scales and supercriticality might be relevant in the determination of the dynamic length scales of planetary core flows. In particular, models that directly quantify the length scales of QGT flow are needed. Nonetheless, this work illuminates the co-scaling of theoretical length and velocity scalings of rotating convection in existing models of core-style convection.

The work in Chapters 4 and 5 improves our understanding of the leading order forces involved in planetary dynamo action by clarifying the relevance of long theorized and poorly tested dynamic length and velocity scalings of planetary core flows. Quasi-geostrophic turbulence, argued to be relevant to flows in planetary cores, exists when the Coriolis and pressure gradient forces of the system balance at leading order in the presence of inertially turbulent convective motions. Here, the CIA velocity scaling and VAC magnitude equivalence both hold. Accordingly, the onset and turbulent length scales co-scale. This described QGT flow regime is robustly found in the laboratory and numerical data of Hawkins et al. (2020) [Chapter 4] that span a broad non-dimensional parameter space, providing a positive outlook for future modeling efforts aimed to further understand QGT flows.

Additional outstanding questions exist regarding the applicability of laboratory and numerical models towards planetary settings. Towards this end, I conducted two studies analyzing the relevance of the physics occurring with different uses of the NoMag large-scale laboratory device. The device and its measuring components are calibrated via a series of spin up experiments discussed in Chapter 7. Using LDV, I find agreement between well-established theory and experimental measurements of fluid spin up in an axisymmetric con-

tainer confined by smooth boundaries, thus validating the use of the NoMag experimental apparatus. Additionally, my experiments of spin up with rough boundaries show that the spin up process is quickened, and ongoing efforts with regards to this work will help provide an explanation for the difference in the physical processes that occur with the introduction of small-scale roughness. The results of this work might have geophysical implications for the possible viscous coupling at Earth's core mantle boundary, as well as turbulent mixing in the global ocean.

I separately conducted a study to examine the effects of centrifugal buoyancy in rapidly rotating laboratory devices such as the NoMag device. The results from my collected data using both water and liquid metal, detailed in Chapter 6, agree with the recent numerical results of Horn and Aurnou (2018) and Horn and Aurnou (2019). My experimental results extend findings far past the onset of convection for the first time. The transition from Coriolis to centrifugally dominated RC depends on the strength of the centrifugal buoyancy relative to the gravitational buoyancy and the geometry of the cylinder in which experiments are conducted. In addition, a horizontal dependence on temperature in which an anomalous strong central upwelling and a simultaneous outer downwelling develops in a regime described as Coriolis-centrifugal (CC) convection. These results are useful to ensure that the regime of RC explored in a given experiment is relevant to planetary core flows, i.e. not centrifugally dominated. Thus, the work described in Chapters 6 and 7 helps validate the use of laboratory devices in the exploration of the properties of rapidly rotating convective turbulence.

Future work using the NoMag laboratory device will be invaluable for enhancing our understanding of the multi-scale turbulent physics driving planetary dynamo systems. In particular, the combined results of the studies presented in this dissertation motivate a study to directly measure the characteristic length scales of QGT flows. The results of such a study will undoubtably shed light on the connection between dynamic length scales and the leading order forces involved in planetary dynamo action.

In the future, I plan to use the knowledge and tools I gained from completing these studies to further enhance our understanding of the key dynamical processes of planetary dynamo systems. In particular, I would like to build an experiment with a spherical shell

geometry and compare turbulent RC measurements of heat and momentum transfer to those of cylindrical experiments. In addition, I plan to extend my knowledge of the fluid physics involved in dynamo action to the study of subsurface ocean dynamics on icy bodies including Europa (a moon of Jupiter) and Enceladus (a moon of Saturn). These fluid layers are subject to strong rotational forces that exist in the presence of both thermal convection and near surface density-driven brine convection. The interaction between global subsurface oceans and observed geologic surface features, while largely unexplored, has important implications for the potential habitability of icy bodies and even Earth-like exoplanets.

Bibliography

G. Ahlers and X. Xu. Prandtl-number dependence of heat transport in turbulent Rayleigh-Bénard convection. *Phys. Rev. Lett.*, 86:3320, 2001.

G. Ahlers, S. Grossmann, and D. Lohse. Heat transfer and large scale dynamics in turbulent Rayleigh-Bénard convection. *Rev. Mod. Phys.*, 81(503), 2009.

T. J. Ahrens, editor. *Mineral physics and crystallography: A handbook of physical constants.* American Geophysical Union, 1995.

H. Amit, R. Leonhardt, and J. Wicht. Polarity reversals from paleomagnetic observations and numerical dynamo simulations. *Space Sci. Rev.*, 155:293–335, 2010.

E. Andrade and C. Da. A theory of the viscosity of liquids. Part II. *Phil. Mag. J. Sci*, 113: 698–732, 1934.

M. Assael, I. Armyra, J. Brillo, S. Stankus, and J. Wu. Reference data for the density and viscosity of liquid cadmium, colbalt, gallium, indium, mercury, silicon, thallium, and zinc. *Phys. Chem. Ref. Data*, 41(3):033101, 2012.

J. Aubert. Steady zonal flows in spherical shell dynamos. *J. Fluid Mech.*, 542:53–67, 2005.

J. Aubert. Approaching Earth's core conditions in high-resolution geodynamo simulations. *Geophys. J. Int.*, 219:137–151, May 2019.

J. Aubert, D. Brito, H. Nataf, P. Cardin, and J. Masson. A systematic experimental study of rapidly rotating spherical convection in water and liquid gallium. *Phys. Earth Planet. Inter.*, 128(1):51–74, 2001.

J. Aubert, N. Gillet, and P. Cardin. Quasigeostrophic models of convection in rotating spherical shells. *Geochemistry Geophysics Geosystems*, 4(1052), 2003.

J. Aubert, J. Aurnou, and J. Wicht. The magnetic structure of convection-driven numerical dynamos. *Geophys. J. Int.*, 172:945–956, 2008.

J. Aubert, T. Gastine, and A. Fournier. Spherical convective dynamos in the rapidly rotating asymptotic regime. *J. Fluid Mech.*, 813:558–593, 2017.

J. Aurnou and E. King. The cross-over to magnetostrophic convection in planetary dynamo systems. *Proc. R. Soc. A*, 473, 2017.

J. Aurnou and P. Olson. Experiments on Rayleigh–Bénard convection, magnetoconvection and rotating magnetoconvection in liquid gallium. *J. Fluid Mech.*, 430:283–307, 2001.

J. Aurnou, S. Andreadis, L. Zhu, and P. Olson. Experiments on convection in Earth's core tangent cylinder. *Earth and Planetary Science Letters*, 212(119-234), 2003.

J. Aurnou, M. Calkins, K. Julien, D. Nieves, K. Soderlund, and S. Stellmach. Rotating convective turbulence in Earth and planetary cores. *Earth and Planetary Science Letters*, 246:52–71, 2015.

J. Aurnou, V. Bertin, A. Grannan, S.Horn, and T. Vogt. Rotating thermal convection in liquid gallium: multi-modal flow, absent steady columns. *J. Fluid Mech.*, 846:846–876, 2018.

J. M. Aurnou. Planetary core dynamics and convective heat transfer scaling. *Geophys. Astrophys. Fluid Dyn.*, 101:327–345, 2007.

J. M. Aurnou, S. Horn, and J. Julien. Free-fall transport predictions in rapidly rotating turbulent convection systems. In prep, 2020.

J. Bailon-Cuba, M. Emran, and J. Schumacher. Aspect ratio dependence of heat transfer and large-scale flow in turbulent convection. *J. Fluid Mech.*, 655:152–173, 2010.

V. Barcilon and J. Pedlosky. On the steady motions produced by a stable stratification in a rapidly rotating fluid. *J. Fluid Mech.*, 29:673–690, 1967.

A. Barker, A. Dempsey, and Y. Lithwick. Theory and simulations of rotating convection. *Astrophys. J.*, 791(13), August 2014.

G. Batchelor. *The Theory of Homogeneous Turbulence*. Cambrdige University Press, 1953.

N. Becker, J. Scheel, M. Cross, and G. Ahlers. Effect of the centrifugal force on domain chaos in Rayleigh-Bénard convection. *Phys. Rev. E*, 73, 2006.

P. Bell and A. Soward. The influence of surface topography on rotating convection. *J. Fluid Mech.*, 313:147–180, 1996.

E. R. Benton and A. Clark. Spin-up. *Ann. Rev. of Fluid Mech.*, 6(1):257–280, 1974.

J. Bloxham and D. Gubbins. The secular variation of Earth's magnetic field. *Nature*, 317 (31), October 1985.

J. Bloxham and A. Jackson. Time-dependent mapping of the magnetic field at the core-mantle boundary. *J. Geophys. Res. Solid Earth*, 97:19537–19563, 1992.

J. Bloxham, D. Gubbins, and A. Jackson. Geomagnetic secular variation. *Philosophical Transactions Of The Royal Society Of London*, 329(1606):415–502, 1989.

G. Boer and T. Shepherd. Large-scale two-dimensional turbulence in the atmosphere. *J. Atmos. Sci.*, 40:164–184, 1984.

G. Boffetta and R. Ecke. Two-dimensional turbulence. *Ann. Rev. Fluid Mech.*, 44:427–451, January 2012.

M. Bouffard, G. Choblet, S. Labrosse, and J. Wicht. Chemical convection and stratification in the Earth's outer core. *Fronteirs in Earth Science*, 7(99), 2019.

A. Bracco and J. C. McWilliams. Reynolds-number dependency in homogeneous, stationary two-dimensional turbulence. *J. Fluid Mech.*, 646:517–526, 2010.

S. Braginsky. Self-excitation of a magnetic field during motion of a highly conducting fluid. *Soviet Physics*, 20(3):726, 1965.

S. Braginsky and V. Meytlis. Local turbulence in the Earth's core. *Geophys. Astrophys. Fluid Dyn.*, pages 71–87, 1990.

S. Braginsky and P. Roberts. A model-Z geodynamo. *Geophys. Astrophys. Fluid Dyn.*, 38: 327–349, 1987.

E. Brandes and G. Brook. *Smithells Metals Reference Book*. 7th edition, 1992.

D. Brito, J. M. Aurnou, and P. Cardin. Turbulent viscosity measurements relevant to planetary core-mantle dynamics. *Phys. Earth Planet. Inter.*, 141(1):3–8, 2004.

E. Brown, D. Funfschilling, and G. Ahlers. Anomalous Reynolds-number scaling in turbulent Rayleigh-Bénard convection. *J. Stat. Mech.*, 2007.

B. Buffett. The thermal state of Earth's core. *Science*, 299(5613):167501677, March 2003.

B. Buffett and U. Christensen. Magnetic and viscous coupling at the core-mantle boundary: inferences from observations of Earth's rotation. *Geophys. J. Int.*, 171:145–152, 2007.

F. Burmann and J. Noir. Effects of bottom topography on the spin-up in a cylinder. *Phys. Fluids*, 30(106601), 2018.

F. Busse and C. Carrigan. Laboratory simulation of thermal convection in rotating planets and stars. *Science*, 191(4222):81–83, 1976.

F. H. Busse. Thermal instabilities in rapidly rotating systems. *J. Fluid Mech.*, 44(3):441–460, November 1970.

B. Caistaing, G. Gunaratne, L. Kadanoff, A. Libchaber, and F. Heslot. Scaling of hard thermal turbulence in Rayleigh-Bénard convection. *J. Fluid Mech.*, 204(1-30), 1989.

M. Calkins. Quasi-geostrophic dynamo theory. *Phys. Earth Planet. Inter.*, 276:182–189, March 2018.

M. Calkins, J. Aurnou, J. Eldredge, and K. Julien. The influence of fluid properties on the morphology of core turbulence and the geomagnetic field. *Earth and Planetary Science Letters*, 359-360:55–60, 2012a.

M. Calkins, J. Noir, J. Eldredge, and J. M. Aurnou. The effects of boundary topography on convection in Earth's core. *Geophys. J. Int.*, 189:799–814, 2012b.

M. Calkins, K. Julien, S. Tobias, and J. Aurnou. A multi-scale dynamo model driven by quasigeostrophic convection. *J. Fluid Mech.*, 780(143-166), 2015.

H. Cao, R. Yadav, and J. Aurnou. Geomagnetic polar minima do not arise from steady meridional circulation. *Proc. Natl. Acad. Sci.*, 44:11186–11191, October 2018.

X. Capet, P. Klein, B. Hua, G. Lapeyre, and J. McWilliams. Surface kinetic energy transfer in surface quasi-geostrophic flows. *J. Fluid Mech.*, 604:165–174, 2008.

P. Cardin and P. Olson. Chaotic thermal convection in a rapidly rotating spherical shell: consequences for flow in the outer core. *Phys. Earth Planet. Inter.*, 82:235–259, 1994.

C. Carrigan and F. Busse. An experimental and theoretical investigation of the onset of convection in rotating spherical shells. *J. Fluid Mech.*, 126:287–305, 1983.

D. Cébron and R. Hollerbach. Tidally driven dynamos in a rotating sphere. *Astrophys. J. Let.*, 789(1):L25, 2014.

D. Cébron, M. Le Bars, C. Moutou, and P. Le Gal. Elliptical instability in terrestrial planets and moons. *Astro. Astrophys.*, 539:A78, 2012.

D. Cébron, R. Laguerre, J. Noir, and N. Schaeffer. Precessing spherical shells: flows, dissipation, dynamo and the lunar core. *Geophys. J. Int.*, 219:S34–S57, January 2019.

S. Chandrasekhar. *Hydrodynamic and Hydromagnetic Stability.* Dover Publications, 1961.

J. S. Cheng, S. Stellmach, A. Ribeiro, A. Grannan, E. King, and J. M. Aurnou. Laboratory-numerical models of rapidly rotating convection in planetary cores. *Geophys. J. Int.*, 201: 1–17, 2015.

J. S. Cheng, J. M. Aurnou, K. Julien, and R. Kunnen. A heuristic framework for next-generation models of geostrophic convective turbulence. *Geophys. Astrophys. Fluid Dyn.*, 112(4):277–300, 2018.

J. S. Cheng, M. Madonia, A. A. Guzman, and R. Kunnen. Laboratory exploration of heat transfer regimes in rapidly rotating turbulent convection. *Phys. Fluid Dynamics*, 2020. In Review.

F. Chilla and J. Schumacher. New perspectives in turbulent Rayleigh-Bénard convection. *Eur. Phys. J. E*, 35, 2012.

F. Chilla, S. Ciliberto, C. Innocenti, and E. Pampaloni. Boundary layer and scaling properties in turbulent thermal convection. *Il Nuovo Cimento D*, 15:1229–1249, 1993.

G. Choblet. On the scaling of heat transfer for mixed heating convection in a spherical shell. *Phys. Earth Planet. Inter.*, 2012.

U. Christensen, V. Holzwarth, and A. Reiners. Energy flux determines magnetic field strength of planets and stars. *Nature*, 457, January 2009.

U. R. Christensen. Zonal flow driven by strongly supercritical convection in rotating spherical shells. *J. Fluid Mech.*, 470(115-133), 2002.

U. R. Christensen. Dynamo scaling laws and applications to the planets. *Space Sci. Rev.*, pages 565–590, 2010.

U. R. Christensen. Planetary magnetic fields and dynamos. *Oxford Research Encyclopedia of Planetary Science*, 2019.

U. R. Christensen and J. Aubert. Scaling properties of convection-driven dynamos in rotating spherical shells and applications to planetary mangetic fields. *Geophys. J. Int.*, 166:97–114, 2006.

R. L. Comstock and B. G. Bills. A solar system survey of forced librations in longitude. *J. Geophys. Res. Planets*, 108:1–13, 2003.

J. Connerney, M. Acuna, P. Wasilewski, G. Kletetschka, N. Ness, H. Reme, R. Lin, and D. Mitchell. The global magnetic field of Mars and implications for crustal evolution. *Geophys. Res. Lett.*, 28(21):4015–4018, December 2001.

J. Connerney, S. Kotsiaros, R. Oliversen, J. Espley, J. Joergensen, P. Joergensen, J. Merayo, J. Bloxham, K. Moore, S. Bolton, and S. Levin. A new model of Jupiter's magnetic field from Juno's first nine orbits. *Geophys. Res. Lett.*, March 2018.

C. Constable, C. Johnson, and S. Lund. Global geomagnetic field models for the past 3000 years: transient for permanent flux lobes? *Philosophical Transactions Of The Royal Society Of London*, 358(1768):991–1008, 2000.

J. Curbelo, J. Lopez, A. Mancho, and F. Marques. Confined rotating convection with large Prandtl number: Centrifugal effects on wall modes. *Phys. Rev. E*, 89, 2014.

B. Cushman-Roisin and J. Beckers. *Introduction to geophysical fluid dynamics: physical and numerical aspects*, volume 101. Academic Press, 2011.

P. Davidson. *An Introduction to Magnetohydrodynamics*. Cambridge University Press University Press, 2001.

P. Davidson. *Turbulence in rotating, stratified, and electrically conducting fluids*. Cambridge University Press University Press, 2012.

C. Davies and D. Gubbins. A buoyancy profile for the Earth's core. *Geophys. J. Int.*, 187 (2):549–563, November 2011.

X. de Wit, A. A. Guzman, M. Madonia, J. S. Cheng, H. Clercx, and R. Kunnen. Turbulent rotating convection confined in a slender cylinder: the sidewall circulation. *Phys. Fluid Dynamics*, 2020. Submitted.

S. Ding, K. Chong, J. Shi, G. Ding, H. Lu, K. Xia, and J. Zhong. Anomalous vortex motion induced by asymmetric vorticity distribution in rapidly rotating thermal convection. *Phys. Fluid Dynamics*, 2020. In Review.

C. Doering, S. Toppaladoddi, and J. Wettlaufer. Absence of evidence for the ultimate regime in two-dimensional Rayleigh-bénard convection. *Phys. Rev. Lett.*, 123:259401, December 2019.

C. Doglioni, J. Pignatti, and M. Coleman. Why did life develop on the surface of the Earth in the Cambrian? *Geoscience Fronteirs*, 7(6):865–873, November 2016.

E. Dormy and D. Gérard-Varet. Time scales separation for dynamo action. *Eur. Phys. Lett.*, 81(64002), 2008.

E. Dormy, A. Soward, C. Jones, D. Jault, and P. Cardin. The onset of thermal convection in rotating spherical shells. *J. Fluid Mech.*, 501:43–70, 2004.

P. Driscoll and D. Bercovici. Divergent evolution of Earth and Venus: Influence of degassing, tectonics, and magnetic fields. *Icarus*, 226(2):1447–1464, December 2013.

P. Driscoll and D. Bercovici. On the thermal and magnetic histories of Earth and Venus: Influences of melting, radioactivity, and conductivity. *Phys. Earth Planet. Inter.*, 236: 36–51, November 2014.

P. Duck and M. Foster. Spin-up of homogeneous and stratified fluids. *Ann. Rev. of Fluid Mech.*, 33:231–263, 2001.

R. Ecke and J. Niemela. Heat transport in the geostrophic regime of rotating Rayleigh-Bénard convection. *Phys. Rev. Lett.*, 113(114301), 2014.

R. E. Ecke. Scaling of heat transport near onset in rapidly rotating convection. *Phys. Letters A*, 379:2221–2223, 2015.

W. Elsassar. On the origin of the Earth's magnetic field. *Phys. Rev.*, 55:489–498, 1939.

W. M. Elsasser. The Earth's interior and geomagnetism. *Reviews of Modern Physics*, 22(1), January 1950.

M. Evonuk. The role of density stratification in generating zonal flow structures in a rotating fluid. *Astrophys. J.*, 673(2):1154, 2008.

B. Favier, L. J. Silvers, and M. R. E. Proctor. Inverse cascade and symmetry breaking in rapidly rotating Boussinesq convection. *Phys. Fluids*, 9:096605, 2014.

C. Finlay and A. Jackson. Equatorially dominated magnetic field change at the surface of Earth's core. *Science*, 300:2084–2086, 2003.

C. C. Finlay, A. Jackson, N. Gillet, and N. Olsen. Core surface magnetic field evolution 2000-2010. *Geophys. J. Int.*, 189(2):761–781, 2012.

W. Folkner, C. Yoder, D. Yuan, E. Standish, and R. Preston. Interior structure and seasonal mass redistribution of Mars from radio tracking of Mars Pathfinder. *Science*, 278(5344): 1749–1752, 1997.

R. R. Fu, B. P. Weiss, D. L. Shuster, J. Gattacceca, T. L. Grove, C. Suavet, E. A. Lima, L. Li, and A. T. Kuan. An ancient core dynamo in asteroid Vesta. *Science*, 338:238–241, 2012.

D. Funfschilling, E. Brown, A. Nikolaenko, and G. Ahlers. Heat transport by turbulent Rayleigh-Bénard convection in cylindrical samples. *J. Fluid Mech.*, 536:145–154, 2005.

T. Gastine, L. Duarte, and J. Wicht. Dipolar versus multipolar dynamos: the influence of the background density stratification. *Astro. Astrophys.*, 546, 2012.

T. Gastine, J. Wicht, and J. Aurnou. Turbulent Rayleigh–Bénard convection in spherical shells. *J. Fluid Mech.*, 778:721–764, 2015.

T. Gastine, J. Wicht, and J. Aubert. Scaling regimes in spherical shell rotating convection. *J. Fluid Mech.*, pages 690–732, 2016.

N. Gillet and C. A. Jones. The quasi-geostrophic model for rapidly rotating spherical convection outside the tangent cylinder. *J. Fluid Mech.*, 554:343–369, 2006.

N. Gillet, D. Jault, E. Canet, and A. Fournier. Fast torsional waves and strong magnetic field within Earth's core. *Nature*, 465:74–77, 2010.

G. A. Glatzmaier. Geodynamo simulations-how realistic are they? *Ann. Rev. of Earth and Plan. Sci.*, 30:237–257, 2002.

G. A. Glatzmaier. *Introduction to modeling convection in planets and stars: Magnetic field, density stratification, rotation*. Princeton University Press, 2013.

G. A. Glatzmaier and C. Clune. Computational aspects of geodynamo simulations. *Comp. Sci. Eng.*, 2(61-67), 2000.

G. A. Glatzmaier and P. Roberts. An anelastic evolutionary geodynamo simulation driven by compositional and thermal convection. *Physica D*, 97:81–94, 1996.

G. Glatzmeier and P. Roberts. Rotation and magnetism of Earth's inner core. *Science*, 274: 1887–1891, 1996.

J. Glazier, T. Segawa, A. Naert, and M. Sano. Evidence against 'ultrahard' thermal turbulence at very high Rayleigh numbers. *Nature*, 398:307–310, 1999.

H. Goldstein, E. Knobloch, I. Mercader, and M. Net. Convection in a rotating cylinder. Part 1: Linear theory for moderate Prandtl numbers. *J. Fluid Mech.*, 248:583–604, 1993.

A. Grannan. *Characterizing Mechanically- and Convectively-Driven Geophysical Turbulence*. PhD thesis, University of California-Los Angeles, 2017.

A. Grannan, B. Favier, M. Le Bars, and J. M. Aurnou. Tidally forced turbulence in planetary interiors. *Geophys. J. Int.*, 208:1690–1703, December 2017.

A. M. Grannan, M. Le Bars, D. Cébron, and J. M. Aurnou. Experimental study of global-scale turbulence in a librating ellipsoid. *Phys. Fluids*, 26:126601, 2014.

H. P. Greenspan. On the non-linear interaction of inertial modes. *J. Fluid Mech.*, 36:257–264, 1969a.

H. P. Greenspan. *The Theory of Rotating Fluids*. Cambridge University Press, 1969b.

H. P. Greenspan and L. N. Howard. On a time-dependent motion of a rotating fluid. *J. Fluid Mech.*, 17(3):385–404, 1963.

I. Grooms, K. Julien, J. Weiss, and E. Knobloch. Model of convective Taylor columns in rotating Rayleigh-Bénard convection. *Phys. Rev. Lett.*, 104, 2010.

S. Grossman and D. Lohse. Prandtl and Rayleigh number dependence of the Reynolds number in turbulent thermal convection. *Phys. Rev. E*, 66, 2002.

S. Grossmann and D. Lohse. Scaling in thermal convection: a unifying theory. *J. Fluid Mech.*, 407:27–56, 2000.

D. Gubbins and J. Bloxham. Morphology of the geomagnetic field and implications for the geodynamo. *Nature*, 325:509–511, 1987.

C. Guervilly, P. Cardin, and N. Schaeffer. Turbulent convective length scales in planetary cores. *Nature*, 570:368–371, 2019.

T. Guillot. Interiors of giant planets: models and outstanding questions. *Ann. Rev. of Earth and Plan. Sci.*, 33:493–530, 2005.

J. Hart. On the influence of centrifugal buoyancy on rotating convection. *J. Fluid Mech.*, 403:133–151, 2000.

J. Hart and D. Ohlsen. On the thermal offset in turbulent rotating convection. *Phys. Fluids*, 11(8):2101–2107, 1999.

E. K. Hawkins, J. S. Cheng, T. Pilegard, S. Stellmach, and J. M. Aurnou. Separate regime transitions of heat transfer and bulk dynamics in models of planetary core convection. *Geophys. J. Int.*, 2020. In prep.

J. Herring and J. McWilliams. *Lecture Notes on Turbulence*. World Scientific, 1989.

J. Herrmann and F. Busse. Asymptotic theory of wall-attached convection in a rotating fluid layer. *J. Fluid Mech.*, 255:183–194, 1993.

R. Hide. Jupiter and Saturn. *Proc. R. Soc. Lond. A.*, 336:63–84, 1974.

G. M. Homsy and J. L. Hudson. Centrifugally driven thermal convection in a rotating cylinder. *J. Fluid Mech.*, 35:33–52, 1967.

S. Horn and J. Aurnou. Regimes of Coriolis-Centrifugal convection. *Phys. Rev. Lett.*, 120 (204502), 2018.

S. Horn and J. M. Aurnou. Rotating convection with centrifugal buoyancy: Numerical predictions for laboratory experiments. *Phys. Rev. Fluids*, 4, 2019.

S. Horn and O. Shishkina. Rotating non-Oberbeck-Boussinesq Rayleigh-Bénard convection in water. *Phys. Fluids*, 26(055111), 2014.

Y. Hu, R. E. Ecke, and G. Ahlers. Convection under rotation for Prandtl numbers near 1: Linear stability, wave-number selection, and pattern dynamics. *Phys. Rev. E*, 55:6928–6949, 1997.

G. Hulot, C. Eymin, B. Langlais, M. Mandea, and N. Olsen. Small-scale structure of the geodynamo inferred from Oersted and Magsat satellite data. *Nature*, 416:620–623, 2002.

G. Hulot, C. Finlay, C. Constable, N. Olsen, and M. Mandea. The magnetic field of planet Earth. *Space Sci. Rev.*, 152:159–222, 2010.

A. Ingersoll and D. Pollard. Motion in the interiors and atmospheres of Jupiter and Saturn: scale analysis, anelastic equations, barotropic stability criterion. *Icarus*, 52:62–80, 1982.

A. Jackson. Intense equatorial flux spots on the surface of the Earth's core. *Nature*, 424: 760–763, 2003.

C. A. Jones. *Core Dynamics*, volume 8. Elsevier, 2009.

C. A. Jones. Planetary magnetic fields and fluid dynamos. *Ann. Rev. of Fluid Mech.*, 43(1): 583–614, 2011.

C. A. Jones. *Treatise on Geophysics*, pages 115–159. Elsevier, 2015.

C. A. Jones, A. M. Soward, and A. I. Mussa. The onest of thermal convection in a rapidly rotating sphere. *J. Fluid Mech.*, 405:157–179, 2000.

K. Julien and E. Knobloch. Strongly nonlinear convection cells in a rapidly rotating fluid layer: the tilted f-plane. *J. Fluid Mech.*, 360:141–178, 1998.

K. Julien, S. Legg, J. McWilliams, and J. Werne. Rapidly rotating turbulent Rayleigh-Bénard convection. *J. Fluid Mech.*, 322:243–273, 1996.

K. Julien, E. Knobloch, and J. Werne. *Turbulence and Shear Flows, I*, chapter Reduced equations for rotationally constrained convection. Begell House, 101-106 edition, 1999.

K. Julien, E. Knobloch, A. M. Rubio, and G. M. Vasil. Heat transport in low-Rossby-number Rayleigh-Bénard convection. *Phys. Rev. Lett.*, 109(254503), 2012a.

K. Julien, A. M. Rubio, I. Grooms, and E. Knobloch. Statistical and physical balances in low-Rossby-number Rayleigh-Bénard convection. *Geophys. Astrophys. Fluid Dyn.*, 106:4-5: 392–428, 2012b.

K. Julien, J. Aurnou, M. Calkins, E. Knobloch, P. Marti, S. Stellmach, and G. Vasil. A nonlinear model for rotationally constrained convection with Ekman pumping. *J. Fluid Mech.*, 798:50–87, 2016.

E. Kaplan, N. Schaeffer, J. Vidal, and P. Cardin. Subcritical thermal convection of liquid metals in a rapidly rotating sphere. *Phys. Rev. Lett.*, 119(094501), 2017.

S. Katsanoulis, M. Farazmand, M. Serra, and G. Haller. Vortex boundaries as barriers to diffusive vorticity transport in two-dimensional flows. *Phys. Rev. Fluids*, 5(024701), 2020.

R. M. Kerr and J. R. Herring. Prandtl number dependence of Nusselt number in direct numerical simulations. *J. Fluid Mech.*, 419:325–344, 2000.

E. King. *An Investigation of Planetary Convection: The Role of Boundary Layers*. PhD thesis, University of California-Los Angeles, 2009.

E. King and J. M. Aurnou. Turbulent convection in liquid metal with and without rotation. *Proc. Natl. Acad. Sci.*, 110:6688–6693, January 2015.

E. King and B. Buffett. Flow speeds and length scales in geodynamo models: the role of viscosity. *Earth and Planetary Science Letters*, 371:156–162, 2013.

E. King, S. Stellmach, J. Noir, U. Hansen, and J. M. Aurnou. Boundary layer control of rotating convection systems. *Nature*, 457(7227):301–304, 01 2009.

E. King, K. Soderlund, U. R. Christensen, J. Wicht, and J. M. Aurnou. Convective heat transfer in planetary dynamo models. *Geochemistry Geophysics Geosystems*, 11(6), June 2010.

E. King, S. Stellmach, and J. M. Aurnou. Heat transfer by rapidly rotating Rayleigh-Bénard convection. *J. Fluid Mech.*, 691:568–582, 2012.

M. Korte and M. Mandea. Magnetic poles and dipole tilt variation over the past decades to millenia. *Earth, planets and space*, pages 937–948, 2008.

E. L. Koschmieder. On convection on a uniformly heated rotating plate. *Beitr. Phys. Atmos.*, 40:216–225, 1967.

R. H. Kraichnan. Turbulent thermal convection at arbitrary prandtl number. *Phys. Fluids*, 5:1374–1389, 1962.

F. Krause and K. Radler. *Mean-field magnetohydrodynamics and dynamo theory*. Elsevier, 2016.

W. Kuang and J. Bloxham. An Earth-like numerical dynamo model. *Nature*, 389:371–371, 1997.

P. K. Kundu, I. M. Cohen, and D. R. Dowling. *Fluid Mechanics*. Academic Press, 5th edition, 2012.

R. Kunnen, B. Geurts, and H. Clercx. Experimental and numerical investigation of turbulent convection in a rotating cylinder. *J. Fluid Mech.*, pages 445–476, 2010.

R. Kunnen, R. Stevens, J. Overkamp, C. Sun, G. van Heijst, and H. Clercx. The role of Stewartson and Ekman layers in turbulent rotatin Rayleigh-Bénard convection. *J. Fluid Mech.*, 688(422-442), 2011.

R. Kunnen, R. Ostilla-Monico, E. V. D. Poel, R. Verzicco, and D. Lohse. Transition to geostrophic convection: the role of boundary conditions. *J. Fluid Mech.*, 799:413–432, 2016.

E. Kunze and S. G. L. Smith. The role of small-scale topography in turbulent mixing of the global ocean. *Oceanography-Washington DC-Oceanography Society-*, 17(1):55–64, 2004.

B. Langlais, V. Lesur, M. Purucker, J. Connerney, and M. Mandea. Crustal magnetic fields of terrestrial planets. *Space Sci. Rev.*, 152:223–249, 2010.

M. Le Bars, D. Cébron, and P. Le Gal. Flows driven by libration, precession, and tides. *Ann. Rev. of Fluid Mech.*, 47:163–194, 2015.

D. Lide. *Handbook of Chemistry and Physics*. CRC Press, 2000.

R. Lillis, D. Mitchell, R. Lin, J. Connerney, and M. Acuna. Mapping crustal magnetic fields at Mars using electron reflectometry. *Geophys. Res. Lett.*, 31(15), August 2004.

P. Livermore, R. Hollerbach, and C. Finlay. An accelerating high-latitude jet in Earth's core. *Nat. Geosci*, 10:62–68, 2017.

R. S. Long, J. E. Mound, C. J. Davies, and S. M. Tobias. Scaling behaviour in spherical shell rotating convection with fixed-flux thermal boundary conditions. *J. Fluid Mech.*, 2020. Submitted.

J. Lopez and F. Marques. Centrifugal effects in rotating convection: nonlinear dynamics. *J. Fluid Mech.*, 628(269), 2009.

J. Lopez, A. Rubio, and F. Marques. Travelling circular waves in axisymmetric rotating convection. *J. Fluid Mech.*, 569(331), 2006.

W. V. R. Malkus. The heat transport and spectrum of thermal turbulence. *Proc. R. Soc. A*, 225:196–212, 1954.

M. Mandea and M. Korte, editors. *Geomagnetic Observations and Models*. Springer New York, 2011.

F. Marques, I. Mercader, O. Batiste, and J. Lopez. Centrifugal effects in rotating convection: axisymmetric states and three-dimensional instabilities. *J. Fluid Mech.*, 580:303–318, 2007.

P. Marti, M. Calkins, and K. Julien. A computationally efficient spectral method for modeling core dynamics. *Geochemistry Geophysics Geosystems*, 17(8):3031–3053, 2016.

M. W. McElhinny and W. E. Senanayake. Paleomagnetic evidence for the existence of the geomagnetic field 3.5 ga ago. *Journal of Geophysical Research: Solid Earth*, 85(B7): 3523–3528, 1980.

P. McFadden, R. Merrill, M. McElhinny, and S. Lee. Reversal's of the Earth's magnetic field and temporal variations of the dynamo families. *J. Geophys. Res.*, 96(B3):3923–3933, 1991.

J. McWilliams. The elemental shear dynamo. *J. Fluid Mech.*, 699:414–452, 2012.

J. McWilliams. Atmospheric and oceanic turbulence. Lecture Notes, 2017.

J. McWilliams, J. Weiss, and I. Yavneh. Anisotropy and coherent vortex structures in planetary trubulence. *Science*, 264(5157):410–413, 1994.

J. C. McWilliams. *Fundamentals of Geophysical Fluid Dynamics*. Cambridge University Press, 2006.

R. T. Merrill, M. W. McElhinny, and P. L. McFadden. *The Magnetic Field of the Earth: Paleomagnetism, the Core and the Deep Mantle*. Academic Press, 1998.

K. Moffatt and E. Dormy. *Self-exciting fluid dynamos*. Cambrdige University Press, 2019.

K. Moore, R. Yadav, L. Kulowski, H. Cao, J. Bloxham, J. Connerny, S. Kotsiaros, J. Jorgensen, J. Merayo, D. Stevenson, S. Bolton, and S. Levin. A complex dynamo inferred from the hemispheric dichotomy of Jupiter's magnetic field. *Nature*, 561:76–78, 2018.

J. Mouel, C. Narteau, M. Greff-Lefftz, and M. Holschneider. Dissipation at the core-mantle boundary on a small-scale topography. *J. Geophys. Res.*, 111(B04):413, 2006.

J. L. L. Mouël, C. Narteau, M. Greff-Lefftz, and M. Holschneider. Dissipation at the core-mantle boundary on a small-scale topography. *J. Geophys. Res. Solid Earth*, 111(B4): B04413, 2006.

Y. Nakagawa and P. Frenzen. A theoretical and experimental study of cellular convection in rotating fluids. *Tellus*, 7:1–21, 1955.

H. Nataf and N. Schaeffer. Turbulence in the core. In G. Schubert, editor, *Treatise on Geophysics*, volume 8, pages 161–181. Oxford: Elsevier, 2 edition, 2015.

J. Niemela, L. Skrbek, K. Sreenivasan, and R. Donnellly. Turbulent convection at very high Rayleigh numbers. *Nature*, 404:837–840, 2000.

F. Nimmo. Why does Venus lack a magnetic field? *Geology*, 30(11):987–990, 2002.

J. Noir, F. Hemmerlin, J. Wicht, S. Baca, and J. M. Aurnou. An experimental and numerical study of librationally driven flow in planetary cores and subsurface oceans. *Physics of the Earth and Planetary Interiors*, 173:141–152, 2009.

J. Noir, M. Calkins, M. Lasbleis, J. Cantwell, and J. M. Aurnou. Experimental study of libration-driven zonal flows in a straight cylinder. *Physics of the Earth and Planetary Interiors*, 182:98–1106, 2010.

N. Olsen and C. Stolle. Satellite geomagnetism. *Ann. Rev. of Earth and Plan. Sci.*, 40: 441–465, May 2012.

P. Olson and H. Amit. Changes in Earth's dipole. *Naturwissenschaften*, 93:519–542, 2006.

P. Olson and J. M. Aurnou. A polar cortex in the Earth's core. *Nature*, 402:170–173, 1999.

P. Olson, U. Christensen, and G. A. Glatzmaier. Numerical modeling of the geodynamo: mechanisms of field generation and equilibrium. *J. Geophys. Res.*, 104:10383–10404, 1999.

A. Or and F. Busse. Convection in a rotating cylindrical annulus. II. Transitions to asymmetric and vacillating flow. *J. Fluid Mech.*, 174:313–326, 1987.

J. O'Rourke, C. Gillmann, and P. Tackley. Prospects for an ancient dynamo and modern crustal remnant megnetism on Venus. *Phys. Earth Planet. Inter.*, 502:46–56, 2018.

A. Pais and G. Hulot. Length of day decade variations, torsional oscillations and inner core superrotation: evidence from recovered core surface zonal flows. *Phys. Earth Planet. Inter.*, 118:291–316, 2000.

R. Panton. *Incompressible Flow*. Wiley and Sons, 4th edition, 2013.

E. Parker. Hydromagnetic dynamo models. *Astrophys. J.*, 121:293–314, 1955.

J. Pedlosky. An intertial theory of the equtorial undercurrent. *J. Phys. Oceanography*, 17: 1978–1985, 1987.

A. Pellew and R. V. Southwell. On maintained convectie motion in a fluid heated from below. *Proc. R. Soc. A*, 176:312–343, 1940.

M. Plumley and K. Julien. Scaling laws in Rayleigh-Bénard convection. *Earth and Space Science*, 2019.

M. Plumley, K. Julien, P. Marti, and S. Stellmach. The effects of Ekman pumping on quasi-geostrophic Rayleigh-Bénard convection. *J. Fluid Mech.*, 803:51–71, 2016.

M. Plumley, K. Julien, P. Marti, and S. Stellmach. Sensitivity of rapidly rotating Rayleigh-Bénard convection to Ekman pumping. *Phys. Rev. Fluids*, 2(094801), 2017.

J. P. Poirier. *Introduction to the physics of Earth's interior*. Cambrdige University Press, 2nd edition, 2000.

M. Pozzo, C. Davies, D. Gubbins, and D. Alfé. Thermal and electrical conductivity of iron at Earth's core conditions. *Nature*, 485:355–358, 2012.

C. Priestly. Buoyant motion in a turbulent environment. *Australian J. Phys*, 6:279–290, 1953.

I. Prigogine and I. Stengers. *Out of order chaos: man's new dialogue with nature*. New York, Bantam, 1984.

J. Proudman. On the motions of solids in a liquid possessing vorticity. *Proc. R. Soc. Lond. A.*, (A92):408–424, 1916.

X. L. Qiu and P. Tong. Large-scale velocity structures in turbulent thermal convection. *Phys. Rev. E*, 64, 2001a.

X. L. Qiu and P. Tong. Onset of coherent oscillations in turbulent Rayleigh Bénard convection. *Phys. Rev. Lett.*, 87(9), 2001b.

K. Radler. *Magnetohydrodynamics*, chapter Mean-field dynamo theory: early ideas and today's problems, pages 55–72. Springer Dordrecht, 2007.

H. Rajaei, K. Alards, R. Kunnen, and H. Clercx. Velocity and acceleration statistics in rapidly rotating Rayleigh–Bénard convection. *J. Fluid Mech.*, 857:374–397, 2018.

P. Rhines. Geostrophic turbulence. *Ann. Rev. Fluid Mech.*, 11(1):401–441, 1979.

P. Roberts. *Treatise on Geophysics*, chapter Theory of the Geodynamo, pages 57–90. Elsevier, 2015.

P. Roberts and J. Aurnou. On the theory of core-mantle coupling. *Geophys. Astrophys. Fluid Dyn.*, 106(2):157–230, 2012a.

P. Roberts and J. M. Aurnou. On the theory of core-mantle coupling. *Geophys. Astrophys. Fluid Dyn.*, 106:157–230, 2012b.

P. H. Roberts and E. M. King. On the genesis of the Earth's magnetism. *Rep. Prog. Phys.*, 76(9):096801, 2013.

H. T. Rossby. A study of Bénard convection with and without rotation. *J. Fluid Mech.*, 36 (2):309–335, 1969.

A. M. Rubio, K. Julien, E. Knobloch, and J. B. Weiss. Upscale energy transfer in three-dimensional rapidly rotating turbulent convection. *Phys. Rev. Lett.*, 112:144501, 2014.

S. Sakai. The horizontal scale of rotating convection in the geostrophic regime. *J. Fluid Mech.*, 333:85–95, 1997.

N. Schaeffer, D. Jault, H. Nataf, and A. Fournier. Geodynamo simulations with vigorous convection and low viscosity. *Geophys. J. Int.*, 2017. Submitted.

S. Schmitz and A. Tilgner. Transitions in turbulent-rotating Rayleigh-Bénard convection. *Geophys. Astrophys. Fluid Dyn.*, 104(5-6):481–489, September 2010.

G. Schubert. *Mantle Convection in the Earth and Planets*. Cambrdige University Press, 2001.

G. Schubert and K. Soderlund. Planetary magnetic fields: observations and models. *Phys. Earth Planet. Inter.*, 187:92–108, 2011.

T. Schwaiger, T. Gastine, and J. Aubert. Force balance in numerical geodynamo simulations: a systematic study. *Geophys. J. Int.*, 219:101–114, April 2019.

X. Shang, X. Qiu, P. Tong, and K. Xia. Measured local heat transport in turbulent Rayleigh-Bénard convection. *Phys. Rev. Lett.*, 90(7), 2003.

A. Sheyko, C. Finlay, J. Favre, and A. Jackson. Scale separated low viscosity dynamos and dissipation within the Earth's core. *Sci. Reports*, 8(1):12566, 2018.

B. Shraiman and E. Siggia. Heat transport in high-Rayleigh-number convection. *Phys. Rev. A*, 42(6):3650–3653, 1990.

S. Smith. The formation of Stewartson layers in a rotating fluid. *J. Mech. Appl. Math*, 40 (4):575–594, 1987.

D. Smylie and M. Rochester. Compressibility, core dynamics and the subseismic wave equation. *Phys. Earth Planet. Inter.*, 24(4):308–319, 1981.

K. Soderlund, E. King, and J. M. Aurnou. The influence of magnetic fields in planetary dynamo models. *Earth and Planetary Science Letters*, 333:9–20, 2012.

K. Soderlund, A. Sheyko, E. King, and J. M. Aurnou. The competition between Lorentz and Coriolis forces in planetary dynamos. *Pro. Earth Planet. Sci.*, 2(24), 2015.

X. Song and P. Richards. Seismological evidence for differential rotation of the Earth's inner core. *Nature*, 382:221–224, July 1996.

K. Spells. The determination of the viscosity of liquid gallium over an extended range of temperature. *Proc. Phys. Soc.*, 48(2):299–311, 1936.

E. A. Spiegel. Convection in stars: I. Basic Boussinesq convection. *Ann. Rev. of Astro. and Astrophys.*, 9:323–352, 1971.

M. Sprague, K. Julien, E. Knobloch, and J. Werne. Numerical simulation of an asymptotically reduced system for rotationally constrained convection. *J. Fluid Mech.*, 551:141–174, 2006.

B. Sreenivasan. Modelling the geodynamo: progress and challenges. *Curr. Sci.*, 99(12), December 2010.

F. D. Stacey. *Physics of the Earth*. Brookfield Press, 3rd edition, 1992.

F. D. Stacey and P. M. Davis. *Physics of the Earth*. Cambrdige University Press, 4 edition, 2008.

S. Stanley and G. A. Glatzmaier. Dynamo models for planets other than Earth. *Space Sci. Rev.*, 152(1-4):617–649, 2010.

S. V. Starchenko. Analytic scaling laws in planetary dynamo models. *Geophys. Astrophys. Fluid Dyn.*, 113(1-2):71–79, 2019.

S. V. Starchenko and C. A. Jones. Typical velocities and magnetic field strengths in plantary interiors. *Icarus*, pages 426–435, 2002.

S. Stellmach and U. Hansen. Cartesian convection driven dynamos at low Ekman number. *Phys. Rev. E*, 70, 2004.

S. Stellmach and U. Hansen. An efficient spectral method for the simulation of dynamos in Cartesian geometry and its implementation on massively parallel computers. *Geochemistry Geophysics Geosystems*, 9(5), 2008.

S. Stellmach, M. Lischper, K. Julien, G. Vasil, J. S. Cheng, A. Ribeiro, E. M. King, and J. M. Aurnou. Approaching the asymptotic regime of rapidly rotating convection: Boundary layers versus interior dynamics. *Phys. Rev. Lett.*, 113:254501, 2014.

R. Stevens, H. Clercx, and D. Lohse. Heat transport and flow structure in rotating Rayleigh-Bénard convection. *Eur. J. Mech Fluids*, 40:41–49, 2013a.

R. Stevens, E. V. D. Poel, S. Grossmann, and D. Lohse. The unifying theory of scaling in thermal convection: the updated prefactors. *J. Fluid Mech.*, 730:295–308, 2013b.

C. Sun, K. Xia, and P. Tong. Three-dimensional flow structures and dynamics of turbulent thermal convection in a cylindrical cell. *Phys. Rev. E*, 72(026302), 2005.

J. Tarduno. Geodynamo history preserved in single silicate crystals: origins and long-term mantle control. *Elements*, 5(4):217–222, 2009.

J. Tarduno, R. Cottrell, M. Watkeys, and D. Bauch. Geomagnetic field strength 3.2 billion years ago by single silicate crystals. *Nature*, pages 657–660, 2007.

J. Tarduno, R. D. Cottrell, W. J. Davis, F. Nimmo, and K. Richard. A Hadean to Paleoarchean geodynamo recorded by single zircon crystals. *Science*, 349:521–524, 2015.

G. Taylor. Motion of solids in fluids when the flow is not irrotational. *Proc. R. Soc. Lond. A.*, (A93):99–113, 1917.

A. Tilgner. Precession driven dynamos. *Phys. Fluids*, 17:034104, 2005.

H. Tkalcic, M. Young, T. Bodin, S. Ngo, and M. Sambridge. The shuffling rotation of the Earth's inner core revealed by earthquake doublets. *Nat. Geosci*, 6:497–502, May 2013.

M. Torrest and J. Hudson. The effect of centrifugal convection on the stability of a rotating fluid heated from below. *Appl. Sci. Res*, 29(273), 1974.

D. Turcotte and G. Schubert. *Geodynamics*. Cambrdige University Press, 2002.

R. Verzicco and K. R. Sreenivasan. A comparison of turbulent thermal convection between conditions of constant temperature and constant heat flux. *J. Fluid Mech.*, 595:203–219, 2008.

J. Vidal and N. Schaeffer. Quasi-geostrophic models in Earth's fluid core with an outer stably stratified layer. *Geophys. J. Int.*, 202(3):2182–2193, 2015.

J. Vidale, D. Dodge, and P. Earle. Slow differential rotation of the Earth's inner core indicated by temporal changes in scattering. *Nature*, 405(6875):445–448, 2000.

T. Vogt, S. Horn, A. Grannan, and J. Aurnou. Jump rope vortex in liquid metal convection. *Proc. Natl. Acad. Sci.*, 2018.

A. Warn-Varnas, W. Fowlis, S. Piacsek, and S. Lee. Numerical solutions and laser-doppler measurements of spin-up. *J. Fluid Mech.*, 85:609–639, 1978.

Y. Wei, Z. Pu, Q. Zong, W. Wan, Z. Ren, M. Fraenz, E. Dubinin, F. Tian, Q. Shi, S. Fu, and M. Hong. Oxygen escape from the Earth during geomagnetic reversals: implications to mass extinction. *Earth and Planetary Science Letters*, 394:94–98, 2014.

P. Weidman. On the spin-up and spin-down of a rotating fluid. Part 2: Measurements and stability. *J. Fluid Mech.*, 77:709–735, 1976.

S. Weiss and G. Ahlers. Heat transport by turbulent rotating Rayleigh-Bénard convection and its dependence on the aspect ratio. *J. Fluid Mech.*, 684:407–426, 2011.

S. Weiss, R. Stevens, , J. Zhong, H. Clercx, D. Lohse, and G. Ahlers. Finite-size effects lead to supercritical bifurcations in turbulent rotating Rayleigh-Bénard convection. *Phys. Rev. Lett.*, 105, 2010.

J. Wicht. Inner-core conductivity in numerical dynamo simulations. *Phys. Earth Planet. Inter.*, 132:281–302, 2002.

J. Wicht and S. Sanchez. Advances in geodynamo modelling. *Geophys. Astrophys. Fluid Dyn.*, page May, 2019.

H. Willoughby. Gradient balance in tropical cyclones. *J. Atmos. Sci.*, 265, 1990.

H. Xi, S. Lam, and K. Xia. From laminar plumes to organized flows: the onset of large-scale circulation in turbulent thermal convection. *J. Fluid Mech.*, 503:47–56, 2004.

H. Xi, Q. Zhou, and K. Xia. Azimuthal motion of the mean wind in turbulent thermal convection. *Phys. Rev. E*, 73, 2006.

R. Yadav, T. Gastine, U. R. Christensen, S. Wolk, and K. Poppenhaeger. Approaching a realistic force balance in geodynamo simulations. *Proc. Natl. Acad. Sci.*, 113(43):12065–12070, 2016.

Y. Yeh and H. Cummins. Localized fluid flow measurements with an He–Ne laser spectrometer. *Applied Phys. Letters*, 4(10):176–178, 1964.

C. Yoder, A. Konopliv, D. Yuan, E. Standish, and W. Folkner. Fluid core size of Mars from detection of the solar tide. *Science*, 300(5617):299–303, 2003.

T. Yousef, T. Heinemann, A. Schekochinin, N. Kleeorin, I. Rogachevskii, A. Iskakov, S. Cowley, and J. McWilliams. Generation of magnetic field by combined action of turbulence and shear. *Phys. Rev. Lett.*, 100(184501), 2008.

K. Zhang and X. Liao. The onset of convection in rotating circular cylinders with experimental boundary conditions. *J. Fluid Mech.*, 622:63–73, 2009.

K. Zhang and G. Schubert. Magnetohydrodynamics in rapidly rotating spherical systems. *Ann. Rev. Fluid Mech.*, 2000.

X. Zhang, D. van Gils, S. Horn, M. Wedi, L. Zwirner, G. Ahlers, R. Ecke, S. Weiss, E. Bodenschatz, and O. Shishkina. Boundary zonal flow in rotating turbuent Rayleigh-Bénard convection. *Phys. Rev. Lett.*, 2020. In press.

F. Zhong, R. E. Ecke, and V. Steinberg. Rotating Rayleigh Bénard convection: asymmetric modes and vortex states. *J. Fluid Mech.*, 249(135-159), 1993.

T. Zurner, F. Schindler, T. Vogt, S. Eckert, and J. Shumacher. Combined measurement of velocity and temperature in liquid metal convection. *J. Fluid Mech.*, 876:1108–1128, 2019.